EMERSON ELECTRIC OF ST. LOUIS

ELECTRONICS AND SPACE DIVISION

8100 florissant avenue. st. louis , mo., 63136 colfax 1-180

NASA-CR-65010

Report Number 1675

PERFORMANCE EVALUATION OF "THERMO-LAG" MATERIAL FOR ENTRY HEAT PROTECTION OF ADVANCED MANNED SPACECRAFT

FINAL REPORT

October 1, 1962 - January 31, 1964

Volume Two - Thermal Investigations

FACILITY FORM 602

N65-24847 (ACCESSION NUMBER)

319 (PAGES)

CR 65010 (NASA CR OR TMX OR AD NUMBER)

1 (THRU)

(CODE)

23 (CATEGORY)

GPO PRICE $ _____

OTS PRICE(S) $ _____

Hard copy (HC) 7.00

Microfiche (MF) 1.75

Prepared For

National Aeronautics and Space Administration

Manned Spacecraft Center

Houston 1, Texas

EMERSON ELECTRIC OF ST. LOUIS
ELECTRONICS AND SPACE DIVISION

8100 florissant avenue, st. louis 36, mo., colfax 1-1800

Report Number 1675

PERFORMANCE EVALUATION OF "THERMO-LAG" MATERIAL FOR ENTRY HEAT PROTECTION OF ADVANCED MANNED SPACECRAFT

FINAL REPORT
October 1, 1962 - January 31, 1964

Volume Two - Thermal Investigations

Prepared For
National Aeronautics and Space Administration
Manned Spacecraft Center
Houston 1, Texas

28 February 1964

TABLE OF CONTENTS

Section	Title	Page
I	INTRODUCTION	1-1
II	MATERIAL PROPERTIES AND CHARACTERISTICS	2-1
	Solid Phase Thermal Properties	2-3
	Thermal Conductivity	2-3
	Specific Heat	2-8
	Density	2-13
	Coefficient of Thermal Expansion	2-18
	Environmental Characteristics	2-24
	Material Behavior Under Vacuum and Temperature Exposure	2-24
	Structural Properties of "THERMO-LAG" T-500 Materials	2-28
	Thermal-Chemical Characteristics	2-28
	Differential Thermal Analysis	2-28
	Heat of Decomposition	2-36
	Thermogravimetric Analysis	2-38
III	THERMAL PERFORMANCE OF "THERMO-LAG" T-500	3-1
	Part A - Experimental Investigations	3-3
	Air Arc Jet Test Models	3-3
	Summary of Air Arc Tests	3-5
	Reliability of Data	3-5
	Series 1 - Transient Performance	3-12
	Series 2 - Effects of Stream Oxygen Concentration	3-37
	Series 3 - Effects of Model Configuration	3-42
	Series 4 - Effects of Stream Pressure	3-46
	Series 5 - Effects of Stream Energy	3-52
	Series 6 - Effects of Gaps and Discontinuities	3-60

Section	Title	Page
	Series 7 - Effects of Vacuum Exposure....	3-72
	Series 8 - Trajectory Simulation.....	3-76
	Series 9 - Effects of Upstream Mass Injection.....	3-78
	Radiation Ablation Tests.....	3-100
	Part B - Analytical Evaluation of Ablation Parameters.....	3-105
	General Approach.....	3-105
	Boundary Layer Thermal Effects.....	3-107
	Heat Addition Produced by Oxidation.....	3-110
	Debris Layer Energy Transfer.....	3-112
	Evaluation of Energy Transfer Parameters..	3-112
	Analysis of Basic Air-Arc Performance Parameters.....	3-125
	Parametric Study.....	3-125
IV	NOMENCLATURE.....	4-1
V	REFERENCES.....	5-1

LIST OF ILLUSTRATIONS

Figure	Title	Page
2-1	Thermal Conductivity of Virgin "THERMO-LAG" T-500-4 and T-500-6	2-5
2-2	Thermal Conductivity Charred "THERMO-LAG" T-500-4 and T-500-6	2-5
2-3	Mean Specific Heat of Virgin "THERMO-LAG" T-500-4 and T-500-6	2-9
2-4	Mean Specific Heat of Charred "THERMO-LAG" T-500-4 and T-500-6	2-10
2-5	Density Versus Temperature for "THERMO-LAG" T-500-4 and T-500-6	2-14
2-6	Laboratory Gravitometer	2-15
2-7	Total Normal Emissivity of Virgin "THERMO-LAG" T-500-4 and T-500-6	2-16
2-8	Total Normal Emissivity of Precharred "THERMO-LAG" T-500-4 and T-500-6	2-16
2-9	Coefficient of Thermal Expansion for Virgin "THERMO-LAG" T-500-4 and T-500-6	2-20
2-10	Coefficient of Thermal Expansion for Charred "THERMO-LAG" T-500-4 and T-500-6	2-20
2-11	Environmental Chamber	2-29
2-12	High Vacuum Exposure Tests on "THERMO-LAG" T-500-4 (20-Mil Samples)	2-30
2-13	High Vacuum Exposure Tests on "THERMO-LAG" T-500-4 (100-Mil Samples)	2-31
2-14	High Vacuum Exposure Tests on "THERMO-LAG" T-500-4 (50-Mil Samples)	2-32
2-15	Coefficient and Exponents of Modified Arrhenius Equation as a Function of Initial Specimen Thickness	2-33
2-16	Isothermal Weight Loss Rate As A Function of Time	2-34
2-17	Temperature Dependence of Weight Loss Rate for Constant Exposure Times	2-35

2-18	Deltatherm Differential Thermal Analyzer....	2-37
2-19	Differential Thermal Analyses of "THERMO-LAG" T-500-6 for a Temperature Increase Rate of 3.6°F per Minute	2-39
2-20	Differential Thermal Analyses of "THERMO-LAG" T-500-6 for a Temperature Increase Rate of 3.6°F per Minute	2-40
2-21	Differential Thermal Analysis of "THERMO-LAG" T-500-6 for a Temperature Increase Rate of 3.6°F per Minute	2-41
2-22	Differential Thermal Analysis of "THERMO-LAG" T-500-6 for a Temperature Increase Rate of 18°F per Minute	2-42
2-23	Differential Thermal Analysis of "THERMO-LAG" T-500-4 for a Temperature Increase Rate of 3.6°F per Minute	2-42
2-24	Differential Thermal Analyses of "THERMO-LAG" T-500-4 for a Temperature Increase Rate of 9°F per Minute	2-43
2-25	Differential Thermal Analysis of "THERMO-LAG" T-500-4 for A Temperature Increase Rate of 9°F per Minute	2-44
2-26	Differential Thermal Analysis of "THERMO-LAG" T-500-4 for a Temperature Increase Rate of 18°F per Minute	2-45
2-27	Thermogravimetric Analysis of "THERMO-LAG" T-500-4 for a Temperature Increase of 3.6°F per Minute	2-46
2-28	Thermogravimetric Analysis of "THERMO-LAG" T-500-4 for a Temperature Increase of 3.6°F per Minute	2-47
2-29	Thermogravimetric Analyses of "THERMO-LAG" T-500-4 for a Temperature Increase Rate of 9°F per Minute	2-48
2-30	Thermogravimetric Analysis of "THERMO-LAG" T-500-4 for a Temperature Increase Rate of 9°F per Minute	2-49
2-31	Thermogravimetric Analyses of "THERMO-LAG" T-500-4 for a Temperature Increase Rate of 18°F per Minute	2-50
2-32	Thermogravimetric Analyses of "THERMO-LAG" T-500-6 for a Temperature Increase of 3.6°F per Minute	2-51
2-33	Thermogravimetric Analyses of "THERMO-LAG" T-500-6 for a Temperature Increase Rate of 9°F per Minute	2-52

Figure	Title	Page
2-34	Thermogravimetric Analyses of "THERMO-LAG" T-500-6 for a Temperature Increase Rate of 18°F per Minute.....	2-53
3-1	Flight Simulation Regime for Typical Manned Super Orbital Re-Entry Trajectories	3-4
3-2	Photograph of Re-Entry Simulation Models Tested in the Arc Plasmajet Tunnel	3-10
3-3	Hemisphere-Cylinder Test Model	3-13
3-4	Flat-Face Cylinder Test Model.....	3-14
3-5	Sphere-Cone Test Model	3-15
3-6	Design of a Water-Cooled Copper Hemisphere Calorimeter.....	3-16
3-7	Sphere-Cone Calorimeter Design.....	3-17
3-8	Hemisphere-Cylinder Calorimeter Design.....	3-18
3-9	Cold Wall Stagnation Heat Flux Btu/Ft^2-Sec .	3-19
3-10	Cold Wall Effective Gross Efficiency vs. Boundary Layer Enthalpy Difference for Constant Pressure and Exposure Time.....	3-20
3-11	Transient Histories.....	3-25
3-12	Transient Histories.....	3-26
3-13	Transient Histories.....	3-27
3-14	Transient Histories.....	3-28
3-15	Transient Histories.....	3-30
3-16	Transient Histories.....	3-31
3-17	Sidewall transient Histories.....	3-32
3-18	Density of Debris Layer as a Junction of Debris Layer Thickness.....	3-33
3-19	Surface Temperature Versus Oxygen Concentration of Stream.....	3-34
3-20	Total Recession Versus Concentration of Stream	3-35
3-21	Correlation of Debris Recession Data.....	3-36
3-22	Effect of Stagnation Pressure on Average Gross Effective Heat of Ablation at Constant Boundary Layer Enthalpy Difference.....	3-47
3-23	Measured Surface Temperature Versus Environmental Conditions for a 2.2" Diameter Model in Plasmadyne Air Arc Facility.....	3-48
3-24	Effect of Stagnation Pressure on Average Net Effective Heat of Ablation at Constant Boundary Layer Enthalpy Difference.....	3-49
3-25	Dependence of Average Net Effective Heat of Ablation on Boundary Layer Enthalpy Difference at Constant Stagnation Pressure.....	3-50
3-26	Variation of Average Net Effective Heat of Ablation With Boundary Layer Enthalpy Difference at Constant Heat Flux.....	3-55

Figure	Title	Page
3-27	Variation of Average Surface Temperature with Enthalpy for Constant Heat Flux.....	3-56
3-28	Surface Temperature of a Function of Stagnation Enthalpy for Constant Pressure P_t = .05 atm.	3-57
3-29	Surface Temperature as a Function of Stagnation Enthalpy for Constant Pressure P_t = .014 atm.....	3-58
3-30	Effect of Model Configuration on Stagnation Point Debris Thickness.....	3-59
3-31	Two Dimensional Water Cooled Test Model Showing Test Specimen in Sample Holder.....	3-62
3-32	Simulated Flight Test Model, Water Cooled Copper Nose.....	3-63
3-33	Material Gap Specimen with Holder Showing Thermocouple Locations.....	3-64
3-34	Variation of Thermal Loss Index to Gap Dimension Ratio of Width to Height (W/H) for Gap Orientation.....	3-65
3-35	Apollo Overshoot Design Trajectory.....	3-66
3-36	Variation of Enthalpy with Time for Overshoot Trajectory Simulation Test.....	3-69
3-37	Post-Test Photograph of Trajectory Simulation, Model N-57.....	3-70
3-38	Comparison of Ablation Phase Results - Trajectory Simulation.....	3-71
3-39	Temperature - Time Histories of Thermocouples 1, 2, 3, and 4.....	3-74
3-40	Transient Histories of "THERMO-LAG" T-500 Models N-13 and N-41.....	3-75
3-41	"THERMO-LAG" T-500 Model N-13 After Exposure to Vacuum.....	3-[illegible]
3-42	Plasma Jet Post-Test Photograph of Vacuum Exposed "THERMO-LAG" T-500 Model N-13..	3-[illegible]
3-43	Plasma Jet Post-Test Photograph of "THERMO-LAG" T-500 Model N-41.....	3-[illegible]
3-44	Virgin Material Recession Versus Distance from Front Edge of the Panel - Test Point 6.....	3-87
3-45	Virgin Material Recession Versus Distance from Front Edge of the Panel - Test Point 12.....	3-88
3-46	Virgin Material Recession Versus Distance from Front Edge of the Panel - Test Point 24.....	3-89
3-47	Theoretical Heat Transfer with Zero Injection...	3-90
3-48	Variation of Heat Transfer with Mass Injection Parameter for "THERMO-LAG" T-500.....	3-91

Figure	Title	Page
3-49	Simulated Flight Test Model, Water Cooled Copper Nose	3-96
3-50	Simulated Flight Test Model (Type V) Graphite Nose, "THERMO-LAG" Body	3-97
3-51	Simulated Flight Test Model (Type VI) "THERMO-LAG" Nose, "THERMO-LAG" Body	3-98
3-52	Test Plate Locations for Calorimeters and Thermocouples	3-99
3-53	Schematic Diagrams of Molybdenum Calorimeter and Radiation Ablation Model	3-102
3-54	Temperature Traces for Test Conditions at 225 V. and 287 V	3-103
3-55	Recession Histories for Test Conditions at 225V. and 287 V	3-104
3-56	Variation of Gross Effective Heat of Ablation with Boundary Layer Enthalpy Difference	3-106
3-57	Variation of Net Effective Heat of Ablation with Boundary Layer Enthalpy Difference	3-109
3-58	Relationship Between Debris Thickness, Virgin Material Recession, Surface Temperature, and 21 Percent of Oxygen Concentration for Several Constant Values of Exposure Time (Sheet 1 of 2)	3-114
3-58	Relationship Between Debris Thickness, Virgin Material Recession, Surface Temperature, and 21 Percent of Oxygen Concentration for Several Constant Values of Exposure Time (Sheet 2 of 2)	3-115
3-59	Variation of Virgin Mass Loss Rate with Debris Surface Temperature	3-116
3-60	Variation of Mean Effective Specific Heat of Gaseous Ablation Products with Debris Surface Temperature	3-118
3-61	Variation of Mean Effective Specific Heat of Gaseous Ablation Products with Mass Loss Rate for a Range of Total Enthalpy from 10,000 Btu/Lb to 23,000 Btu/Lb	3-119
3-62	Variation of Mean Effective Specific Heat of Gaseous Ablation Products with Total Enthalpy for the Weakly Oxidized Debris Engine	3-120
3-63	Effec of Oxygen on the Mean Specific Heat of Gaseous Ablation Products	3-120
3-64	Variation of Debris Layer Effective Thermal Conductivity with Temperature	3-121

Figure	Title	Page
3-65	Effective Thermal Conductivity of the Debris Layer and the Specific Energy of the Gaseous Ablation Products	3-124
3-66	Comparison of Experimental and Theoretical Heat Flux	3-129
3-67	Experimentally Correlated Approximate Solution to the Ablation Model and the Effect of C_p/C_{p_o} on Correlation Parameter $M \Delta x/K$	3-130
3-68	Results of Ablation Performance Parametric Study	3-131
3-69	Results of Ablation Performance Parametric Study	3-132
3-70	Results of Ablation Performance Parametric Study	3-133
3-71	Results of Ablation Performance Parametric Study	3-134
3-72	Results of Ablation Performance Parametric Study	3-135
A- 1	Temperature-Time History of Model M-6	A-2
A- 2	Temperature-Time History of Model M-9	A-3
A- 3	Temperature-Time History of Model M-10	A-4
A- 4	Temperature-Time History of Model M-18	A-5
A- 5	Temperature-Time History of Model M-16	A-6
A- 6	Temperature-Time History of Model M-19	A-7
A- 7	Temperature-Time History of Model M-21	A-8
A- 8	Temperature-Time History of Model M-22	A-9
A- 9	Temperature-Time History of Model M-23	A-10
A-10	Temperature-Time History of Model O-1	A-11
A-11	Temperature-Time History of Model O-2	A-12
A-12	Temperature-Time History of Model O-3	A-13
A-13	Temperature-Time History of Model O-6	A-14
A-14	Temperature-Time History of Model O-7	A-15
A-15	Temperature-Time History of Model O-8	A-16
A-16	Temperature-Time History of Model O-9	A-17
A-17	Temperature-Time History of Model O-11	A-18
A-18	Temperature-Time History of Model O-13	A-19
A-19	Temperature-Time History of Model O-14	A-20
A-20	Temperature-Time History of Model O-15	A-21
A-21	Temperature-Time History of Model O-16	A-22
A-22	Temperature-Time History of Model D-12	A-23
A-23	Temperature-Time History of Model D-2-2	A-24
A-24	Temperature-Time History of Model E-12	A-25
A-25	Temperature-Time History of Model E-22	A-26
A-26	Temperature-Time History of Model GG-1	A-27

Figure	Title	Page
A-27	Temperature-Time History of Model GG-3	A-28
A-28	Temperature-Time History of Model HH-1	A-29
A-29	Temperature-Time History of Model HH-2	A-30
A-30	Temperature-Time History of Model D-1	A-31
A-31	Temperature-Time History of Model D-2	A-32
A-32	Temperature-Time History of Model D-9	A-33
A-33	Temperature-Time History of Model D-10	A-34
A-34	Temperature-Time History of Model D-11	A-35
A-35	Temperature-Time History of Model D-12	A-36
A-36	Temperature-Time History of Model E-15	A-37
A-37	Temperature-Time History of Model E-16	A-38
A-38	Temperature-Time History of Model E-17	A-39
A-39	Temperature-Time History of Model E-18	A-40
A-40	Temperature-Time History of Model GG-1A	A-41
A-41	Temperature-Time History of Model CG-2	A-42
A-42	Temperature-Time History of Model GG-4	A-43
A-43	Temperature-Time History of Model GG-5	A-44
A-44	Temperature-Time History of Model GG-7	A-45
A-45	Temperature-Time History of Model GG-8	A-46
A-46	Temperature-Time History of Model GG-9	A-47
A-47	Temperature-Time History of Model GG-11	A-48
A-48	Temperature-Time History of Model D-2-4	A-49
A-49	Temperature-Time History of Model D-2-5	A-50
A-50	Temperature-Time History of Model N-2	A-51
A-51	Temperature-Time History of Model N-6	A-52
A-52	Temperature-Time History of Model N-9	A-53
A-53	Temperature-Time History of Model N-11	A-54
A-54	Temperature-Time History of Model N-15	A-55
A-55	Temperature-Time History of Model N-21	A-56
A-56	Temperature-Time History of Model N-22	A-57
A-57	Temperature-Time History of Model N-26	A-58
A-58	Temperature-Time History of Model N-29	A-59
A-59	Temperature-Time History of Model N-30	A-60
A-60	Temperature-Time History of Model N-35	A-61
A-61	Temperature-Time History of Model N-36	A-62
A-62	Temperature-Time History of Model N-46	A-63
A-63	Temperature-Time History of Model N-48	A-64
A-64	Temperature-Time History of Model N-53	A-65
A-65	Temperature-Time History of Model N-54	A-66
A-66	Temperature-Time History of Model N-64	A-67
A-67	Temperature-Time History of Model N-65	A-68
A-68	Temperature-Time History of Model N-71	A-69
A-69	Temperature-Time History of Model N-73	A-70
A-70	Temperature-Time History of Model N-75	A-71
A-71	Temperature-Time History of Model N-82	A-72

Figure	Title	Page
A-72	Temperature-Time History of Model N-92.....	A-73
A-73	Temperature-Time History of Model N-94.....	A-74
A-74	Temperature-Time History of Model N-105.....	A-75
A-75	Temperature-Time History of Model N-106.....	A-76
A-76	Temperature-Time History of Model N-110.....	A-77
A-77	Temperature-Time History of Model N-112.....	A-78
A-78	Temperature-Time History for Material Gap Test....	A-79
A-79	Temperature-Time History for Material Gap Test....	A-80
A-80	Temperature-Time History for Material Gap Test....	A-81
A-81	Temperature-Time History for Material Gap Test....	A-82
A-82	Temperature-Time History for Material Gap Test....	A-83
A-83	Temperature-Time History for Material Gap Test	A-84
A-84	Temperature-Time History for Material Gap Test ...	A-85
A-85	Temperature-Time History for Material Gap Test ...	A-86
A-86	Temperature-Time History for Material Gap Test ...	A-87
A-87	Temperature-Time History for Material Gap Test ...	A-88
A-88	Trajectory No. 1 Temperature-Time History	A-89
A-89	Trajectory No. 1 Temperature-Time History	A-90
A-90	Temperature-Time History of Mass Injection Test Model M-I.....	A-91
A-91	Temperature-Time History of Mass Injection Test Model M-IV.....	A-92
A-92	Temperature-Time History of Mass Injection Test Model M-II.....	A-93
A-93	Temperature-Time History of Mass Injection Test Model M-V.....	A-94
A-94	Temperature-Time History of Mass Injection Test Model V-III	A-95
A-95	Temperature-Time History of Mass Injection Test Model M-VI-I.....	A-96
A-96	Temperature-Time History of Mass Injection Test Model M-VI-2.....	A-97
A-97	Temperature-Time History of Model M-I-6.....	A-98
A-98	Temperature-Time History of Model M-IV-6.....	A-99
A-99	Temperature-Time History of Model M-III-6.....	A-100
A-100	Temperature-Time History of Model M-VI-6.....	A-101
A-101	Temperature-Time History of Model M-I-24.....	A-102
A-102	Temperature-Time History of Model M-V-24.....	A-103
A-103	Temperature-Time History of Model M-IV-24.....	A-104
A-104	Temperature-Time History of Model M-II-24.....	A-105
A-105	Temperature-Time History of Model M-III-24.....	A-106
A-106	Temperature-Time History of Model M-VI-24-I....	A-107
A-107	Temperature-Time History of Model M-VI-24-2....	A-108

LIST OF TABLES

Table	Title	Page
2-1	Test Results - Thermal Conductivity (Sheet 1 of 3)	2-6
2-1	Test Results - Thermal Conductivity (Sheet 2 of 3)	2-7
2-1	Test Results - Thermal Conductivity (Sheet 3 of 3)	2-8
2-2	Test Results - Specific Heat (Sheet 1 of 3)	2-10
2-2	Test Results - Specific Heat (Sheet 2 of 3)	2-11
2-2	Test Results - Specific Heat (Sheet 3 of 3)	2-12
2-3	Total Normal Emissivities of "THERMO-LAG" T-500-4 and T-500-6	2-17
2-4	Coefficient of Thermal Expansion Test Results (Sheet 1 of 3)	2-21
2-4	Coefficient of Thermal Expansion Test Results (Sheet 2 of 3)	2-22
2-4	Coefficient of Thermal Expansion Test Results (Sheet 3 of 3)	2-23
2-5	Vacuum Exposure Test Conditions	2-24
2-6	Gas Analysis of Noncondensable Ablation Products By Gas Chromatograph	2-55
2-7	Chromatograph Analysis of Pyrolysis Products of "THERMO-LAG" T-500-4	2-56
3-1	Summary of Air-Arc Test Data (Sheet 1 of 4)	3-6
3-1	Summary of Air-Arc Test Data (Sheet 2 of 4)	3-7
3-1	Summary of Air-Arc Test Data (Sheet 3 of 4)	3-8
3-1	Summary of Air-Arc Test Data (Sheet 4 of 4)	3-9
3-2	Transient Test Matrix	3-12
3-3	Oxidation Test Matrix	3-38
3-4	Stagnation Point Oxidation Results	3-39
3-5	Test Matrix - Evaluation of Pressure Effect on Stagnation Point Ablation Kinetics	3-46
3-6	Test Matrix - Variation of Enthalpy and Pressure with Constant Heat Flux	3-52
3-7	Material Gap Test Matrix	3-67

Table	Title	Page
3-8	Material Gap Test Model Data	3-68
3-9	Air Arc Plasma Jet Test Conditions	3-72
3-10	Upstream Mass Injection Test Matrix	3-92
3-11	Results of Mass Injection Tests	3-93
3-12	Material Gap Post-Test Data	3-94
3-13	Mass Injection Study - 3-Dimensional Models Tested	3-95
3-14	Radiation Ablation Test	3-101
3-15	Additional Heating Due to Oxidation Results	3-111

SECTION I

INTRODUCTION

In accordance with the requirements of National Aeronautics and Space Administration, Manned Spacecraft Center Contract No. NAS 9-877, The Emerson Electric Manufacturing Company of St. Louis, Missouri has performed an investigation and test program to determine the thermal properties, the thermal performance characteristics, and the behavior of "THERMO-LAG" T-500 thermostatic, subliming, heat shield material in the space environment. These investigations and analyses of results therefrom are reported in this volume as a part of the final report of the contract work.

The report includes detailed descriptions of the investigations performed and the results obtained pertinent to the use of "THERMO-LAG" T-500 materials for the design of manned entry vehicle heat shield systems. Thermal conductivity, specific heat, emissivity, and density values for T-500 materials, both in the virgin state and in the charred state, were determined over a range of temperatures. Rates and temperatures of decomposition were determined by thermogravimetric analysis. Overall heats of decomposition were measured and reactions were studied by means of differential thermal analysis. Chromatographic procedures were used for the identification of ablation products.

An extensive experimental study of T-500 thermal performance was conducted employing air arc plasma flight simulation facilities and an infrared radiation apparatus. The thermal performance of the "THERMO-LAG" material was studied for environments typical of Apollo class vehicles during the entry maneuver. Tests were also performed to assess the effects of vacuum exposure upon subsequent performance of the ablation material.

The experimental results of the program were intensively evaluated for the derivation of basic parameters defining the ablation mechanism. This information was used in the establishment of an IBM computer program for the rapid prediction of heat shield material requirements for a given sequence of thermal environments and material characteristics.

Two forms of "THERMO-LAG" T-500 were evaluated. The T-500-4 designation refers to spray deposited material cured according to prescribed procedures. The designation T-500-6 is applied to srpay deposited material, reinforced with loose weave glass cloth weighing 1.94 ounces per square yard interlaminated during the spray operation at intervals of 0.050 inches, which has been vacuum bag molded and cured according to prescribed procedures.

SECTION II

MATERIAL PROPERTIES AND CHARACTERISTICS

SOLID PHASE THERMAL PROPERTIES

Tests were performed to provide measured values of "THERMO-LAG" T-500 thermal properties over the temperature range from -150°F to 400°F where appropriate, both virgin and precharred materials were tested.

THERMAL CONDUCTIVITY

TEST EQUIPMENT. A Cenco-Fitch thermal conductivity unit was used for the thermal conductivity tests. This unit consists primarily of an insulated cooper mass and a vessel to contain a constant temperature fluid.

TEST SPECIMEN. The material test specimens were 0.125-inch thick circular disks, 2.5 inches in diameter.

TEST METHOD. The thermal conductivity of both virgin and charred "THERMO-LAG" T-500 material specimens was measured by the method prescribed in ASTM C177-45. This method employs the principle of energy balance by equating the heat transferred through the test specimen to the heat absorbed by an insulated copper mass, which acts as a heat sink. One face of the test specimen was in direct contact with the constant temperature source, while the other face was in contact with the copper mass, whose remaining sides were thermally insulated. The log of the differences in temperature between the constant temperature source and the rising temperature in the copper mass was recorded. The final calculation was based on the principle that the test specimen thermal conductivity is proportional to the slope of the linear log temperature versus time curve.

RESULTS. Multiple observations were made for each specimen tested. Observations were made at intervals not exceeding one hour. Measurements made at these time intervals gave a linear log temperature versus time relationship which was used to define the thermal conductivity by the equation:

$$K = \frac{L W_{Cu} C \varrho_{Cu}}{A_{Cu}} \times \frac{\log_e (T_2/T_1)}{(t_2 - t_1)}$$

where:

W_{cu} = Weight of copper heat sink
k = Thermal conductivity of specimen
L = Specimen thickness
C_{cu} = Specific heat of copper
A_{cu} = Effective sample area = area of copper sink
T_2/T_1 = The temperature difference ratio corresponding to the time (t_2-t_1)

$$\frac{1}{M} \frac{\log_e (T_2-T_1)}{(t_2-t_1)}$$

For the virgin "THERMO-LAG" materials, seven tests were performed on "THERMO-LAG" T-500-4 and ten tests were performed on "THERMO-LAG" T-500-6. The results of these tests are recorded in Table 2-1 and shown in Figure 2-1. The data indicates that the thermal conductivity, k, of "THERMO-LAG" T-500-4 is approximately linear over the test temperature range.

For the charred materials, nine tests were performed on "THERMO-LAG" T-500-4 and ten tests were performed on "THERMO-LAG" T-500-6. The test results are recorded in Table 2-1 and shown in Figure 2-2. The data indicates that over the test temperature range the variation in thermal conductivity is about 12 percent.

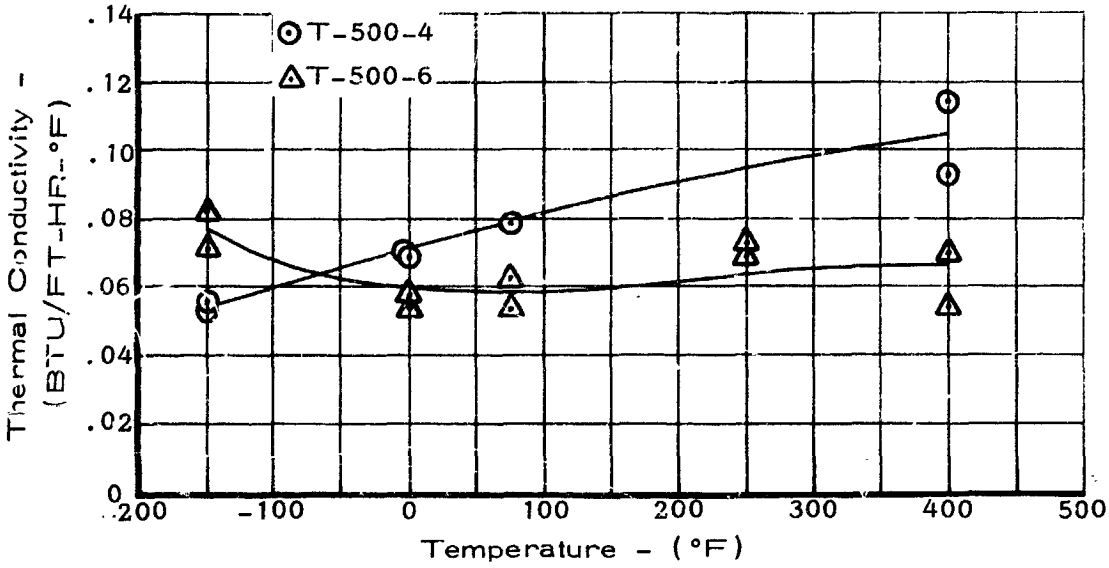


Figure 2-1. Thermal Conductivity of Virgin "THERMO-LAG" T-500-4 and T-500-6

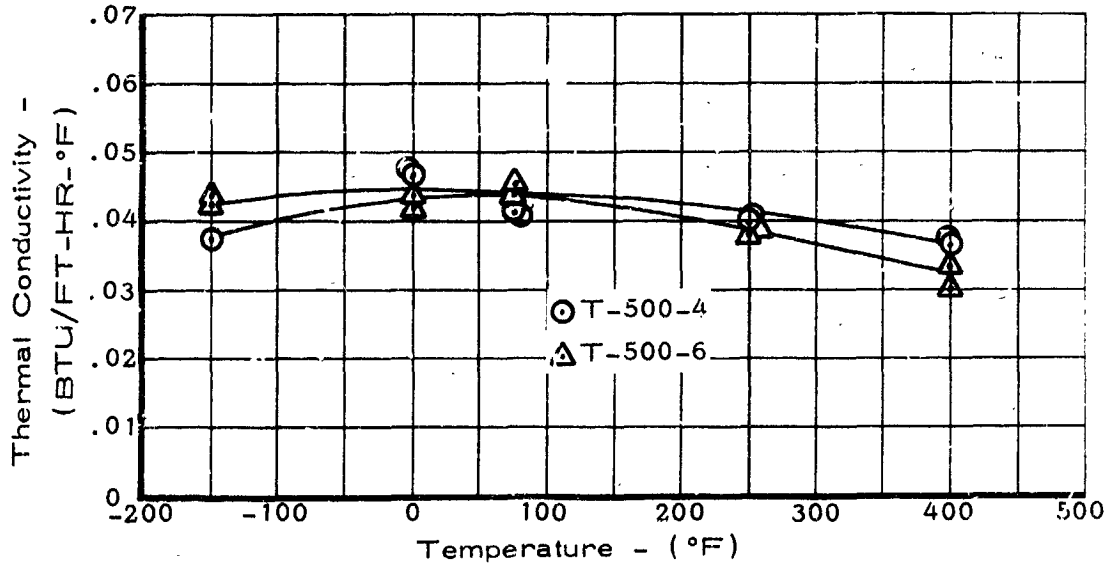


Figure 2-2. Thermal Conductivity Charred "THERMO-LAG" T-500-4 and T-500-6

Material	Specimen No.	Test Temperature °F	Weight of Copper W_{Cu} GMS	Specific Heat of Copper $C_{P_{Cu}}$ CAL/GM°C	Specimen Thickness l, CM	Area Copper A_{Cu} CM^2	Slope M	Conversion Factor	Thermal Conductivity κ BTU/HR-FT-°F
T-500-4 Charred	10-G-1-4B-4	-150	340	.0940	.300	15.22	9360	242.0	.0376
T-500-4 Virgin	10-G-1-1-4	-150	340	.0940	.320	15.22	6970	242.0	.0536
T-500-4 Virgin	10-G-1-8-4	-150	340	.0940	.3225	15.22	6930	242.0	.0544
T-500-4 Virgin	10-G-1-16-4	0	340	.0940	.3185	15.22	5400	242.0	.0690
T-500-4 Virgin	10-G-1-6-4	0	340	.0940	.3165	15.22	5340	242.0	.0694
T-500-4 Charred	10-G-1-4C-4	0	340	.0940	.307	15.22	7740	242.0	.0466
T-500-4 Charred	10-G-1-4E-4	0	340	.0940	.400	15.22	7520	242.0	.0466
T-500-4 Charred	10-G-1-4A-4	77	340	.0940	.3145	15.22	8430	242.0	.0436
T-500-4 Charred	10-G-1-4B-4	77	340	.0940	.300	15.22	8430	242.0	.0418
T-500-4 Virgin	10-G-1-4-4	77	340	.0940	.3225	15.22	4730	242.0	.0798
T-500-4 Charred	10-G-1-19-4	250	340	.0941	.3045	15.22	8940	242.0	.0309
T-500-4 Charred	10-G-1-19A-4	250	340	.0941	.3110	15.22	9260	242.0	.0394
T-500-4 Charred	10-G-1-1-4	400	340	.0941	.3125	15.22	9460	242.0	.0369
T-500-4 Charred	10-G-1-9-4	400	340	.0945	.310	15.22	9960	242.0	.0366
T-500-4 Virgin	10-G-1-10-4	400	340	.0945	.3165	15.22	1500	242.0	.1135

Table 2-1. Test Results - Thermal Conductivity (Sheet 1 of 3)

Material	Specimen No.	Test Temperature F	Weight of Copper W_{cu} GMS	Specific Heat of Copper C_{pcu} CAL GM C	Specimen Thickness 1, CM	Area Copper A_{cu} CM^2	Slope M	Conversion Factor	Thermal Conductivity K BTU HR-FT- F
T-500-4 Virgin	10-G-1-17-4	400	340	.0945	.3235	15.22	2280	242.0	.0923
T-500-6 Charred	10-H-1-17A-6	-150	340	.0940	.3125	15.22	8540	242.0	.0429
T-500-6 Charred	10-H-1-17B-6	-150	340	.0940	.310	15.22	8160	242.0	.0434
T-500-6 Virgin	10-H-2-17-6	-150	340	.0940	.320	15.22	5281	242.0	.0710
T-500-6 Virgin	10-H-2-17-6A	-150	340	.0940	.320	15.22	4560	242.0	.0820
T-500-6 Virgin	10-G-2-5-6	77	340	.0940	.320	15.22	7050	242.0	.0532
T-500-6 Virgin	10-G-2-2-6	77	340	.0940	.310	15.22	5870	242.0	.0623
T-500-6 Virgin	10-G-2-4-6	250	340	.0941	.3275	15.22	5650	242.0	.0698
T-500-6 Virgin	10-G-2-9-6	250	340	.0941	.317	15.22	5240	242.0	.0717
T-500-6 Virgin	10-H-2-16-6	400	340	.0945	.320	15.22	7040	242.0	.0537
T-500-6 Virgin	10-G-2-10-6	400	340	.0945	.337	15.22	5650	242.0	.0699
T-500-6 Virgin	10-H-2-20-6	0	340	.0940	.3264	15.22	1150	242.0	.0566
T-500-6 Virgin	10-G-2-11-6	0	340	.0940	.3264	15.22	1660	242.0	.0543
T-500-6 Charred	10-H-2-15-6	0	340	.0940	.3175	15.22	6840	242.0	.0422
T-500-6 Charred	10-H-2-6-6	0	340	.0940	.3022	15.22	8170	242.0	0.433

Table 2-1. Test Results - Thermal Conductivity (Sheet 2 of 3)

Material	Specimen No.	Test Temperature F	Weight of Copper W_{Cu} GMS.	Specific Heat of Copper C_{PCu} CAL/GM C	Specimen Thickness 1, CM	Area Copper A_{Cu} CM^2	Slope M	Conversion Factor	Thermal Conductivity K BTU HR-FT- F
T-500-6 Charred	10-H-2-17-6	77	340	.0940	.3145	15.22	8175	242.0	.0452
T-500-6 Charred	10-H-2-19-6	77	340	.0940	.320	15.22	8840	242.0	.0422
T-500-6 Charred	10-G-2-8-6	250	340	.0941	.3045	15.22	9300	242.0	.0384
T-500-6 Charred	10-H-2-15-6	250	340	.0941	.3125	15.22	9260	242.0	.0395
T-500-6 Charred	10-H-2-19-6	400	340	.0945	.3085	15.22	10960	242.0	.0332
T-500-6 Charred	10-G-2-8-6	400	340	.0945	.310	15.22	9500	242.0	.0300

Table 2-1. Test Results - Thermal Conductivity (Sheet 3 of 3)

SPECIFIC HEAT

TEST EQUIPMENT. A Parr Adiabatic Calorimeter (Model 1221) was used in the specific heat tests. The tests were calibrated with a standard sample of copper, whose specific heat is accurately known over the test temperature range.

TEST SPECIMEN. The material test specimens were 0.075-inch thick rectangles, 1 inch by 4 inches, of sufficient quantity to give a total weight of approximately 100 grams.

TEST METHOD. The method used to measure the specific heat was that specified in ASTM C351-61. This method consists of: (1) adding a known mass of material at a given temperature to a known mass of a calorimetry liquid (toluene or tricresyl phosphate) at a higher or lower temperature, and (2) determining the resulting equilibrium temperature. The specific heats were calculated from the energy balance:

$$M_S C_S \Delta T_S = M_L C_L \quad T_L$$

where:

M_s = Specimen mass

C_s = Specimen specific heat

ΔT_s = Specimen temperature change

M_L = Effective mass of liquid = liquid mass + liquid mass equivalent of the calorimeter

C_L = Liquid specific heat

ΔT_L = Liquid temperature change

RESULTS. Test results are recorded in Table 2-2 and illustrated in Figures 2-3 and 2-4. Figure 2-3 shows values of the mean specific heat of virgin "THERMO-LAG" T-500-4 and T-500-6 as a function of temperature.

The values of charred "THERMO-LAG" T-500-4 and T-500-6, as a function of temperature are shown in Figure 2-4. The trends of the plotted data are typical for the materials tested.

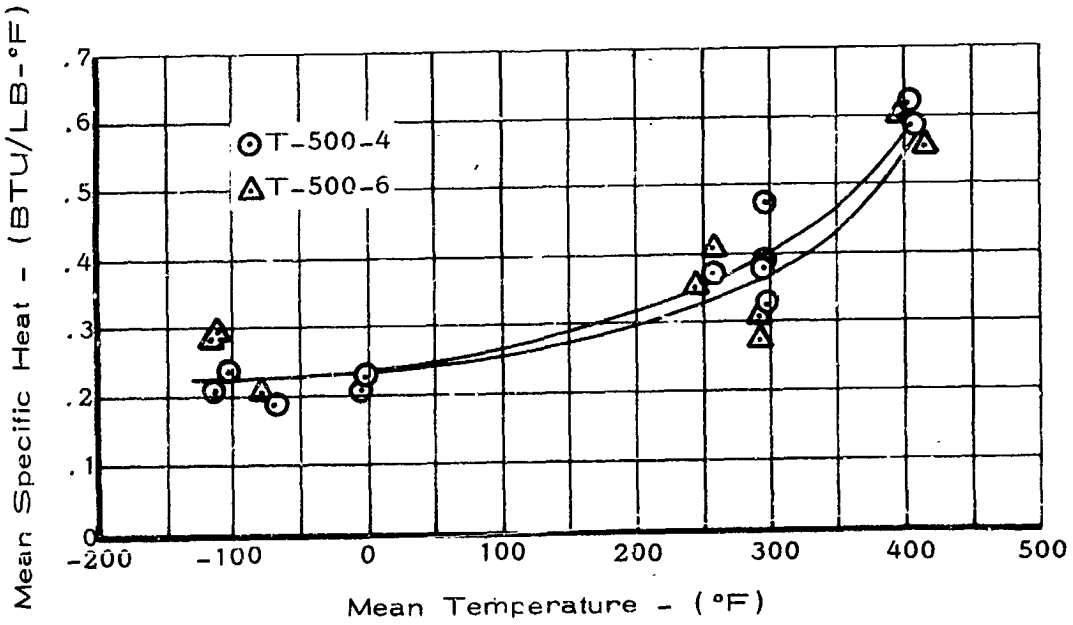


Figure 2-3. Mean Specific Heat of Virgin "THERMO-LAG" T-500-4 and T-500-6

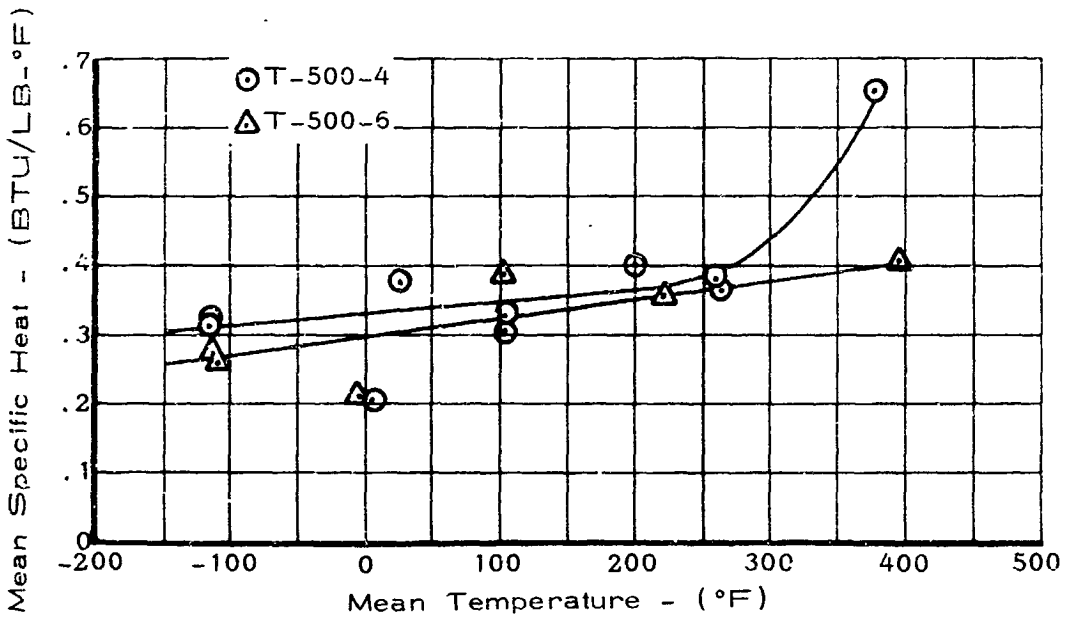


Figure 2-4. Mean Specific Heat of Charred "THERMO-LAG" T-500-4 and T-500-6

Material	Specimen Weight GMS	Initial Specimen Temperature °F	Initial Toluene Temperature °F	Equilibration Temperature °F	T_t °F	T_s °F	Toluene Weight GMS	C_{pt} BTU/LB-°F	Specific Heat of Specimen BTU/LB-°F
T-500-6 Charred	98.24	130	72.55	75.10	2.55	54.90	2091	.395	0.389 at 102
T-500-6 Charred	99.77	350	81.03	91.68	10.65	256.32	2122	.403	0.358 at 221
T-500-6 Charred	98.89	-295	81.72	70.01	11.71	365.01	2056	.403	0.271 at -113
T-500-6 Charred	98.60	-295	82.40	71 29	11.11	366.29	2099	.404	0.261 at -112
T-500-6 Charred	99.04	-89.5	91.10	86.64	4.46	176.14	2002	.403	0.208 at -2

Table 2-2. Test Results - Specific Heat (Sheet 1 of 3)

Material	Specimen Weight GMS	Initial Specimen Temperature °F	Initial Toluene Temperature °F	Equilibration Temperature °F	T_t °F	T_s °F	Toluene Weight GMS	C_{pt} BTU/LB-°F	Specific Heat of Specimen BTU/LB-°F
T-500-4 Charred	99.74	350	78.57	90.75	12.18	259.25	2116	.402	0.400 at 200
T-500-4 Charred	98.20	429	76.36	90.88	14.52	338.12	2150	.401	0.377 at 260
T-500-4 Charred	99.91	130	76.03	78.03	2.00	51.97	2110	.401	0.326 at 104
T-500-4 Charred	99.52	130	75.35	77.24	1.89	52.76	2113	.401	0.305 at 103
T-500-4 Charred	98.69	-300	80.75	66.65	14.1	366.65	2042	.403	0.312 at -117
T-500-4 Charred	98.68	-295	81.51	67.70	13.81	362.70	2009	.403	0.312 at -116
T-500-4 Charred	98.16	-70	81.74	78.21	3.53	148.21	2085	.403	0.204 at 4
T-500-6 Virgin	94.70	500	70.28	85.36	15.08	414.64	1990	.402	0.308 at 292
T-500-6 Virgin	100.71	500	69.90	84.48	14.58	415.52	1960	.402	0.274 at 292
T-500-4 Virgin	99.40	496	76.05	93.46	17.41	402.54	2159	.403	0.378 at 294
T-500-4 Virgin	93.83	502	78.96	93.87	14.91	408.13	2045	.404	0.322 at 298
T-500-4 Virgin	104.04	-275	78.22	68.10	10.12	343.10	1983	.400	0.234 at -103
T-500-4 Virgin	98.32	-81	81.30	77.05	4.25	158.05	2060	.403	0.226 at -2
T-500-4 Virgin	97.46	-81	76.55	72.73	3.82	153.73	2043	.401	0.210 at -4
T-500-4 Virgin	95.60	-298	79.06	70.30	8.76	368.30	2081	.401	0.208 at -114
T-500-4 Virgin	94.03	-210	75.43	69.41	6.02	279.41	2070	.400	0.190 at -70

Table 2-2. Test Results - Specific Heat (Sheet 2 of 3)

Material	Specimen Weight GMS	Initial Specimen Temperature °F	Initial Toluene Temperature °F	Equilibration Temperature °F	T_t °F	T_s °F	Toluene Weight GMS	C_{pt} BTU/LB-°F	Specific Heat of Specimen BTU/LB-°F
T-500-6 Virgin	95.44	-221	73.80	67.00	6.80	288.00	2035	0.399	0.201 at -77
T-500-6 Virgin	95.70	-302	83.20	71.15	12.05	373.15	2104	0.402	0.286 at -116
T-500-6 Virgin	95.28	-293	78.53	66.35	12.18	359.53	2080	0.400	0.296 at -114
T-500-6 Virgin	93.46	417	Toluene 81.80	66.20	15.60	319.60	Toluene 1917	Toluene .407	.406 at 257
T-500-6 Virgin	96.21	400	Toluene 79.58	66.31	13.27	307.15	Toluene 1910	Toluene .405	.353 at 245
T-500-6 Virgin	83.84	493	TCP 296	286	8	189	TCP 2430	TCP .490	.600 at 399
T-500-6 Virgin	83.85	516	TCP 308	300	8	202	TCP 2387	TCP .490	.553 at 415
T-500-4 Charred	98.2	429	Toluene 76.36	61.84	14.52	338.12	Toluene 2150	Toluene .401	.377 at 26
T-500-4 Charred	97.88	432	Toluene 77.65	63.52	14.13	340.22	Toluene 2152	Toluene .402	.367 at 262
T-500-4 Charred	195	431	TCP 313	301	12	106	TCP* 2295	TCP .490	.652 at 378
T-500-6 Charred	198.88	461	TCP 320	310	10	130	TCP 2150	TCP .490	.407 at 396
T-500-4 Virgin	85.5	400	Toluene 69.11	56.92	12.19	318.7	Toluene 2070	Toluene .401	.371 at 241
T-500-4 Virgin	90.40	495	Toluene 77.90	55.30	22.60	394.5	Toluene 1832	Toluene .406	.473 at 295
T-500-4 Virgin	99.4	496	Toluene 76.05	58.64	17.41	402.54	Toluene 2159	Toluene .403	.378 at 294
T-500-4 Virgin	129.69	496	TCP 302	290	12	182	TCP 2344	TCP .490	.583 at 405
T-500-4 Virgin	185.59	460	TCP 318	304	14	138	TCP 2297	TCP .490	.615 at 401

*Tritoluyl Phosphate

Table 2-2. Test Results - Specific Heat (Sheet 3 of 3)

DENSITY.

TEST EQUIPMENT. A laboratory gravitometer as illustrated in Figure 2-5 was used for density measurements. The balance of this device can be calibrated to 0.1 milligram. The liquid bath maintains the specimen at a uniform temperature.

TEST SPECIMENS. Material specimens were 1-inch squares 1/4-inch thick.

TEST METHOD. Density tests were performed in accordance with the method prescribed in ASTM D792-50. The method consists of immersing the specimen in a known volume of liquid (cyclohexane) and weighing the change produced by the displaced liquid of known density.

RESULTS. Eleven specimens each of "THERMO-LAG" T-500-4 and T-500-6 were tested. The results of these tests are presented in Figure 2-6. Within the range of experimental accuracy, the densities of the two materials correspond, and vary in an almost linear relationship with temperature.

TOTAL NORMAL EMISSIVITY.

TEST EQUIPMENT. The measuring apparatus consisted of an environmental guard maintained at a constant level of temperature by an electrical heater and blower; a reference black body heated to the appropriate temperature; and a thermopile radiometer. The radiometer (essentially a box) was blackened inside, pierced by two tubes on the front face, and fitted with a gold mirror.

TEST SPECIMEN. Specimens were 1.344 inch circular disks 0.5 inch wide. A thermocouple was embedded in each face. The specimens were held in a 0.074-inch thick stainless steel disk.

TEST METHOD. The specimens to be tested were immersed in a heated air stream above the test temperature and maintained at their test temperature. The specimen temperatures were measured by embedded thermocouples installed at fabrication. The radiation coming from the specimen, or alternately from the guard or black body furnace, was focused by a concave gold surface mirror on the sensitive area of the total radiation thermopile and recorded in terms of sensitive galvanometer deflection. These radiometer readings, combined with independently measured temperatures of the specimen, the environmental guard, and the black body furnace, were combined by means of the governing equations to yield the total normal emissivity.

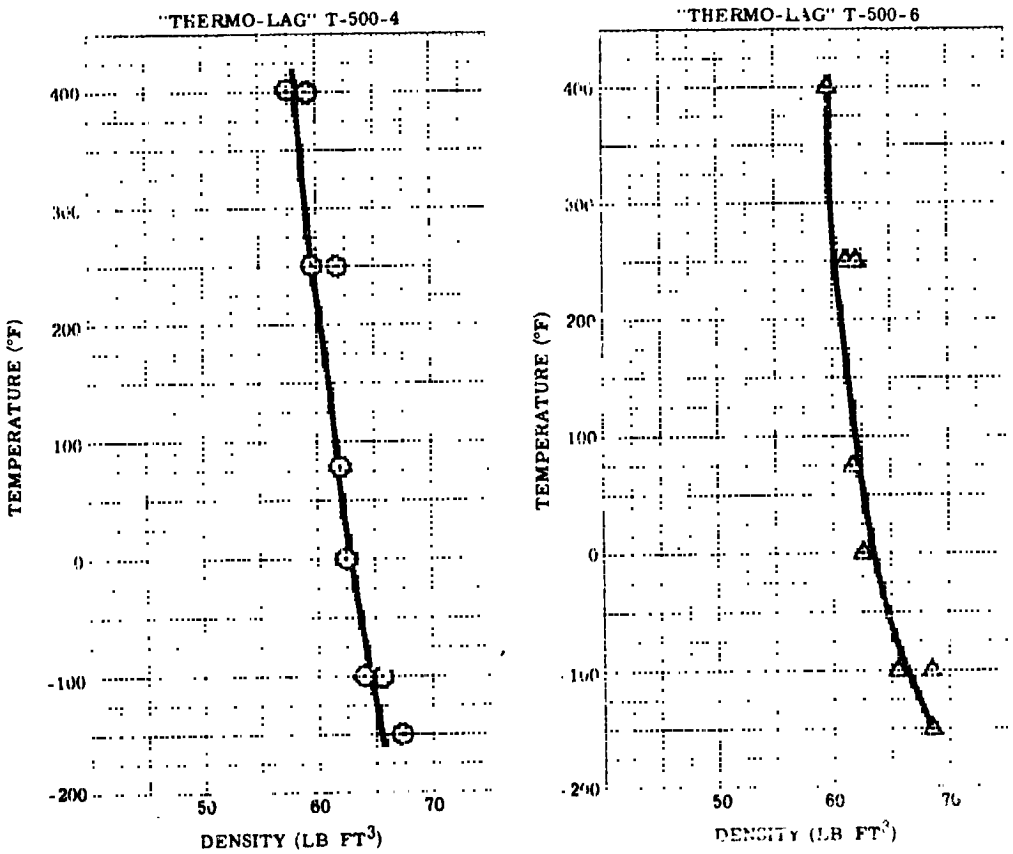


Figure 2-5. Density Versus Temperature for "THERMO-LAG" T-500-4 and T-500-6

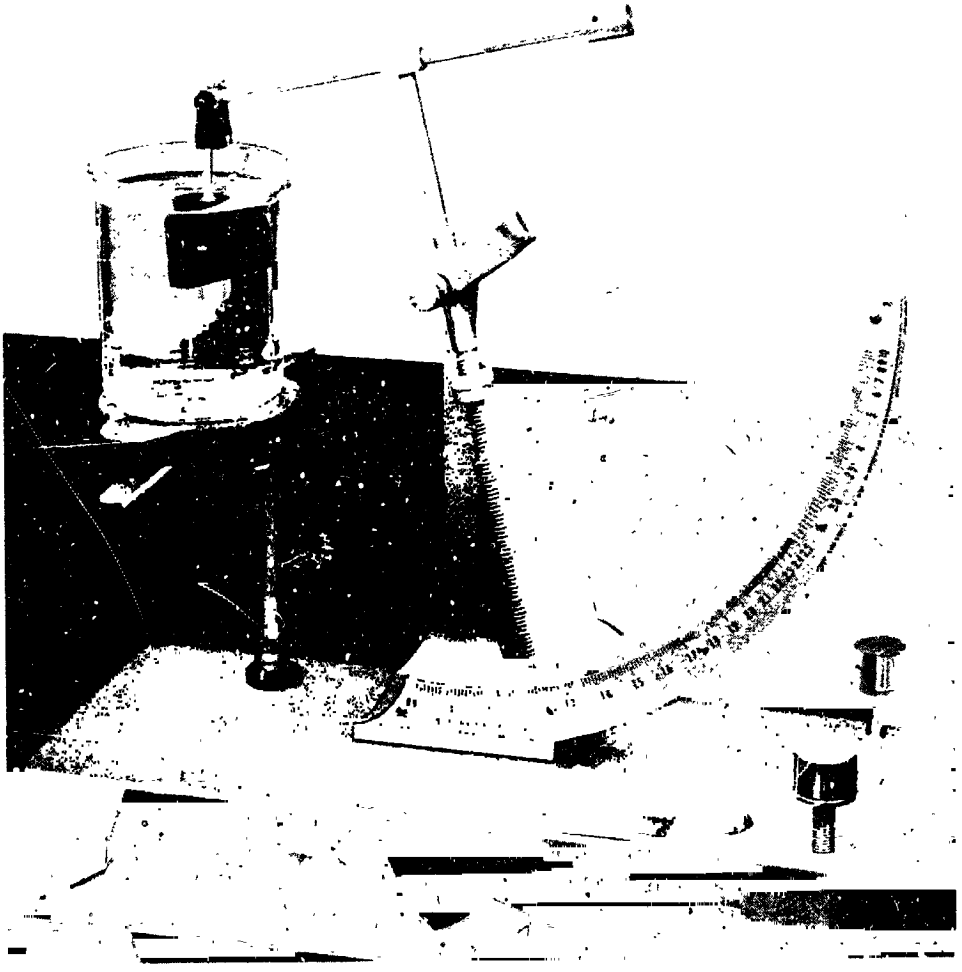


Figure 2-6. Laboratory Gravitometer

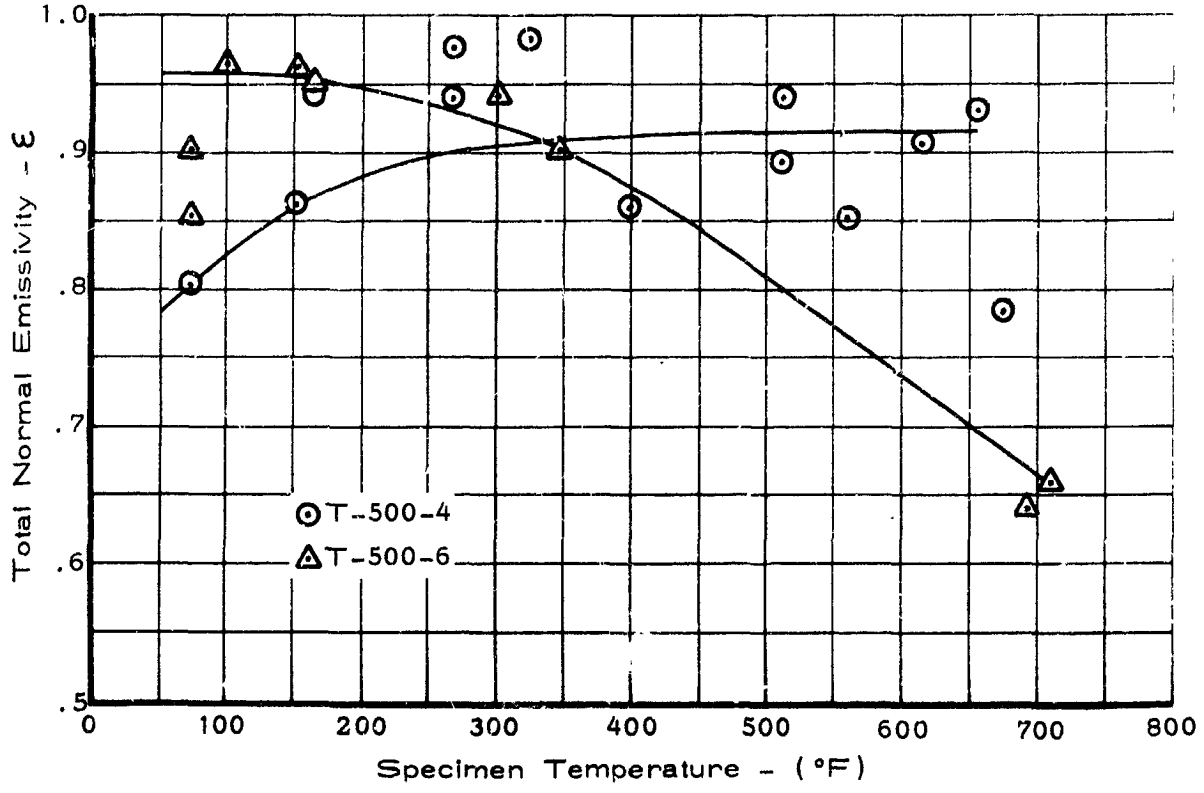


Figure 2-7. Total Normal Emissivity of Virgin "THERMO-LAG" T-500-4 and T-500-6

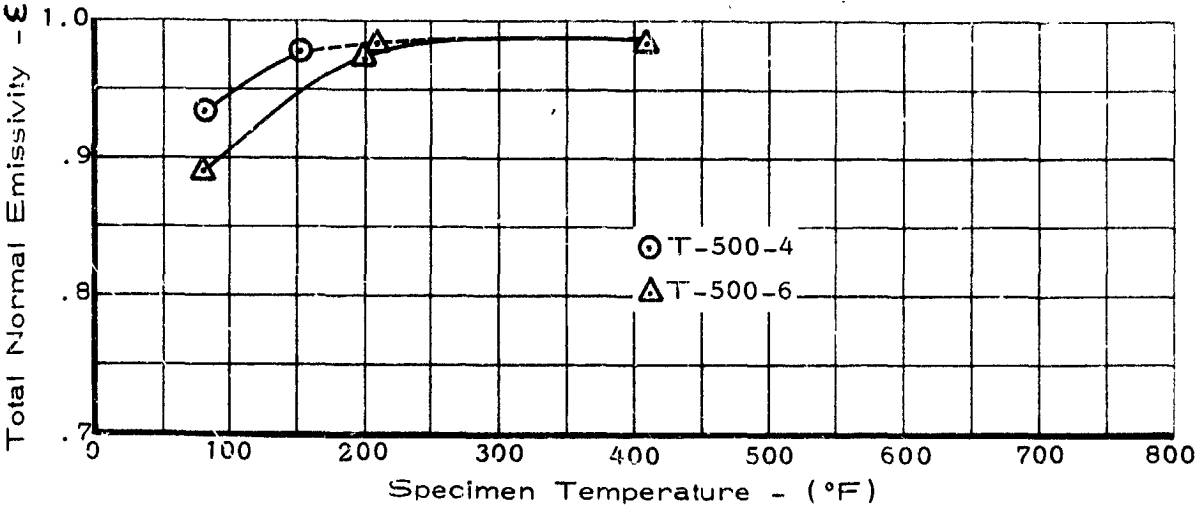


Figure 2-8. Total Normal Emissivity of Precharred "THERMO-LAG" T-500-4 and T-500-6

Specimen Emissivity,						
Temperature (°F)	12 G-1-	12 G-1-3-4	12 G-1-2-6	12 G-1-3-6	Precharred 12 G-6-4	12 G-6-6
73	.804		.854	.902		
80.8					.933	.891
100.6				0.965		
151	.862			.962	.978	
165	.945			.946		
198.5						.973
209.9						.982
270	.976	.940				
301			.942			
325	0.984					
348			.903			
390		.861				
410						.983
513		.893				
		.940				
560	0.851					
614		.906				
656		.931				
675	.784					
695			.649			
710			.660			

Table 2-3. Total Normal Emissivities of "THERMO-LAG" T-500-4 and T-500-6

RESULTS. All black body measurements were made in steady-state. The emissivity tests were performed on eight specimens of "THERMO-LAG" T-500-4 and T-500-6, both virgin and precharred, fabricated by spraying and precasting. The results of the tests are recorded in Table 2-3 and illustrated in Figures 2-7 and 2-8. At least five measurements were made for each point plotted for temperatures below the sublimation temperature. All three specimens tested at the high temperatures (two of "THERMO-LAG" T-500-4 and one of "THERMO-LAG" T-500-6) were of virgin material at the beginning of the test and went through the sublimation phase while the emissivity measurements were in progress. The data indicates that changes in emissivity are produced near sublimation temperatures. The values for "THERMO-LAG" T-500-4 decrease at temperatures preceding sublimation and then increase with temperatures following sublimation. Plotted data for "THERMO-LAG" T-500-6 indicates a decrease in emissivity during the sublimation phase, which is compatible with data for fused silica. These T-500-6 specimens exhibited a hard glossy char layer of silica deposits. Plasma jet tests indicate that the emissivity values for T-500-6 level off at about 0.65.

COEFFICIENT OF THERMAL EXPANSION

TEST EQUIPMENT. A fused-quartz-tube dilatometer was used to measure the expansion of "THERMO-LAG" T-500 test specimens resulting from a change in temperature.

TEST SPECIMEN. Material test specimens were 5/16-inch square bars 2 inches long. A thin steel plate was cemented to each end of the sample to protect it against indentation during the test.

TEST METHOD. The method which was used to measure the coefficient of linear thermal expansion of "THERMO-LAG" T-500 materials is described in ASTM D696-44. A test sample was immersed in several constant temperature baths, and its length was then measured with a dial gage calibrated to 0.0001 inch per division. The coefficient of thermal expansion, α, (in/in°C) was calculated from the measured data between the test temperature and 30°C above and below test temperature using the equation:

$$\alpha = \frac{\Delta L}{L \Delta T}$$

where:

ΔL = Average of three changes in length of the samples due to heating (inches).

L = Length of test sample at test temperature (Inches).

ΔT = Temperature difference over which the changes in length of the specimen are measured. (°C)

RESULTS. Eight tests were performed on each of the virgin "THERMO-LAG" T-500-4 and T-500-6 materials. The results of these tests are illustrated in Figure 2-9 and recorded in Table 2-4.

Study of the plotted data indicates certain behavior characteristics of the two materials.

1. A phase transition from the elastic to the glass state occurs in the temperature regime below room value for "THERMO-LAG" T-500-6.

2. The erratic behavior above 250°F indicated where "THERMO-LAG" T-500-4 began to behave as a viscous fluid.

Ten tests were performed on each of the charred "THERMO-LAG" T-500-4 and T-500-6 materials. The results of the tests are plotted in Figure 2-10 and recorded in Table 2-4.

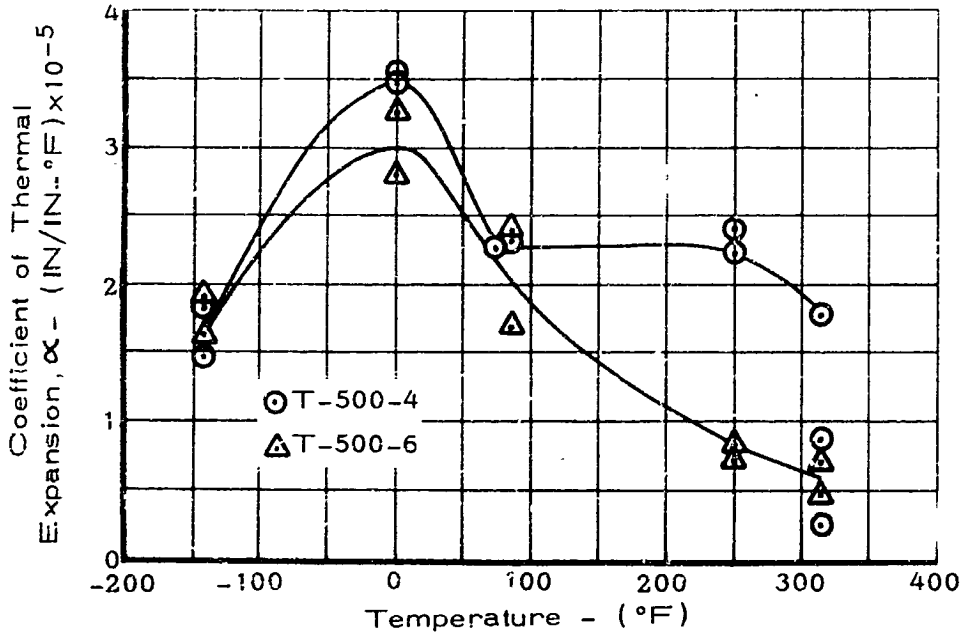


Figure 2-9. Coefficient of Thermal Expansion for Virgin "THERMO-LAG" T-500-4 and T-500-6

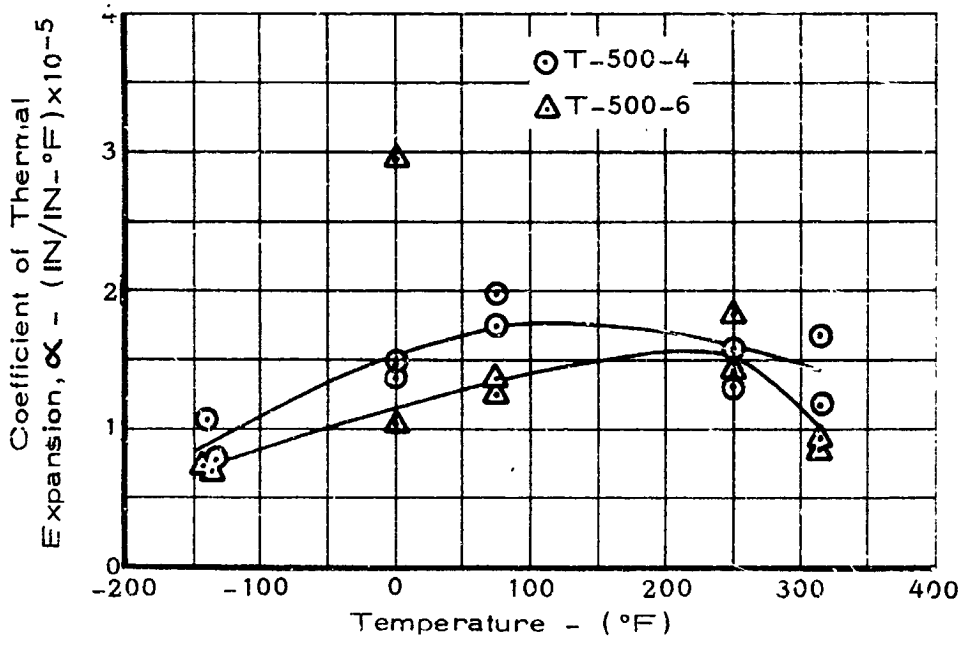


Figure 2-10. Coefficient of Thermal Expansion for Charred "THERMO-LAG" T-500-4 and T-500-6

Material	Sample No.	Temperature		L inches	ΔL inches	ΔT °C	$\alpha = \frac{\Delta L}{L \times \Delta T}$ IN./IN.-°F x 10^{-5}
		°C	°F				
T-500-4 charred	13-G-1-21-4	-95	-139	2.0174	.00117	30	1.07
T-500-4 charred	13-G-1-30-4	-91	-132	2.0410	.00087	30	0.788
T-500-4 charred	13-G-1-22-4	-18	0	2.0468	.00161	30	1.46
T-500-4 charred	13-G-1-23-4	-18	0	2.0550	.00154	30	1.39
T-500-4 charred	13-G-1-25-4	24	75	2.0497	.00218	30	1.97
T-500-4 charred	13-G-1-29-4	24	75	2.0535	.00193	30	1.74
T-500-4 charred	13-G-1-24-4	121	250	2.0583	.00148	30	1.33
T-500-4 charred	13-G-1-26-4	121	250	2.0620	.00175	30	1.57
T-500-4 charred	13-G-1-28-4	157	315	2.0710	.00132	30	1.18
T-500-4 charred	13-G-1-27-4	157	315	2.0640	.00186	30	1.67
T-500-4	13-G-1-13-4	-96	-141	2.0722	.00206	30	1.84
T-500-4	13-G-1-16-4	-96	-141	2.0384	.00162	30	1.47
T-500-4	13-G-1-6-4	-18	0	2.0719	.00389	30	3.48
T-500-4	13-G-1-1-4	-18	0	2.0629	.00385	30	3.46

Table 2-4. Coefficient of Thermal Expansion Test Results (Sheet 1 of 3)

Material	Sample No.	Temperature		L inches	ΔL inches	ΔT °C	$\alpha = \frac{\Delta L}{L \times \Delta T}$ IN./IN.-°F x 10^{-5}
		°C	°F				
T-500-4	13-G-1-4-4	24	76	2.0780	.00255	30	2.27
T-500-4	13-G-1-17-4	30	86	2.0801	.00260	30	2.32
T-500-4	13-G-1-20-4	157	315	2.0589	.00092	30	0.826
T-500-4	13-G-1-14-4	157	315	2.0735	.00030	30	0.268
T-500-4	13-G-1-11-4	157	315	2.0897	.00201	30	1.78
T-500-6 charred	13-G-1-27-6	-94	-137	2.0549	.00078	30	0.705
T-500-6 charred	13-G-1-22-6	-96	-141	2.0621	.00080	30	0.715
T-500-6 charred	13-G-1-25-6	-18	0	2.0817	.00116	30	1.03
T-500-6 charred	13-G-1-8-6	-18	0	2.0814	.00332	30	2.96
T-500-6 charred	13-G-1-24-6	24	75	2.0730	.00141	30	1.26
T-500-6 charred	13-G-1-26-6	24	75	2.0738	.00152	30	1.35
T-500-6 charred	13-G-1-23-6	121	250	2.0587	.00162	30	1.40
T-500-6 charred	13-G-1-21-6	121	250	2.0551	.00203	30	1.83
T-500-6 charred	13-G-1-12-6	157	315	2.0588	.00103	30	0.927

Table 2-4. Coefficient of Thermal Expansion Test Results
(Sheet 2 of 3)

Material	Sample No.	Temperature		L inches	ΔL inches	ΔT °C	$\alpha = \frac{\Delta L}{L \times \Delta T}$ IN./IN.-°F x 10^{-5}
		°C	°F				
T-500-6 charred	13-G-1-7-6	157	315	2.0461	.00098	30	0.887
T-500-6	13-G-1-15-6	-96	-141	2.0496	.00179	30	1.616
T-500-6	13-G-1-7-6	-96	-141	2.0636	.00205	30	1.89
T-500-6	13-G-1-10-6	-18	0	2.1000	.00318	30	2.80
T-500-6	13-G-1-9-6	-18	0	2.0827	.00367	30	3.26
T-500-6	13-G-1-3-6	30	86	2.0854	.00180	30	1.69
T-500-6	13-G-1-6-6	30	86	2.0975	.00270	30	2.38
T-500-6	13-G-1-17-6	157	315	2.1030	.00081	30	0.712
T-500-6	13-G-1-14-6	157	315	2.0809	.00052	30	0.462
T-500-4	13-G-1-2-4	121	250	2.0933	.0027	30	2.39
T-500-4	13-G-1-9-4	121	250	2.0867	.0025	30	2.22
T-500-6	13-H-2-1-6	121	250	2.074	.0009	30	0.805
T-500-6	13-H-2-10-6	121	250	2.0625	.0008	30	0.715

Table 2-4. Coefficient of Thermal Expansion Test Results (Sheet 3 of 3)

ENVIRONMENTAL CHARACTERISTICS

MATERIAL BEHAVIOR UNDER VACUUM AND TEMPERATURE EXPOSURE.

OBJECTIVE. Vacuum exposure tests were conducted to determine the effect of low pressure upon the weight loss of "THERMO-LAG" T-500 material as a function of exposure time and temperature. The conditions at which these tests were performed on "THERMO-LAG" T-500 material are given in Table 2-5.

Specimen area (iN^2)	1.0
Specimen thicknesses (mils)	20, 50, 100
Vacuum (TORR)	10^{-4}
Specimen temperature (°F)	80, 250

Table 2-5. Vacuum Exposure Test Conditions

TEST EQUIPMENT. The tests were performed in a vacuum chamber with a cryogenic wall maintained at -300°F. Two quartz infrared lamps installed inside an inner chamber of the vacuum test facility provided precise and stabilized specimen temperature. A view of the test chamber is shown in Figure 2-11.

TEST SPECIMENS. "THERMO-LAG" test specimens were prepared from chemically cleaned 14-inch x 16-inch x .047-inch number 1010 cold rolled steel plates sprayed with T-500-4 material to 0.020, 0.50, and 0.100 inch thicknesses. The plates were cured according to "THERMO-LAG" T-500-4 cure schedule and 1-inch x 1-inch x .047-inch steel sections were cut. To position thermocouples, used as sensors, the 1-inch x 1-inch x .047-inch pieces were drilled

from the metal back in the center with a 0.050-inch diameter drill to a .005-inch depth from the "THERMO-LAG" surface.

DATA REDUCTION AND ANALYSIS. The weight loss curves for the specimen thicknesses tested are shown in Figures 2-12, 2-13, and 2-14. The test data indicates that the weight loss is composed of two distinct periods. The first period comprises an initial weight loss of entrapped solvents and volatilization of the monomolecular layer at the surface of the sample. This initial period lasts as long as 10 to 15 hours, depending upon the pretreatment of the specimens. It is the period after the initial weight loss period, however, which is of interest for predicting weight loss under sustained vacuum exposure for extended periods of time.

The second weight loss period (designated the rate period) was used to analyze the amount of material that would be lost over long exposure periods. The total weight loss for a unit area, being the sum of the losses for each period, is expressed as:

$$\left(\frac{W}{A}\right)_T = \left(\frac{W}{A}\right)_0 + \left(\frac{W}{A}\right)_R \qquad (1)$$

where the subscripts refer to the initial period and the rate period.

For the second period the weight loss is expressed by:

$$\frac{d\left(\frac{W}{A}\right)}{dt} \qquad (2)$$

The rate expression can be expressed for the initial weight loss exposure time, t_o, to any time, t, at constant temperature and initial thickness, by:

$$\left(\frac{W}{A}\right)_R = \int_{t_o}^{t} \left[\frac{d\left(\frac{W}{A}\right)}{dt}\right] dt$$

As the weight loss expression for the total exposure time is achieved, then:

$$\left(\frac{W}{A}\right)_T = \left(\frac{W}{A}\right)_0 + \int_{t_0}^{t} \left[\frac{d\left(\frac{W}{A}\right)}{dt}\right] dt \qquad (3)$$

The expression indicates that quantitative results of total weight loss must be determined from the effect of temperature, time of exposure, and initial specimen thickness on the rate of weight loss for the rate period. (The initial weight loss period does not enter into the problem, as its weight loss is a function of pre-treatment of the specimen, which was not controlled.)

The rate of weight loss was postulated by a generalized rate equation of the form of the modified Arrhenius expression:

$$\frac{d\left(\frac{W}{A}\right)}{dt} = A(\Delta x_i) t^{-n(\Delta x_i)} e^{-B(\Delta x_i)/T} \qquad (4)$$

where the terms $A(\Delta x_i)$, $n(\Delta x_i)$ and $B(\Delta x_i)$ are functions only of the initial thickness. These terms are determined for a given specimen thickness, and are defined herein as:

n = Slope of the weight loss rate versus exposure time curve (Figure 2-15).

B = Slope of the curve for weight loss rate as a function of the reciprocal absolute temperature for constant exposure times (Figure 2-16).

A = Term derived from the modified Arrhenius equation for the known parameters n and B.

The terms A, n, and B were calculated for a given specimen thickness in the manner described in Reference No. 10. These coefficients and exponents of the modified Arrhenius equation are plotted in Figure 2-17 as a function of the initial sample thickness.

RESULTS OF EMERSON ELECTRIC TESTS. The following rate equations were derived from the data shown in Figure 2-17 (reduced in terms of the modified Arrhenius equation) for the specimen thicknesses tested by Emerson Electric.

1. For 20 mil specimen thickness:

$$\frac{d\left(\frac{W}{A}\right)}{dt} = 225 t^{-1.88} e^{-6640/T} \qquad (5)$$

2. For 50 mil specimen thickness:

$$\frac{d\left(\frac{W}{A}\right)}{dt} = 3.14 \times 10^{-2}\, t^{-0.60}\, e^{-2590/T}$$

3. For 100 mil specimen thickness:

$$\frac{d\left(\frac{W}{A}\right)}{dt} = 6.09 \times 10^{-3}\, t^{-0.495}\, e^{-1770/T}$$

The results of the vacuum tests on "THERMO-LAG" T-500-4 performed by Emerson are shown in Figures 2-15 and 2-16. Figure 2-15 indicates that the rate of weight loss decreases as the time of exposure increases for all samples tested.

The weight loss rate as postulated by the generalized rate equation is inversely proportioned to the exposure time raised to a power $n(\Delta x_i)$ which is a function of the initial thickness. The functional dependence of Δx_i (the initial specimen thickness) on $n(\Delta x_i)$ is shown in Figure 2-17.

Figure 2-17 shows that the term $n(\Delta x_i)$ decreases as the initial thickness increases. Examination of the $n(\Delta x_i)$ curve indicates that for initial thicknesses greater than 80 mils, the exponent $n(\Delta x_i)$ approaches a constant value. The approach of $n(\Delta x_i)$ to an asymptotic value indicates that the time dependence of the weight loss rate is approximately independent of specimen thicknesses exceeding 80 mils.

The test data illustrated that as the temperature of exposure increased, the rate of weight loss increased. The generalized rate equation shows that the rate is inversely proportional to an exponential of reciprocal absolute temperature $e^{\frac{-B(\Delta x_i)}{T}}$, where $B(\Delta x_i)$ is a function of the initial thickness. This initial thickness dependence is shown in Figure 2-17. Examination of the $B(\Delta x_i)$ curve shows that its decrease in value becomes less evident as Δx_i increases above 80 mils. The data indicates that for specimen thicknesses exceeding 80 mils the temperature dependence of the rate is approximately independent of thickness.

Figure 2-15 shows that after an exposure duration of approximately 30 hours the weight loss rate increases as the initial specimen thickness increases. For specimen thicknesses greater than 80 mils, that rate can be considered independent of initial thickness. Figure 2-17 indicated that the coefficient and exponents $A(\Delta x_i)$, $B(\Delta x_i)$, and $n(\Delta x_i)$ of the modified Arrhenius equation become independent of the initial thickness after 80 mils. As these terms approach a constant value for $\Delta x_i > 80$ mils, the rate expression can then be expressed as a function only of temperature and time. The rate of weight loss

for a 500-mil specimen should, therefore, be approximately the same as the rate for a 100-mil specimen if tested under isothermal conditions.

The following conclusions can be drawn from the rate of weight loss study:

1. The rate decreases as vacuum exposure time increases.

2. The rate increases with an increase in the exposure temperature.

3. The rate increases as the initial specimen thickness increases until a limiting thickness is encountered, at which thickness the rate becomes a function only of temperature and time. For thicknesses less than 80 mils, the generalized rate equation can be used to consider the effect of specimen thickness.

The implications of the space environment simulation study findings were considered with regard to their effect upon the predicted design weight of a "THERMO-LAG" T-500 heat shield system for entry protection of an advanced manned spacecraft. Assuming the vehicle surface to be maintained at 250°F during a 14-day space transit allowance for thermal barrier material weight loss results in an increase in the design weight from 858 to 978 pounds for an entry trajectory imposing an integrated stagnation heating load of 108,000 Btu/Ft^2.

STRUCTURAL PROPERTIES OF "THERMO-LAG" T-500 MATERIALS

The structural properties of both "THERMO-LAG" T-500-4 and T-500-6 were determined over the temperature range of interest. The determinations are reported in Volume III.

THERMAL-CHEMICAL CHARACTERISTICS

DIFFERENTIAL THERMAL ANALYSIS

OBJECTIVE. Tests were performed to determine characteristic temperatures produced by thermal reactions of "THERMO-LAG" T-500 materials.

TEST EQUIPMENT. A Deltatherm Differential Thermal Analyzer, manufactured by Technical Equipment Corporation, was used. The DTA unit is shown in Figure 2-18.



Figure 2-11. Environmental Chamber

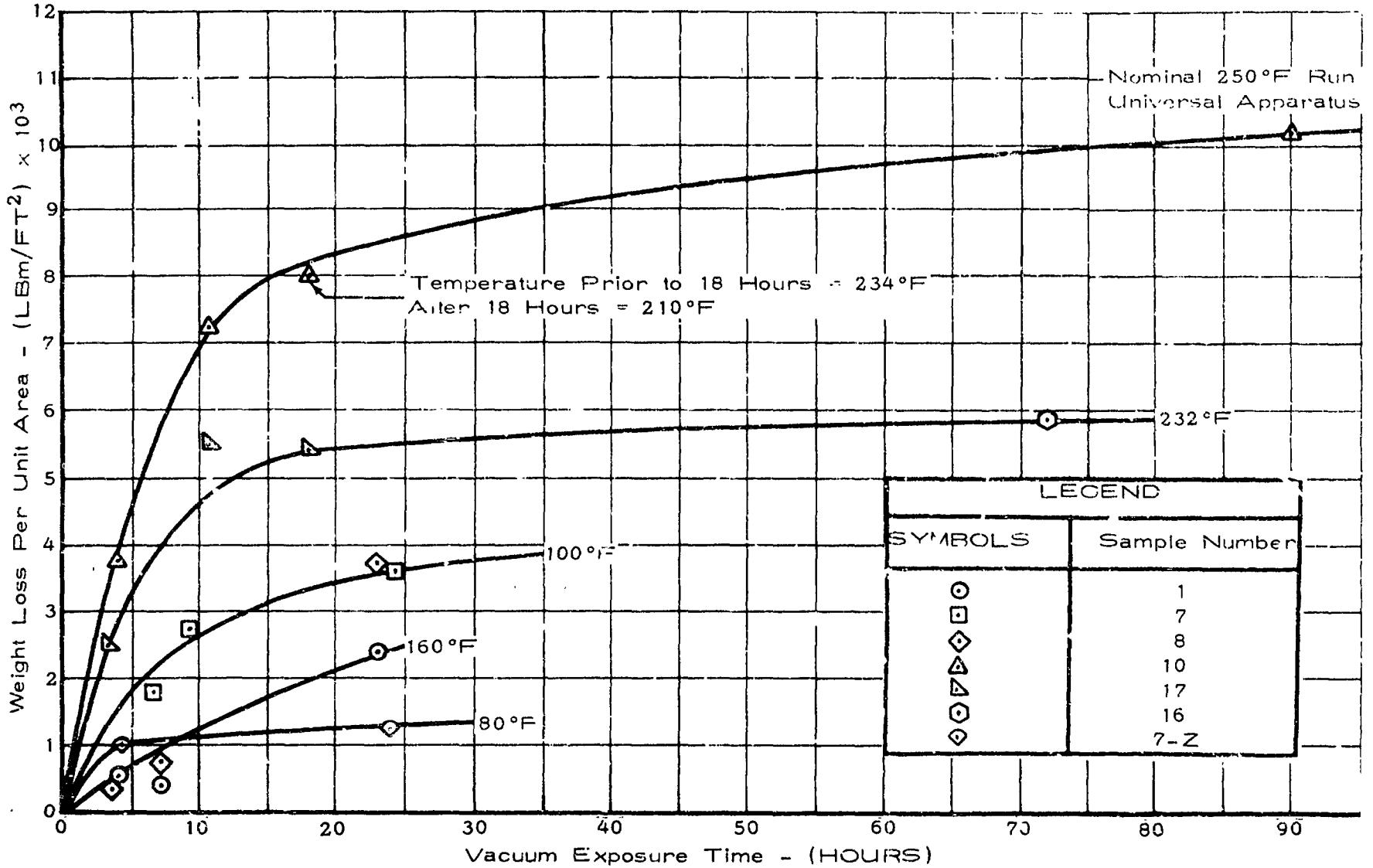


Figure 2-12. High Vacuum Exposure Tests on "THERMO-LAG" T-500-4 (20-Mil Samples)

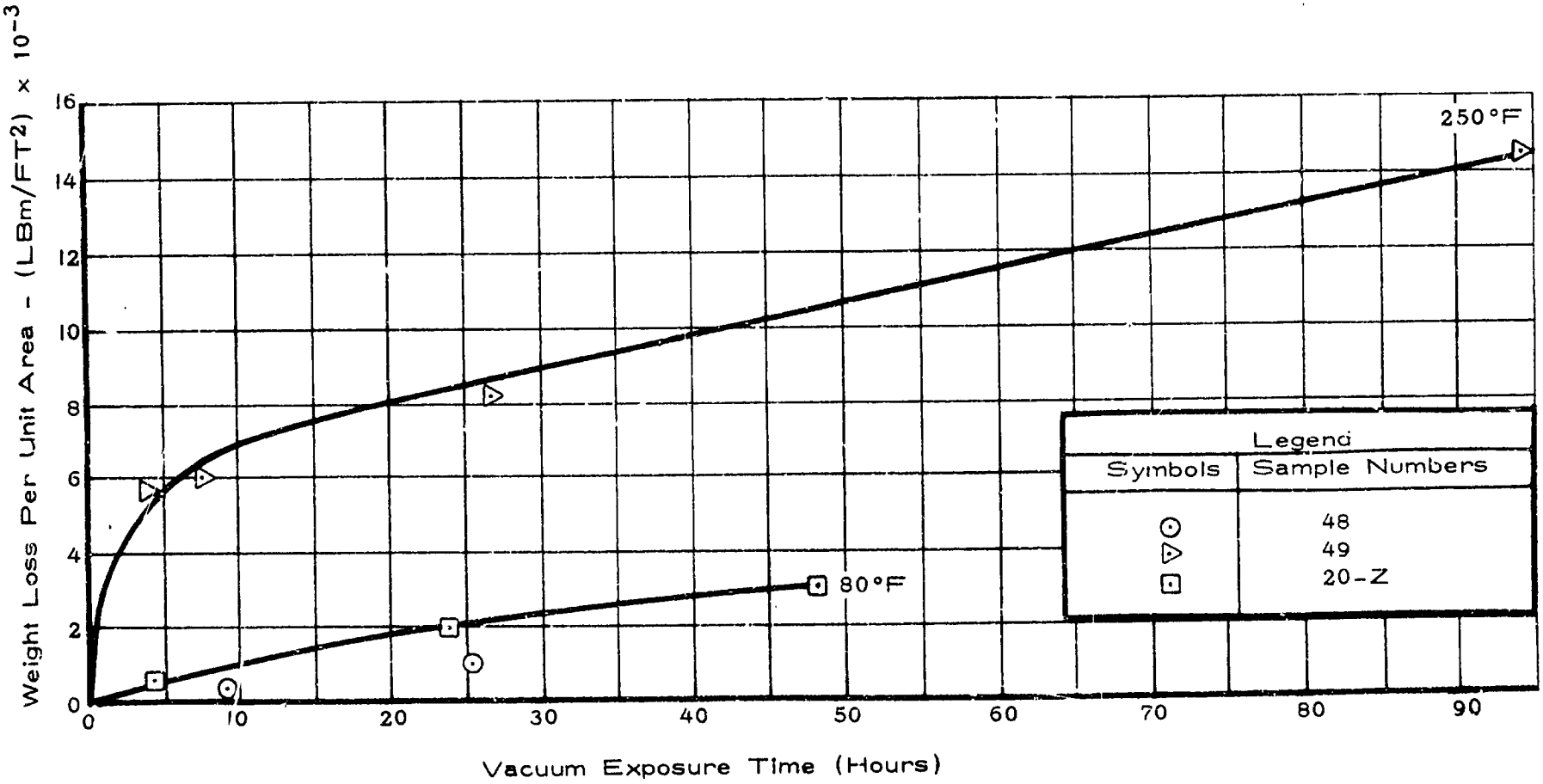


Figure 2-13. High Vacuum Exposure Tests on "THERMO-LAG" T-500-4 (100-Mil Samples)

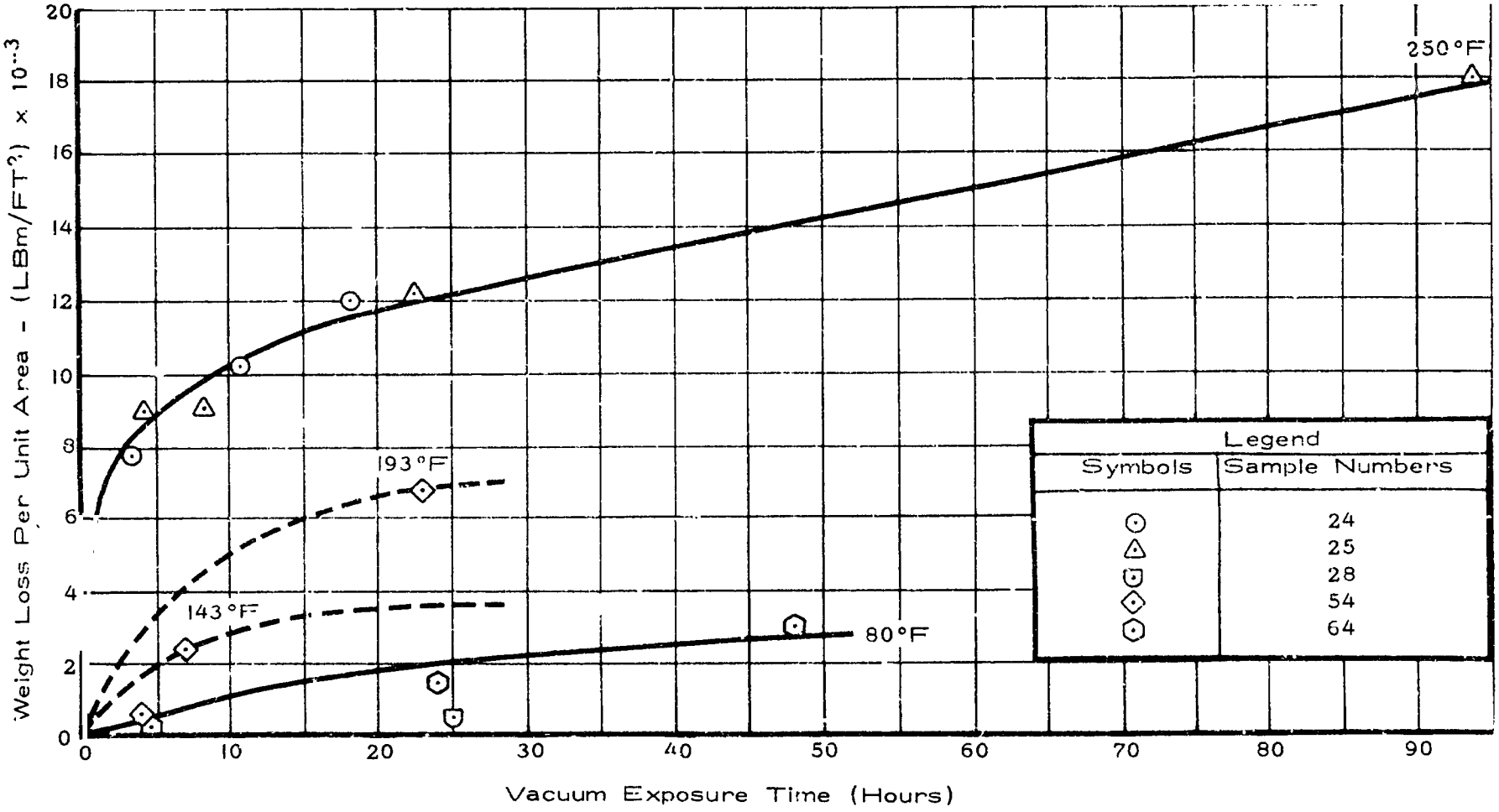


Figure 2-14. High Vacuum Exposure Tests on "THERMO-LAG" T-500-4 (50-Mil Samples)

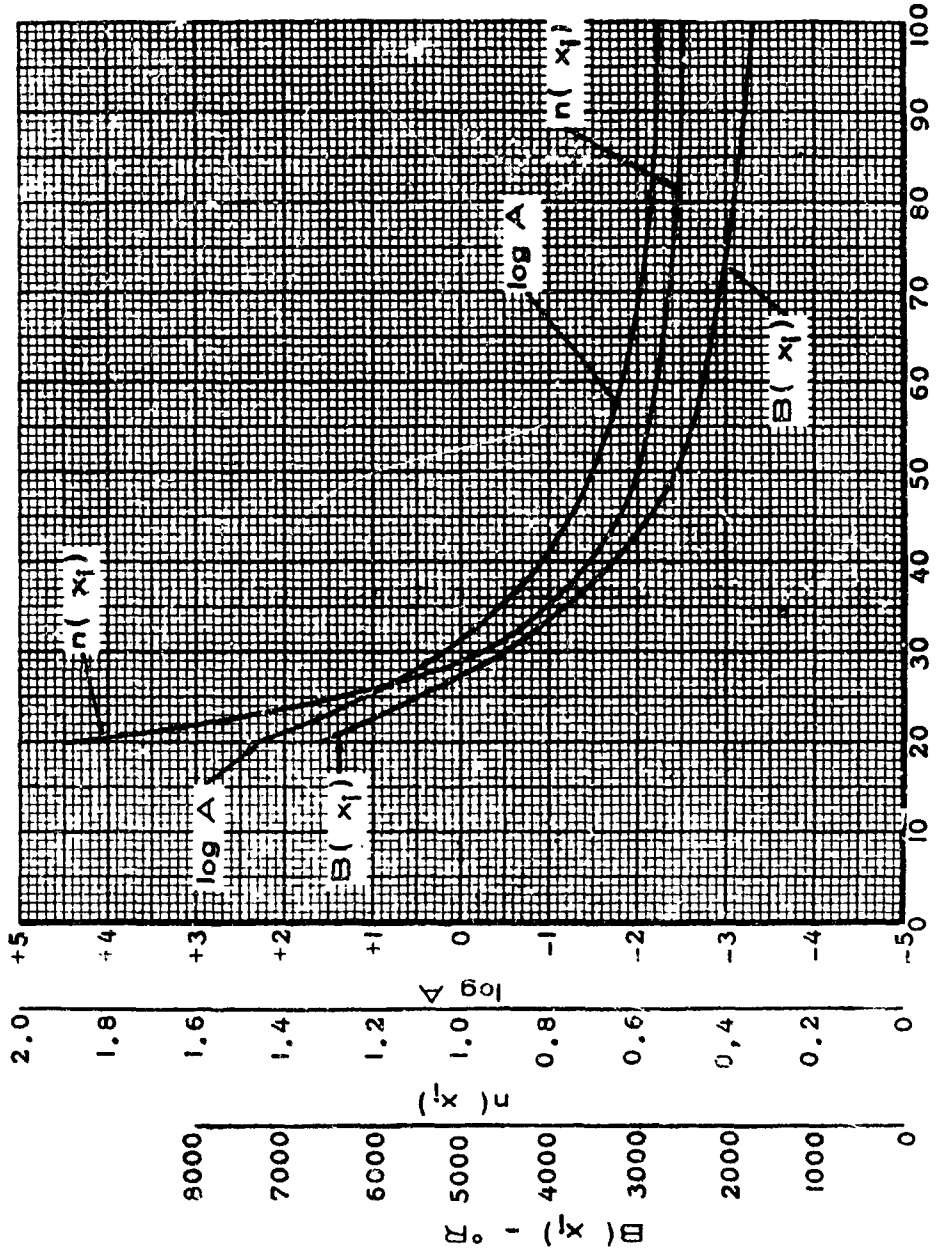


Figure 2-15. Coefficient and Exponents of Modified Arrhenius Equation as a Function of Initial Specimen Thickness

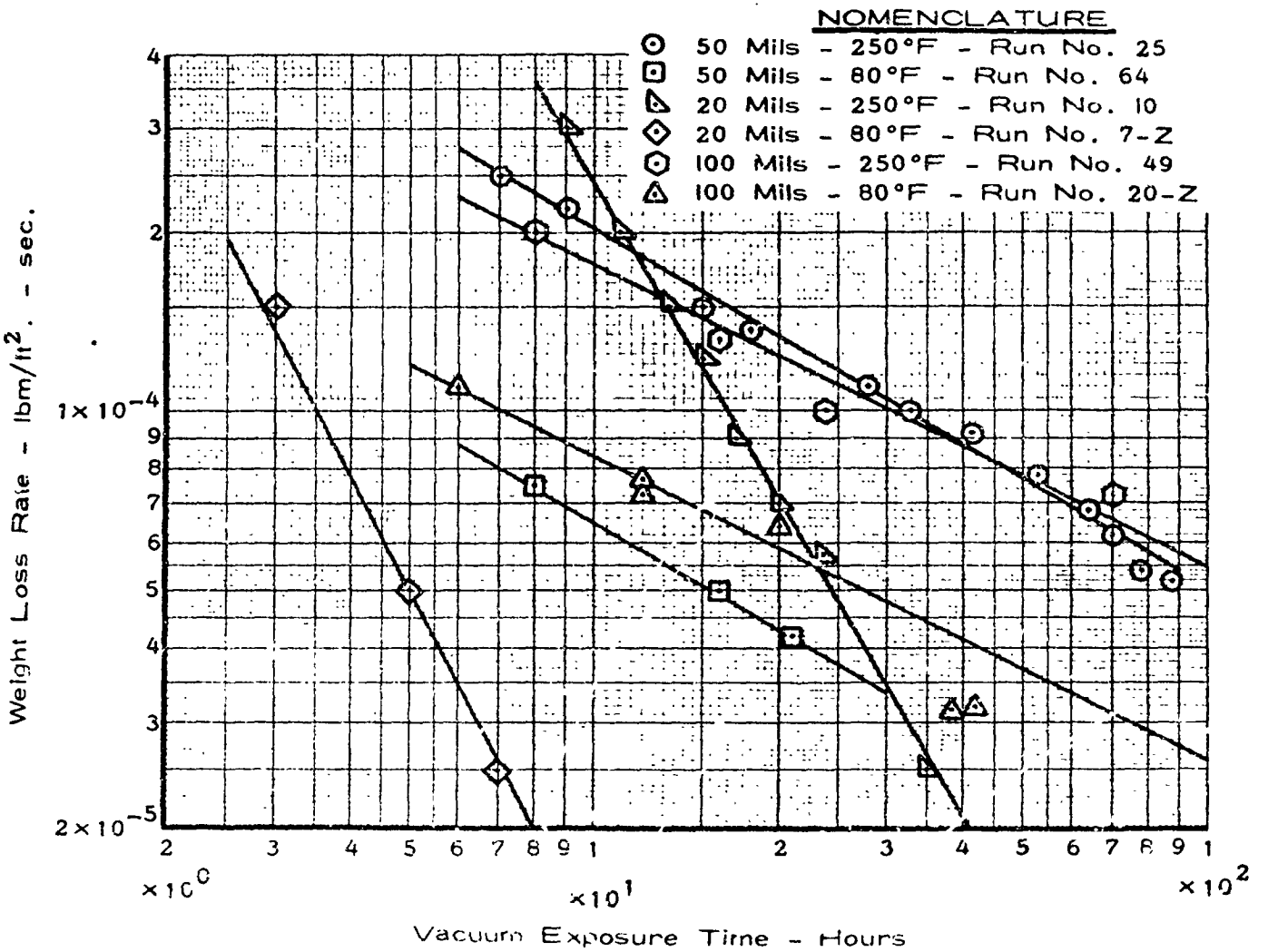


Figure 2-16. Isothermal Weight Loss Rate As A Function of Time.

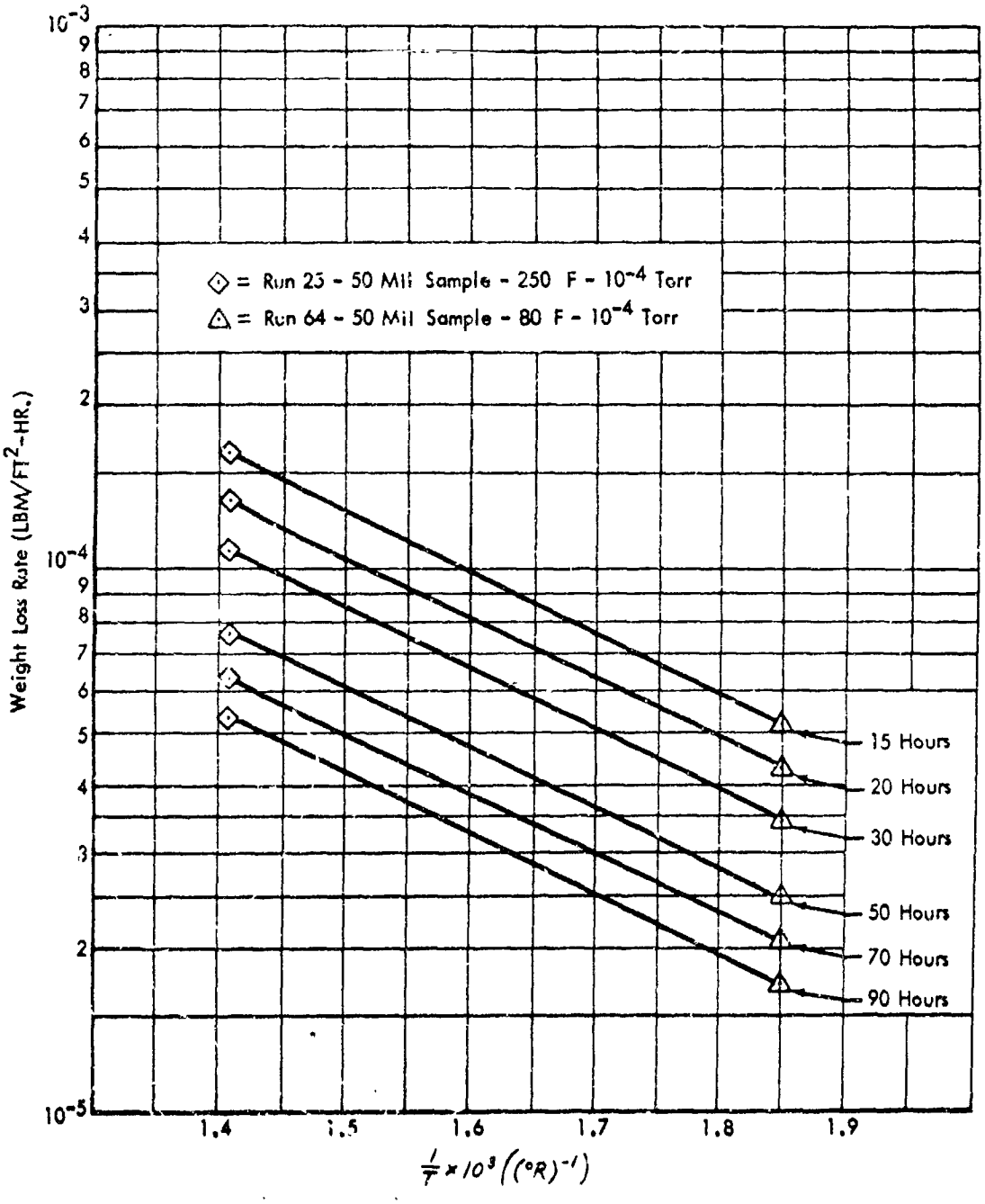


Figure 2-17. Temperature Dependence of Weight Loss Rate for Constant Exposure Times

TEST SPECIMEN. Test specimens weighing approximately one gram were prepared in a pulverized form.

TEST METHOD. The method of analysis involved a comparison of the thermal behavior of T-500 with that of a thermally inert silica material. The thermal behavior of the specimen and the thermally inert silica material was recorded by differential thermocouples at the temperature increase rates of 3.6°F/min., 9°F/min., and 18°F/min. Variations in temperature between the specimen and reference material produced by a phase change were recorded as a function of the specimen temperature.

RESULTS. Figures 2-19 through 2-26 present results of the analysis for "THERMO-LAG" T-500-4 and T-500-6 at the imposed temperature increase rates of 3.6, 9, and 18°F/minute. A study of recorded data indicates that two distinct phase changes occurred for each test. The first endotherm indicates a phase change in the crystal structure of the subliming material. The second endotherm indicates the temperature of sublimation of the subliming material taken as the point at which the slope change is first observed. The sublimation temperature, as indicated in the illustrations, averages approximately 560°F for "THERMO-LAG" T-500-4; and 545°F for "THERMO-LAG" T-500-6.

HEAT OF DECOMPOSITION

Differential thermal analyses were performed to measure the heats of decomposition of "THERMO-LAG" T-500-4 and T-500-6. Test samples were run with known weights of silver nitrate ($AgNO_3$) and potassium dichromate (KCr_2O_7), whose heats of fusion are known to be 16.2 cal/gm and 28.9 cal/gm, respectively. Figure 2-27 shows the DTA curves for these tests.

Heats of decomposition of the "THERMO-LAG" T-500-4 and T-500-6 were calculated by the equation:

$$\Delta H_2 = \frac{(\Delta H_1)(W_1)(A_2)}{(W_2)(A_1)}$$

where:

ΔH_2 = Heat of sublimation of "THERMO-LAG"

ΔH_1 = Heat of fusion of $AgNO_3$ or KCr_2O_7

W_2 = Weight of "THERMO-LAG"



Figure 2-18. Deltatherm Differential Thermal Analyzer

W_1 = Weight of $AgNO_3$ or $KCr2O_7$

A_2 = Integrated valley area of "THERMO-LAG"

A_1 = Integrated valley area of "THERMO-LAG"

Calculated results show that the heats of decomposition of "THERMO-LAG" T-500-4 and T-500-6 are 1400 Btu/Lbm and 1700 Btu/Lbm, respectively.

THERMOGRAVIMETRIC ANALYSIS

OBJECTIVE. Tests were performed to determine, as a function of a linear temperature rise, the rate at which "THERMO-LAG" T-500 material loses weight during the sublimation process and the temperature range at which the maximum weight loss of "THERMO-LAG" T-500 occurs.

TEST EQUIPMENT. A Deltatherm Thermogravimetric Analyzer, which incorporates an electronic balance and an external furnace, was used. The TGA unit is shown in Figure 2-18.

TEST SPECIMEN. Approximately three to four milligrams of pulverized "THERMO-LAG" T-500-4 or T-500-6 were analyzed in each test.

TEST METHOD. The electronic balance of the test equipment continuously recorded sample weights as the specimen was heated at a linear rate of temperature rise.

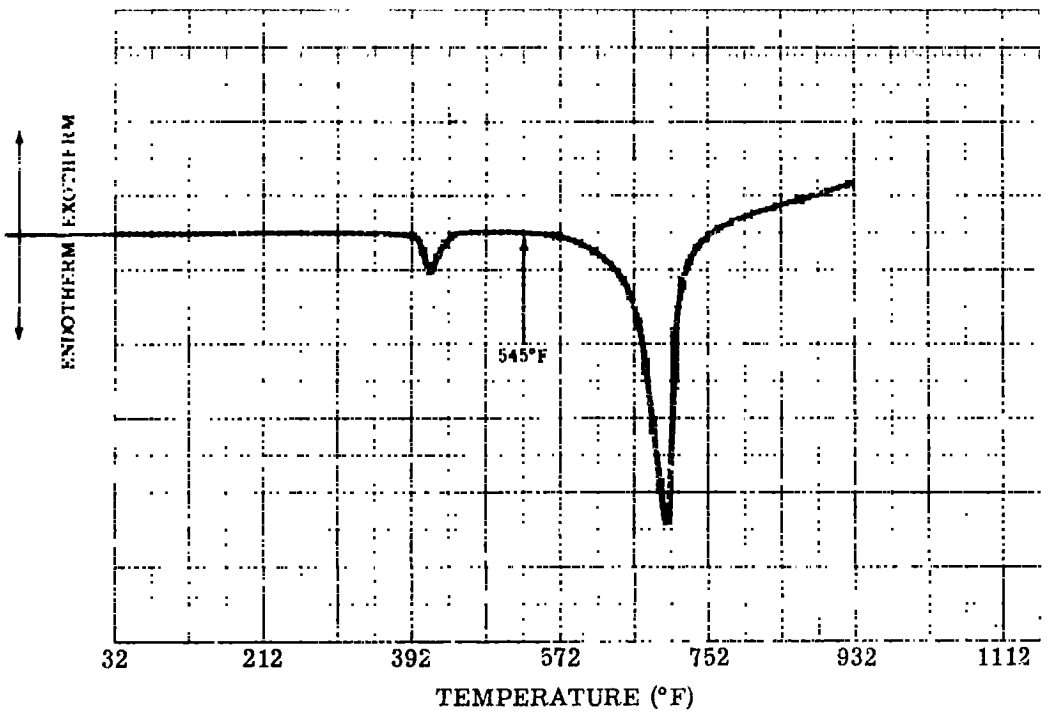
RESULTS. The test results for "THERMO-LAG" T-500-4, where two or more temperature increase rates of 3.9, 9, and 18°F/minute were imposed, are illustrated in Figures 2-28 through 2-32. Figures 2-33 through 2-35 illustrate the test results for "THERMO-LAG" T-500-6 for the same imposed temperature increase rates.

GAS ANALYSIS.

OBJECTIVE. An analysis was performed to determine the primary gas products evolved during the ablation of "THERMO-LAG" T-500-4.

TEST EQUIPMENT. A Beckman Model GC-2A chromatograph with a silicone column and a molecular sieve column was used. The silicone column was calibrated for hydrocarbons and other gases, while the molecular sieve column was calibrated for atmospheric gases.

TEST SPECIMEN. The specimens analyzed were trapped gases given off from the ablation process of "THERMO-LAG" T-500-4 during exposure to infrared heat lamps.



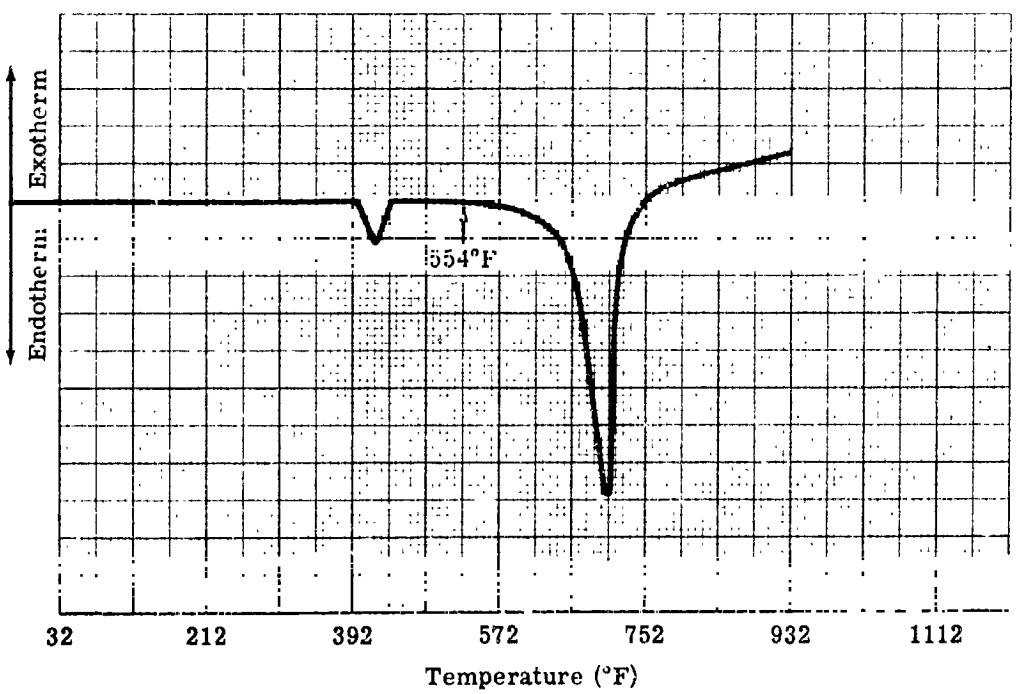
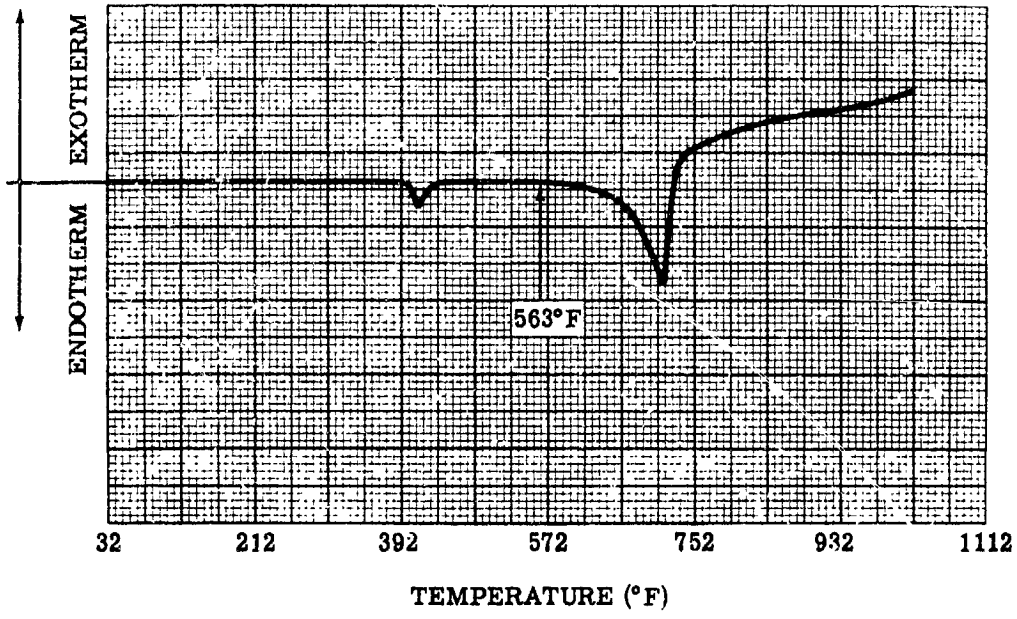


Figure 2-19. Differential Thermal Analyses of "THERMO-LAG" T-500-6 for a Temperature Increase Rate of 3.6°F per Minute



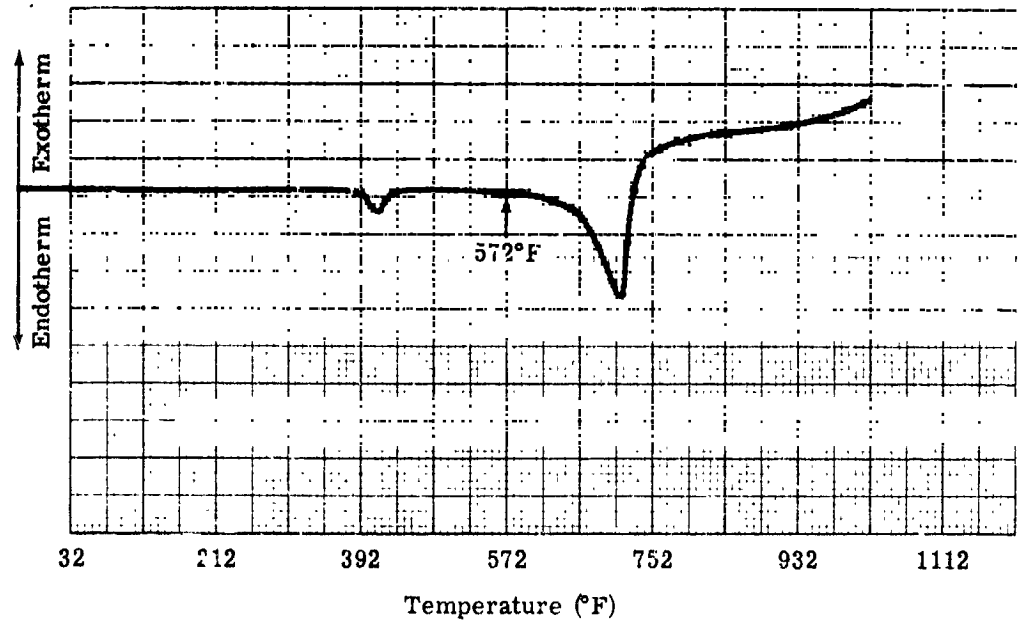


Figure 2-20. Differential Thermal Analyses of "THERMO-LAG" T-500-6 for a Temperature Increase Rate of 3.6°F per Minute

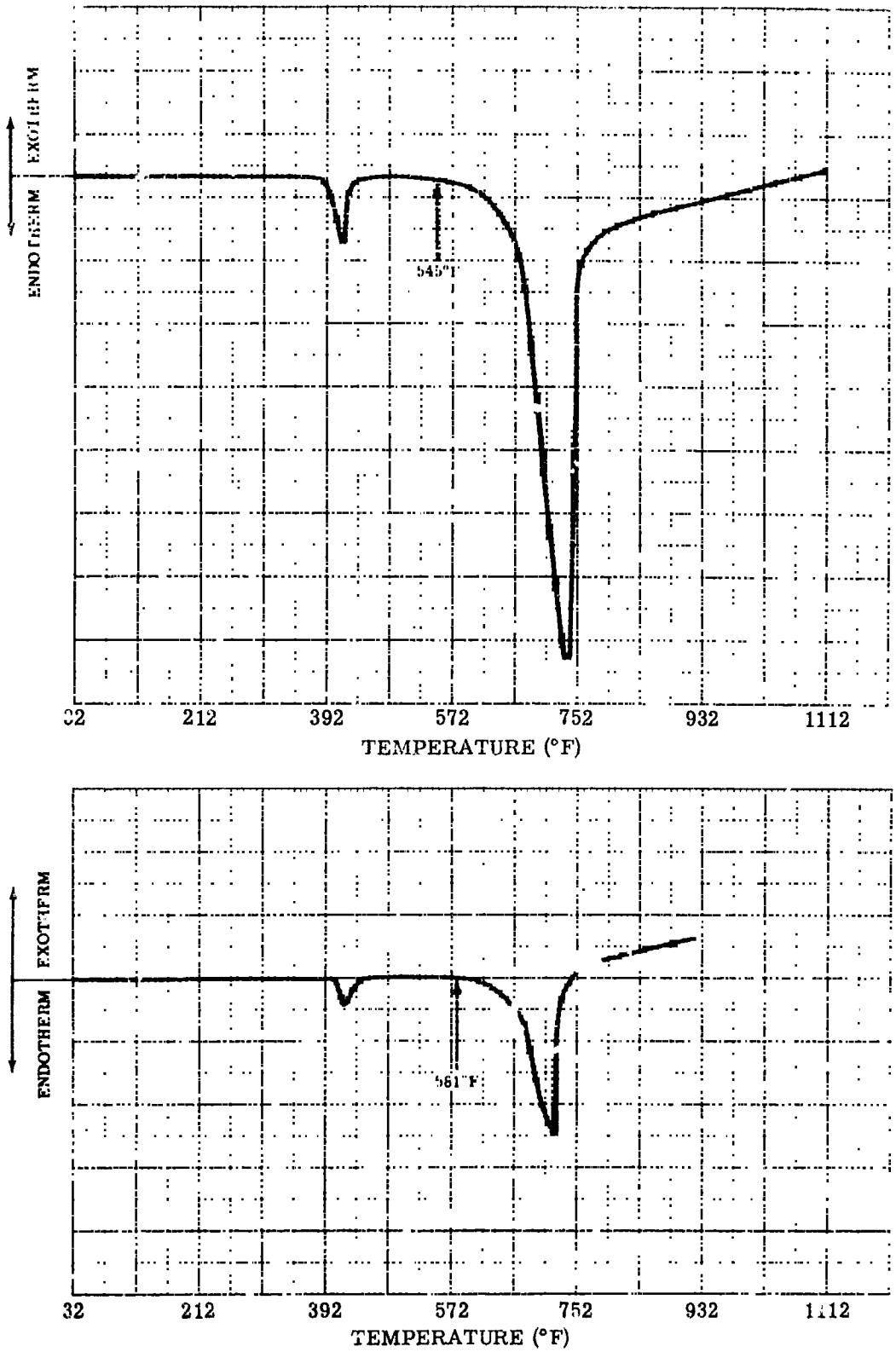


Figure 2-21. Differential Thermal Analysis of "THERMO-LAG" T-500-6 for a Temperature Increase Rate of 9°F per Minute

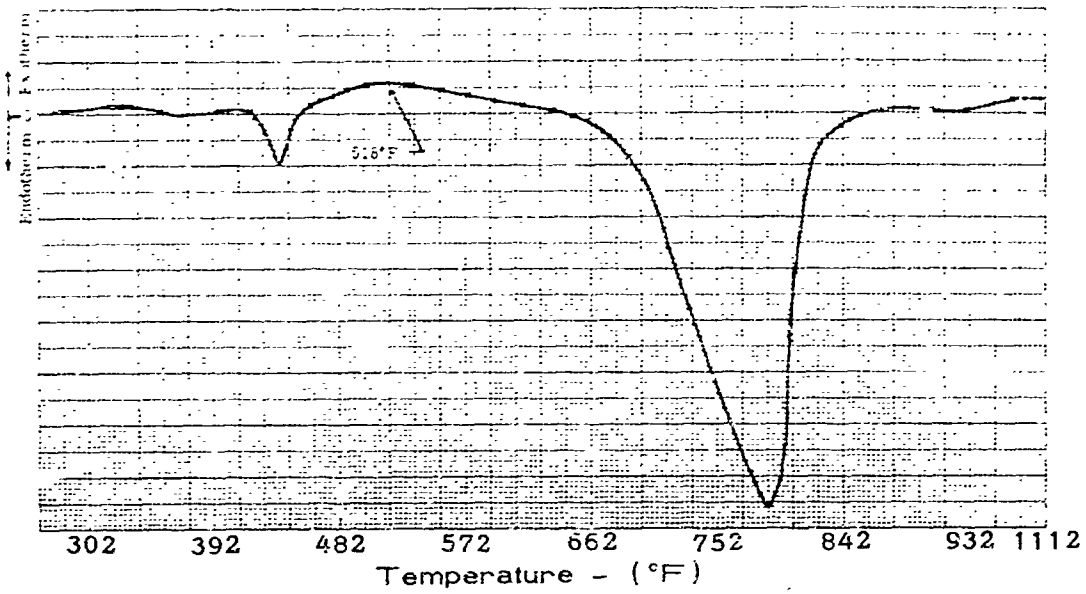


Figure 2-22. Differential Thermal Analysis of "THERMO-LAG" T-500-6 for a Temperature Increase Rate of 18°F per Minute

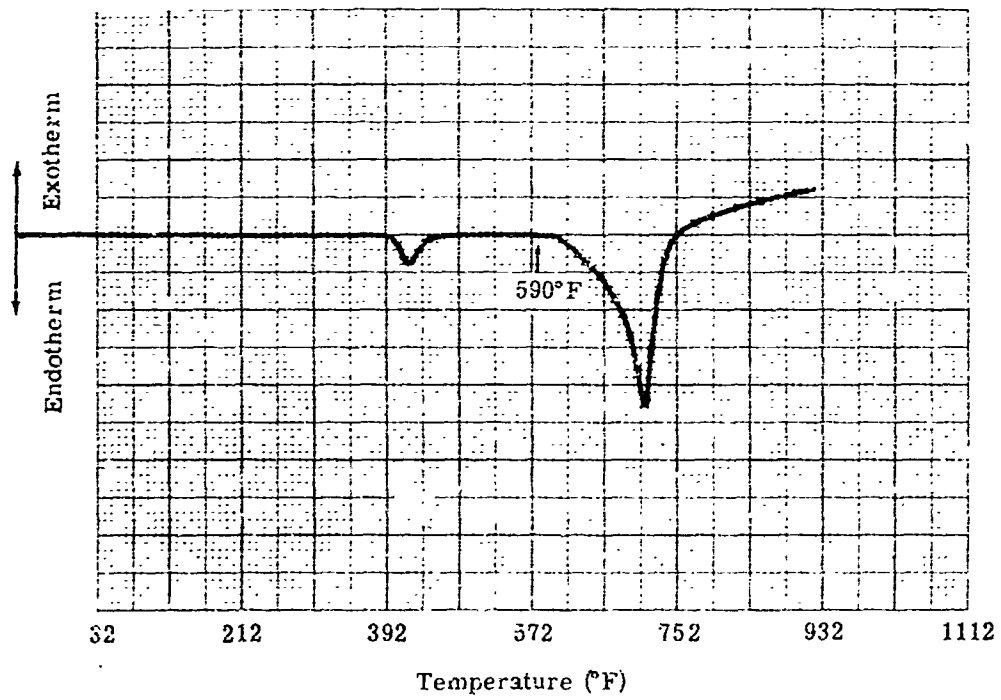
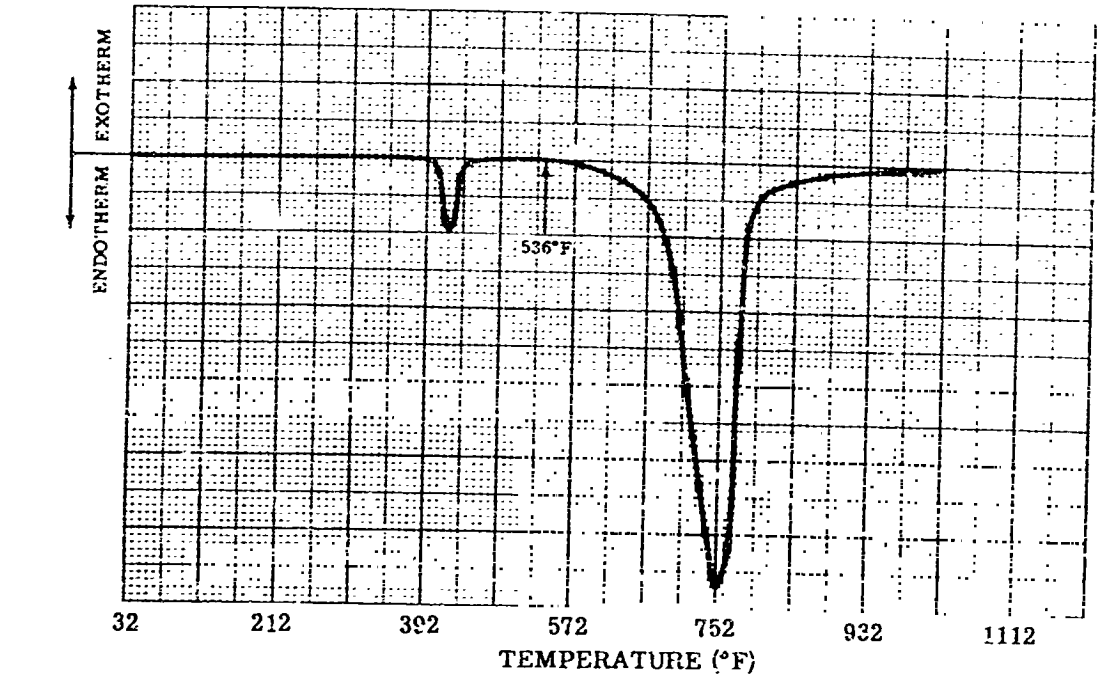


Figure 2-23. Differential Thermal Analysis of "THERMO-LAG" T-500-4 for a Temperature Increase Rate of 3.6°F per Minute



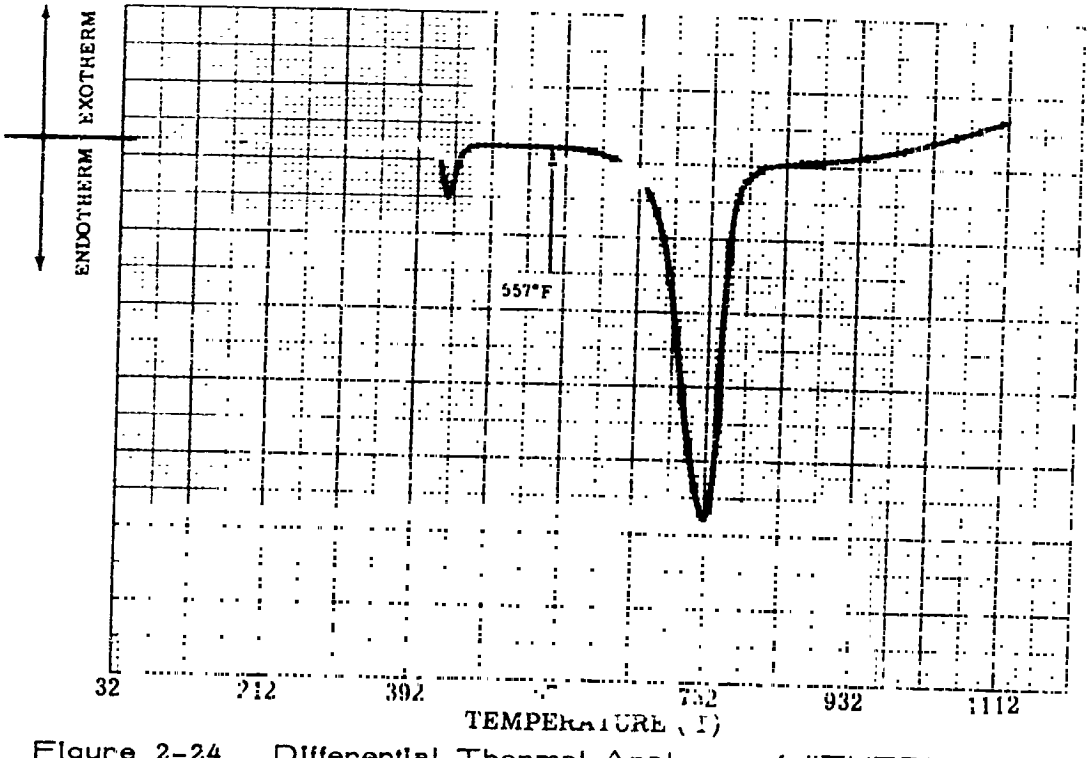


Figure 2-24. Differential Thermal Analyses of "THERMO-LAG" T-500-4 for a Temperature Increase Rate of 9°F per Minute

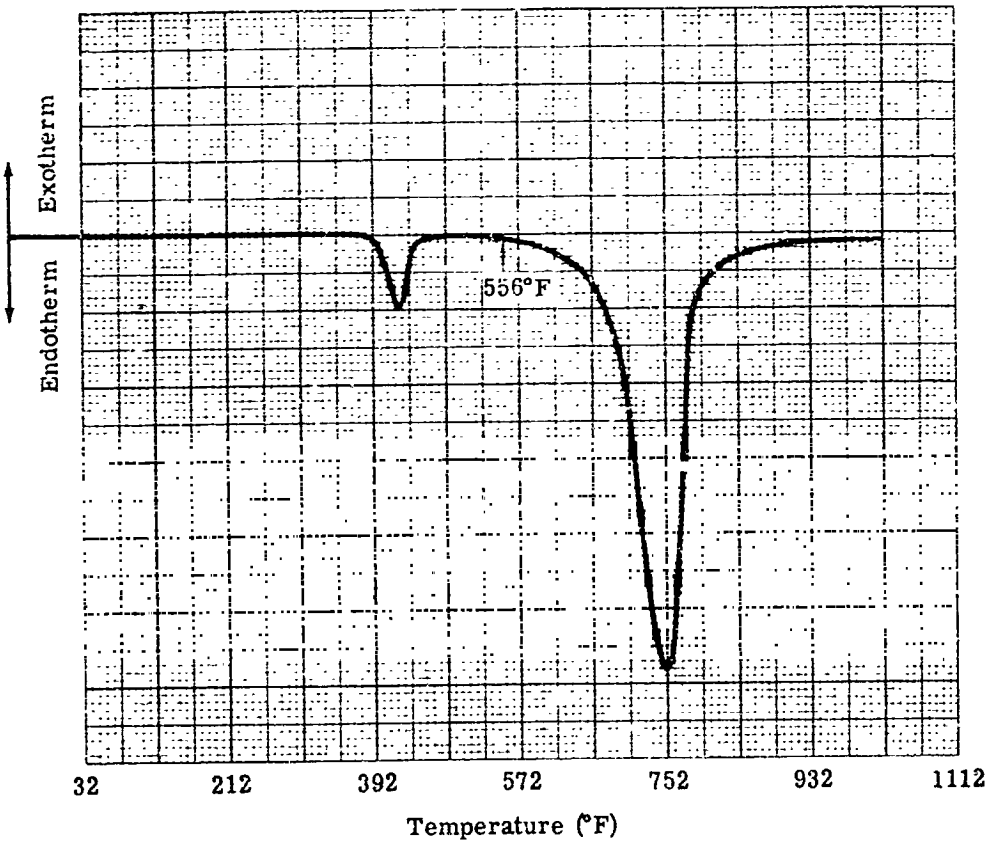


Figure 2-25. Differential Thermal Analysis of "THERMO-LAG" T-500-4 for a Temperature Increase Rate of 9°F per Minute

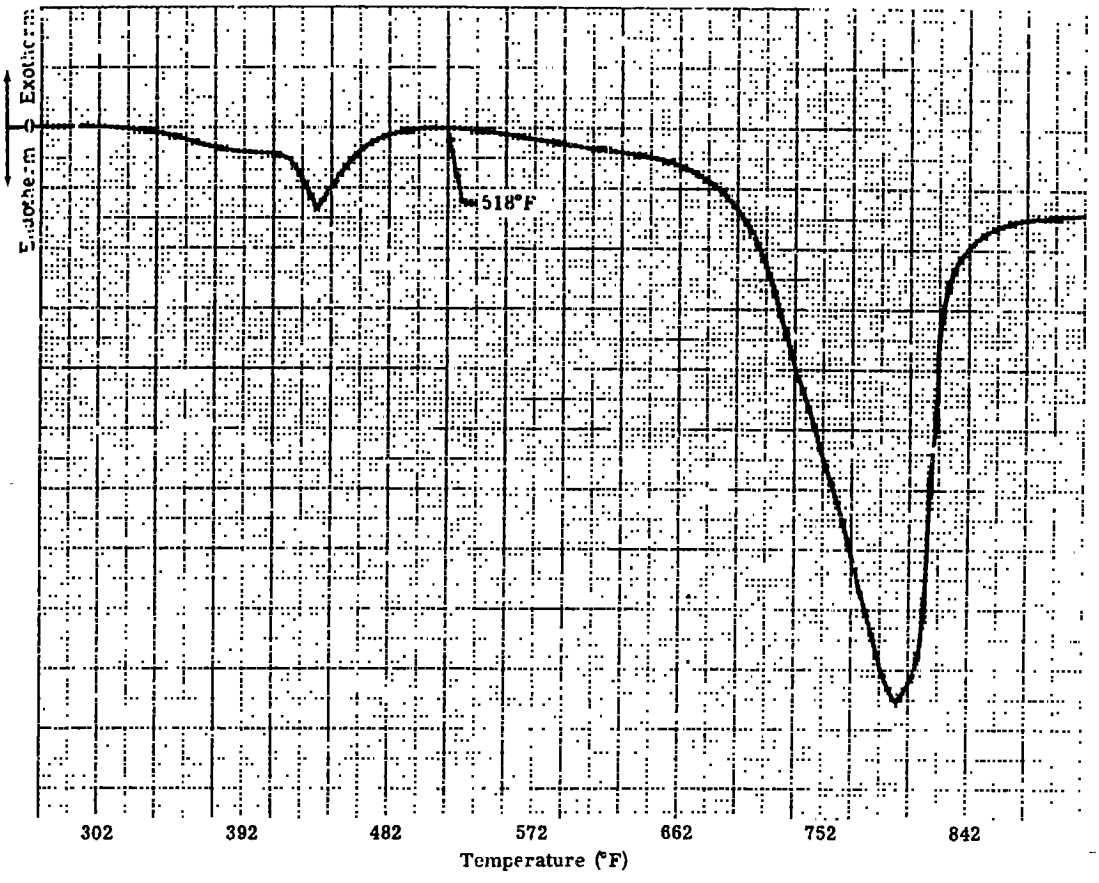


Figure 2-26. Differential Thermal Analysis of "THERMO-LAG" T-500-4 for a Temperature Increase Rate of 18°F per Minute

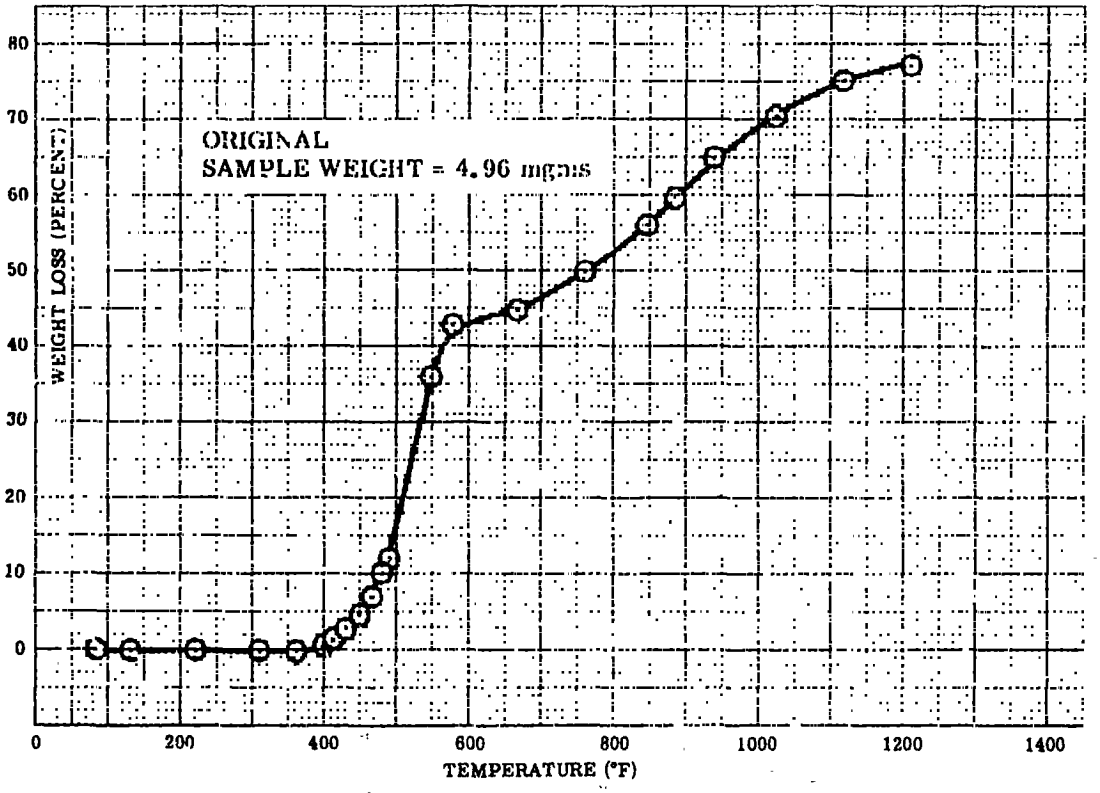


Figure 2-27. Thermogravimetric Analysis of "THERMO-LAG" T-500-4 for a Temperature Increase Rate of 3.6°F per Minute

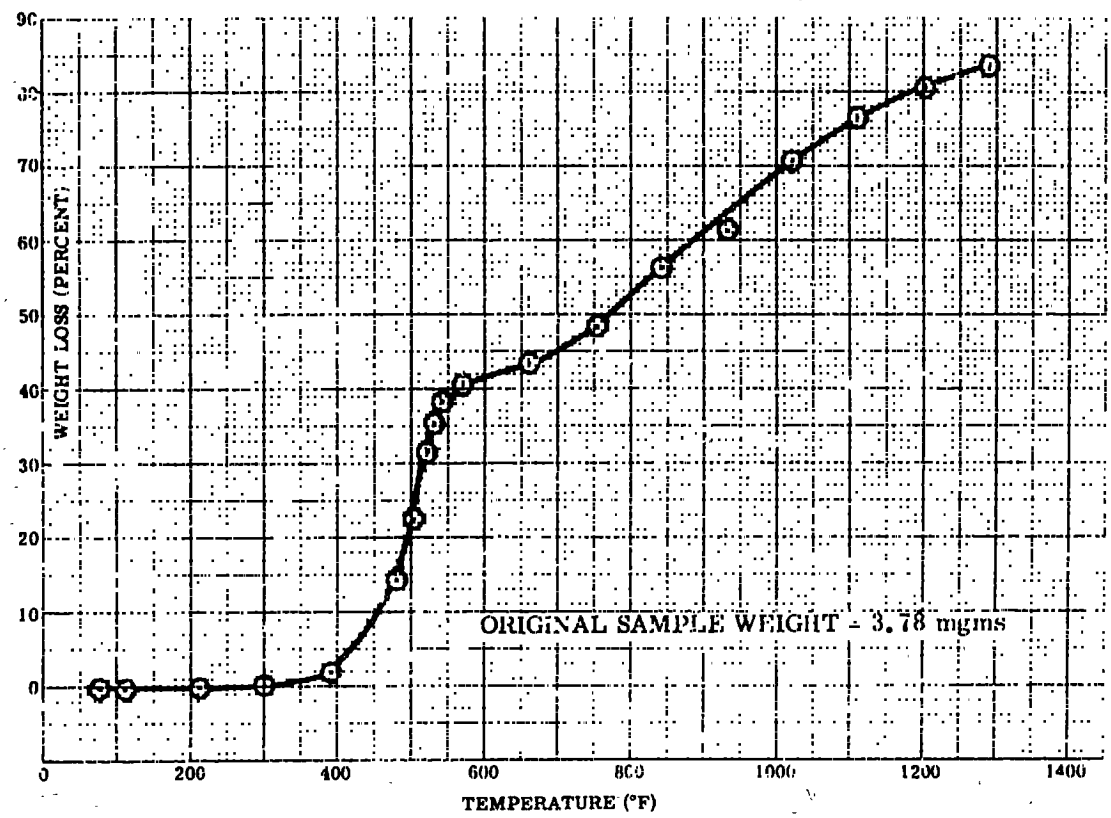


Figure 2-28. Thermogravimetric Analysis of "THERMO-LAG" T-500-4 for a Temperature Increase Rate of 3.6°F per Minute

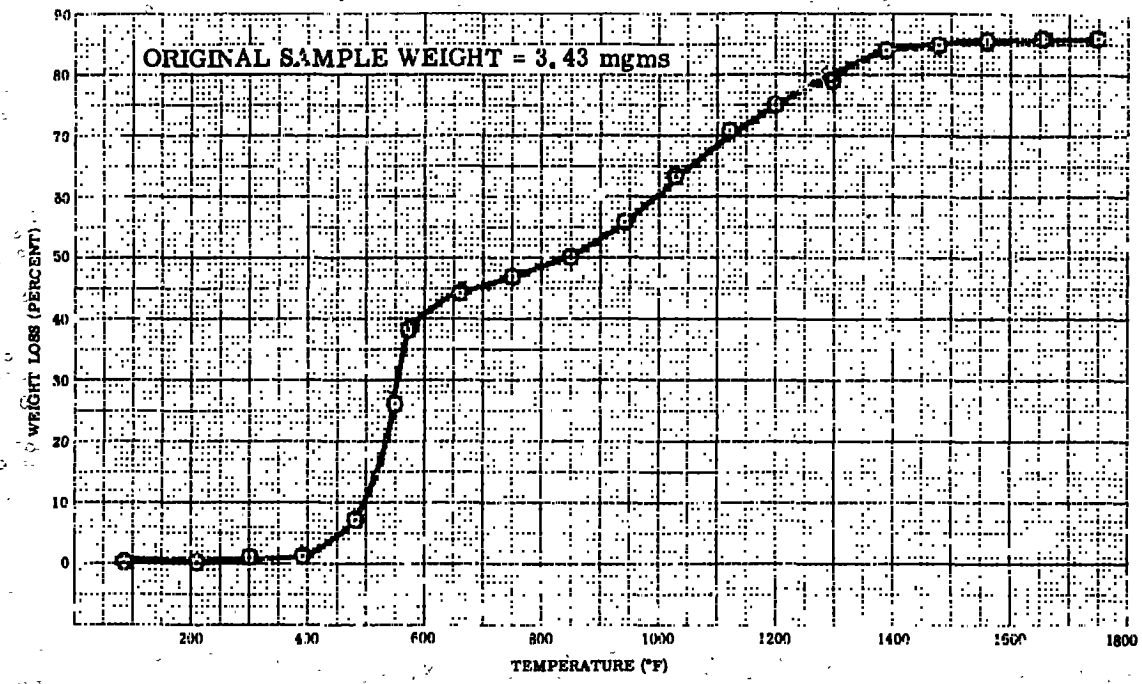


Figure 2-29. Thermogravimetric Analyses of "THERMO-LAG" T-500-4 for a Temperature Increase Rate of 9°F per Minute

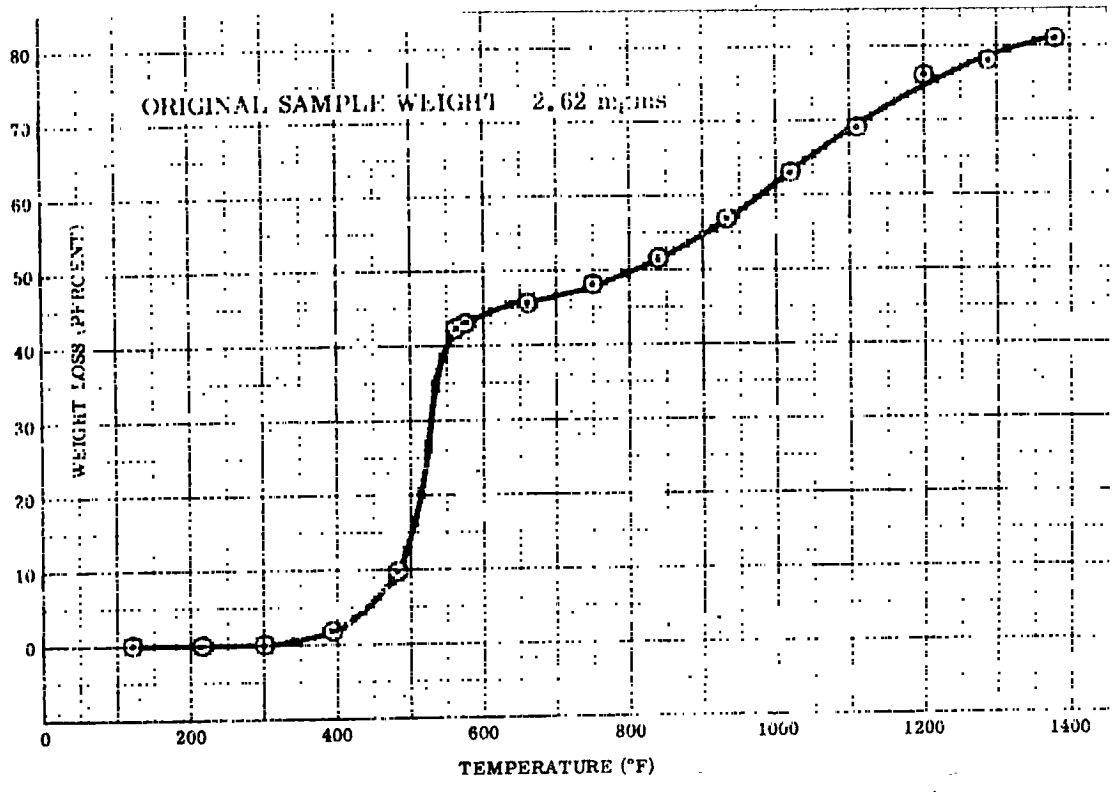
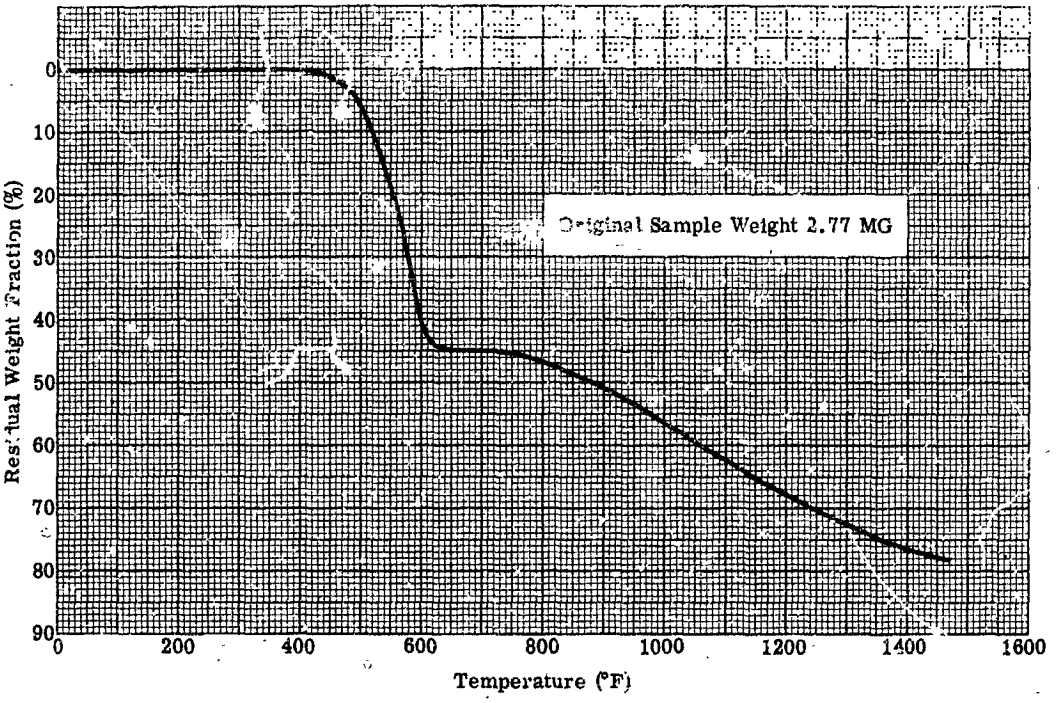


Figure 2-30. Thermogravimetric Analysis of "THERMO-LAG" T-500-4 for a Temperature Increase Rate of 9°F per Minute



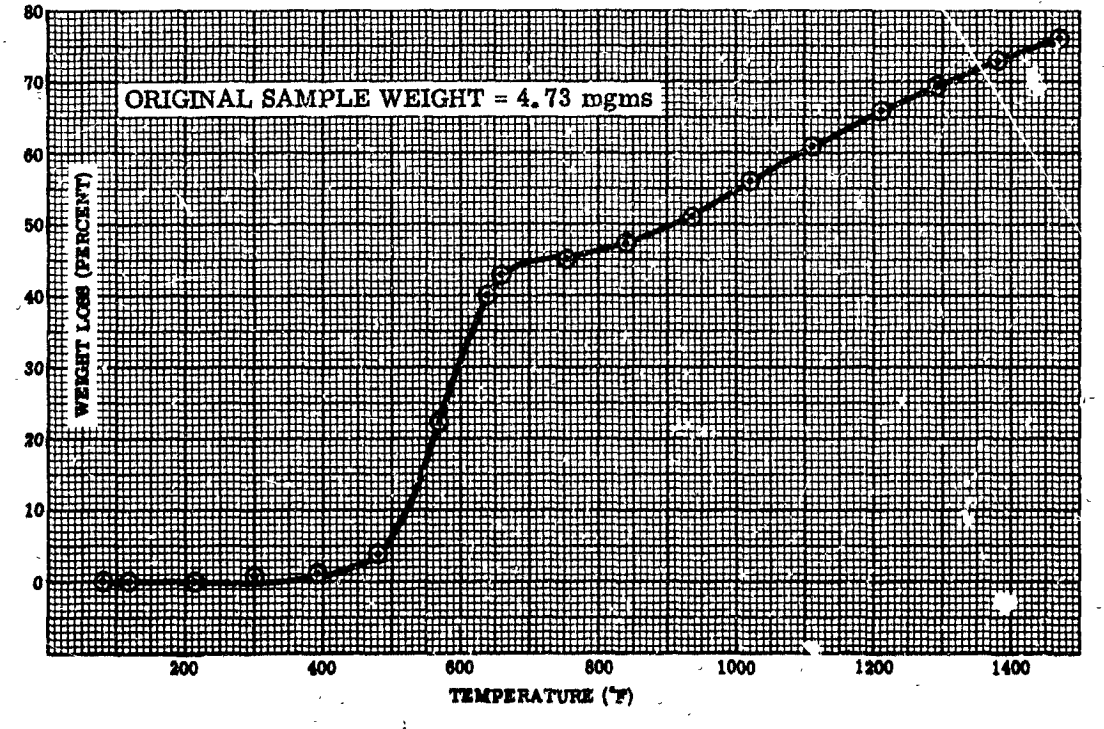


Figure 2-31. Thermogravimetric Analyses of "THERMO-LAG" T-500-4 for a Temperature Increase Rate of 18°F per Minute

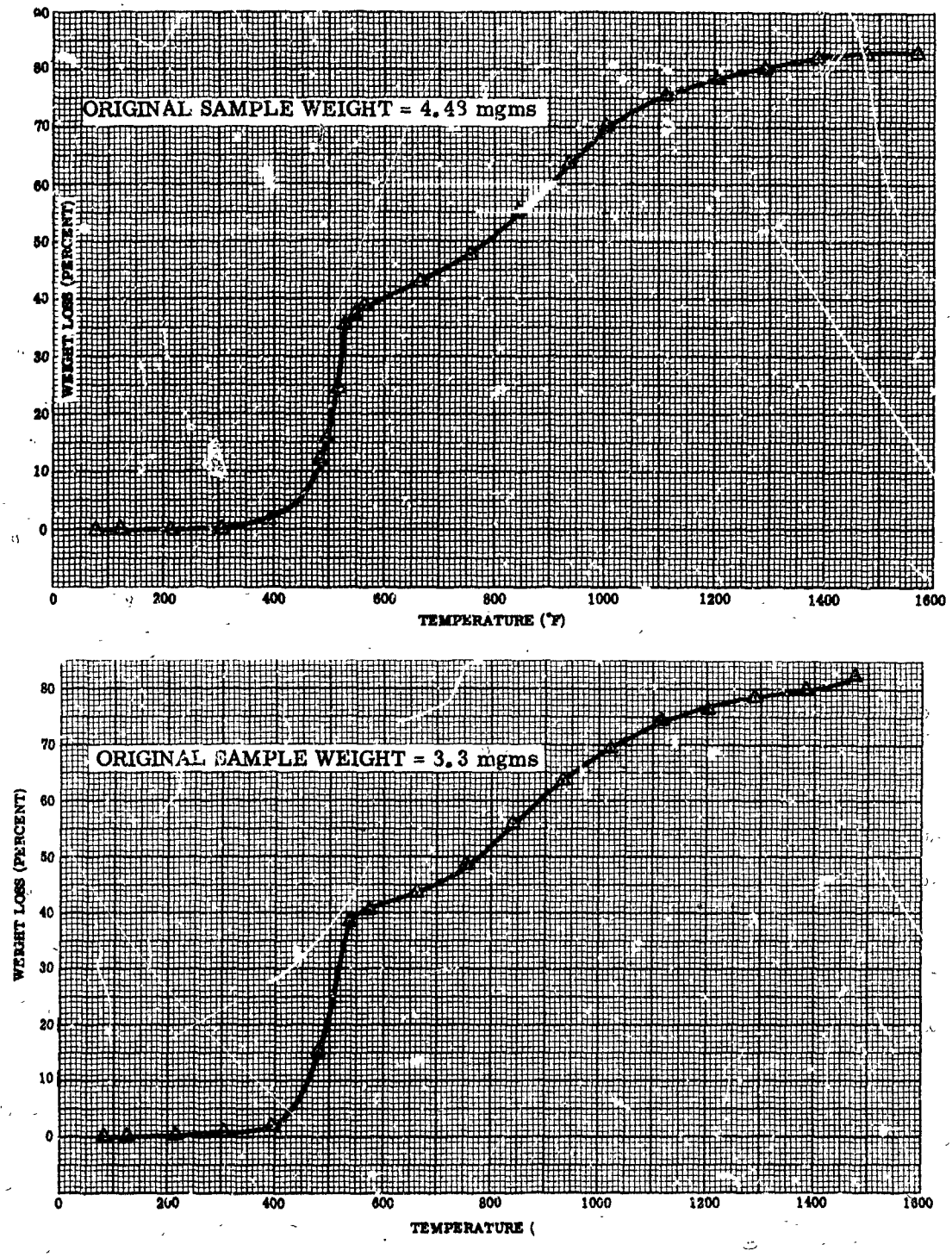
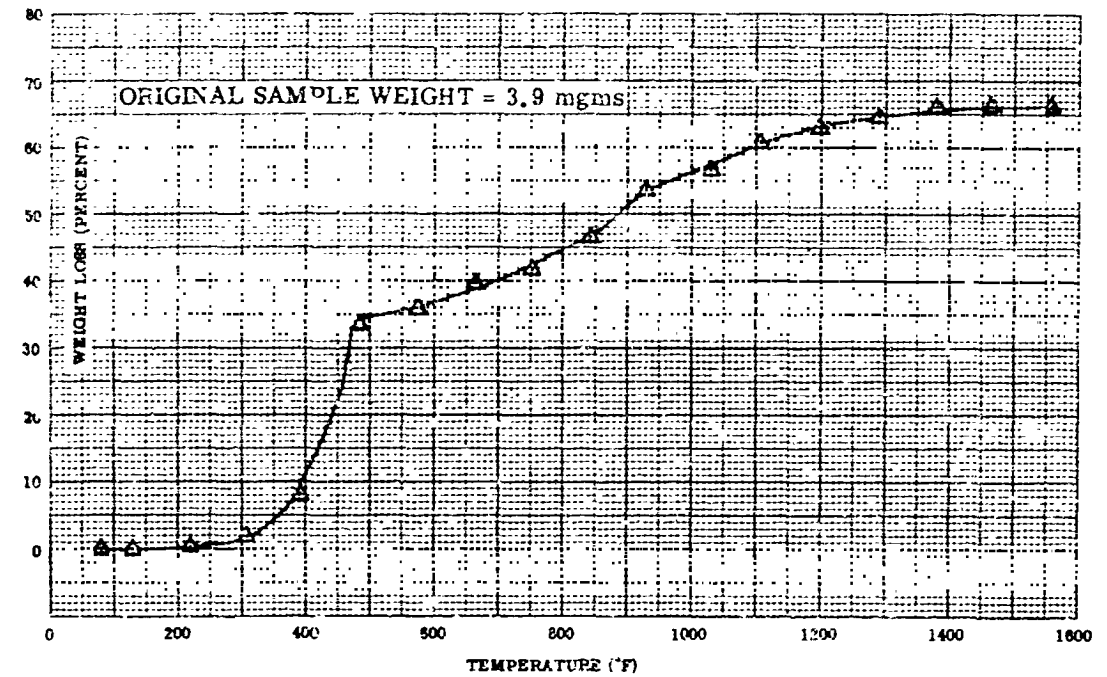


Figure 2-32, Thermogravimetric Analyses of "THERMO-LAG" T-500-6 for a Temperature Increase Rate of 3.6°F per Minute



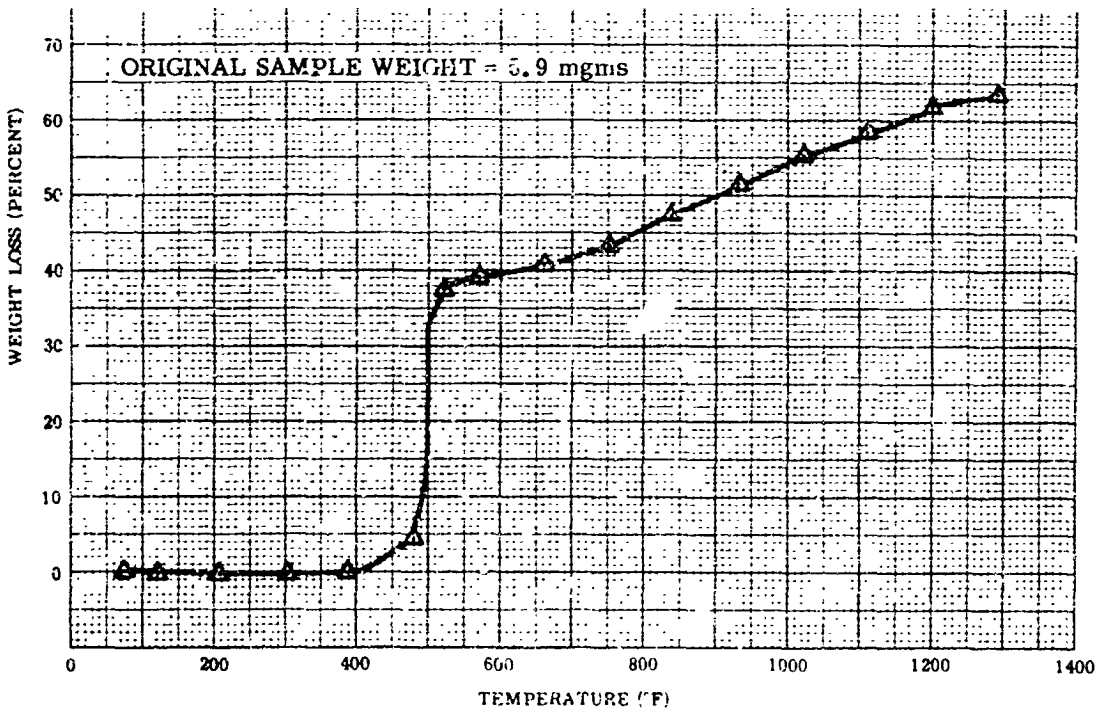
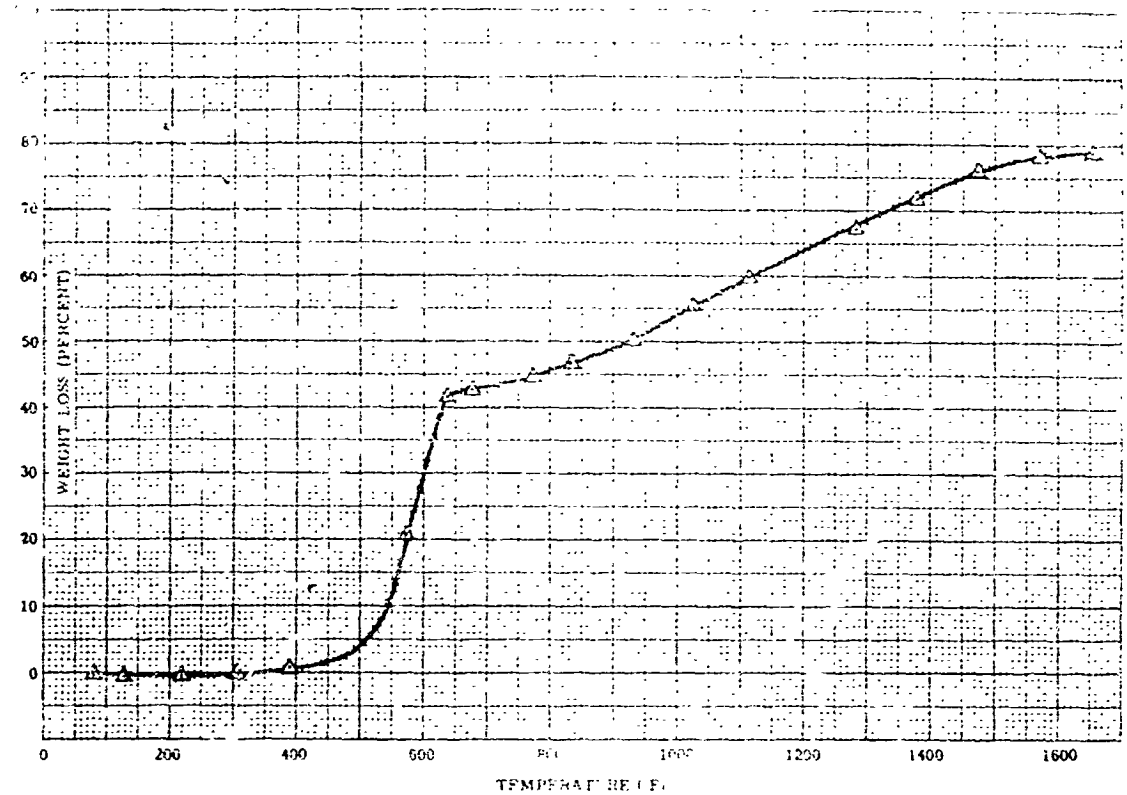


Figure 2-33. Thermogravimetric Analyses of "THERMO-LAG" T-500-6 for a Temperature Increase Rate of 9°F per Minute



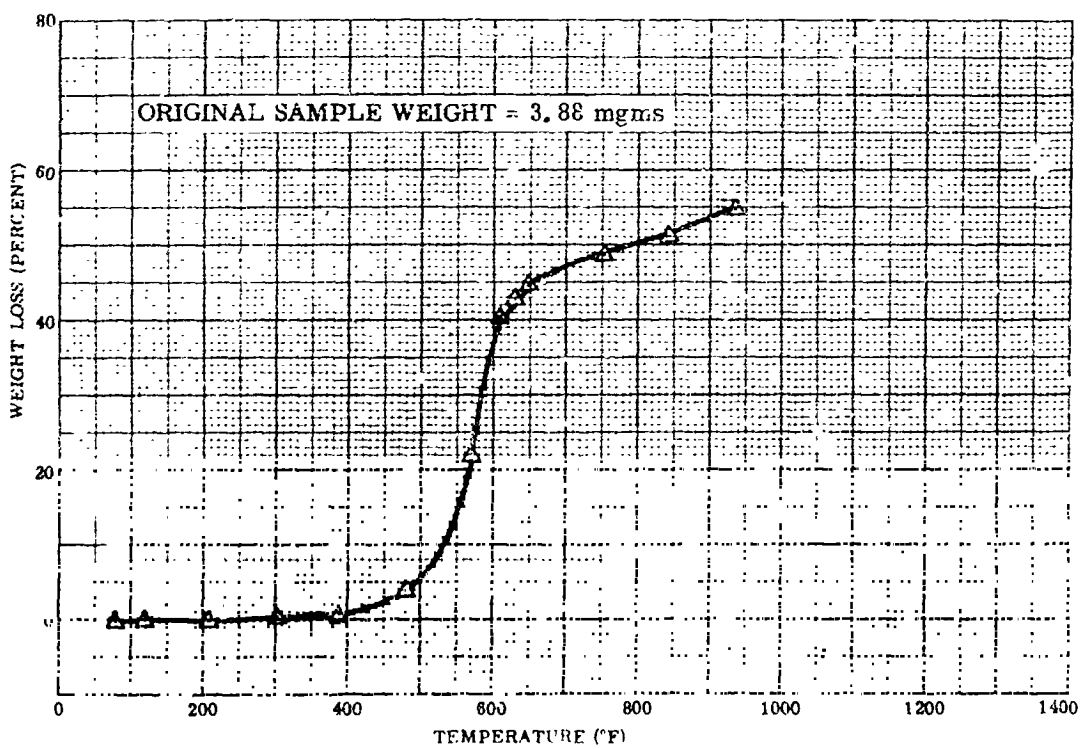


Figure 2-34. Thermogravimetric Analyses of "THERMO-LAG" T-500-6 for a Temperature Increase Rate of 18°F per Minute

TEST METHOD. The gas analyses were performed with the column temperature at 40°C, an applied detector current of 200 milliamps, and with helium pressurized at 25 psig. The gases used for calibration were those indicated by an analytical study as possible ablation products.

Gas samples for calibration were prepared by successively injecting 2-ml samples of a calibrated gas into a 270-ml sample pyrex bulb of helium gas. The mixture was analyzed after each addition of gas so that the location and amplitude of each peak could be identified with the particular gas component. The sample system was initially under a vacuum of 10^{-2} mm Hg.

RESULTS. Data for the chromatograms obtained for the ablation gases are recorded in Table 2-6. Five major peaks were recorded with the silicone column. The first two listed peaks are definitely mixtures of various gases. The fourth and fifth peaks did not correspond with any of the gas components used in calibration. The nine minor peaks indicated traces of hydrocarbons. The molecular sieve column gave definite evaluation of gases, recording six definite peaks which corresponded to calibrated gases. Calibration of the silicone column for the gases hydrogen fluoride (HF) and boron trifluoride (BF_3) were unsuccessful.

The indicated compositions of the gas products of "THERMO-LAG" T-500-4 are recorded in Table 2-7. The recorded data represents approximately 87 percent of the total sample.

"THERMO-LAG" T-500-4	
Gas	Mole %
H_2	45
H_2O	not detected
O_2	0.1
N_2	0.8
Methane	17.6
CO	6.6
CO_2	8.2
Ethylene	
Ethane	1.4
H_2S	5.8

Table 2-6. Gas Analysis Of Noncondensable Ablation Products By Gas Chromatograph

Silicone Column			Molecular Sieve		
Retention Time (MIN)	Peak Height (IN)	Gases	Retention Time (MIN)	Peak Height (IN)	Cases
0.56	271.5	(Methane, Air, NH_3 CO_2, H_2)	0.50	7.36	H_2
			0.87	1.28	O_2
0.66	4.82	(Ethane, Ethylene, CO_2)	1.43	3.67	N_2
1.05	26.8	(H_2S)	2.29	63.1	Methane
2.03	5.92		3.65	18.75	CO
2.33	7.94		22.43	0.80	Ethane
1.53	0.58				
2.72	0.71				
4.65	0.35				
6.1	0.50	traces of			
6.5	0.65	Hydrocarbons			
7.43	0.80	(Ethane)			
8.33	0.63				
9.07	0.66				
11.58	0.10				

Table 2-7. Chromatograph Analysis of Pyrolysis Products of "THERMO-LAG" T-500-4

SECTION III

THERMAL PERFORMANCE OF "THERMO-LAG" T-500

PART A - EXPERIMENTAL INVESTIGATIONS

An investigation was conducted to obtain and interpret experimental data relating to the thermal performance of "THERMO-LAG" materials in environment typical of Apollo class vehicles. The program objective was to secure information necessary to the design of a T-500 heat shield system for entry heat protection of advanced manned spacecraft. The experimental phase of the investigation was based upon environmental criteria derived from the entry trajectory shown in Figure 3-1, and was performed to determine the effects of specific environmental condition variations upon the ablation performance of "THERMO-LAG" material. Experimental air-arc test series were conductec as follows:

Series 1 - Transient Performance
Series 2 - Effects of Stream Oxygen Concentration
Series 3 - Effects of Model Configuration
Series 4 - Effects of Stream Pressure
Series 5 - Effects of Stream Energy
Series 6 - Effects of Gaps and Discontinuities
Series 7 - Effects of Vacuum Exposure
Series 8 - Trajectory Simulation
Series 9 - Effects of Upstream Mass Injection

The ablation performance of T-500 material during exposure to a radiative infrared heat flux was also investigated.

AIR ARC JET TEST MODELS

The three model configurations listed below with both 5/8-inch and 1.0-inch nose radii, were used:

1. Hemisphere-cone
2. Hemisphere-cylinder
3. Flat-faced cylinder

A photograph of the three basic models tested is shown in Figure 3-2. The models consisted of a hollow 0.02 inch thick steel aft body two inches long, spray-coated with "THERMO-LAG" T-500 and a two-inch long solid molded nose section. Figures 3-3 through 3-5 show details of test model construction and instrumentation. The aft body was sprayed to a thickness in excess of 0.100-inch, cured, and then machined to a thickness of 0.100 ± 0.005 inch. Instrumentation of the aft body consisted of three 28-gage chromel-

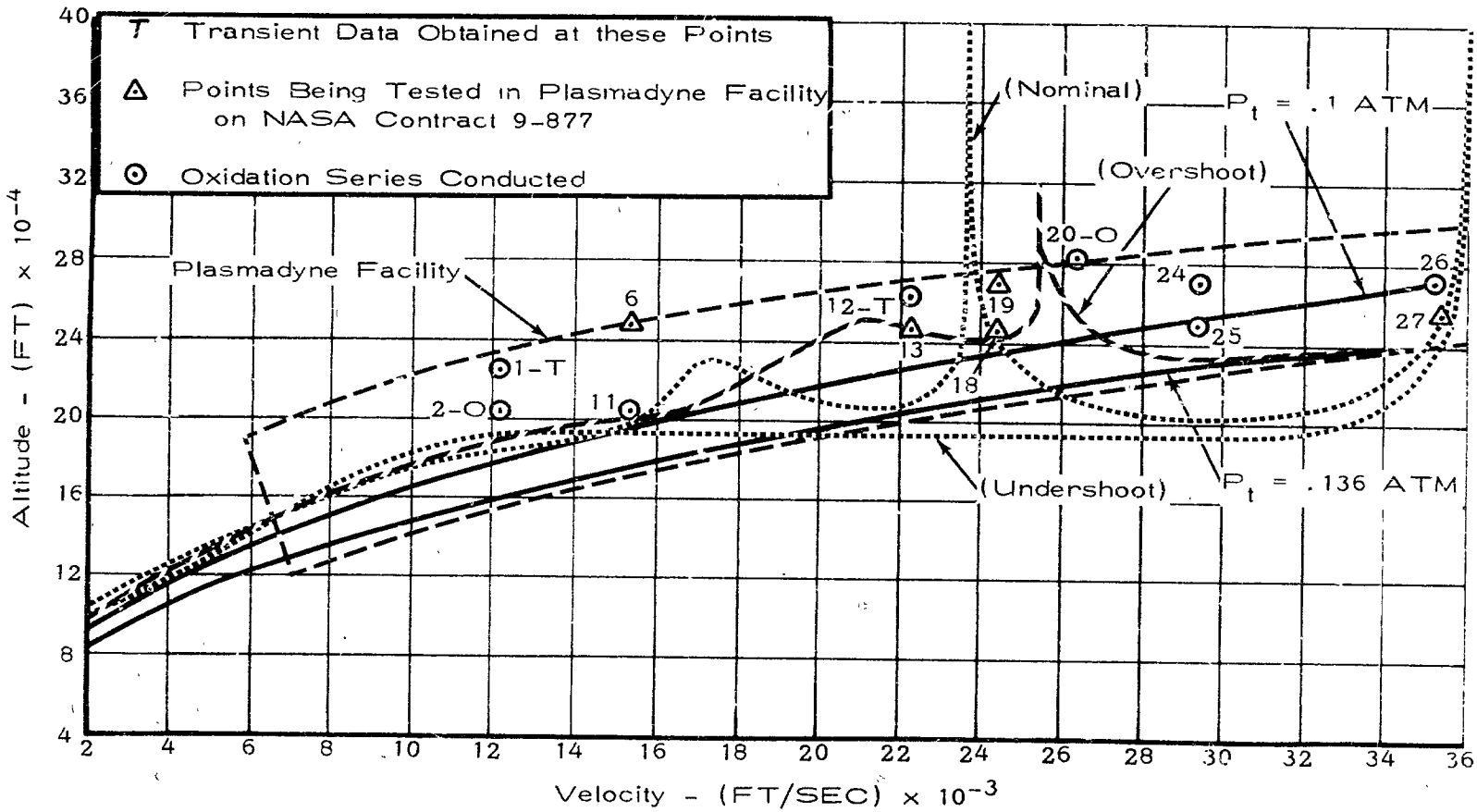


Figure 3-1. Flight Simulation Regime for Typical Manned Super Orbital Reentry Trajectories.

alumel thermocouples located 120 degrees apart and spot welded to the steel sleeve, 1-inch from the aft end of the sleeve. The nose section stagnation region was provided with a thermocouple affixed to a 5/16-inch diameter, 0.030-inch thick copper disk which was positioned 1.250 inches aft of the stagnation point.

CALORIMETERS. The air-arc jet was calibrated for stagnation point conditions with the steady state, 5/8-inch nose diameter water-cooled calorimeter shown in Figure 3-6.

A measurement was made to verify tunnel performance prior to each test run. The stagnation point heat transfer rate was corrected for model geometry and wall temperature by the familiar relationship:

$$\frac{q_s \text{ model}}{q_s \text{ calor.}} = \left[\frac{\text{Model Radius}}{\text{Calor. Radius}}\right]^{-1/2} \left[\frac{h_t - h_w \text{ model}}{h_t - h_w \text{ calor.}}\right] \times \text{Shape Factor}$$

where the shape factor for flat face models is 0.55 and is 1.00 for hemispherical models.

Heat flux at aft body areas was determined by short duration, hot wall calorimeters having configurations as shown in Figures 3-7 and 3-8. Both copper and graphite calorimeters were constructed using copper and graphite sensors, respectively. Sensors were fitted with thermocouples with junctions located at a point L/ 3 from the back of the sensor. Data obtained from stagnation region sensors were compared with time-temperature data from side wall sensors to establish a relationship which, with stagnation region data obtained from co'd wall steady state calorimeter results, was used to determine the magnitude of side wall heating rates.

Calibration results are presented in Figure 3-9 where the ratio of local heat flux to stagnation heat flux is shown versus stagnation heat flux.

SUMMARY OF AIR-ARC TESTS

Table 3-1 is a tabular summary of all data pertinent to air-arc testing performed under this contract.

RELIABILITY OF DATA

To achieve a wide variation of test conditions, isolated tests were run at particular conditions which were not a part of a transient series. These data were used for comparison purposes where an energy balance was not involved. The complication which prevented the assurance of an accurate energy balance

Model No.	Nose Geometry (IN.)	Plasmadyne Test Point	Percent Oxygen	Run Duration (SEC)	Stagnation Enthalpy (BTU/LB) h_T	Stagnation Cold Wall Heat Flux (BTU/FT^2-SEC) q_c	Stagnation Pressure (ATM) P_T	Average Surface Temperature (°F) (ε = .9) T_w	Enthalpy Difference (BTU/LB) ΔH
M-6	1 cone	20	21	30	14890	110	.00267	3650	13840
M-9	1 cone	12	21	150	9865	110	.0064	3840	8705
M-10	1 cone	12	21	300	9900	110	.0064	3840	8740
M-18	5/8 cone	13	21	420	10100	215	.016	290	8750
M-16	1 cone	24	21	420	17576	170	.005	70	16365
M-19	5/8 cone	18	21	300	11980	300	.023	0	10530
M-21	5/8 con	28	21	45	17658	300	.01	41	16358
M-22	5/8 cone	28	21	90	17680	300	.01	429	16330
M-23	5/8 cone	28	21	150	17500	300	.01	1230	16150
O-1	5/8 hc	15	15	150	9897	297	.0291	1870	8737
O-2	5/8 hc	16	7	150	10055	295	.0289	376C	9005
O-3	5/8 hc	17	0	150	10165	301	.0291	2840	9415
O-6	1 hc	21	15	300	14988	103	.00267	3640	13968
O-7	1 hc	22	7	300	15185	105	.00265	3570	14185
O-8	1 hc	23	0	300	15052	107	.00266	3510	14087
O-9	1 hc	8	15	300	4965	109	.026	3370	4055
O-11	1 hc	9	7	300	5000	107	.0258	3240	4130
O-13	1 hc	10	0	300	5110	109	.026	3080	4285
O-14	1 hc	3	15	420	2488	48.7	.0255	2470	1858
O-15	1 hc	4	7	420	2510	46.8	.0258	2380	1780
O-16	1 hc	5	0	420	2505	47.9	.0256	2240	1935
D-1-2	1 hc	13	21	300	9526	168	.016	3770	8461
D-2-2	1 hc	13	21	420	9810	168	.016	3730	8770
E-1-2	1 hc	13	21	420	10433	168	.016	3730	9393
E-2-2	1 hc	13	21	300	9870	168	.016	3730	8830
GG-1	1 hc	13	21	165	9486	168	.016	3700	8451
GG-3	1 hc	13	21	420	9489	168	.016	3750	8439
HH-1	1 hc	13	21	420	9899	168	.016	3770	8834
HH-2	1 hc	13	21	175	9211	168	.016	3750	8161
D-1	1 hc	12	21	75	9855	109	.0064	3930	8835
D-2	1 hc	12	21	80	9826	109	.0064	3890	8811
D-9	1 hc	12	21	370	9926	109.6	.0064	3930	8906
D-10	1 hc	12	21	330	9871	109	.0064	3930	8851
D-11	1 hc	12	21	840	10109	110	.0064	3930	9089
D-12	1 hc	12	21	300	9875	109	.0064	3960	8853
E-15	1 hc	12	21	75	9801	109	.0064	3930	8781
E-16	1 hc	12	21	75	10024	109.6	.0064	3910	9006
E-17	1 hc	12	21	50	10125	11	.0064	3910	9107
E-18	1 hc	12	21	50	10035	109.6	.0064	3960	9013
GG-1A	1 hc	12	21	140	10001	109.6	.0064	4000	8976
GG-2	1 hc	12	21	75	10179	109.6	.0064	3960	9157
GG-4	1 hc	12	21	150	10101	109.6	.0064	3960	9079

Table 3-1. Summary of Air-Arc Test Data (Sheet 1 of 4)

Model No.	Stagnation Hot Wall Heat Flux q_h (BTU/FT^2-SEC)	Recession to Surface (IN.)	Debris Layer Thickness (IN.)	Total Recession (IN.)	Cold Wall Gross Heat Blockage H_{eff_c} (BTU/LB)	Hot Wall Gross Heat Blockage H_{eff_h} (BTU/LB)	Sidewall Average Thickness (IN.)	Time for Sidewall Substrate To Reach 500°F (SEC)
M-6	103.2	.039	.047	.086	5750	5395	.036 & .100	25.20
M-9	93.5	.141	.110	.251	9860	8840	.0325 & .0975	35.85 & 106.5
M-10	97.5	.346	.125	.471	10480	9290	.035 & .096	28.5 & 79.95
M-18	189	1.112	.094	1.206	11220	9870	.050 & .0995	60.0 & 96.0
M-16	159.5	.461	.149	.610	17580	16480	.0415 & .100	48 & 53.8
M-19	267	.902	.094	.996	13560	12050	.0505 & .1005	49.2 & 78
M-21	280	.078	.070	.148	13680	12767	.051 & .0945	36.6
M-22	279.5	.169	.102	.271	14920	13900	.052 & .100	58.8 & 97.5
M-23	279	.259	.110	.369	18280	17000	.050 & .100	45 & 84
O-1	268	.280	.080	.360	18525	16720	.110	
O-2	267.8	.117	.170	.287	23100	20950	.109	
O-3	282	.022	.200	.222	30500	28580	.110	
O-6	102.25	.268	.170	.438	11090	10500	.1055	300
O-7	98.8	.156	.250	.406	11610	10925	.106	
O-8	101.5	.063	.270	.333	14475	13170	.1035	
O-9	91.6	.068	.300	.368	13310	11190	.109	
O-11	90.8	.042	.300	.342	14080	11925	.1025	
O-13	93.8	.026	.310	.336	14590	12560	.10 5	
O-14	38.5	.035	.190	.225	13620	10780	.1065	
O-15	35.15	.023	.190	.215	13690	10290	.1075	
O-16	39.15	.009	.170	.179	16805	13780	.105	
D-1-2	151.8	.370	.118	.488	15490	13990		
D-2-2	152.25	.490	.118	.608	17390	15780		
E-1-2	153.5	.458	.138	.596	17725	16200		
E-2-2	152.5	.433	.116	.549	13780	12500		
GG-1	152	.211	.093	.294	8890	8045	.10167	48.0
GG-3	151.75	.511	.112	.623	16990	15320		132.0
HH-1	152	.527	.142	.669	15800	14300		
HH-2	151.2	.186	.135	.321	13720	12375		
D-1	99	.113	.063	.176	6960	6325		
D-2	99.4	.124	.068	.192	6805	6205		
D-9	99.9	.436	.142	.578	9100	8300		
D-10	99.2	.531	.118	.649	8790	8000		
D-11	99.45	1.331						
D-12	99.25	.505	.091	.596	8210	7475		
E-15	98.95	.128	.077	.205	5975	5425		
E-16	101.7	.128	.079	.207	5950	5510		
E-17	100.3	.061	.073	.134	6150	5610		
E-18	99.8	.116	.078	.194	4235	3855	.10167	96.0
GG-1A	99.6	.206	.093	.299	7690	6955	.029	19.338
GG-2	99.85	.095	.079	.174	7075	6445	.10567	94.2
GG-4	99	.238	.087	.325	7580	6850	.0320	21.0

Note: hc = Hemispherical cylinder nose body
FF = Flat face nose body

Table 3-1. Summary of Air-Arc Test Data (Sheet 2 of 4)

Model No.	Nose Geometry (IN.)	Plasmadyne Test Point	Percent Oxygen	Run Duration (SEC)	Stagnation Enthalpy (BTU/LB) h_T	Stagnation Cold Wall Heat Flux (BTU/FT^2-SEC) q_c	Stagnation Pressure (ATM) P_T	Average Surface Temperature (°F) (ξ = .9) T_w	Enthalpy Difference (BTU/LB) Δh
GG-5	1 hc	12	21	90	9872	109	.0064	3980	8850
GG-7	1 hc	12	21	780	9865	109	.0064	3960	8843
GG-8	1 hc	12	21	35	9987	109	.0064	3960	8965
GG-9	1 hc	12	21	40	9900	109	.0064	3930	8880
GG-11	1 hc	12	21	390	10291	109.6	.0064	3930	9271
D-2-4	1 hc	12	21	345	10334	109.6	.0064	3980	9310.5
D-2-5	1 hc	12	21	420	10230	109.6	.0064	3940	9209
N-2	1 hc	27	21	90	23100	456	.0270	4720	21520
N-6	1 hc	27	21	30	22900	457	.0270	4640	21380
N-9	1 hc	7	21	2280	4950	104	.0260	3120	4105
N-11	1 hc	27	21	45	23250	457	.0270	4590	21780
N-15	1 hc	1	21	420	3560	48.5	.0150	3030	2750
N-21	1 hc	20	21	300	15150	105	.0027	3700	14080
N-22	1 hc	27	21	15	23500	455	.0270	4090	22320
N-26	1 hc	27	21	150	23330	453	.0270	4690	21780
N-29	1 hc	25	21	150	17650	317	.0200	4770	16030
N-30	1 hc	11	21	765	5050	163	.0590	3570	4080
N-35	1 hc	6	21	00	4950	48.5	.0076	3030	4140
N-36	1 hc	6	21	420	5125	48	.0076	3170	4265
N-45	1 hc	13	21	465	9850	163	.0160	4090	8650
N-48	1 hc	13	21	45	10120	162	.0160	4090	8920
N-53	1 hc	6	21	30	5065	48	.0076	2980	4275
N-54	1 hc	7	21	300	5100	105	.0260	3060	4280
N-64	1 hc	2	21	420	2550	47.4	.0210	2900	1.85
N-65	1 hc	27	21	270	23000	457	.0270	4660	21460
N-71	1 FLat	25	21	300	17480	174	.0200	4490	16070
N-73	1 FLat	27	21	100	23050	251	.0270	4330	21730
N-75	1 hc	26	21	150	22850	253	.0088	4540	21290
N-82	1 hc	6	21	900	4890	48	.0076	3230	4020
N-92	5 8 hc	14	21	210	9950	280	.0290	4330	8630
N-94	5 8 hc	19	21	300	11785	154	.0058	3960	10595
N-105	5 8 hc	14	21	150	10085	279	.0290	4440	8725
N-106	5 8 hc	18	21	150	11850	280	.023	4420	10470
N-110	5 8 hc	28	21	300	17480	280	.016	4180	16240
N-112	5 8 FF	18	21	300	12120	154	.023	4310	10790

Table 3-1. Summary of Air-Arc Test Data (Sheet 3 of 4)

Model No.	Stagnation Hot Wall q_h Heat Flux (BTU/FT^2-SEC)	Recession to Surface (IN.)	Debris Layer Thickness (IN.)	Total Recession (IN.)	Cold Wall Gross Heat Blockage H_{eff_c} (BTU/LB)	Hot Wall Gross Heat Blockage H_{eff_h} (BTU/LB)	Sidewall Average Thickness (IN.)	Time for Sidewall Substrate To Reach 500°F (SEC)
GG-5	99.2	123	083	.206	7130	6495	.10333	102 0
GG-7	99.1	1 246					.029	22 4
GG-8	99 4	.048	049	.097	5695	5370	.03333	24.0
GG-9	99 05	048	.049	.097	6745	6125	.1025	103.5
GG-11	100 05	582	.096	678	9450	8640		
D-2-4	100.1	540	.108	648	8745	7995		
D-2-5	100 05	676						
N-2	428	.210	.061	271	21950	20575	101	78.0
N-6	430	.063	.055	.118	17410	16390	.10167	
N-9	88.6	.383	.553	.936	37950	32350	.10433	429
N-11	431	.096	.067	.163	18920	17880	.10133	
N-15	39	055	.289	.344	8875	7140	.102	366
N-21	98 4	.289	.164	453	10420	9760	.10267	118.5
N-22	435	.019	.049	.068	14000	13390	.10067	
N-26	425	.435	.061	.496	20500	19225	.101	87.0
N-29	290 25	.514	.068	.582	12250	11205	.10367	98.6
N-30	134.75	.478	.100	.578	11200	9260	.103	112.5
N-35	41 65	.013	.093	.106	6175	5305	.10533	
N-36	41 1	139	.205	.344	8945	7525	.10467	367.5
N-46	145.1	1.173	.144	1 317	8620	7680	.10333	100.1
N-48	141 9	.097	048	.145	7540	6740	.102	
N-53	41.6	001	052	.053	4075	3530	.10233	
N-54	90.45	047	.238	285	16580	14260	.10167	
N-64	35.1	042	.244	.286	10420	7720	.10167	420
N-65	429.5	.785	.090	.875	21100	19850	.10133	82.4
N-71	161	675	.094	.769	10290	7625	.10367	243
N-73	238	.055	.115	.170	22100	20975	.10533	100.2
N-75	237.25	342	.092	.434	13100	12280	.10267	85.8
N-82	40.6	326	.353	.679	9545	8085	.10233	307.5
N-92	246.25	.733	.058	.791	11125	9800	.10167	93.3
N-94	140	430	153	.583	11890	10795	.09467	93.0
N-105	244 5	.584	.062	.646	9705	8540	.101	106.5
N-106	250	.511	.072	.586	10720	9590	.100	96
N-110	262.25	587	095	.682	18450	17290	.101	76.5
N-112	138.8	755	.071	.829	8375	7540	.100	79.8

Table 3-1. Summary of Air-Arc Test Data (Sheet 4 of 4)



Figure 3-2. Photograph of Re-Entry Simulation Models Tested In The Air-Arc Plasmajet Tunnel

for an isolated test was the nonlinearity of recession rate and surface heating with time. Two factors involved were: debris layer growth until a maximum thickness was achieved, and model shape change due to nonuniform heating along the surface. To consider peculiarities found for certain tests, a method was necessary to compare all data to ascertain the validity of these tests. The performance consistency of the material was obtained by correlating the surface temperature with total virgin material recession at several constant exposure times. A definite relationship between surface temperature and recession was obtained and gave an average deviation from the mean value of 4.8 percent. Consistent material ablation performance was therfore achieved. The second factor was the magnitude accuracy of the actual plasma properties at the model stagnation region, which could vary from reported conditions due to off-design operation or model misalignment with the location of maximum plasma stream enthalpy. The latter effect was apparent at the 23,000 Btu/Lb enthalpy level. The chosen method of comparison concerned the computation of an effective gross heat of ablation or "efficiency" defined as:

$$H_{eff} \quad \frac{q_{cw} \times \text{total exposure time}}{\rho_{vm} \times \text{total recession}}$$

where q_{cw} is the calorimeter measured cold wall total heat flux and ρ_{vm} is the virgin material density.

The resulting values were compared at several constant stagnation pressures for a given constant exposure time (Figure 3-10). A certain degree of scatter was produced but consistent trends were established. Several test runs showed a poor correlation with other data in this figure, and were not considered in the evaluation of material performance. The particular models showing inferior performance with respective models of similar geometry were N-21, N-29, N-75, and M-6. This comparison process was not necessarily valid for the low enthalpy runs since the test models performed as though near radiation equilibrium as noted by the 38,000 Btu/Lb efficiency of Model N-9. An increase in effective gross efficiency with respect to test duration at a given pressure and enthalpy difference existed because of the nature of the definition of the efficiency term. The actual heat flux to the hemispherical nosed models at the higher enthalpies was less than the calorimeter measured value for the larger durations because of shape change. At the smaller durations the value of total heat flux to the model was as measured but the average mass loss rate was higher than the instantaneous rate. The overall result gives values of effective efficiency

lower at short exposure times and higher at large exposure times than the corresponding value of true efficiency at a particular enthalpy level. This result is valid only for the hemispherical nosed models. Thus, ablation histories rather than isolated test points were used as the basis for the analytical evaluation of ablation performance parameters.

SERIES 1-TRANSIENT PERFORMANCE

PURPOSE. The purpose of the transient test series was to establish the virgin material thickness, the debris layer thickness, the debris layer surface temperature, and the temperature response within the T-500 material as functions of time for selected environmental conditions.

TEST CONDITIONS. The nominal test conditions are shown in Table 3-2.

TEST MODELS. The test models used for this series of tests were two-inch diamter hemispherical cylinders.

Number of Tests Performed	Stagnation Pressure (Atm)	Stagnation Enthalpy (Btu/Lb)	Stagnation Heat Flux (Btu/Ft^2-Sec)	Type of Model	Test Duration (Sec)
6	0.0098	3,500	35	2"-D H-C	300 to 3600
4	0.0076	5,000	48	"	25,75,420,900
4	0.0064	9,440	110	"	90,150,320,380
22	0.0160	9,780	170	"	45 to 600
3	0.0100	17,500	300	"	45,90,150
6	0.0270	23,000	456	"	15,30,45,90 150,270

Table 3-2. Transient Test Matrix

For the transient series, duration of model exposure was the primary independent variable. Six air-arc test conditions were investigated. Prior to model exposure, the plasma jet was calibrated. The models were then exposed in sequence at that environmental condition. Test data were obtained for both the stagnation and the aft body regions.

DISCUSSION OF RESULTS. Histories of stagnation point ablation data are given in Figures 3-10 through 3-15 for each test condition. Sidewall ablation data were obtained for a heating range of 5 to 39 Btu/Ft^2-Sec. Typical sidewall ablation results are shown in Figure 3-17.

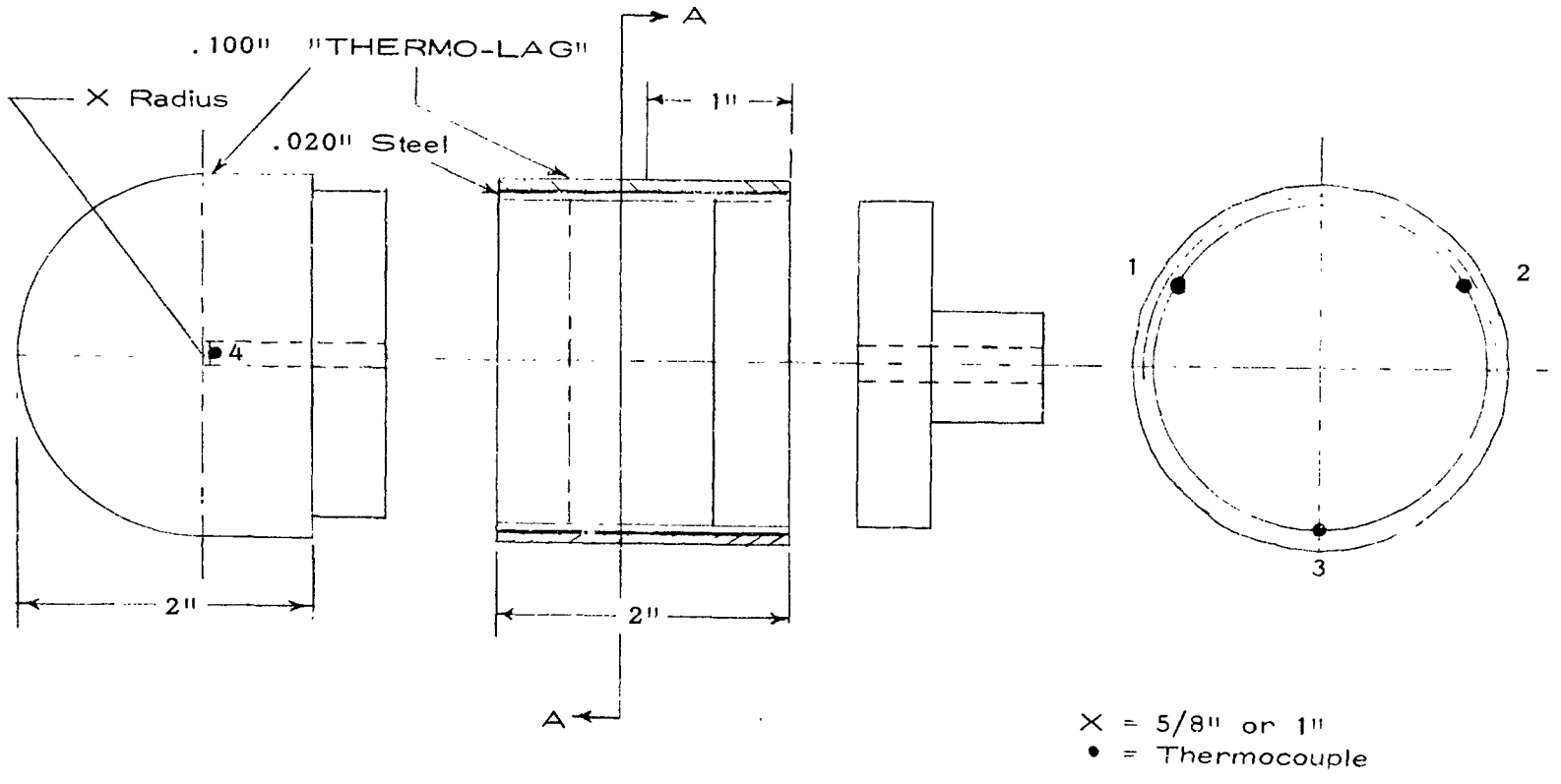


Figure 3-3. Hemisphere-Cylinder Test Model

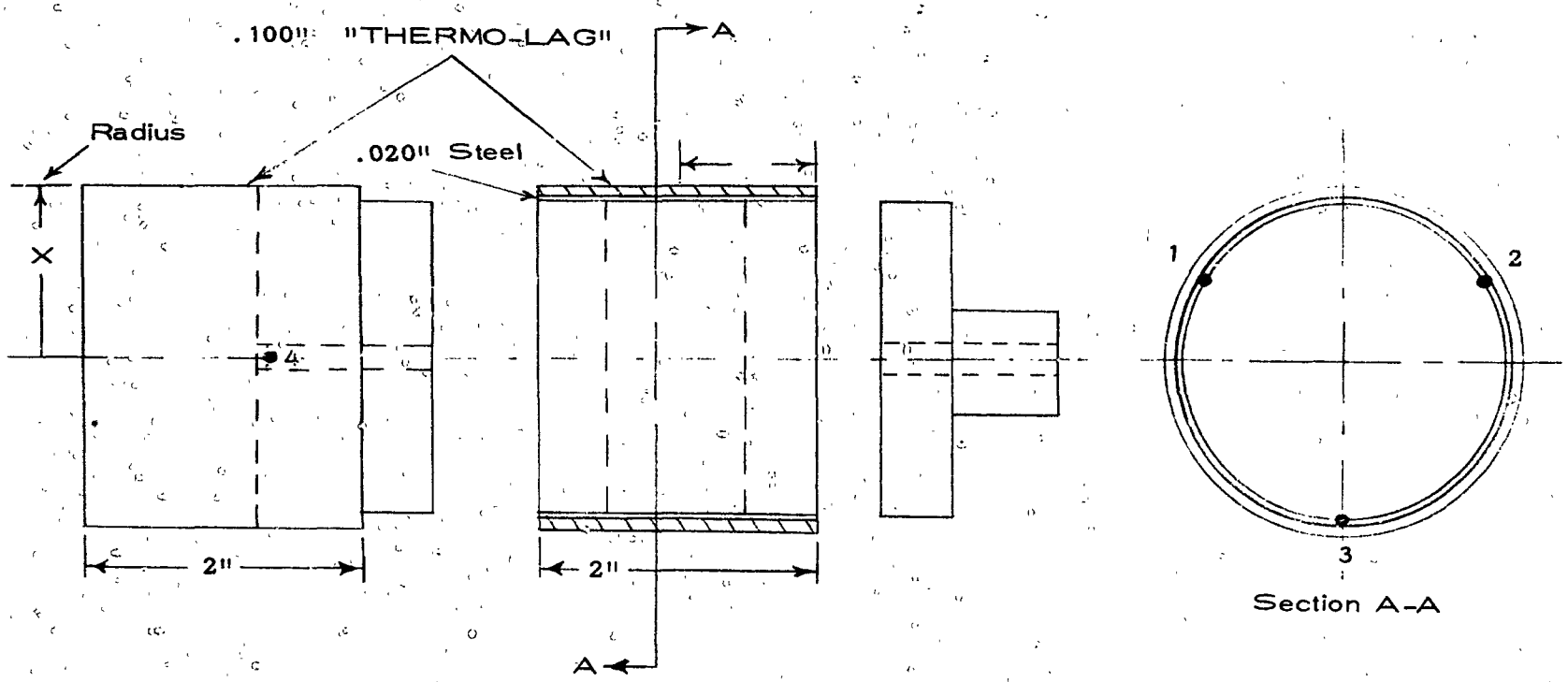


Figure 3-4. Flat Face-Cylinder Test Model

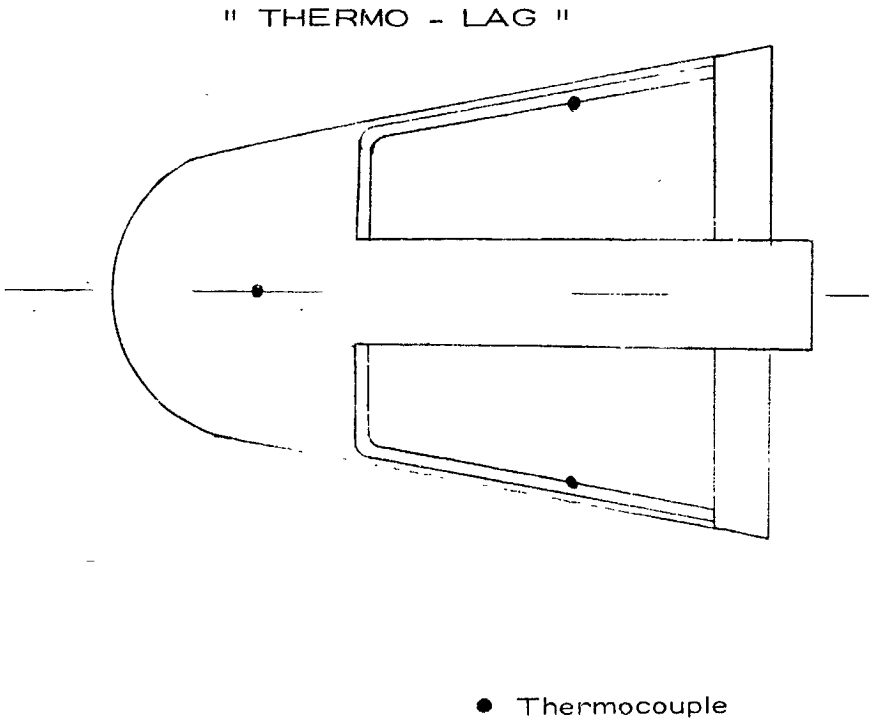
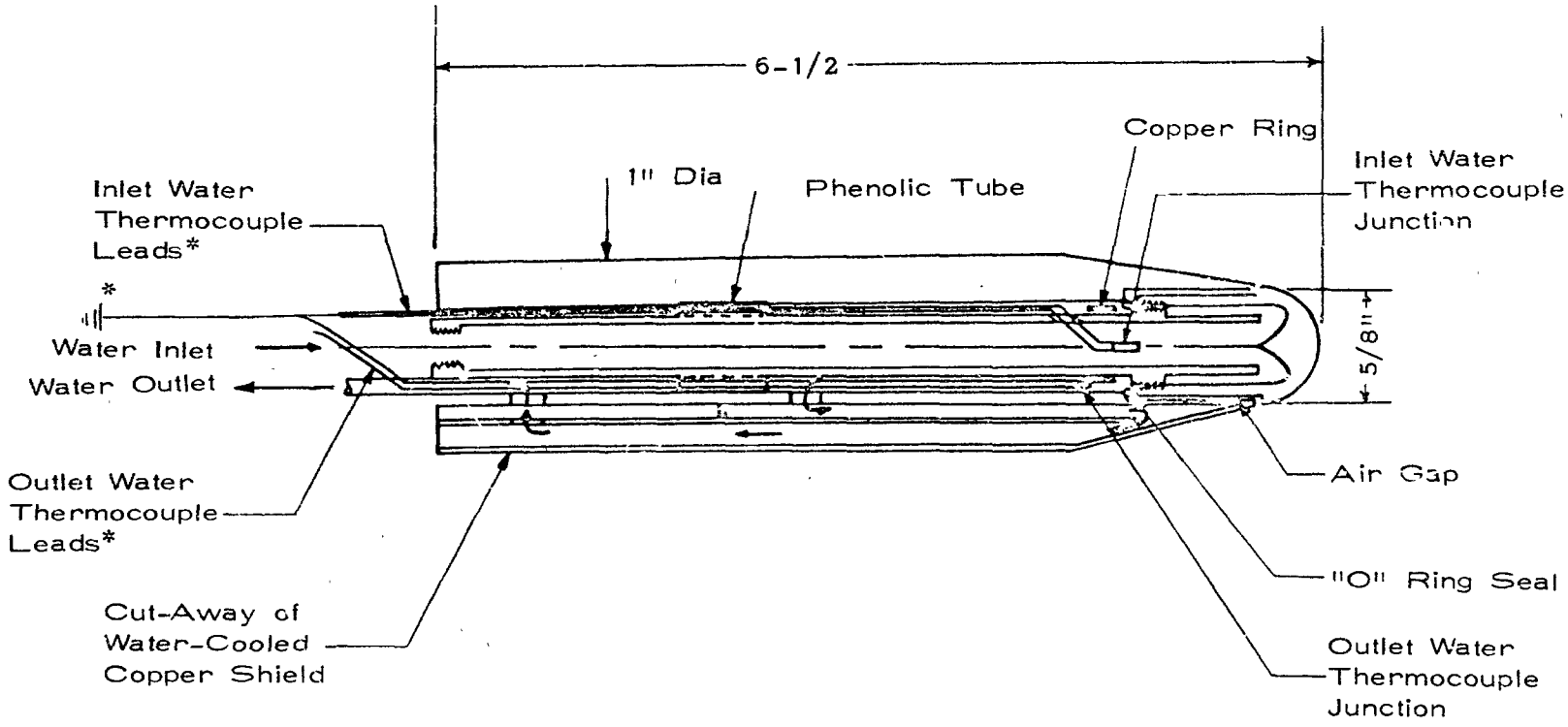


Figure 3-5 Sphere - Cone Test Model



Note: *Thermocouples are copper-constantan with the constantan leads shielded copper leads grounded

Figure 3-6. Design of a Water-Cooled Copper Hemisphere Calorimeter

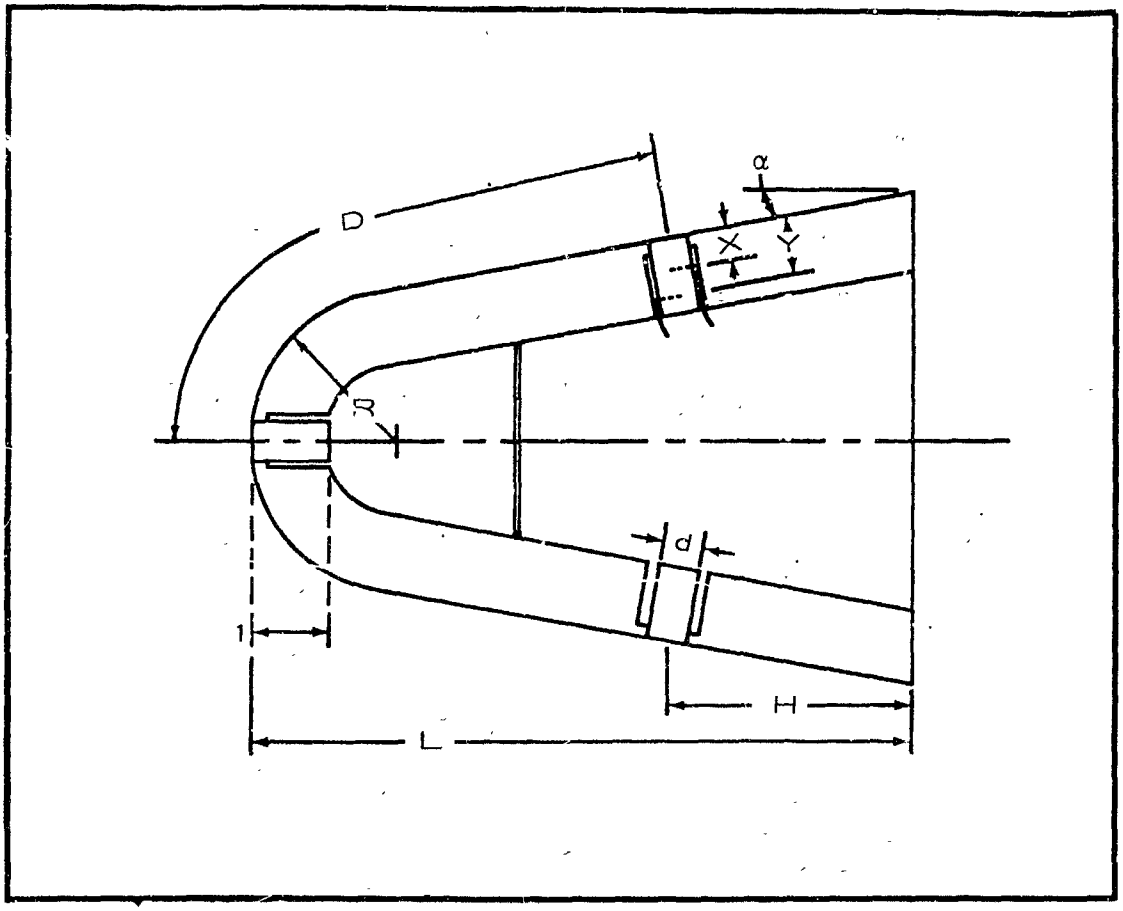


Figure 3-7. Sphere-Cone Calorimeter Design

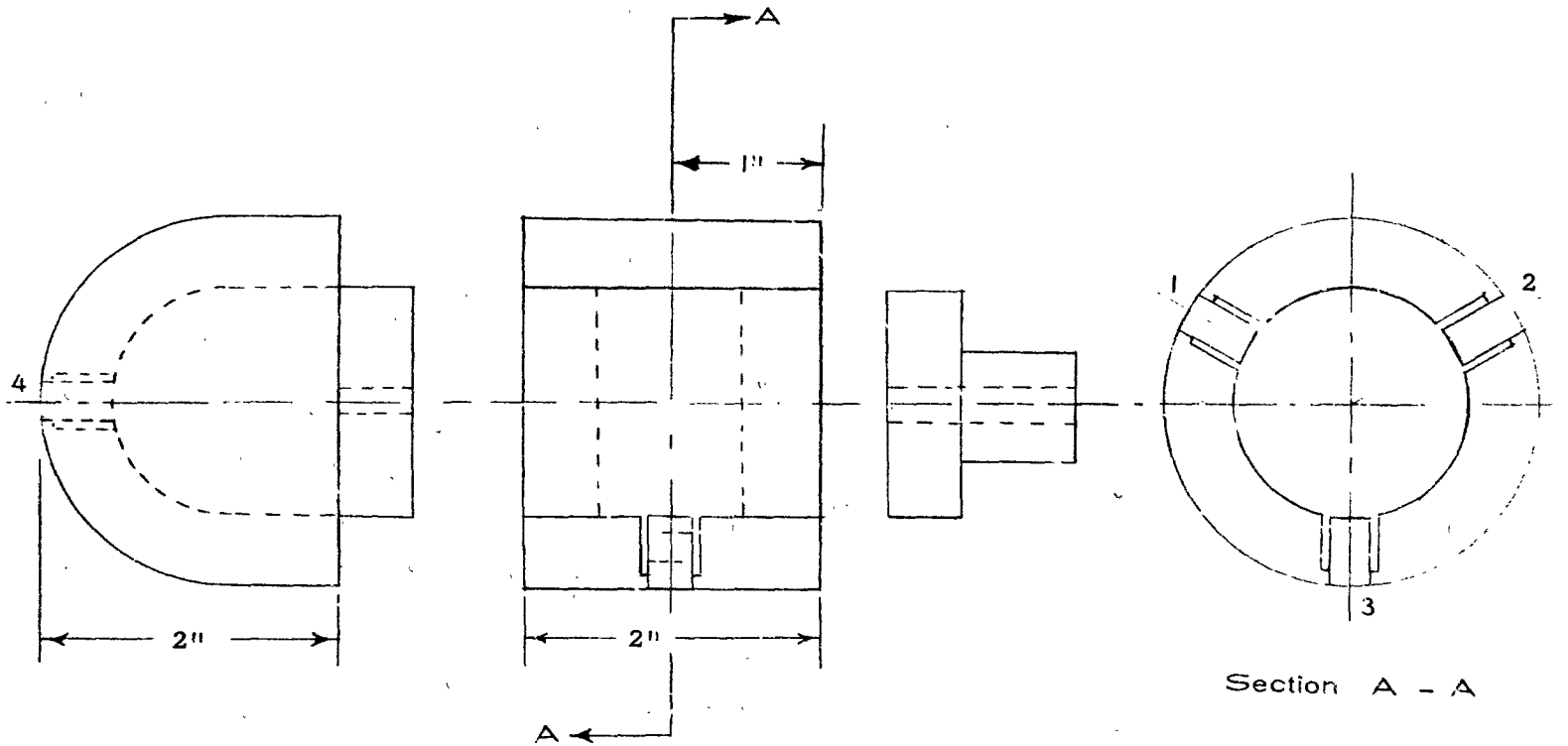


Figure 3-8. Hemisphere - Cylinder Calorimeter Design

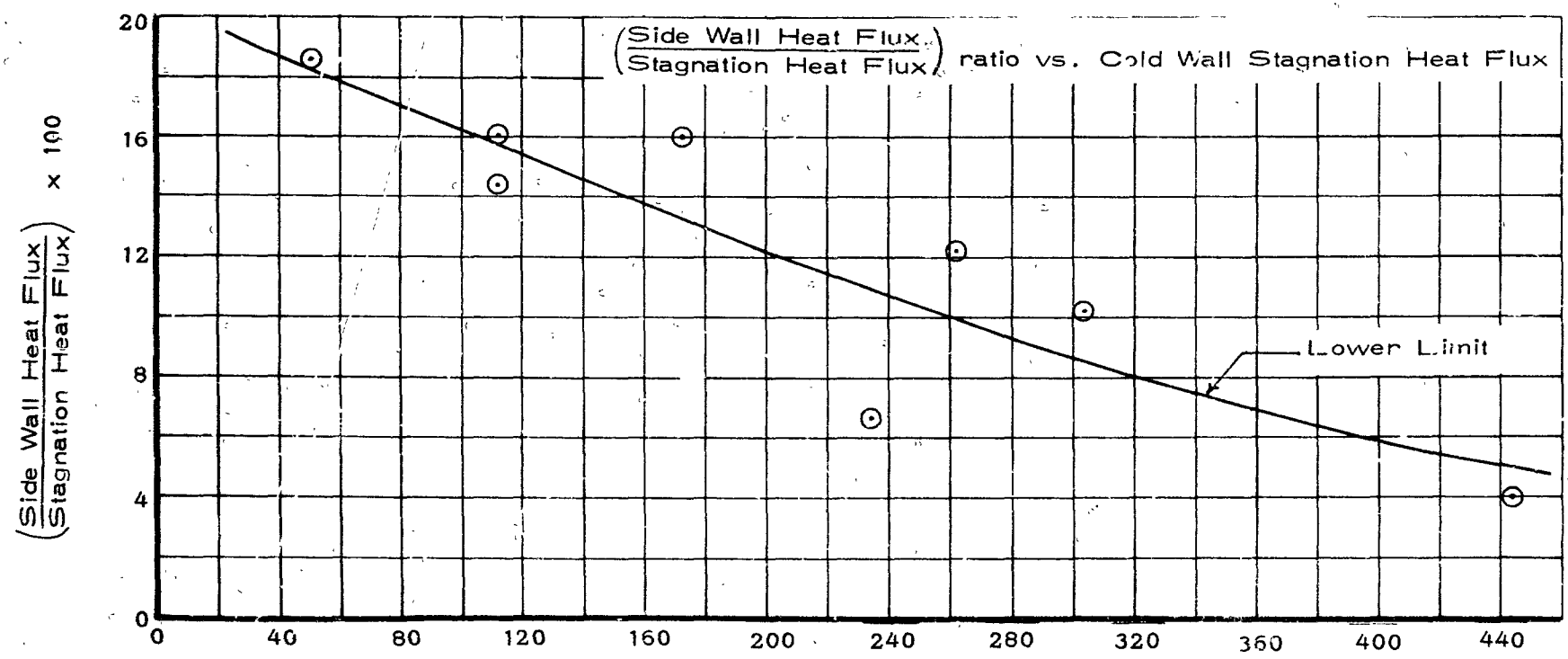


Figure 3-9. Cold Wall Stagnation Heat Flux - Btu/ft^2-sec.

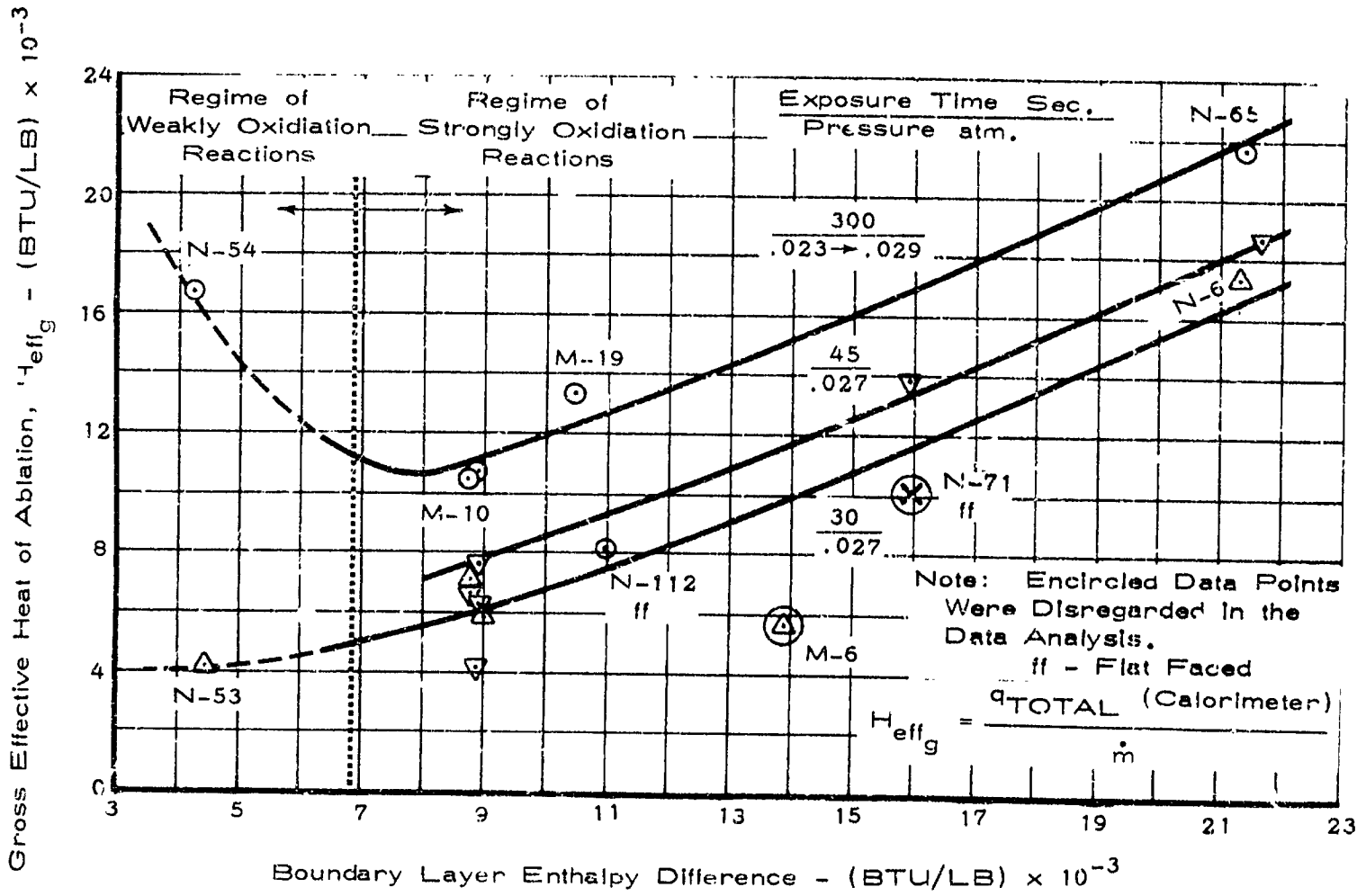


Figure 3-10. Cold Wall Effective Gross Efficiency Versus Boundary Layer Enthalpy Difference for Constant Pressure and Exposure Time (Sheet 1 of 3)

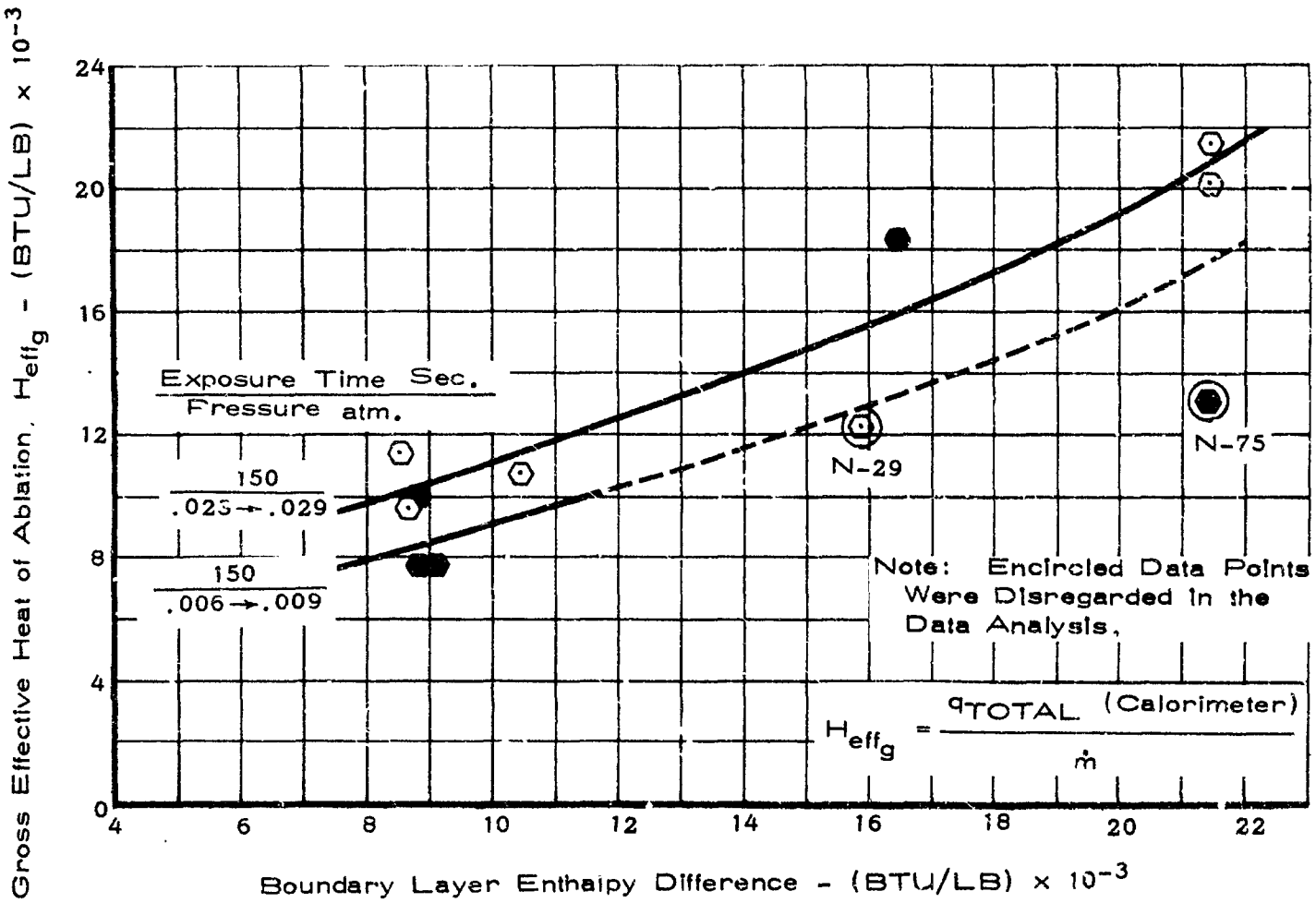


Figure 3-10. Cold Wall Effective Gross Efficiency Versus Boundary Layer Enthalpy Difference for Constant Pressure and Exposure Time (Sheet 2 of 3)

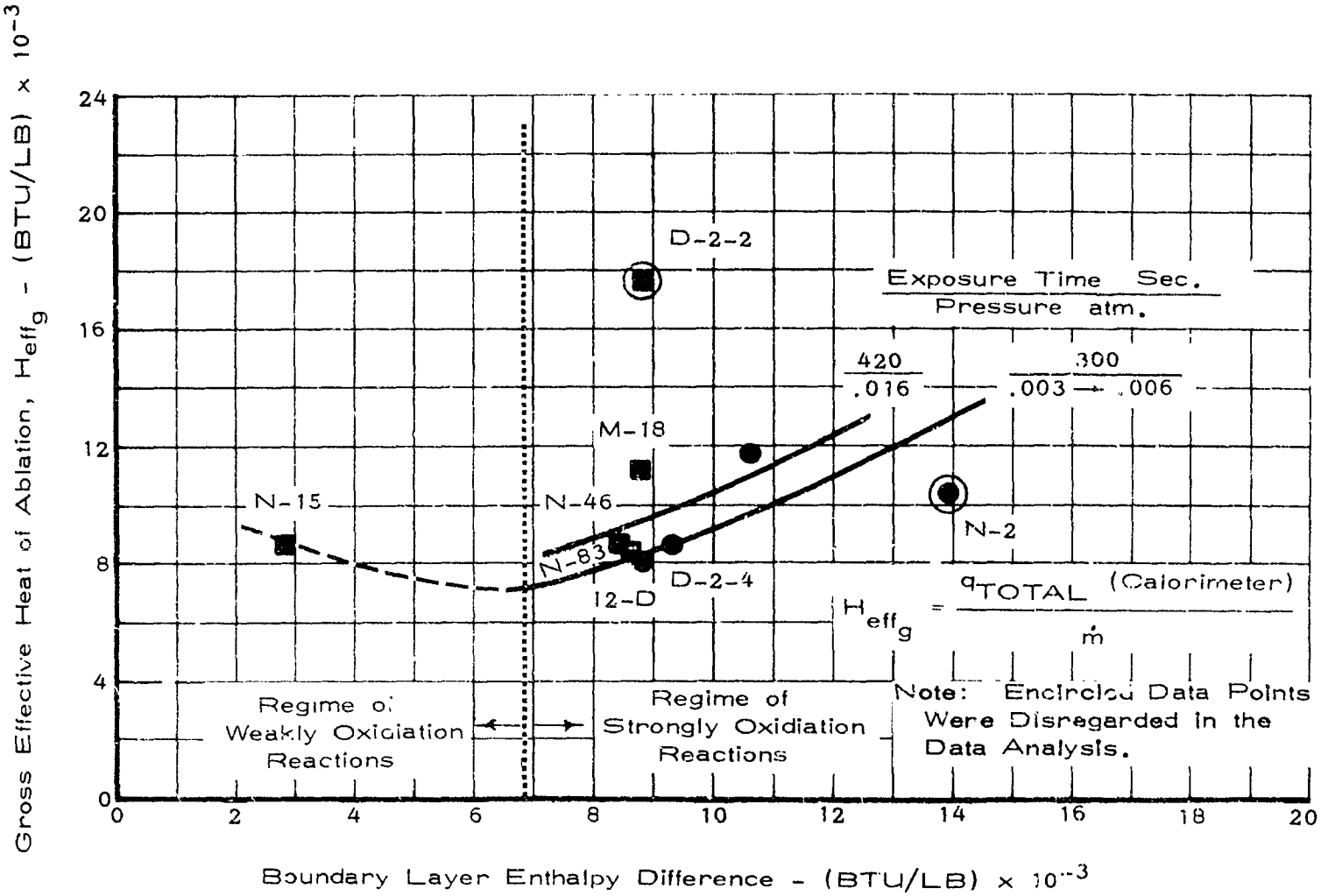


Figure 3-10. Cold Wall Effective Gross Efficiency Versus Boundary Layer Enthalpy Difference for Constant

The models exhibited two basically different types of behavior depending upon the environmental exposure conditions; an essentially nonreceding debris layer was formed under low heat flux-low enthalpy conditions, while receding debris layer was observed at high-heat flux, high enthalpy conditions.

LOW HEAT FLUX CONDITIONS ($<$ 50 BTU/FT^2-SEC) - LOW ENTHALPY ($<$ 5000 BTU). Seven hemisphere-cylinder models of 1.0-inch nose radius were exposed to a cold wall stagnation heat flux of 30 Btu/Ft^2-Sec at a stagnation pressure of 0.0098 atmosphere. Test durations ranged from 12 to 60 minutes. Transient performance was observed for the entire test duration (Figure 3-11) and was characterized by a continued increase in debris layer thickness and a nonlinear recession history. The debris surface approached temperature equilibrium as evidenced by the almost constant observed temperature of 2800°R did not recede and had a glassy appearance. Virgin material recession at a 60-minute exposure time was 1.05 inches, and the corresponding debris thickness was 1.0 inch. The measured debris density was varied from 9 Lb/Ft^3 near the subliming surface to 30 Lb/Ft^3 at the exposed surface. Debris density measurements are presented in Figure 3-18.

Similar performance was noted for the 48 Btu/Ft^2-Sec stagnation heat flux case at a total enthalpy of 5000 Btu/Lb and 0.0076 atmosphere stagnation pressure (Figure 3-12). Four 1.0-inch radius hemisphere models were tested for durations from 25 to 900 seconds. Transient recession occurred for the total exposure time of 900 seconds, and was characterized by a continually increasing debris thickness with the mass loss rate changing as a function of time. The surface attained an equilibrium temperature of 3200°R within 100 seconds. A white-colored glassy surface was formed with moderate debris layer recession. The debris thickness at 900 seconds was 0.35 inch. Data analysis indicates that radiation cooling from the surface of the debris layer was the most significant mode of "heat blockage" at these environmental conditions.

HIGH ENTHALPY ($\geq$ 10,000 BTU/LBM) - HEAT FLUX ($\geq$ 100 BTU/FT^2-SEC). At the higher energy levels the debris layer was consumed and reached a steady-state debris layer thickness. The debris layer surface was black in color and porous. A relatively short transient phase of rapid debris layer growth to a maximum thickness of 0.15 inch was followed by steady-state performance characterized by a nearly constant debris thickness.

A series of tests were conducted at the 10,000 Btu/Lbm enthalpy level for a stagnation heat flux of 170 Btu/Ft^2-Sec and stagnation pressure of 0.016 atmosphere. The maximum duration was 465 seconds, at which time the measured virgin material recession and debris thickness were 1.317 and 0.144 inches, respectively (Figure 3-14). An equilibrium surface temperature of 4200°R was attained within 40 seconds of exposure.

HIGH ENTHALPY (175,000 BTU/LB) - HIGH HEAT FLUX (300 BTU/FT^2-SEC). The 17,500 Btu/Lb total enthalpy condition was attained at a stagnation heat flux of 300 Btu/Ft^2-Sec and a stagnation pressure of 0.01 atmosphere. Four models were tested, three of which were 5/8-inch radius hemisphere cones and the other a 5/8-inch radius hemisphere cylinder. The maximum test duration was 300 seconds. After rapidly achieving a steady-state debris thickness, an increase in debris layer thickness was observed with increase in exposure time (Figure 3-15). This behavior attributed to model shape change during exposure. The maximum debris thickness was 0.110-inch and the virgin surface recession at 300 seconds was 0.682-inch. A maximum surface temperature of 4200°R was observed.

The most severe test conditions were; total enthalpy of 23,000 Btu/Lb, stagnation heat flux of 450 Btu/Ft^2-Sec, and stagnation pressure of 0.027 atmosphere. Six models were tested at this condition for exposure times ranging from 15 seconds to 270 seconds. The models initially possessed a 1.0-inch radius hemisphere-cylinder configuration. After 50 seconds exposure the model showed a visible shape change, giving the appearance of having been slightly misaligned in the jet. The stagnation line virgin surface recession at 270 seconds was 0.875-inch and the corresponding maximum debris thickness was 0.091-inch for a surface temperature of 4660°R. Equilibrium surface temperatures were attained within 25 seconds of exposure (Figure 3-16).

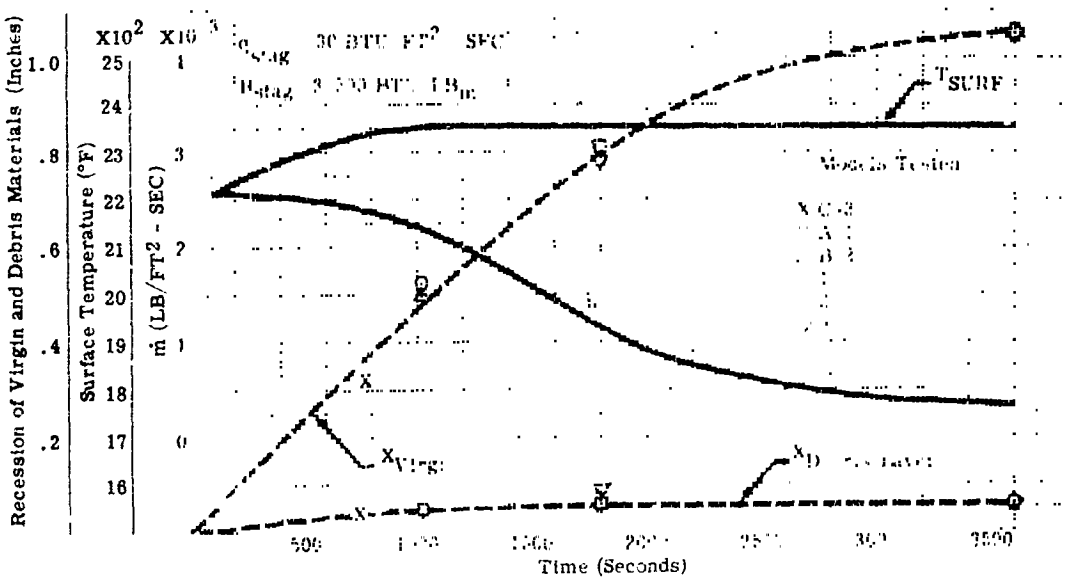


Figure 3-11. Transient Histories

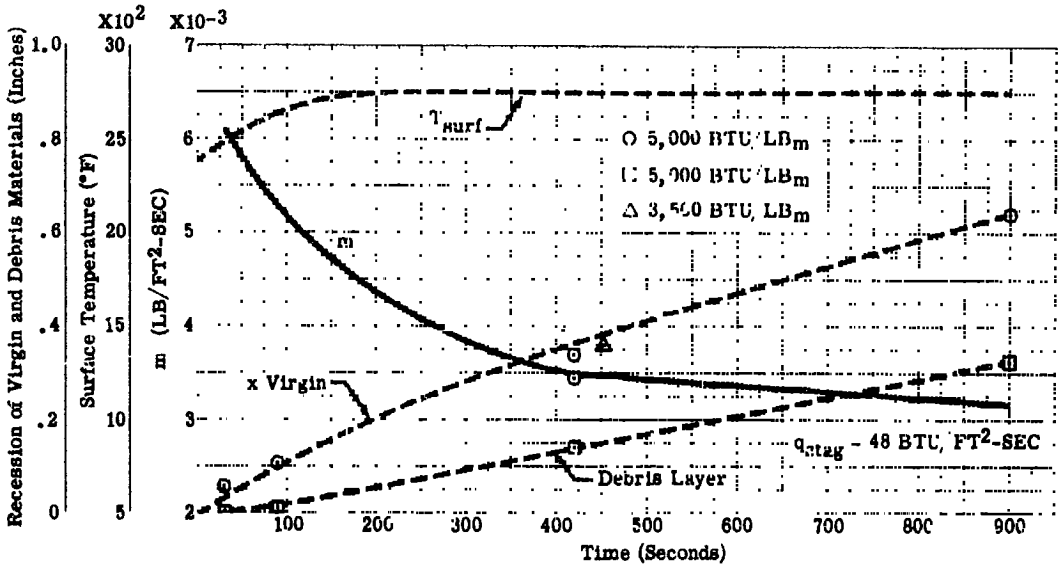


Figure 3-12. Transient Histories

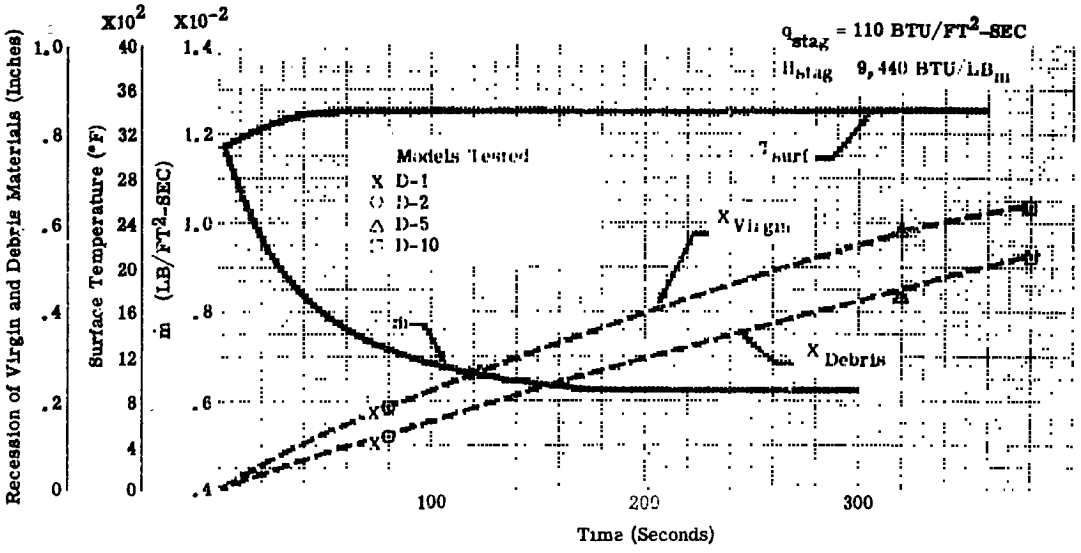


Figure 3-13. Transient Histories

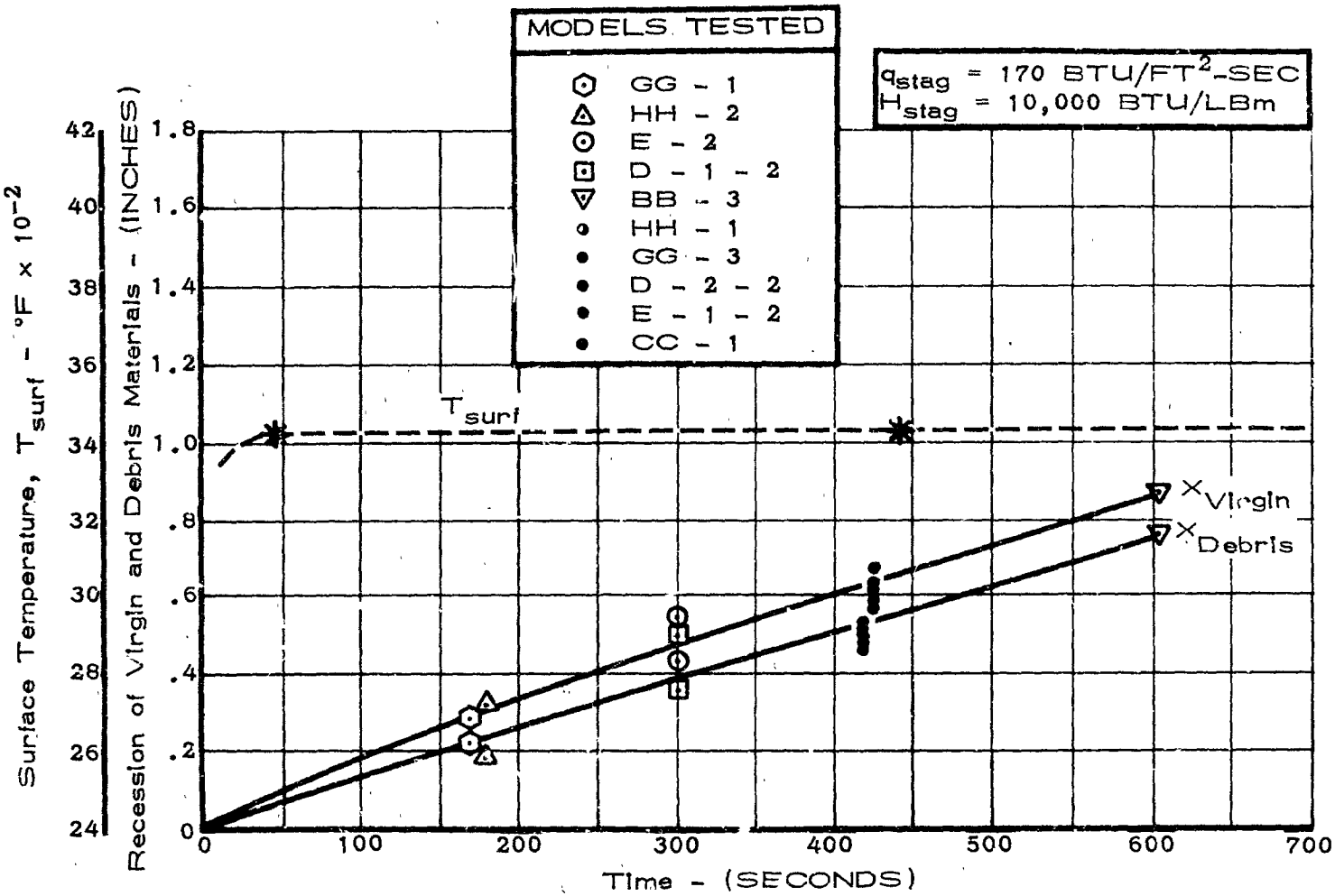


Figure 3-14. Transient Histories (Sheet 1 of 2).

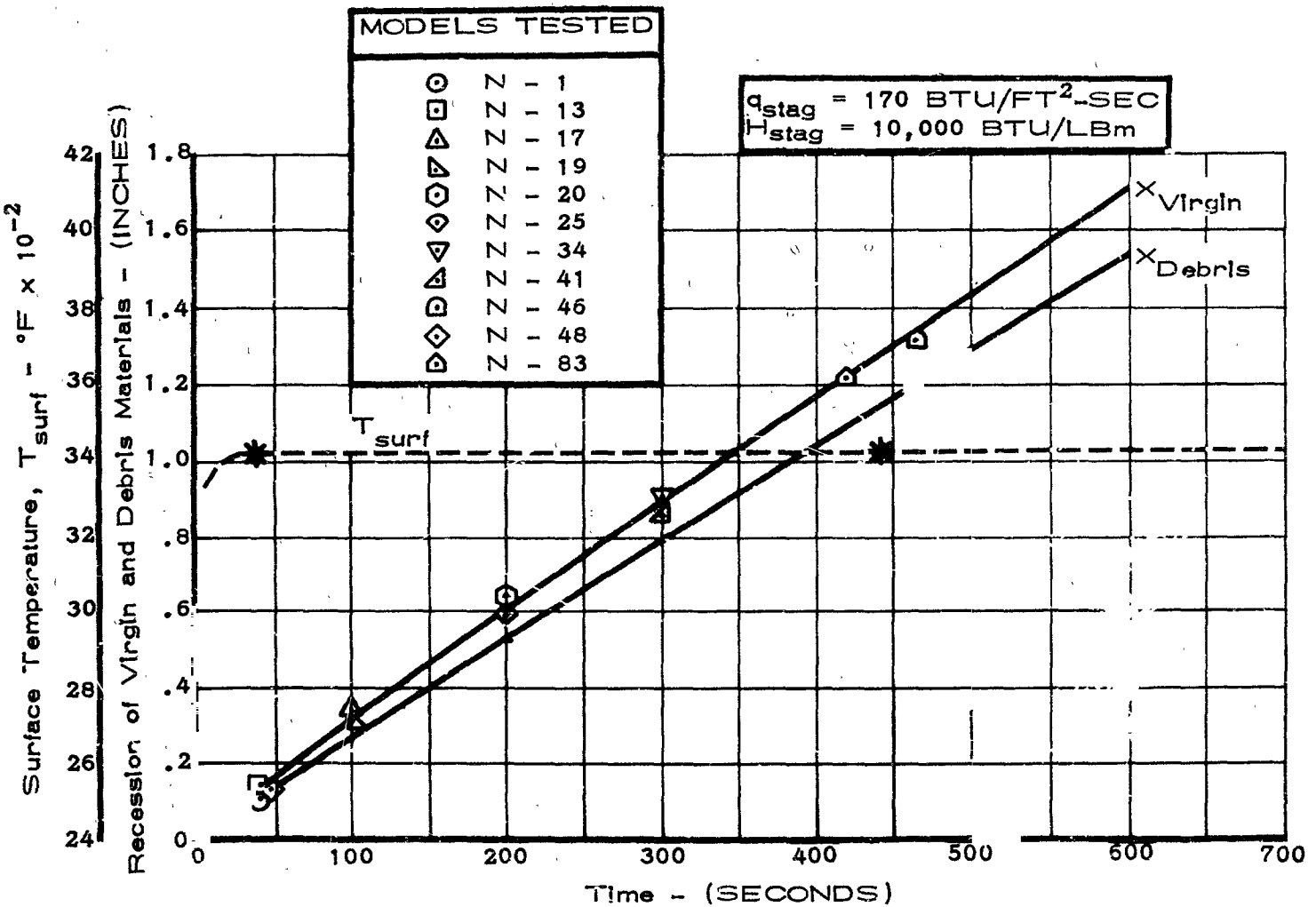


Figure 3-14. Transient Histories (Sheet 2 of 2).

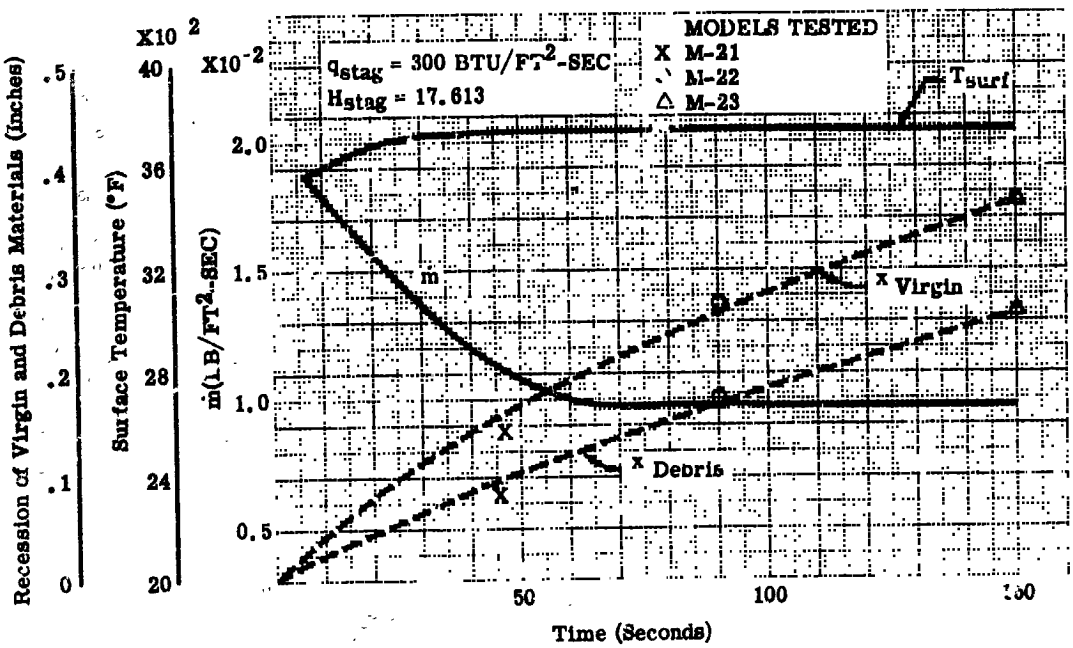


Figure 3-15. Transient Histories

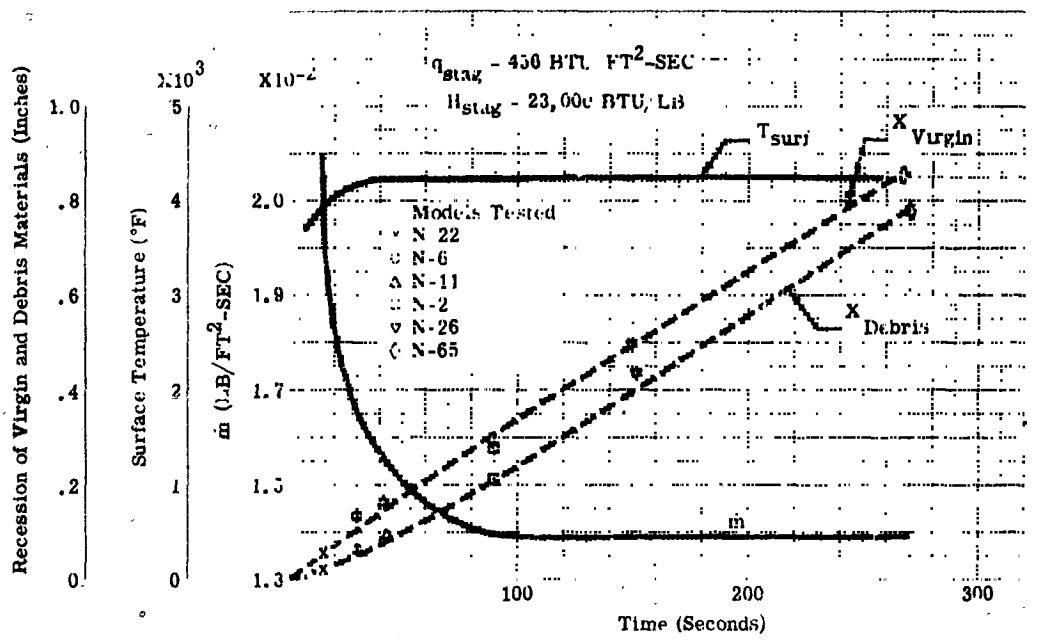


Figure 3-16. Transient Histories

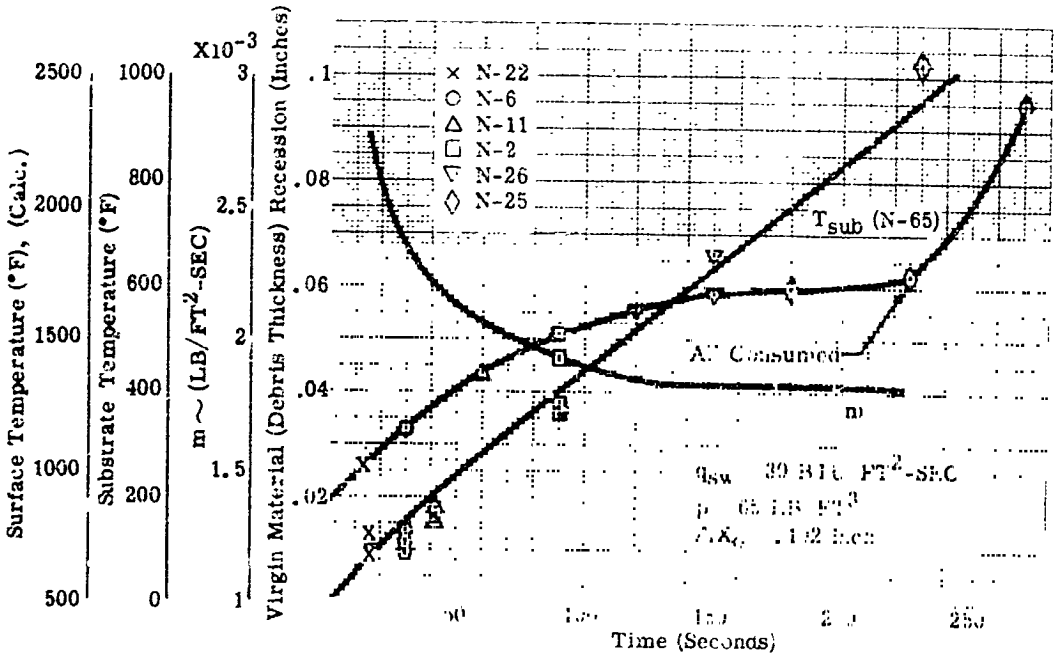


Figure 3-17, Sidewall Transient History

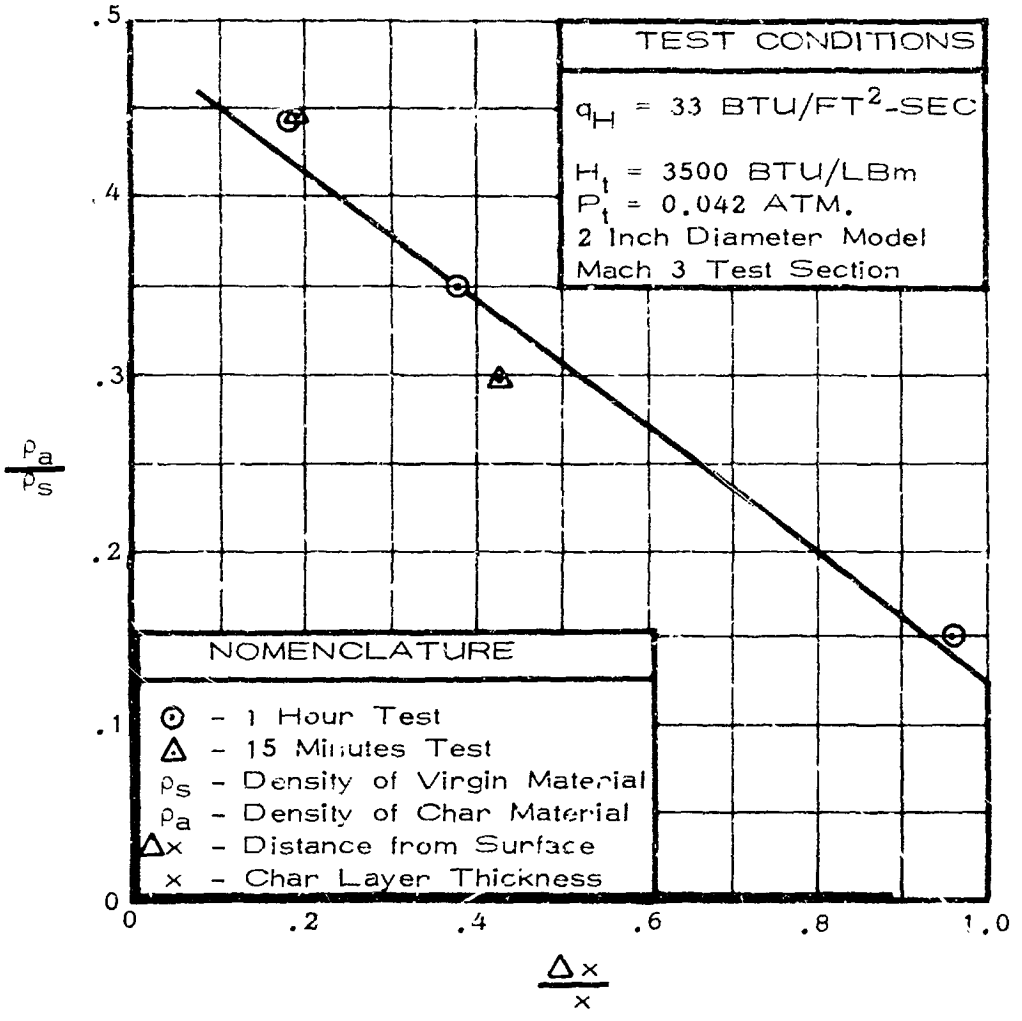


Figure 3-18. Density of Debris Layer as a Function of Debris Layer Thickness.

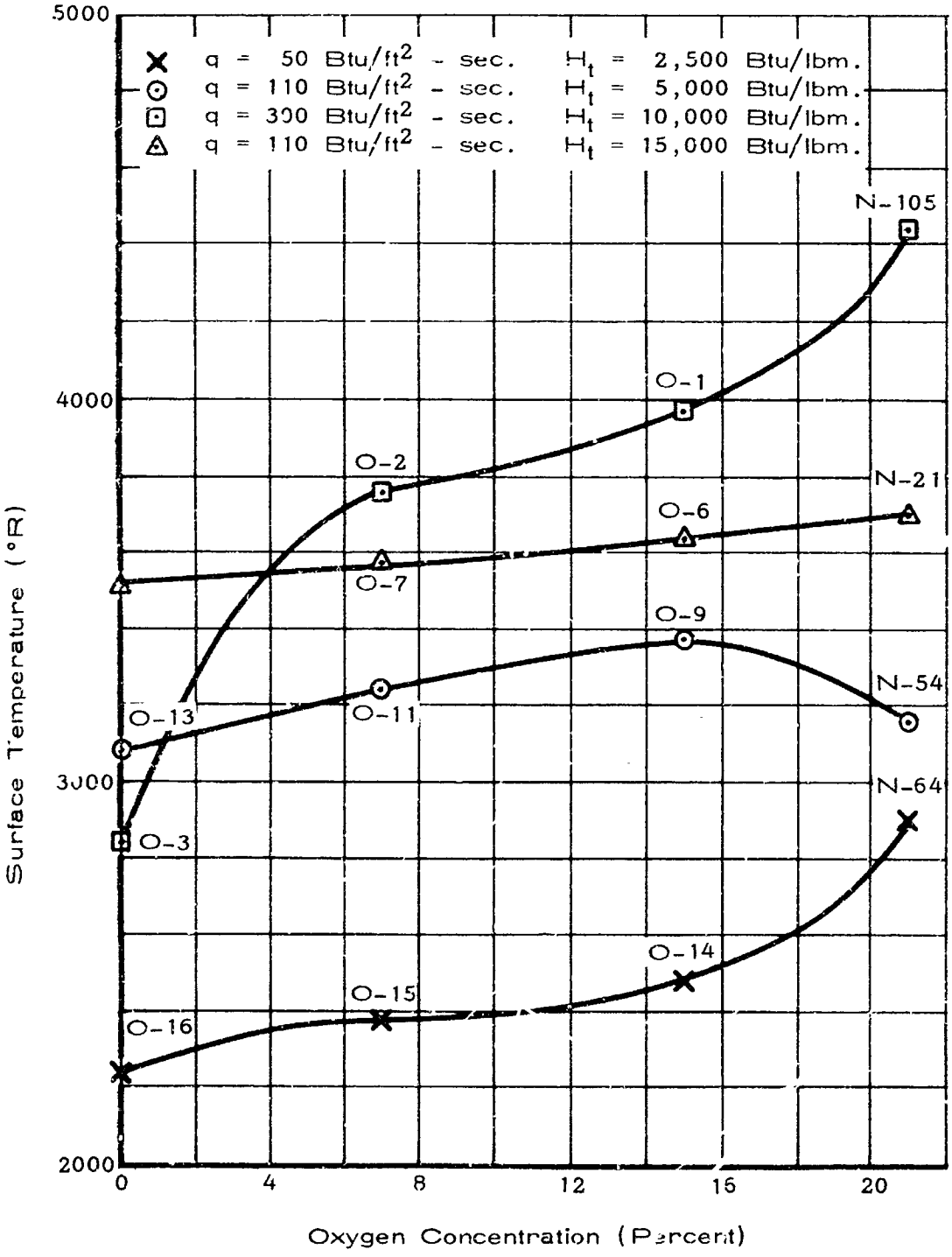


Figure 3-19. Surface Temperature Versus Oxygen Concentration of Stream.

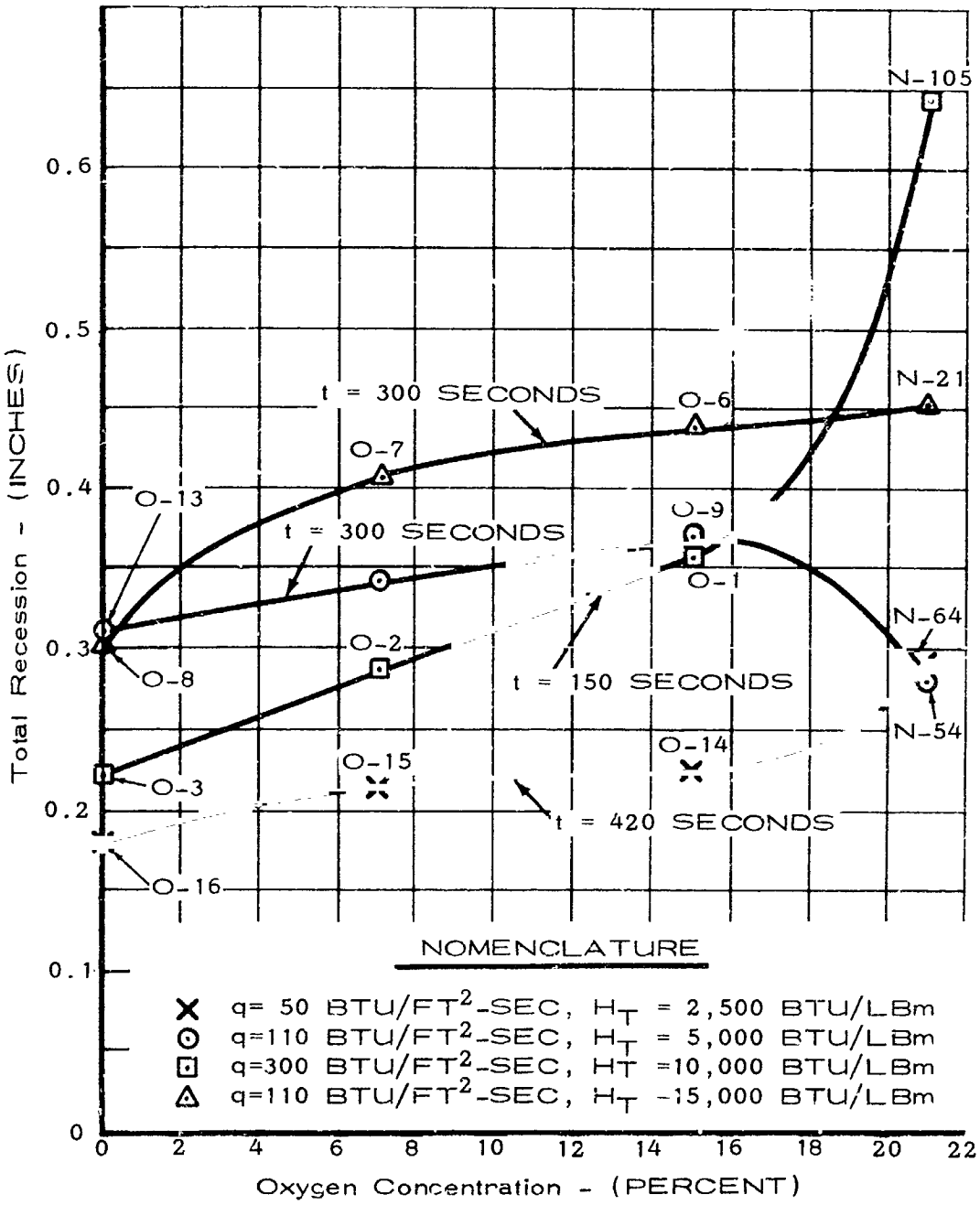


Figure 3-20. Total Recession Versus Oxygen Concentration of Stream

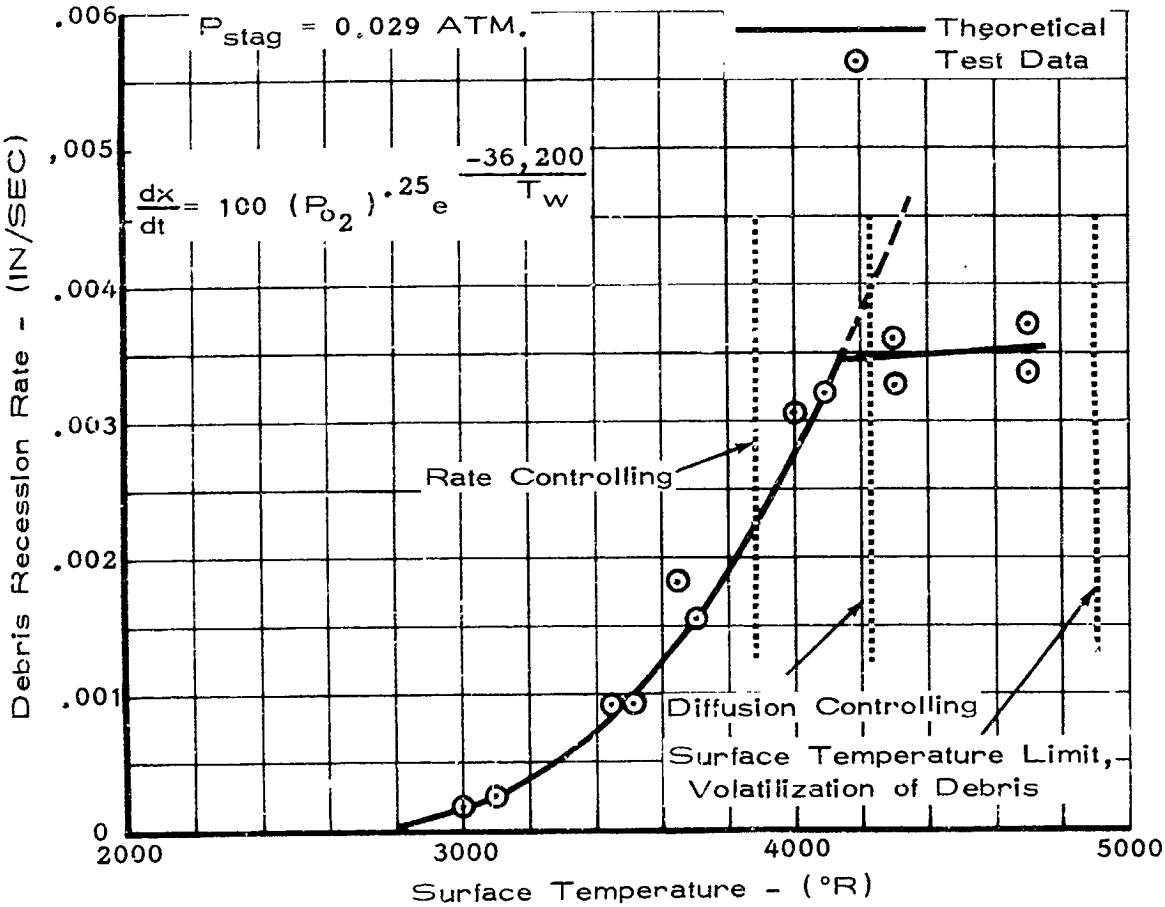


Figure 3-21. Correlation of Debris Recession Data.

SERIES 2-EFFECTS OF STREAM OXYGEN CONCENTRATION

PURPOSE. Tests were conducted to determine the functional relationships between the stream oxygen concentration and the debris layer recession and energy balance. The objective of these tests was to determine:

1. Effect of surface oxidation on the overall gross material performance.
2. Debris layer surface oxidation in the rate-controlled regime as a function of oxygen partial pressure and surface temperature.
3. Identification of the rate-controlled and diffusion-controlled regimes.

TEST MODELS. The model configuration for the 10,000 Btu/Lb_m enthalpy series was a 5/8-inch nose radius hemisphere-cylinder. Hemisphere-cylinders of 1-inch nose radius were used for the remaining tests of the oxidation series.

TEST CONDITIONS. Tests were conducted at the environmental conditions shown in Table 3-3.

For each nominal condition the volume oxygen concentrations of the plasma stream were adjusted to 0, 7, 15, or 21 percent. Test duration, heat flux, and enthalpy were maintained constant for each series of tests. The total enthalpy was varied from 2,500 to 15,000 Btu/Lb_m with corresponding heat fluxes ranging from 48 to 300 Btu/Ft^2-Sec.

All other air arc tests were performed at an oxygen concentration of 21 percent by volume and the data were used to supplement the oxidation series data.

Model Number	Stagnation Cold Wall Heat Flux (Btu/Ft^2-Sec)	Stagnation Enthalpy (But/Lb)	Nose Radius (In)	Oxygen (%)	Test Duration (Sec)
N-105	279	10,085	5/8	21	150
O-1	297	9,897	5/8	15	150
O-2	295	10,055	5/8	7	150
O-3	301	10,165	5/8	0	150
N-21	105	15,150	1	21	300
O-6	108	14,988	1	15	300
O-7	105	15,185	1	7	300
O-8	107	15,052	1	0	300
N-54	105	5,100	1	21	300
O-9	109	4,965	1	15	300
O-11	107	5,000	1	7	300
)-13	109	5,110	1	0	300
N-64	47.4	2,550	1	21	420
O-14	48.7	2,488	1	15	420
O-15	46.8	2,510	1	7	420
O-16	47.9	2,505	1	0	420

Table 3-3. Oxidation Test Matrix

DISCUSSION OF RESULTS. Test results are shown in Table 3-4. The dependency of surface temperature on stream oxygen concentration is shown in Figure 3-19. Virgin surface recessions are presented in Figure 3-20 as a function of oxygen concentration. Figure 3-19 indicates smooth variation of face temperature with change in oxygen concentration except for one run at percent oxygen concentration and 10,000 Btu/Lb enthalpy, and all runs at the 21 percent concentration.

A comparison of these surface temperatures with other test runs at about the same conditions and the correlation of Figure 3-10 provides a basis for determining the validity of the 21 percent oxygen runs at the 10,000 and 15,000 Btu/Lb$_m$ enthalpy levels. The high surface temperature for Model N-105 (q = 300 Btu/Ft^2-Sec, H_t = 10,000 Btu/Lb) was found to be consistent with the other data. The performance of Model N-21 (q = 110 Btu/Ft^2-Sec, H_t = 15,000 Btu/Lb$_m$) was found to be substandard.

An increase in surface temperature as the oxygen concentration was increased from 15 to 21 percent at the higher enthalpy levels is evidently correct. A reverse trend was found from the relationship between virgin material recession and oxygen concentration (Figure 3-20) at the 5,000 Btu/Lb$_m$ enthalpy level. The 21 percent oxygen run (Model N-54) showed considerable decrease in

Model No.	Nose Radius (In.)	Run Duration (Sec.)	Stagnation Enthalpy (Btu/Lb)	Test Point No.	Stagnation Cold Wall Heat Flux (Btu/Ft^2-Sec.)	Percent O_2	Model Stagnation Pressure (Atm.)	Recession to Debris Layer (In.)	Debris Thickness (In.)	Total Recession (In.)	Surface Temp. (^oF) Lot Emissivity = 0.9	Enthalpy Difference (Btu/Lb)	Hot Wall Heat Flux (Btu/Ft^2-Sec)	Cold Wall Heat Blockage (Btu/Lb)
N-105	5/8	150	10,085	14	279	21	.0290	.584	.062	.356	4,440	8,725	244.5	9,705
0-1	5/8	150	9,897	15	297	15	.0291	.28	.08	.360	3,510	8,750	262	18,550
0-2	5/8	150	10,055	16	295	7	.0289	.117	.17	.287	3,300	9,[illegible]	265	23,300
0-3	5/8	150	10,165	17	301	0	.0291	.022	.20	.222	2,380	9,405	279	30,500
N-21	1	300	15,150	20	105	21	.0027	.289	.164	.453	3,700	14,080	98.4	10,420
0-6	1	300	14,988	21	108	15	.00267	.268	.17	.438	3,180	13,968	101	11,100
0-7	1	300	15,185	22	105	7	.00265	.156	.25	.406	3,110	14,185	98.3	11,600
0-8	1	300	15,052	23	107	0	.00266	.063	.27	.333	3,050	14,077	100	14,450
N-54	1	300	5,100	7	105	21	.026	.047	.238	.285	3,060	4,280	90.45	16,580
0-9	1	300	4,965	8	109	15	.026	.068	.30	.368	2,910	4,035	88.7	13,350
0-11	1	300	5,000	9	107	7	.0258	.042	.30	.342	2,780	4,110	88	14,000
0-13	1	300	5,110	10	109	0	.026	.026	.31	.336	2,620	4,270	91	14,600
N-64	1	420	2,550	2	47.4	21	.021	.042	.244	.236	2,900	1,785	35.1	10,420
0-14	1	420	2,488	3	48.7	15	.0255	.035	.19	.225	2,010	1,843	36	13,650
0-15	1	420	2,510	4	46.8	7	.0258	.023	.19	.215	1,920	1,895	35.3	13,750
0-16	1	420	2,505	5	47.9	0	.0256	.009	.17	.179	1,780	1,925	36.8	16,900

Table 3-4. Stagnation Point Oxidation Results

surface temperature with respect to the 15 percent run. This temperature was found to be consistent with that observed for Model N-9, which was tested at the same condition. The corresponding virgin material recession of Figure 3-20 was consistent with the surface temperature-recession correlation of Figure 3-58. The 2500 Btu/Lb enthalpy level showed a result similar to that of the 10,000 Btu/Lb enthalpy level, giving a marked increase in surface temperature at the 21 percent oxygen concentration. Correspondingly, the virgin recession was compatible with the measured surface temperature.

METHOD OF DATA ANALYSIS

Recognizing complicated physical and chemical phenomena arising from oxidation reactions between high temperature (above 5000°R) air and the carbonaceous debris, it was intended in the analysis of the test data to eliminate lower order factors or mechanisms by utilizing published data.

The rate of oxidation of carbon in a high energy air stream is contingent upon the rate of the following five processes:

1. Transport (diffusion) of oxygen to the surface.
2. Chemisorption of oxygen impinging on the surface.
3. Chemical reaction between the chemisorbed oxygen and carbon.
4. Desorption of the product carbon monoxide from the surface.
5. Transport of carbon monoxide away from the surface.

Processes 1 and 3 are acknowledged as controlling actions, where process 3 occurs within the reaction ate-controlled regime below the transition temperature, and process 1 occurs at and above the transition temperature. In the rate-controlled regime the oxidation rate is a strong function of the temperature and partial pressure of oxygen as expressed by the Arrhenius rate equation. In the diffusion-controlled regime, the reaction rate becomes so rapid that the oxygen diffusion rate becomes controlling.

In reducing and correlating the experimental data, an attempt was made to determine the reaction rate and the order of reaction utilizing an activation energy of 40 Kcal/mole. As reported in the literature a check of the analytical values was made from a cross-plot of recession versus surface temperature as a function of test time. The reaction rate and the order of reaction were found to be 100 inches/seconds-atmosphere .25 and 0.25, respectively.

The reaction rate can be expressed in the generalized form:

$$\frac{dx}{dt} = 100\,(pO_2)^{.25}\, e^{-36200/T_w}$$

The terms are expressed in inches, seconds, atmospheres, and degrees Rankine. The ranges of variables at which the expression can be expected to give good correlation with measured recession rates are:

Tw (°R)	3000 - 4000
PO_2 (atm)	.0001 - .006
Hb,stag (Btu/Lb_m)	2500 - 15,000

To determine the oxidation initiation temperature and the transition temperature above which the oxygen diffusion rate becomes controlling, the recession rates versus surface temperature for several oxygen partial pressures levels were plotted. A typical plot for a stagnation pressure of 0.029 atmosphere is presented in Figure 3-21. The oxidation initiation temperature is 3000°R and the transition temperature from rate-controlling to diffusion-controlling was found to be approximately 3900 to 4100°R.

SERIES 3-EFFECTS OF MODEL CONFIGURATION

PURPOSE. Various model configurations were utilized in the air arc test program to achieve, within the limitations of the test facility, a range of heat flux while maintaining constant stagnation pressure and total enthalpy. In the course of the experimental work, it was apparent that the initial model shape had an effect upon the ablation performance of the material and that, in some instances, where model shape varied with exposure time, nonlinear recession histories resulted. An analysis of test data was made to classify, wherever possible, ablation performance characteristics traceable to model geometry.

TEST MODELS. The model configurations tested were 5/8-inch and 1.0-inch radius hemisphere-cylinders, hemisphere-cones, and flat faced cylinders.

TEST CONDITIONS. Data from all test conditions shown in Table 3-1 were considered.

DISCUSSION OF RESULTS. The gross effect of initial geometry x on material performance was discernible over the range of geometries tested; however, only qualitative results were determinable concerning the effects of transient model shape changes during exposure. The ablation data analysis considered model shape effects in terms of debris layer behavior and ablation efficiency.

DEBRIS LAYER BEHAVIOR. Debris layer behavior was studied by comparing: surface effects for different model diameters and surface effects for different nose configurations at a constant diameter.

The measured surface temperature at test termination was plotted against post test measured debris layer thickness for models of a given nose diameter and geometry (Figure 3-30). Results showed that the debris layer thickness for the larger diameter models was greater than for the smaller diameter models at an equal surface temperature for enthalpies of 10,000 Btu/Lb$_m$ and greater. A clearly defined behavior pattern was not available at 5000 Btu/Lb enthalpy and lower where, chemically, the debris is much more stable. The larger debris thickness for the larger models was quite apparent at surface temperatures greater than 4100°R. Lower surface temperatures, of which Model N-94 is typical, did not show a distinct difference. The data indicate that the surface reactions are diffusion-controlled at surface temperatures above 4100°R. The implications are that a nose diameter scale-up would

produce a greater debris layer thickness than exhibited during the plasma jet testing of small nose radii. The increased debris thickness would improve material efficiency.

A trend noticed to a lesser degree is that the flat-faced models, N-71, N-73, and N-112, produced a smaller debris layer thickness than the hemispherical-nosed models of the same diameter. This effect was less clearly discernible, since many of the hemisphere nosed models attained a varying degree of bluntness during ablation. A greater net heat flux to the surface of the flat-faced models at a given surface temperature than to the stagnation region of the hemisphere-nosed model would produce the above result and is possible through increased exothermic reactions within the boundary layer.

ABLATION EFFICIENCY

The existence of transient configurations is evident from the photographs and surface temperature traces of models run at various test points of the Plasmadyne test matrix. For example, consider the models run at test point number 27. Model numbers N-65 and N-73 were a 1-inch radius hemisphere cylinder and a 1-inch radius flat-face model, respectively, and are typical of those run at test point 27. The flat-face model after a 100-second exposure shows a finite radius of curvature at the exposed surface. The temperature trace for this model exhibits an increase in the surface temperature as exposure time increases beyond 55 seconds. This indicates that the heat flux to the model surface increased with the shape change. Model N-65 exhibits a constant surface temperature for the entire run, indicating a constant net heat flux; however, the post-exposure photograph of Model N-65 showed that the point of maximum heating did not occur at the stagnation point, but, at some unknown distance from the centerline. This is a result of the presence of a considerable radial variation of total enthalpy, misalignment of the stagnation point with respect to the point of maximum enthalpy of the flow field. This situation exists to a much lesser degree at the low heat flux - low and moderate enthalpy stagnation conditions since the radial enthalpy variations are much less pronounced. For these low heat flux - low and moderate enthalpy stagnation conditions, the unsymmetrical configurations developed only for exposure times in excess of 100 seconds.

Figure 3-10 is a plot of the average cold wall ablation efficiency, H_{eff}, as a function of the enthalpy difference across the boundary layer for the test runs having a 21 percent oxygen concentration. A comparison of the ablation efficiencies of flat-face and hemispherical

cones and cylinders at similar enthalpy levels gave a measure of the effect of initial model shape upon material performance, provided the models during exposure did not exhibit transient configuration characteristics as mentioned previously. Examination of post-test photographs and surface temperature traces of models M-19, N-106, and N-112 at test point 18 and models N-39 and N-71 at test point 25 showed that these models satisfy the requirements of constant model shape and, therefore, are amenable to analysis.

Models M-19, N-106, and N-112 were hemisphere-cone, hemispher cylinder and flat face models, respectively with 5/8-inch nose radii. Comparison of the ablation efficiency data from these models at test point 18 shows a greater material efficiency to be indicated by the cone than by the flat face model. Using the flat face model results as a basis of reference, the results from the conical model are 60 percent greater and the results from the cylindrical model are approximately 28 percent greater than indicated by the flat face model for an equivalent enthalpy drop across the boundary layer.

Model N-29 and N-71 are a hemisphere cylinder and flat-face models, respectively, both of one inch radius. Test point 25 consisted of a stagnation pressure of 0.020 atmosphere and enthalpy of 17,500 Btu/Lbm. Comparison of the ablation efficiencies indicated by these models shows that the same trend is observed at test point 25 as at test point 18, in that the hemisphere-nosed model indicates greater efficiency than does the flat-face model. For this test point the hemisphere-cylinder result is at least 20 percent greater. The actual efficiency difference is probably greater than 20 percent since model N-29 showed a low rating in the data comparison of Figure 3-10. Analysis of conical and cylindrical models of equal radii tested at other points exhibited the same trends.

Comparison of the effect of initial model geometry at test point 27, the 23,000 Btu/Lb_m enthalpy level, was not possible to the development of transient unsymmetrical configurations as previously pointed out. The transient nature of the model configurations of N-65 and N-73 resulted in the ablation efficiencies being equivalent, approximately 22,100 Btu/Lb_m as noted in Figure 3-10. The requirement of constant model shape during exposure was not achieved here, therefore, no observable trend was noted.

The analysis of the effect of initial model geometry upon material performance led to the conclusion that the observed efficiency

of the material was a function of the initial model geometry. A hemisphere-cone was found to indicate greater efficiency than a flat-face model of the same nose diameter at a given moderate total enthalpy level. At the high heat flux and high enthalpy levels, the difference in indicated efficiency was not discernable.

SERIES 4-EFFECTS OF STREAM PRESSURE

PURPOSE. An air arc test series was performed to assess the effects of stream pressure on the ablation performance of "THERMO-LAG" T-500 material.

TEST CONDITIONS. A test matrix was followed as shown in Figure 3-5. Sufficient test runs were provided to establish the relationship between pressure and effective gross material efficiency at constant total enthalpies of 12,000, 17,500, and 25,000 Btu/Lb. Pressures were varied by a factor of approximately four at each total enthalpy. Data from the transient series were also used so that constant test duration comparisons could be made to compensate for transient behavior.

Model Type and Series	Stagnation Pressure (Atm)	Stagnation Heat Flux (Btu/Ft^2-Sec)	Desired Sidewall Heat Flux (Btu/Ft^2-Sec)	Stagnation Enthalpy (Btu/Lb)
1-1/4 IN. hc (N)	.024	300	24	12,000
1-1/4 IN. hc	.006	165	13.6	12,000
1-1/4 IN. hc	.024	165	13.6	12,000
2 IN. hc	.005	170	13.6	17,500
2 IN. ff	.020	170	13.6	17,500
2 IN. hc	.020	310	25	17,500
2 IN. nc	.009	305	25	25,000
2 IN. ff	.030	305	25	25,000
2 IN. hc	.030	550	44	25,000

Table 3-5. Test Matrix - Evaluation of Pressure Effect on Stagnation Point Ablation Kinetics

DISCUSSION OF RESULTS

Results from the flat face models were disregarded in evaluating the effects of stream pressure because nonconformity with the performance correlation shown in Figure 3-10. Results from the hemisphere-cylinder models of this test series and applicable results from other series are presented in terms of average gross effective heat of ablation in Figure 3-22. Heating rates were based on the cold wall calorimeter value.

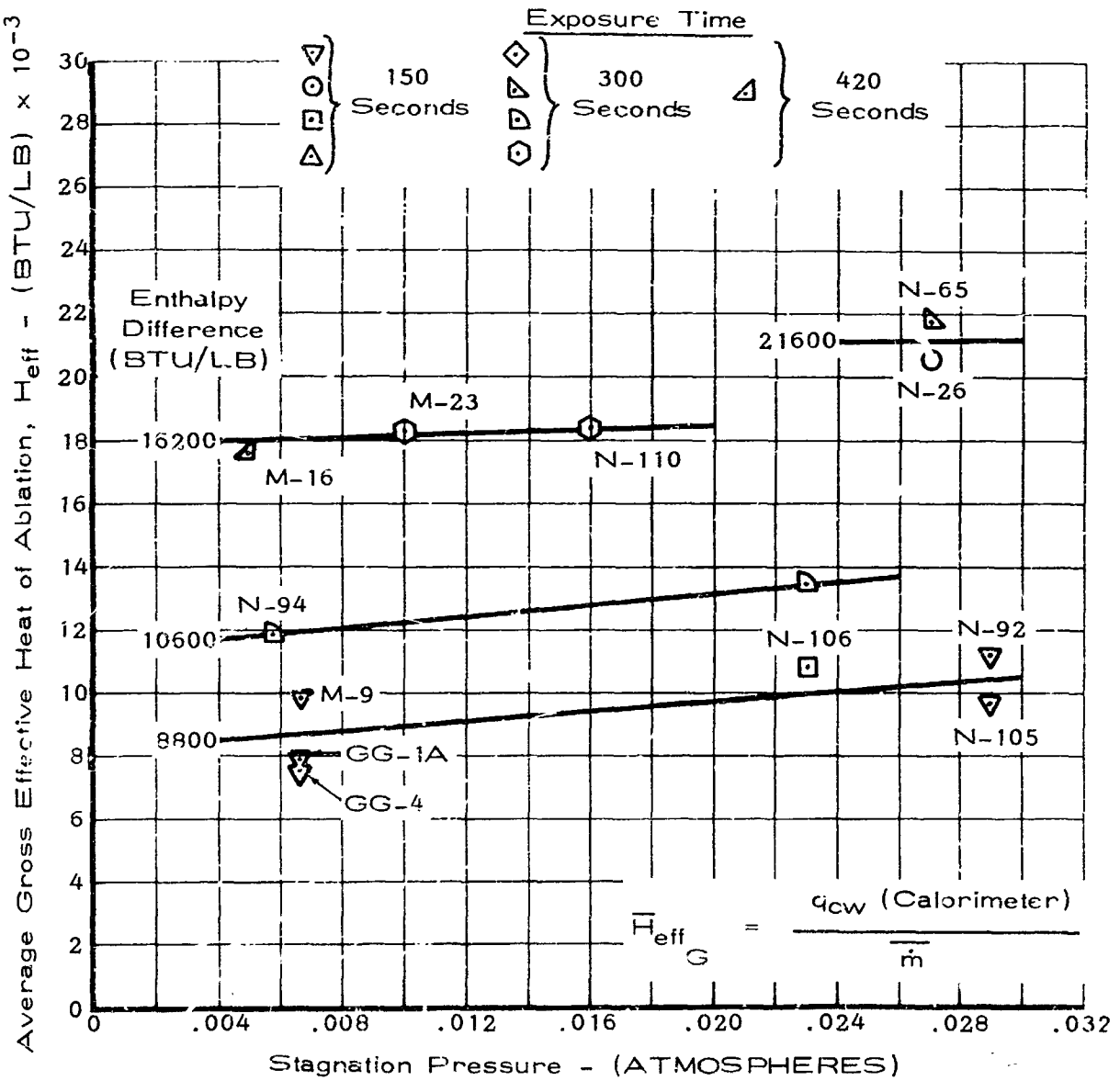


Figure 3-22. Effect of Stagnation Pressure on Average Gross Effective Heat of Ablation At Constant Boundary Layer Enthalpy Difference

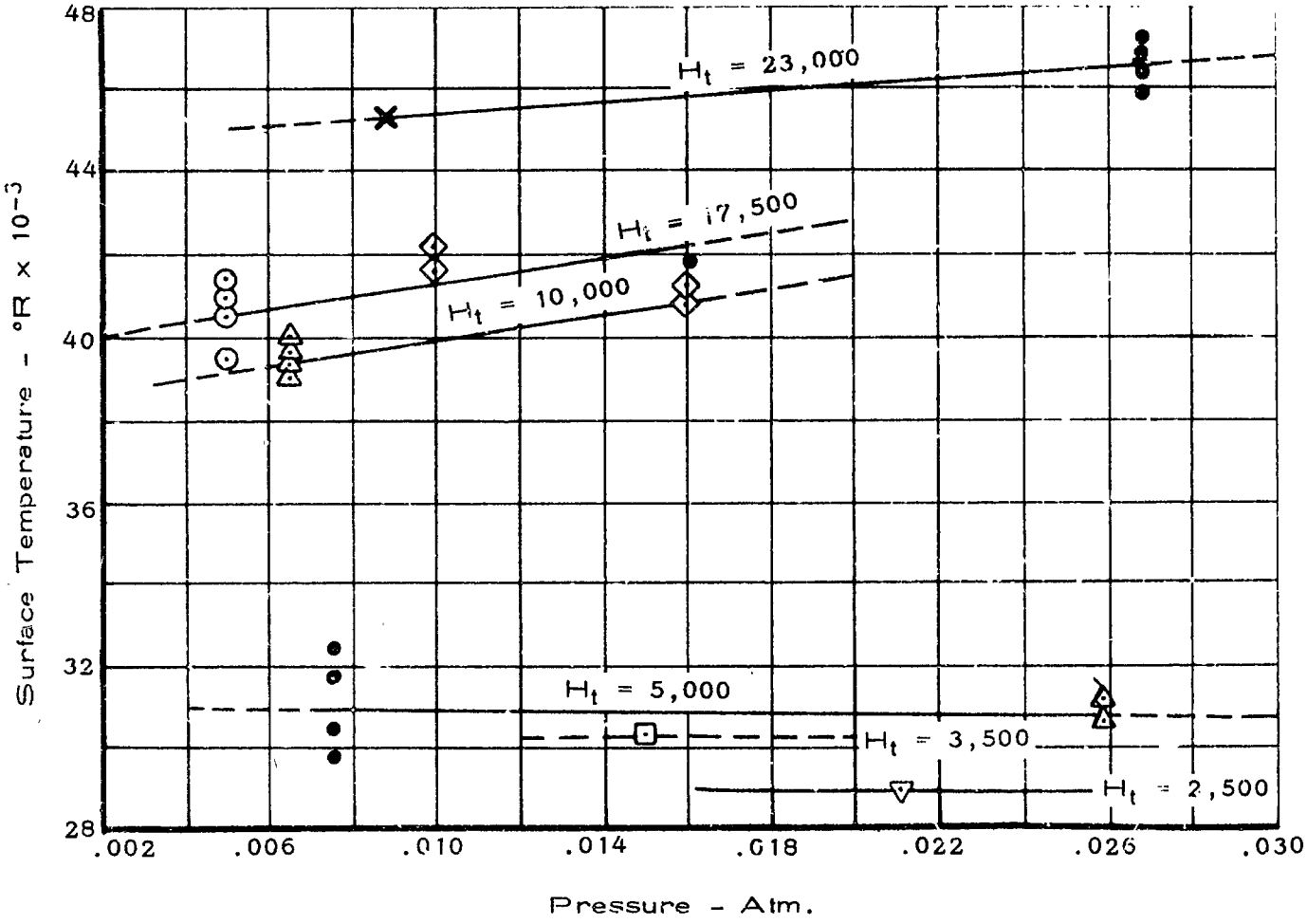


Figure 3-23. Measured Surface Temperature Versus Environmental Conditions for a 2.2" Diameter Model in Plasmadyne Air

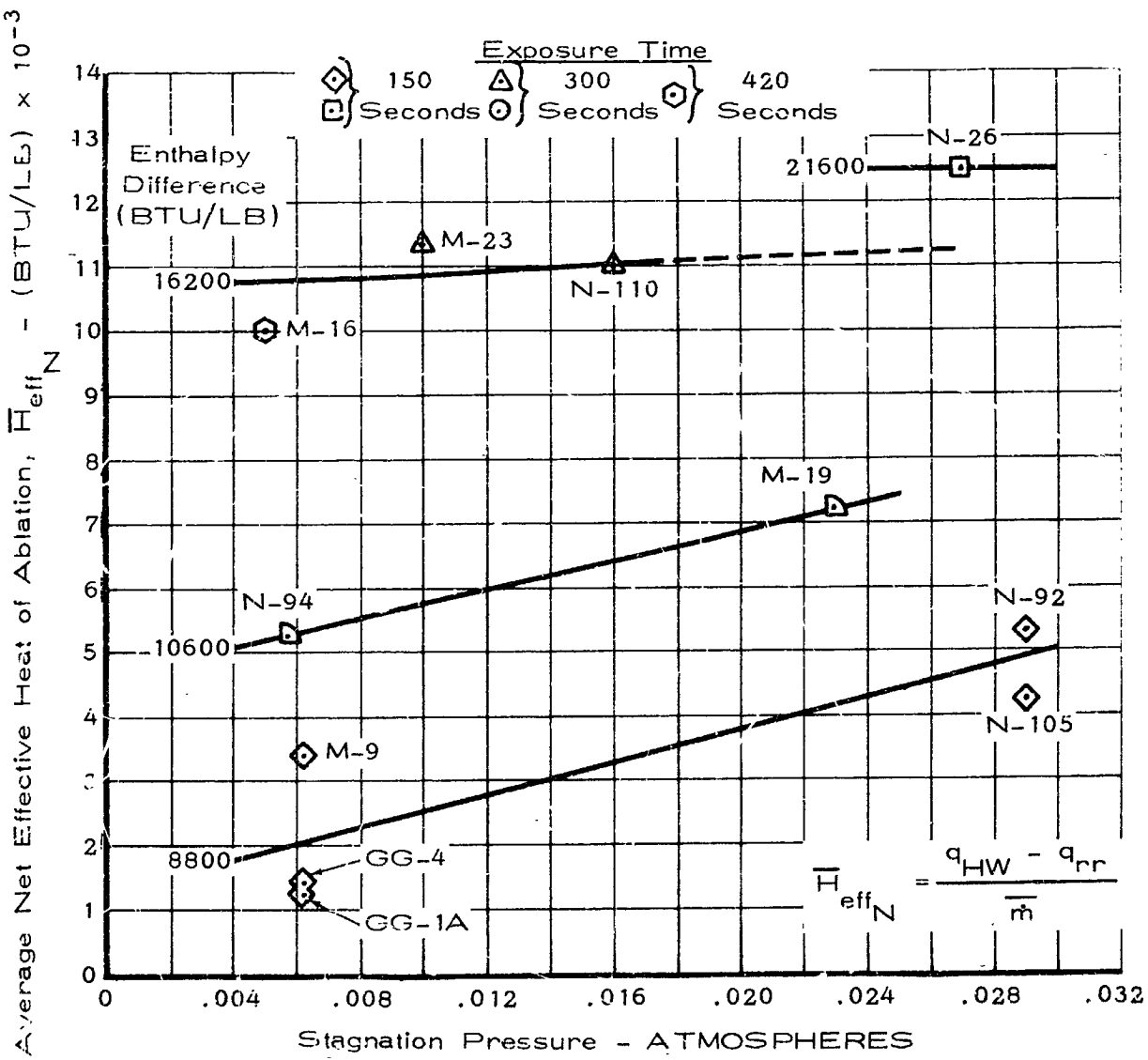


Figure 3-24. Effect of Stagnation Pressure on Average Net Effective Heat of Ablation at Constant Boundary Layer Enthalpy Difference

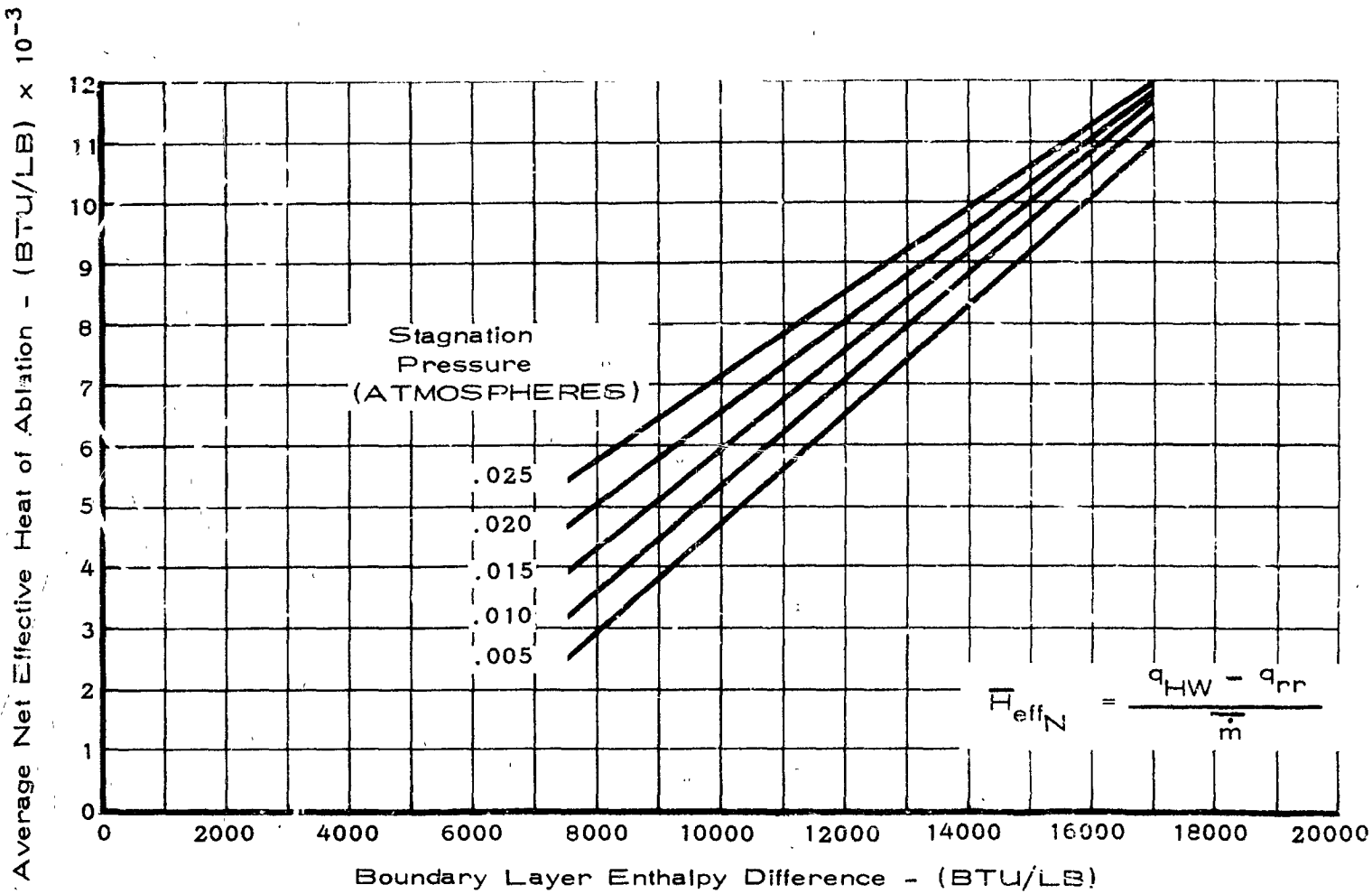


Figure 3-25. Dependence of Average Net Effective Heat of Ablation on Boundary Layer Enthalpy Difference at Constant Stagnation Pressure.

As shown in Figure 3-22, a fourfold increase in pressure from 0.005 to 0.020 atmospheres at a constant boundary layer enthalpy difference of 10,500 Btu/Lb resulted in a 13 percent increase in indicated efficiency. This increase in pressure corresponded to an increase in convective heating rate of 140 percent and a 10 percent increase in debris surface temperature. Figure 3-23 shows the relationship between surface temperature and stream pressure for several constant enthalpies.

A measure of the net energy absorbed through gas phase reactions and sensible heating is given in Figure 3-24. Efficiency here is defined as the net difference between the hot wall calorimeter flux and the reradiation flux divided by the average mass loss rate. A 30 percent indicated increase in net efficiency was found with a fourfold increase in pressure at a constant boundary enthalpy difference of 10,500 Btu/Lb. A weak dependency of efficiency upon pressure was indicated at the 16,200 Btu/Lb enthalpy difference condition. The scatter of data at this condition reflects slight performance variation for difference geometries. A cross plot of Figure 3-24 for the 300-second test runs is shown in Figure 3-25. It was found that the percentage increase in efficiency for a given increase in pressure was considerably greater at the 10,500 Btu/Lb enthalpy difference level than at the 16,000 Btu/Lb level. The increase in indicated material effectiveness resulting from a change in pressure from 0.005 to 0.020 atmospheres at the constant lower enthalpy was 1700 Btu per pound of ablative material. The corresponding value at higher enthalpy was 700 Btu per pound.

The test series has shown that the net efficiency dependence upon pressure is greater at the lower enthalpy levels in the direction of increased effectiveness with increased pressure at a constant total enthalpy. Data scatter did not permit a meaningful determination of the transpiration cooling parameter; however, it can be inferred from the slope of the constant pressure lines shown in Figure 3-25, decreasing with increasing pressure, that the transpiration cooling factor increases with decreasing pressure for the stagnation pressure levels tested.

SERIES E-EFFECTS OF STREAM ENERGY

PURPOSE. An evaluation of the material performance response to varying total enthalpy at constant heat flux was conducted to obtain a measure of the energy transferred within the boundary layer and also to determine the effects at the debris surface under these conditions.

TEST CONDITIONS. An air arc test series was designed to give a total enthalpy range of 2500 Btu/Lb_m to 17,500 Btu/Lb_m with heating rates in the range of 50 to 300 Btu/Ft^2-Sec. (Table 3-6). Four heating rates were obtained at each of three enthalpy levels.

TEST MODELS. Hemisphere-cylinder models of both two inch and 1-1/4 inch diameter were used in this test series.

DISCUSSION OF RESULTS. The results are presented in Figure 3-26 in terms of net efficiency. Net efficiency is defined as the difference between the hot wall calorimeter flux and the reradiation flux divided by the average mass loss rate. An approximation of the transpiration cooling factor was taken as the slope of the constant heat flux curves and found to be 0.80 for the enthalpy differences between 8600 Btu/Lb and 16,200 Btu/Lb_m for models having a 5/8-inch nose radius. A more accurate evaluation of the transpiration cooling factor is given in Analytical Evaluation of Ablation Parameters.

Model Type	Stagnation Pressure (Atm)	Stagnation Heat Flux (Btu/Ft^2)	Desired Sidewall (Btu/Ft^2 Sec)	Stagnation Enthalpy (Btu/Lb)
2 In. hc (M)	.03	50	4-6	2,500
2 In. hc	.015	50	4-6	3,500
2 In. hc	.007	50	4-6	5,000
2 In. hc	.03	110	8.8-12.8	5,000
2 In. hc	.007	110	8.8-12.8	10,000
2 In. hc	.003	110	8.8-12.8	15,000
2 In. hc	.06	170	13.6-19.2	5,000
2 In. hc	.016	170	13.6-19.2	10,000
2 In. hc	.005	170	13.6-19.2	17,500
1-1/4 In. hc	.03	300	24-36	10,000
1-1/4 In. hc	.024	300	24-36	12,000
1-1/4 In. hc	.01	300	24-36	17,500

Table 3-6. Test Matrix - Variation of Enthalpy and Pressure With Constant Heat Flux

The data was correlated for constant exposure time to compensate for transient response due to model nose shape change. Test data from other series was used to complement the data of the present series. Considerable data scatter existed because of ablation performance dependency on initial model shape. The best correlation was obtained from the 300 Btu/Ft^2-Sec heat flux level at the exposure time of 300 seconds. These models were all the same initial nose radius.

The two distinct types of ablation performance were observed here as for the other test series; these characterized by the strongly oxidized and the relatively inert debris layer. Similar to results of the transient ablation series, material performance at total enthalpies of 5000 Btu/Lb$_m$ and below, was found somewhat independent of boundary layer enthalpy difference. The thick debris layer obtained at these enthalpy levels and the absence of significant oxidation reaction levels permitted most of the incident heat flux to be reradiated.

A plot of surface temperature versus total enthalpy for constant heat flux is given in Figure 3-27. The best correlation in the debris oxidation regime here also was achieved with the 300 Btu/Ft^2-Sec cold wall calorimeter flux cases for an exposure time of 300 seconds. Surface temperature remained constant as the total enthalpy was increased from 10,000 to 12,000 Btu/Lb, but further increase in total enthalpy to 17,500 Btu/Lb gave reduced surface temperatures. A stagnation pressure reduction accompanied the increase in total enthalpy for a constant heat flux. The reduction in surface temperature implies that the oxygen reactions are moving away from the debris surface into the fluid boundary layer and debris volatilization is preceding oxidation at the lower pressure.

The surface temperature variation with total enthalpy at constant stagnation pressure is given in Figures 3-28 and 3-29. It was observed that an 800°R to 1000°R temperature increase occurred between the 5000 Btu/Lb$_m$ and 10,000 Btu/Lb$_m$ total enthalpy levels. The initiation of debris combustion is dependent upon stream total enthalpy as well as heat flux for the range of pressures tested. Two test runs, models N-30 and N-46, compared at the same calorimeter heat flux (163 Btu/Ft^2-Sec) gave surface temperatures of 3560°R and 4000°R at 5000 Btu/Lb$_m$ and 10,000 Btu/Lb$_m$ total enthalpy levels. The surface temperature difference was attributed to increased exothermic effects at 10,000 Btu/Lb$_m$ total enthalpy, even though the pressure for N-46 was only one-tenth that of N-30. The heat flux for run N-30 was sufficient to cause

debris combustion at the 5000 Btu/Lb enthalpy level as indicated by the smaller debris thickness than that for lower heat flux at the same total enthalpy, and also as indicated by the disappearance of the glassy surface. A comparison of runs N-30 and N-46 on a net efficiency basis (Figure 3-26) showed the efficiency of N-30 to be considerably higher than that of N-46.

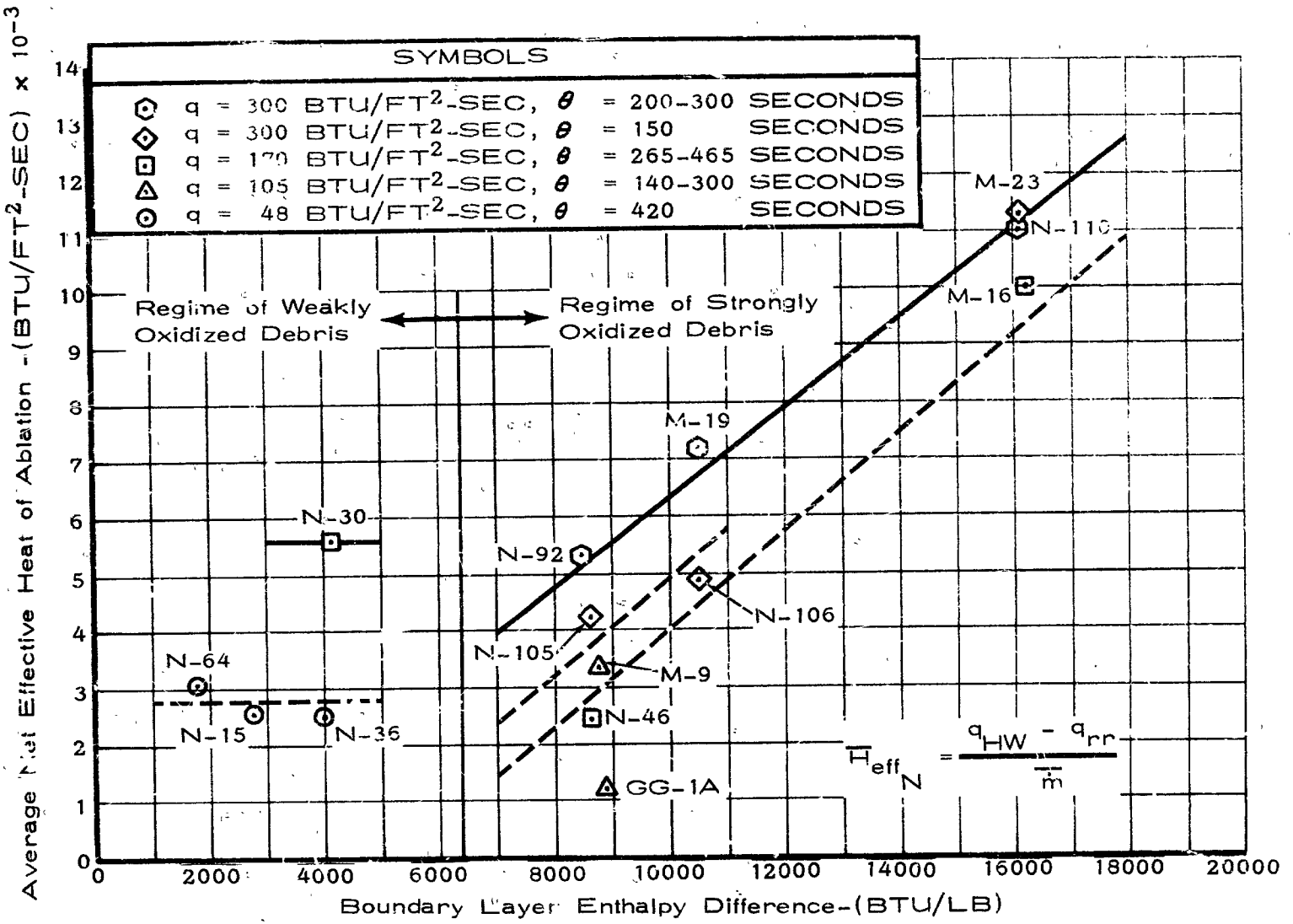


Figure 3-26. Variation of Average Net Effective Heat of Ablation With Boundary Layer Enthalpy Difference At Constant Heat Flux

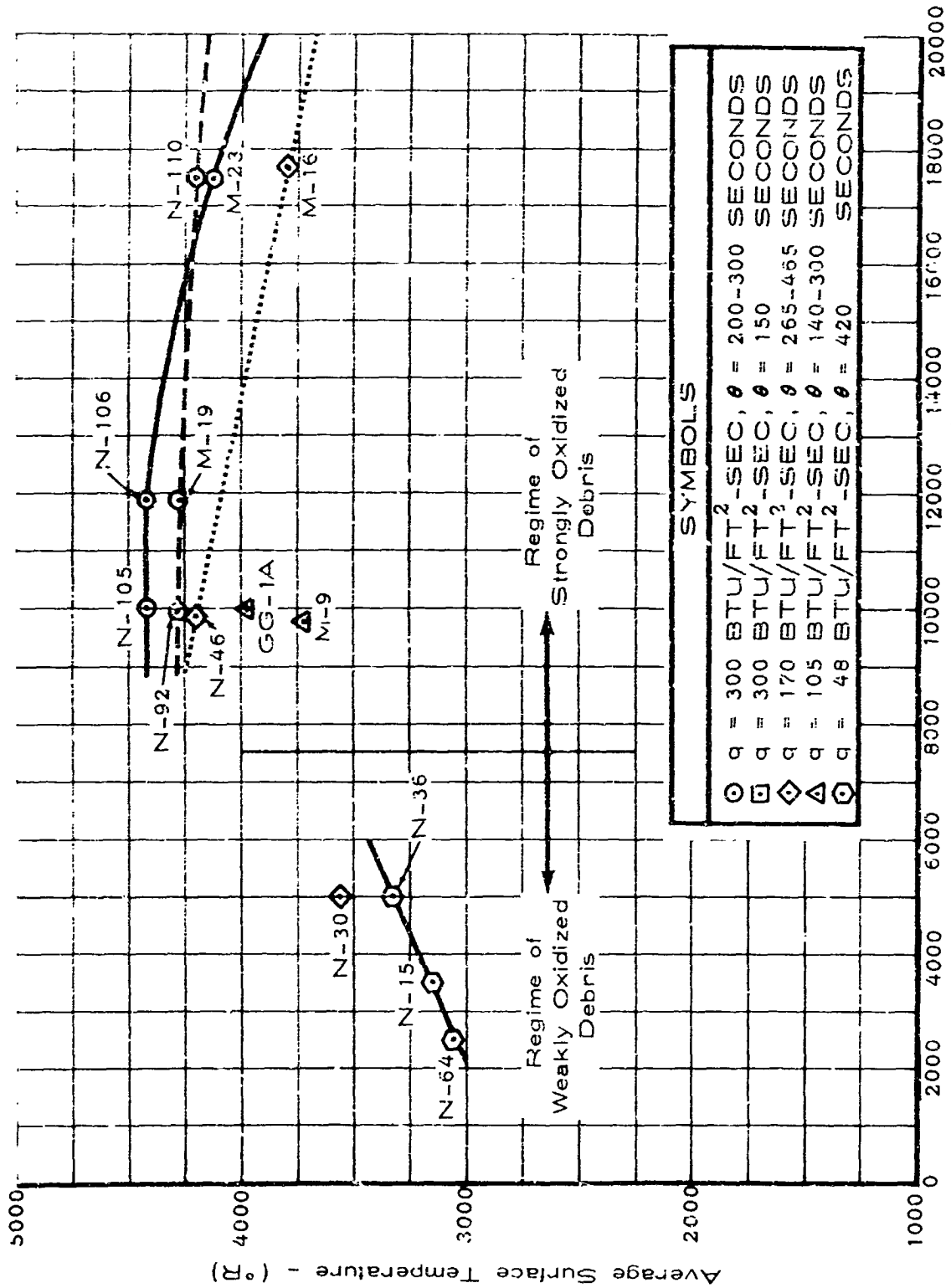


Figure 3-27. Variation of Average Surface Temperature with Total Enthalpy for Constant Heat Flux.

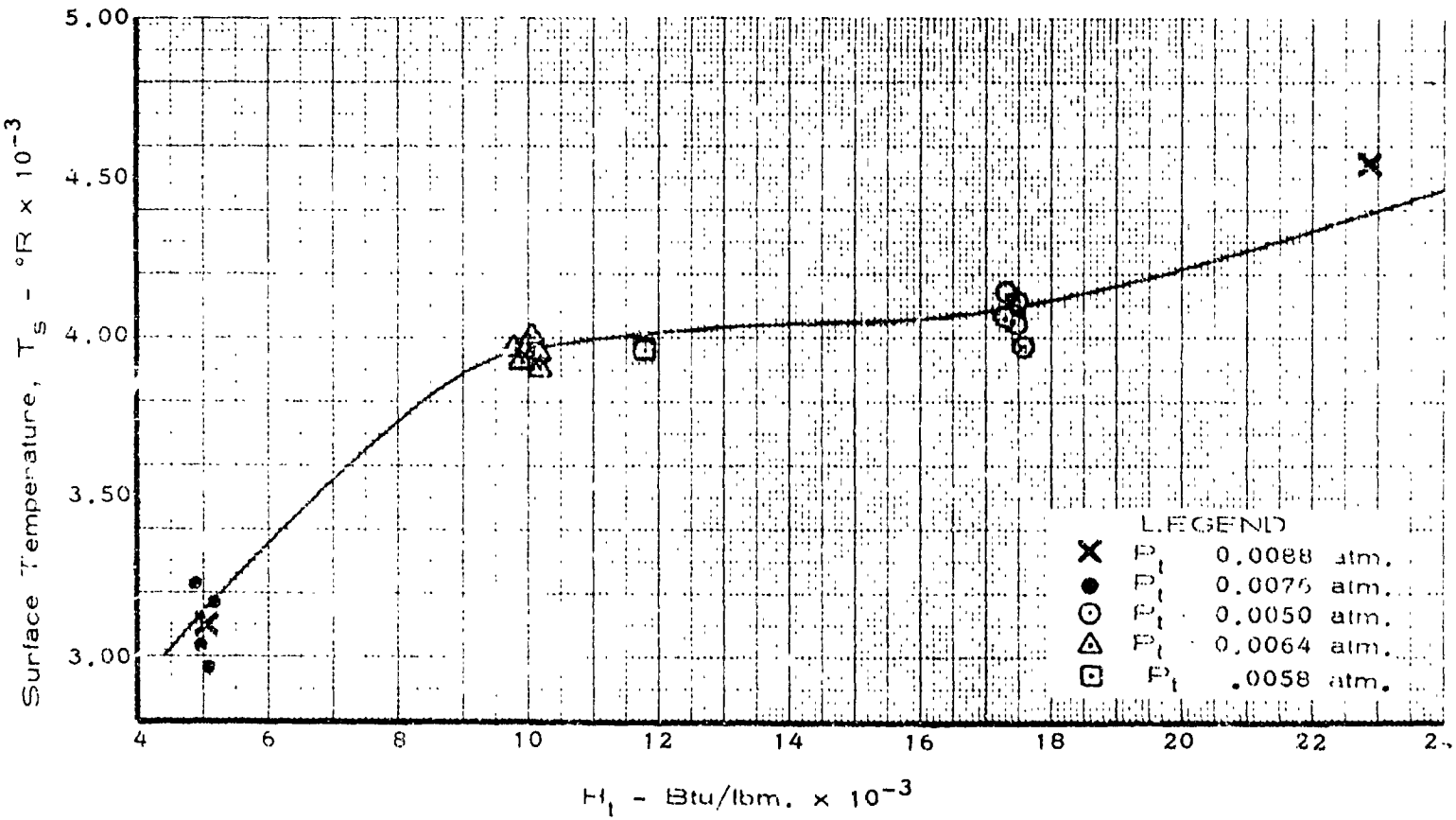


Figure 3-28. Surface Temperature as a Function of Stagnation Enthalpy for Constant Pressure p_t = .0065 atm.

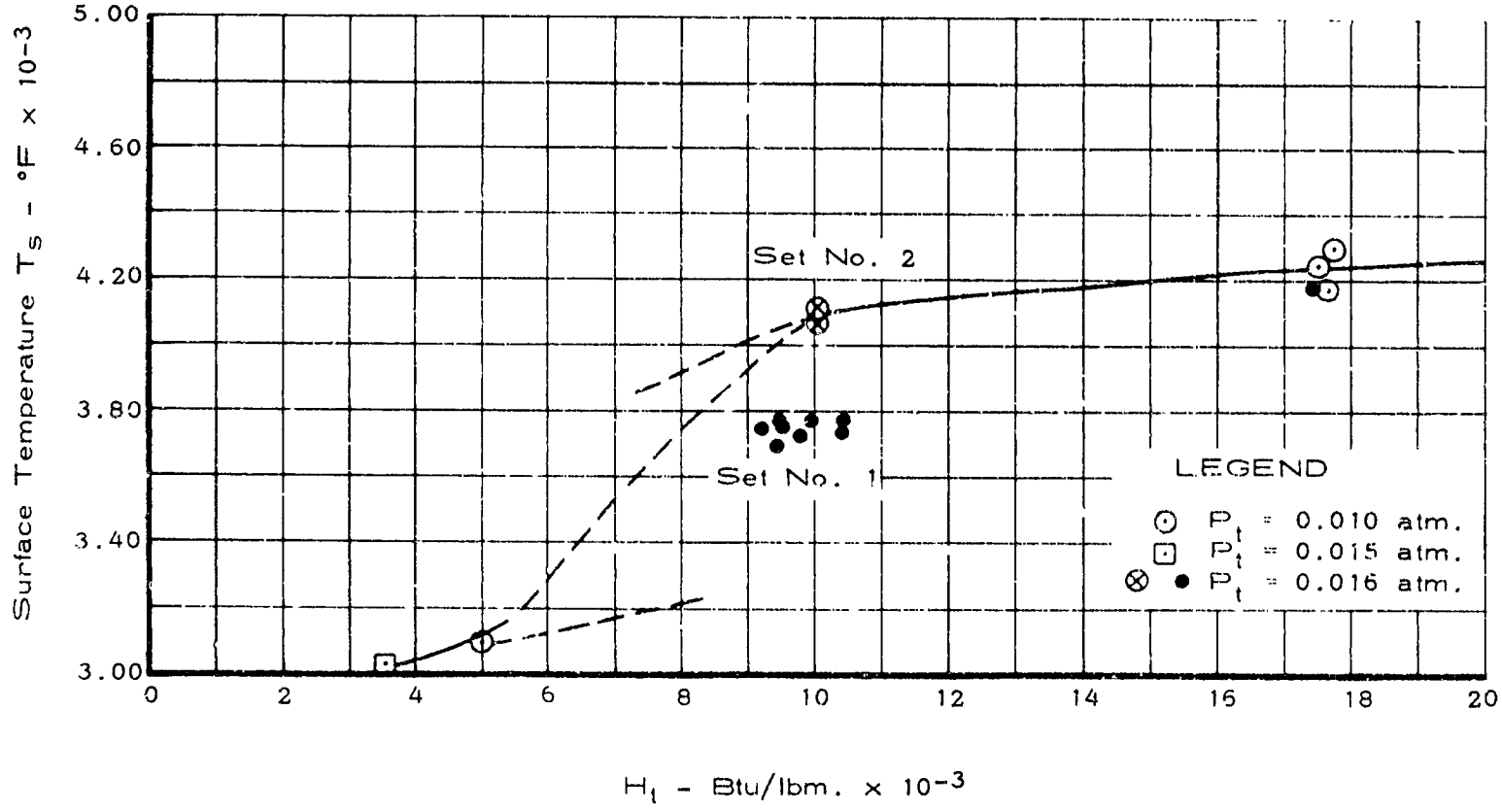


Figure 3-29. Surface Temperature as a Function of Stagnation Enthalpy for Constant Pressure, $P_t \approx .014$ atm.

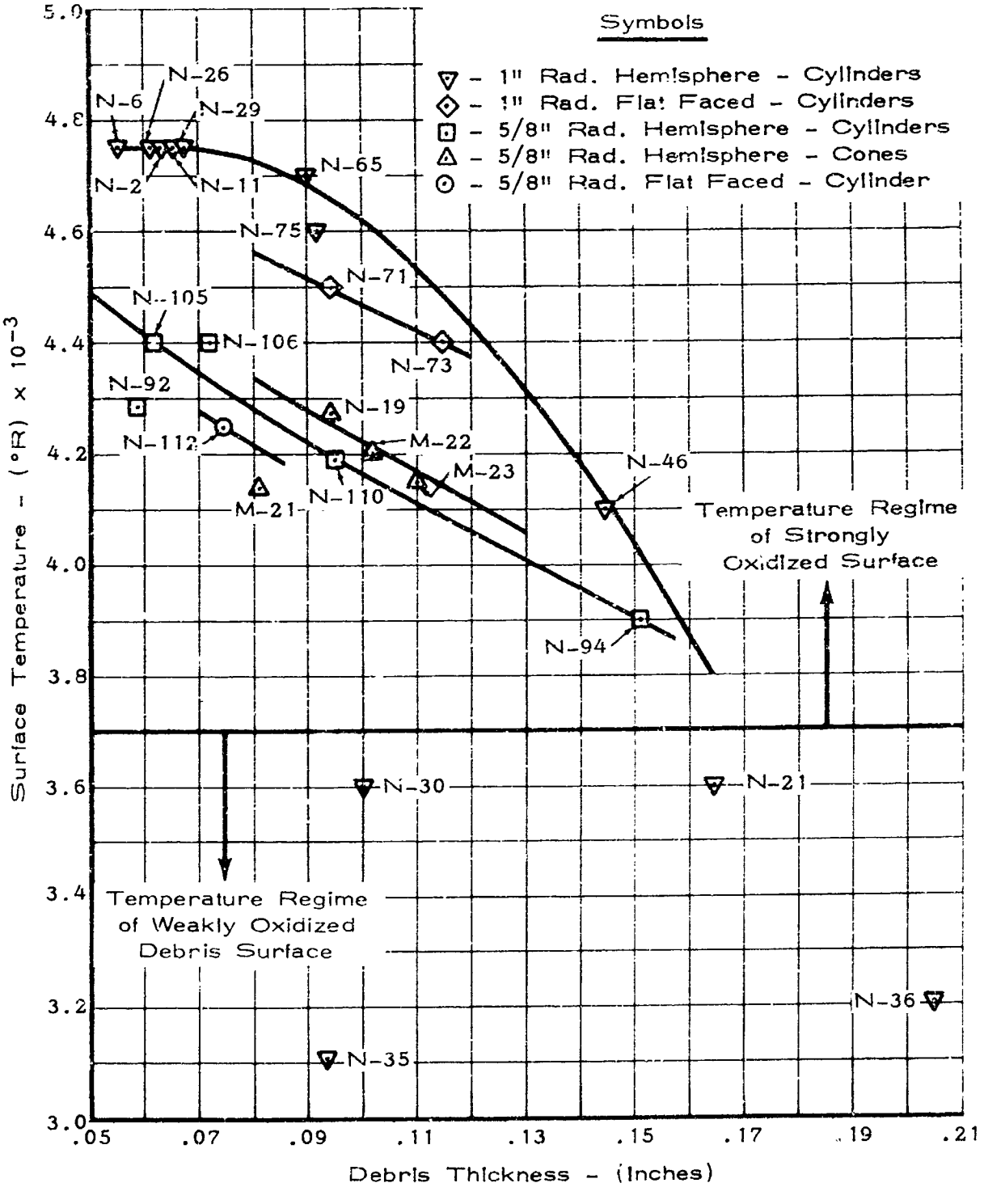


Figure 3-30. Effect of Model Configuration on Stagnation Point Debris Thickness

SERIES 6-EFFECTS OF GAPS AND DISCONTINUITIES

PURPOSE. A test series was performed to determine the effect of various gap widths and depths in the "THERMO-LAG" T-500 heat shield on the temperature attained by the unprotected areas of substrate material during air arc flight simulation. The heat shield thickness and gap dimensions selected are considered proportionately representative of heat shield discontinuities which may be expected at joints, windows, and access hatches of a typical spacecraft heat shield design.

TEST CONDITIONS. Test conditions were established according to the test matrix shown in Table 3-7.

TEST MODELS. Figure 3-31 shows the layout of the two dimensional test model used in this test series. The model was designed to hold two ablative material gap specimens with one aligned parallel to the flow stream and one normal to the flow axis. Gap dimensions and orientation with respect to the flow axis are shown in Table 3-8. Each specimen was instrumented with three thermocouples located identically with respect to the gap location as illustrated in Figure 3-33.

The model cooling system was designed to remove about 200 Btu/ft^2-sec. at the stagnation line. A schematic diagram of the cooling system is shown in Figure 3-32. The cooling water flows through a divergent diffuser which serves to stabilize the downstream flow. From the diffuser, the coolant flows into the cylindrical leading edge flow channel and then through the sidewall passage discharging into the outlet piping through a convergent diffuser.

The results of the material gap tests are presented in Figure 3-34 where the ratios of substrate temperature beneath the gap in degrees F. to the substrate temperature at a position 0.125 inches from the gap center line are shown with respect to the ratio of gap width to gap height for the two gap orientations (Thermal Protection Loss Index). The results indicate that the gaps oriented parallel to the flow axis did not cause an increase in substrate temperature at the gap location. An effect was noted where gap orientation was normal to the flow axis. The higher thermal protection loss indices in the latter case are attributed to higher mass flow exchange as indicated by recent investigations (1).

For gaps normal to the flow axis, Figure 3-34 shows an increase in thermal protection loss index to a constant value of 1.03 for increasing values of width to height ratio greater than unity. As W/H approaches unity, a transitional area is noted. For decreasing W/H less than unity, thermal protection loss indices form an envelope of values for shallow and deep gaps exposed for the same time. For the gap ratio of 0.4, the maximum thermal protection loss index occurs for the most shallow material gap which approaches a "close" cavity characterized by maximum mass discharge. The study indicates that the index of loss of thermal protection of normal oriented gaps is proportional to the "closing" of the cavity as illustrated by the results from test models B-6V, G-6-V, and K-6-V.

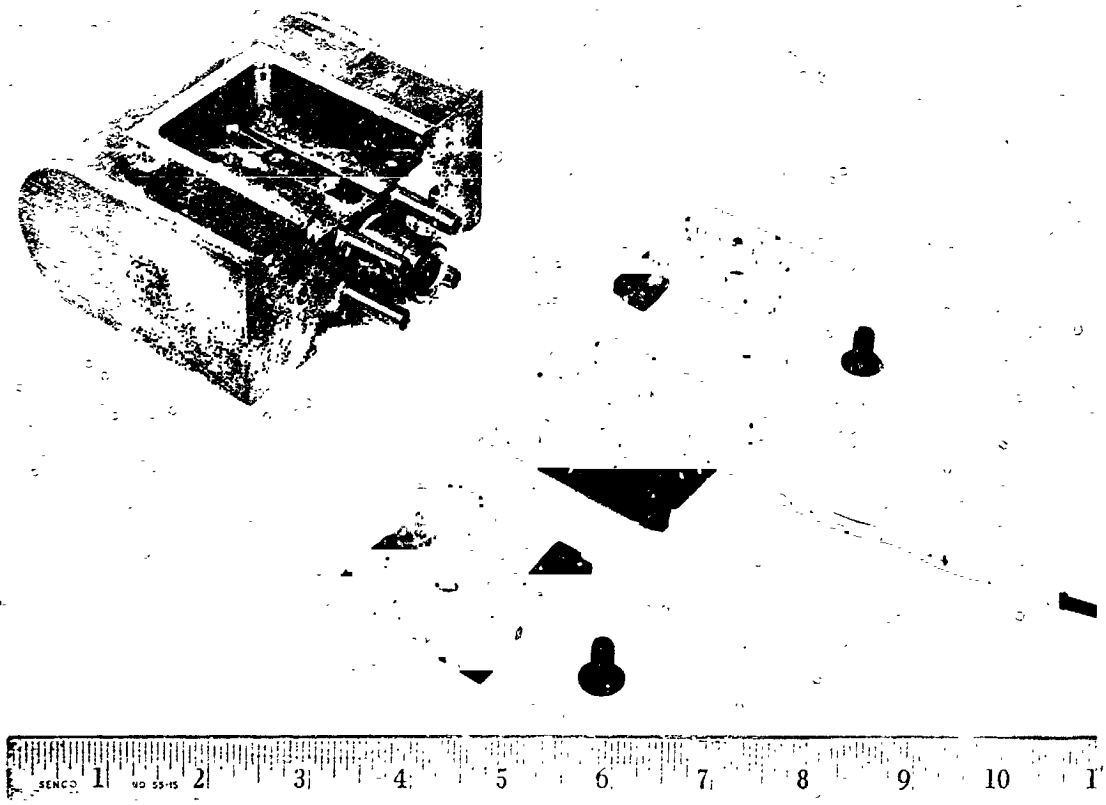


Figure 3-31. Two Dimensional Water-Cooled Test Model Showing Test Specimen in Sample Holder

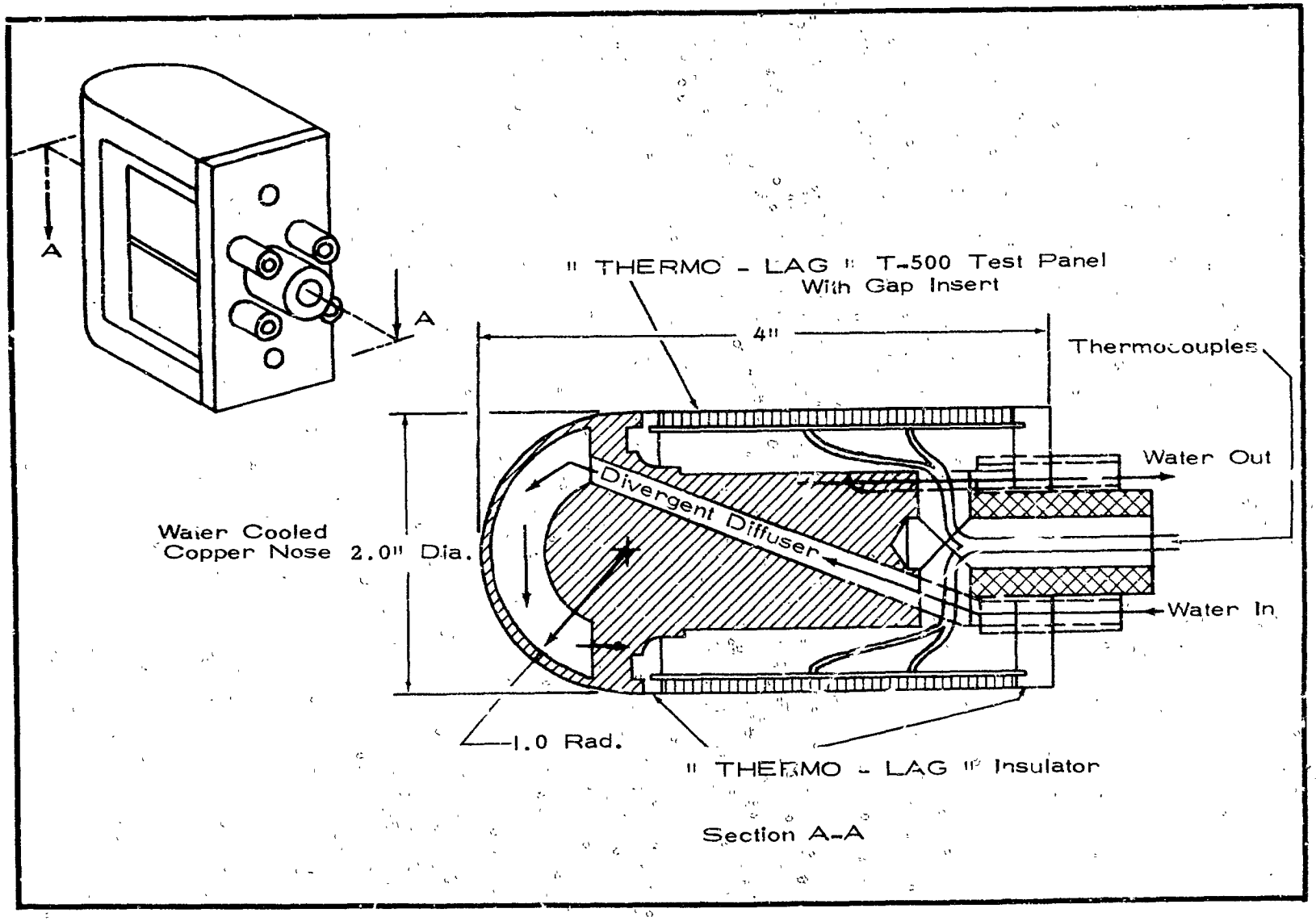


Figure 3-32 Simulated Flight Test Model, Water Cooled Copper Nose

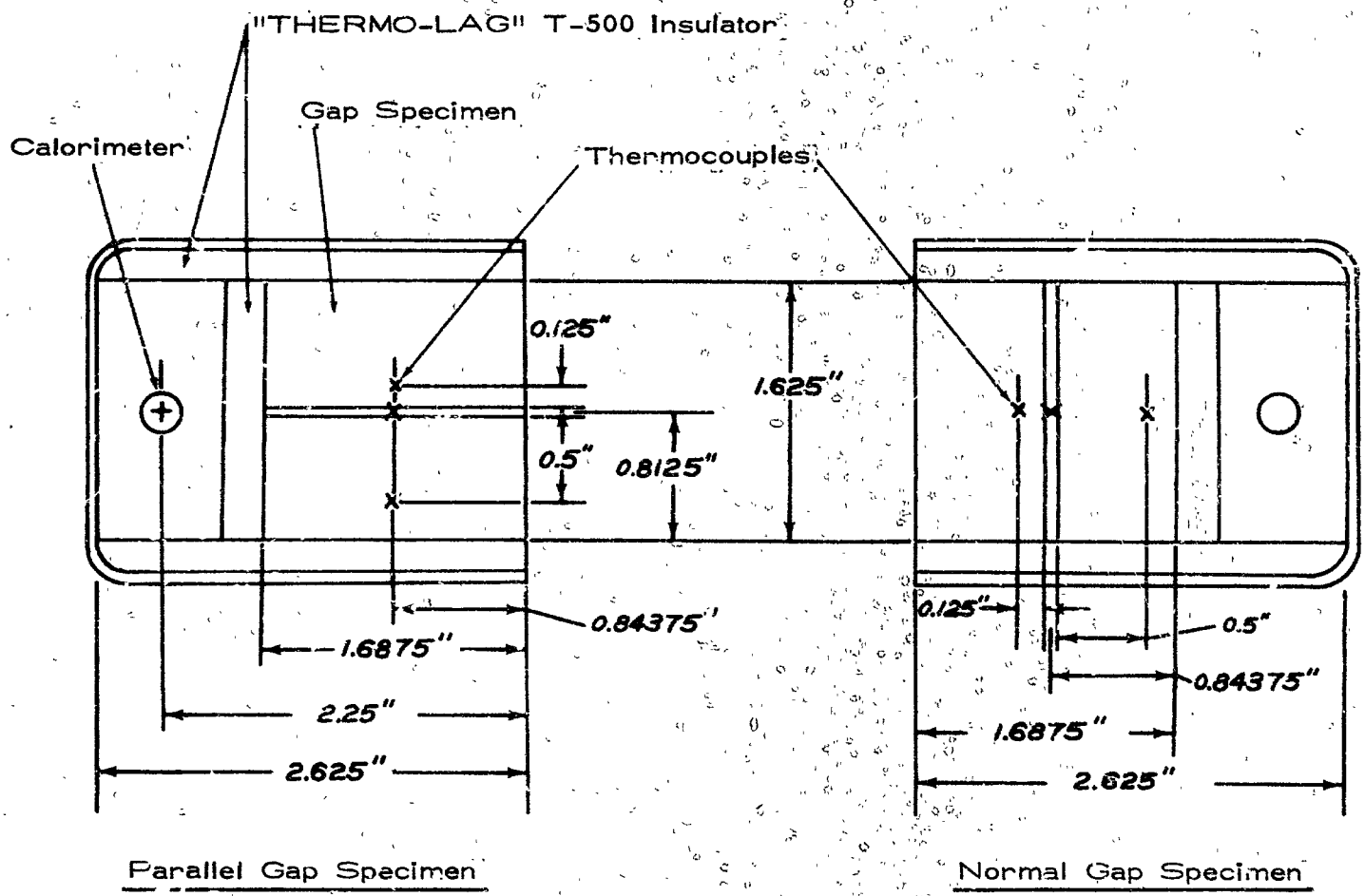


Figure 3-33. Material Gap Specimen with Holder Showing Thermocouple Locations.

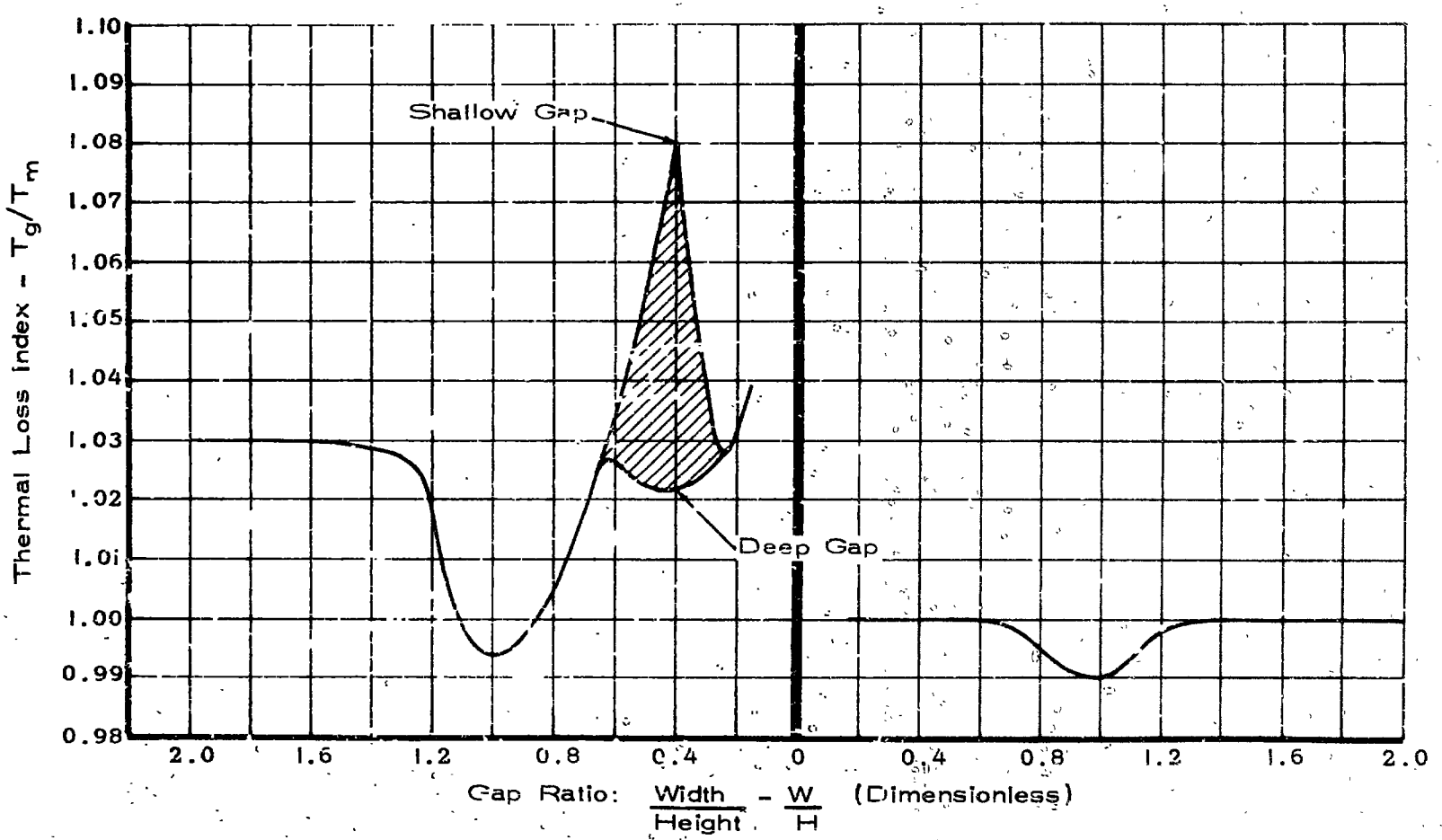


Figure 3-34. Variation of Thermal Loss Index to Gap Dimension Ratio of Width to Heighth (W/H) for Gap Orientation.

Figure 3-35. Apollo Overshoot Design Trajectory.

Model No.	Test Point	Stagnation Enthalpy (BTU/LB)	Model Stagnation Pressure (ATM)	Calorimeter Heat Flux (BTU/FT^2-SEC)	Oxygen (%)	Total Mass Flow (LB/SEC)	Run Time (SEC)
A-4-H, B-6-V	12	10,110	0.0063	79	21	0.00142	1800
C-6-H, D-4-V	12	9,985	0.0063	78	21	0.00142	1220
E-4-H, F-6-V	12	10,200	0.0063	79.4	21	0.00142	1800
G-6-V, H-4-H	12	10,050	0.0063	79	21	0.00142	1065
I -4-V, J-6-H	12	10,150	0.0063	79	21	0.00142	1498
K-6-V, L-4-H	12	9,950	0.0063	78.6	21	0.00142	1800
M-4-H, N-6-V	12	9,900	0.0063	79.4	21	0.00142	1800
O-6-H, P-4-V	12	10,085	0.0063	79.	21	0.00142	1290
Q-4-H, R-6-V	12	10,110	0.0063	79.	21	0.00142	679
3 4, 2-4	25	17,480	0.0189	233.	21	0.00350	583
1-4, 4-4	25	17,480	0.0189	233.	21	0.00350	1498

Table 3-7. Material Gap Test Matrix

Model No.	Test Point	Gap Depth	Gap Width	Gap Orientation	Material	Slug Dia.	Slug Weight
A-4-H	12	.05	.02	Parallel	-4	.251	.4716
B-6-V		.05	.02	Normal	-6	.250	.4701
C-6-H	12	.08	.02	Parallel	-6	.252	.5146
D-4-V		.08	.02	Normal	-4	.252	.4887
E-4-H	12	.125	.02	Parallel	-4	.253	.4826
F-6-V		.125	.02	Normal	-6	.251	.5028
G-6-V	12	.05	.05	Normal	-6	.2525	.5038
H-4-H		.05	.05	Parallel	-4	.2505	.5029
I-4-V	12	.08	.05	Normal	-4	.251	.4910
J-6-H		.08	.05	Parallel	-6	.251	.5059
K-6-V	12	.125	.05	Normal	-6	.254	.503
L-4-H		.125	.05	Parallel	-4	.254	.5021
M-4-H	12	.05	.10	Parallel	-4	.252	.4934
N-6-V		.05	.10	Normal	-6	.254	.5081
O-6-H	12	.08	.10	Parallel	-6	.253	.4936
P-4-V		.08	.10	Normal	-4	.253	.5063
Q-4-H	12	.125	.10	Parallel	-4	.2515	.4975
R-6-V		.125	.10	Normal	-6	.251	.5052
NASA 2-4	25	.05	.10	Parallel	-4	.255	.5053
NASA 3-4	25	.125	.10	Parallel	-4	.254	.5040
NASA 1-4	25	.05	.02	Parallel	-4	.255	.5053
NASA 4-4	25	.125	.02	Parallel	-4	.2535	.5046

Table 3-8. Material Gap Test Model Data

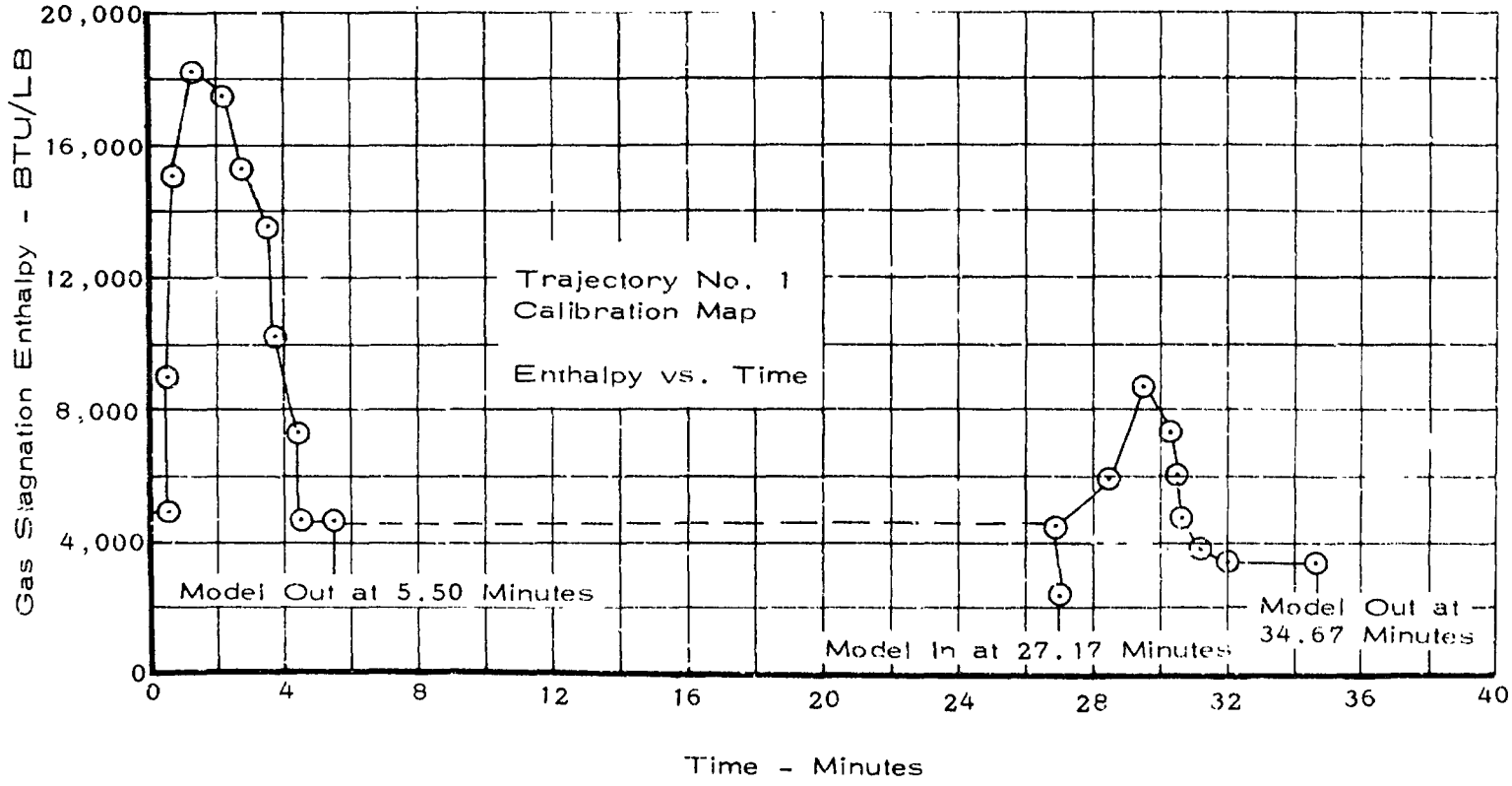


Figure 3-36. Variation of Enthalpy with Time for Overshoot Trajectory Simulation Test

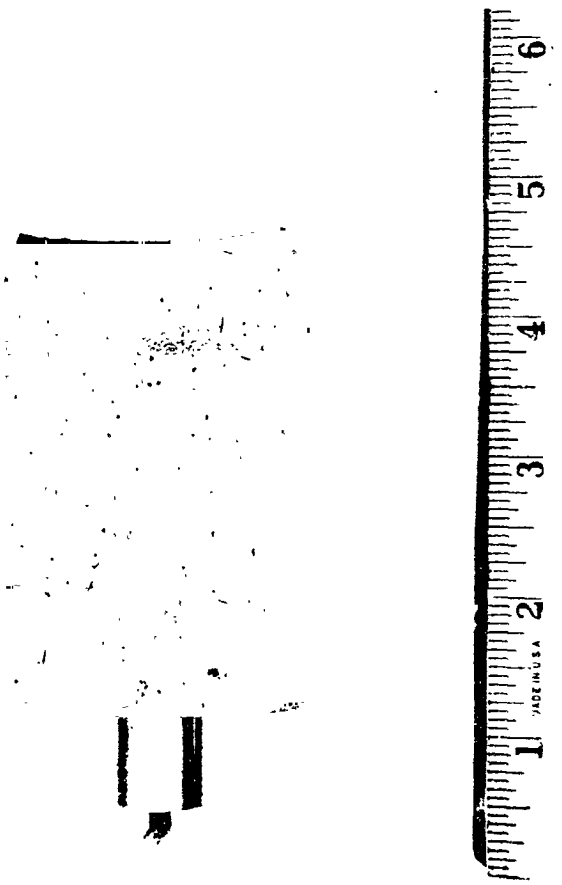


Figure 3-37. Post Test Photograph of Trajectory Simulation Model N-57

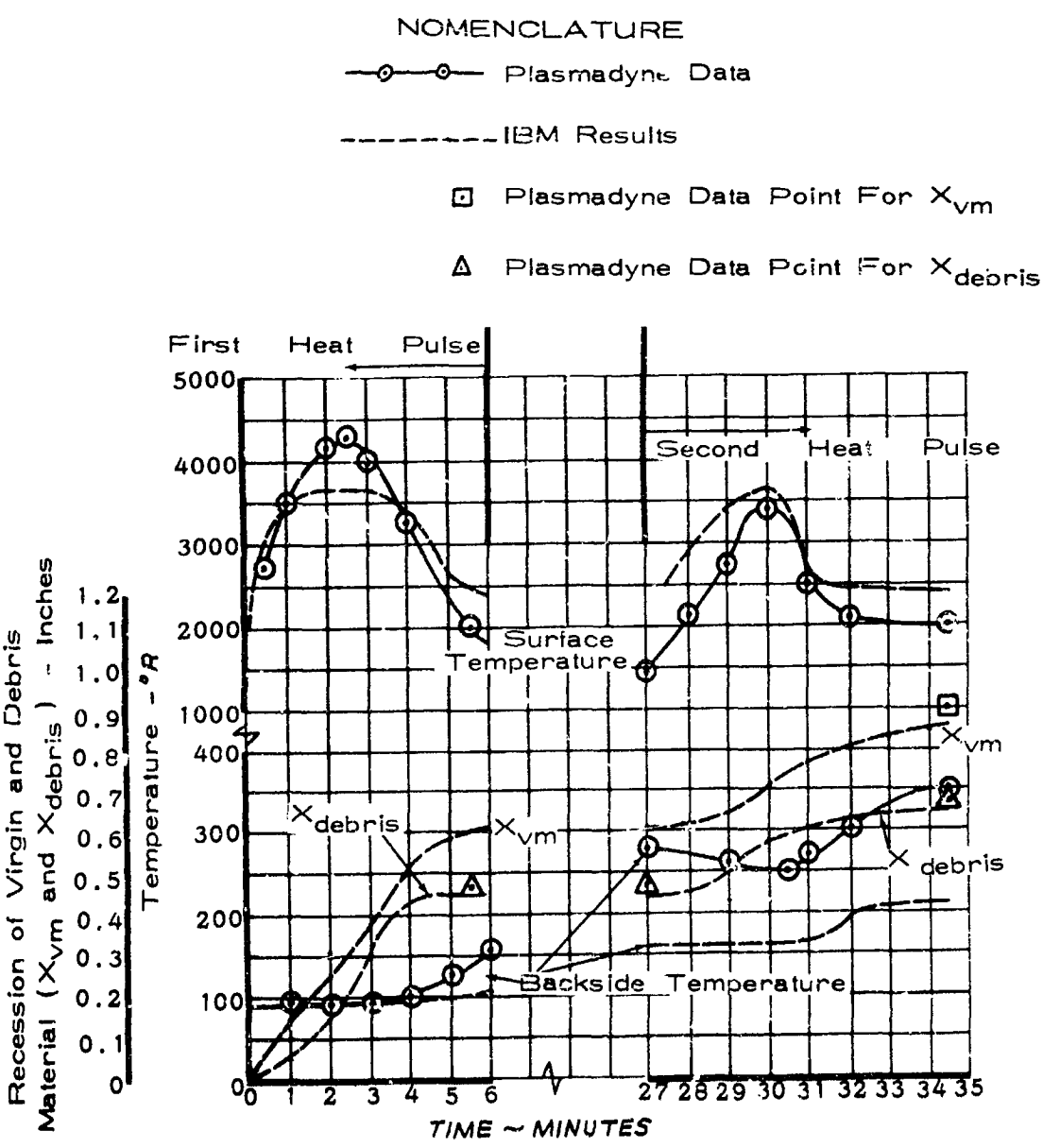


Figure 3-38. Comparison of Ablation Phase Results -Trajectory Simulation

SERIES 7-EFFECTS OF VACUUM EXPOSURE

PURPOSE. Tests were conducted to assess the effect of vacuum exposure on the ablation performance of "THERMO-LAG" T-500.

TEST CONDITIONS. Two hemisphere-cylinder models were exposed to the air-arc plasma jet test conditions given in Table 3-9.

Enthalpy	10,000 Btu/Lbm
Pressure	0.017 Atm
Heat Flux	
Stagnation	100 Btu/Ft^2-Sec
Sidewall	30 Btu/Ft^2-Sec
Test Duration	300 Seconds

Table 3-9. Air-Arc Plasma Jet Test Conditions

TEST MODELS. Two hemisphere cylinder models N-13 and N-41, were tested. Prior to air arc testing, Model N-13 was exposed to a pressure of 10^{-4} Torr for 100 hours. The model surface temperature was controlled at 250°F. for the entire period. Figure 3-41 shows Model N-13 after vacuum exposure. Model N-41, identical in construction to Model N-13, was held at normal atmospheric temperature and pressure for the pre-test period.

DISCUSSION OF RESULTS

The two models were sequentially exposed to the test conditions given in Table 3-9. The temperature-time histories of the models tested are presented in Figure 3-39. The transient ablation histories of the two models are presented in Figure 3-40. The

post-test photograph of Model N-13 is presented in Figure 3-42, while that of Model N-41 is presented in Figure 3-43.

Comparison of the test measurements and corresponding post-test photographs indicates no appreciable difference in performance attributable to vacuum exposure for the simulated flight conditions. More test comparisons at these and other test conditions would be required to adequately support any general conclusion regarding the effects of vacuum exposure on material performance.

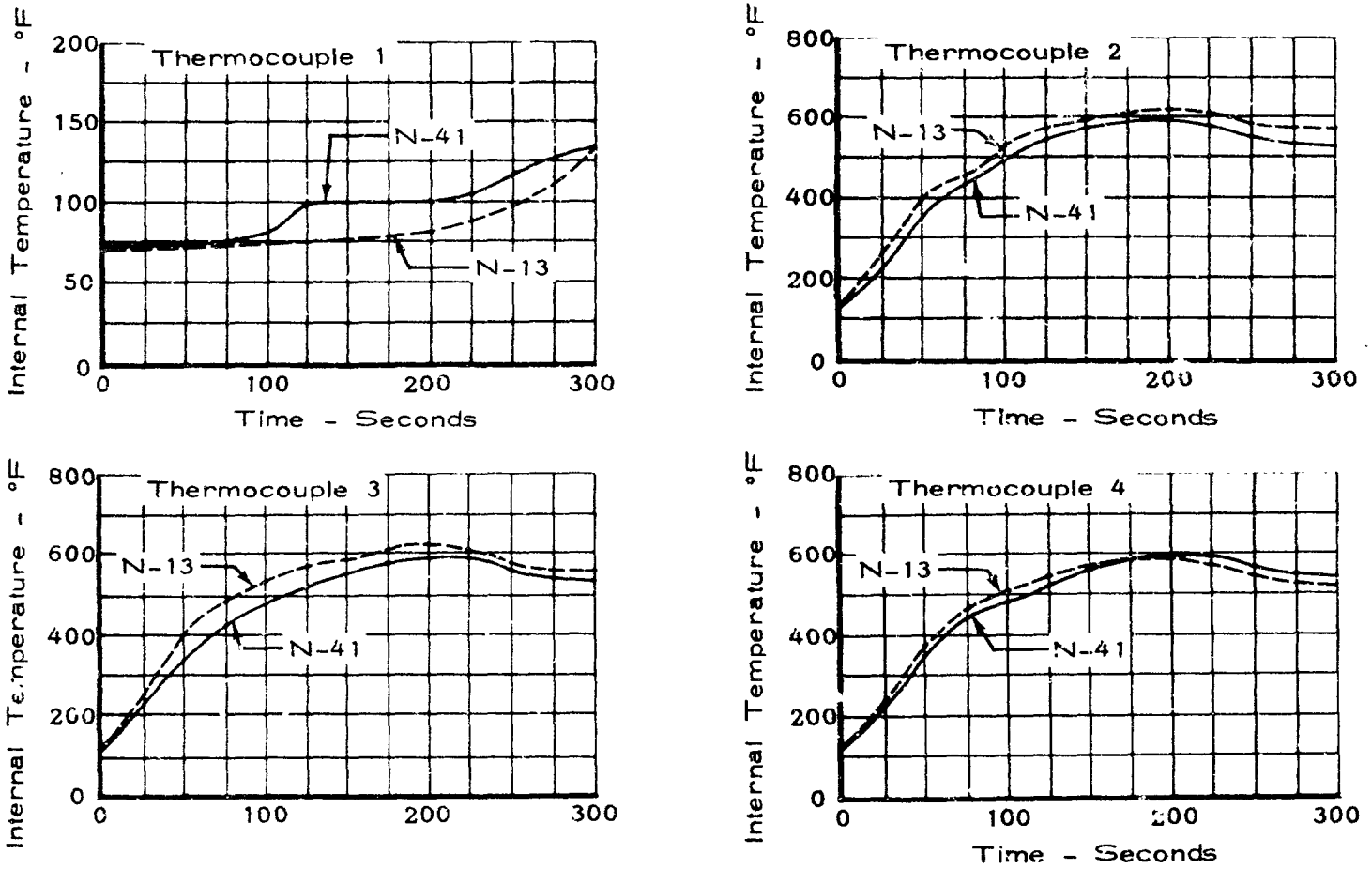


Figure 3-39. Temperature - Time Histories of Thermocouples 1, 2, 3, and 4

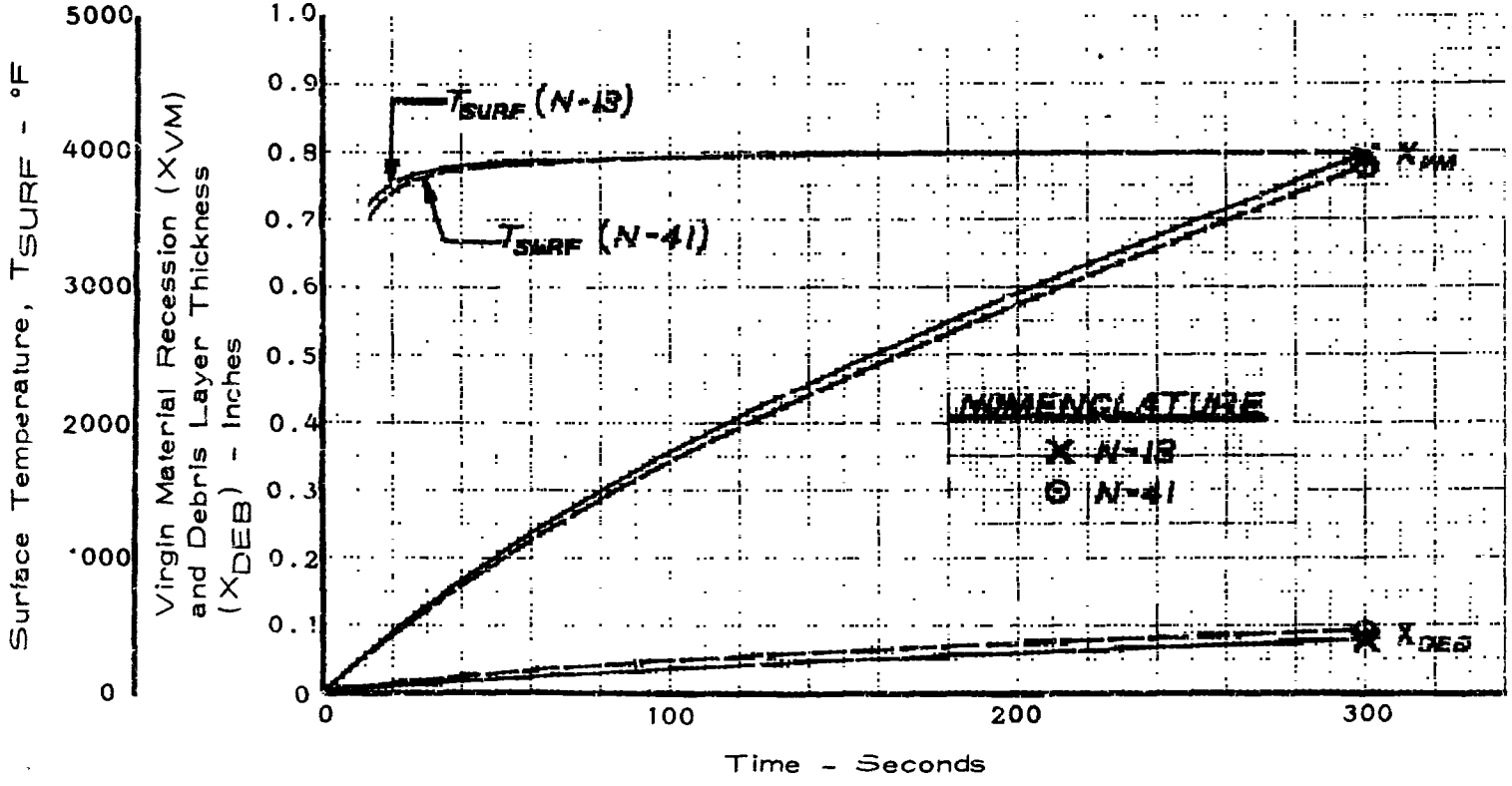


Figure 3-40. Transient Histories of "THERMO-LAG" T-500 Models N-13 and N-41

SERIES 8-TRAJECTORY SIMULATION

PURPOSE. Tests were performed to determine the performance of "THERMO-LAG" T-500 during and following sequential exposure to environment conditions of heat flux, enthalpy, and flow stream so varied as functions of time as to simulate, within the limitations of the test apparatus, an overshoot entry trajectory of an advanced manned spacecraft. The tests had as a further objective the establishment of a correlation between test model performance and the performance predictions of the numerical ablation program.

TEST CONDITIONS. The overshoot trajectory used as a pattern for the simulation tests is shown in Figure 3-35 in terms of velocity, stagnation heating rate, and altitude versus elapsed time. Figure 3-36 presents a calibration map for the simulation test points in terms of stagnation enthalpy versus time.

TEST MODELS. A two-inch diameter hemisphere-cylinder, Model No. N-57 was used for the trajectory simulation test run evaluated in the following paragraphs. A photograph of the model after test is shown in Figure 3-37. A second run was made using a water cooled copper leading edge model designed for the gap test series in an effort to eliminate the effect on afterbody heating of model configuration change during exposure. Attempts to correlate data from this test run were unavailing presumably because of the obscuring effects of the cooled leading edge.

DISCUSSION OF RESULTS. Figure 3-38 shows the correspondence between the thermal performance of the T-500 material indicated by the trajectory simulation test and performance data as predicted by the computer program. A comparison of recession results shows a deviation of five percent or less. With regard to the comparison of model surface temperature results, a deviation of approximately 10 percent is evident during the first heating pulse. This deviation may be partially attributed to the use of optical means of measuring the surface temperature of the test model during exposure in that an accuracy of plus or minus 10 percent is expected from an optical pyrometer.

The surface temperature data for the second heat pulse indicates an approximate deviation of 10 to 30 percent. This deviation can be partially attributed to the expected accuracy of optical measurement and to the unknown tunnel flow conditions existing during the radiation cooling period between heat pulses. In the IEM computations, it is assumed that the surrounding temperature remains

at 600° R, and that no convective cooling or heating occurs other than cooling by surface radiation.

Backside temperature data for the first heating pulse shows a maximum deviation of approximately 50 percent at the end of the period, with the deviation increasing with time. For the second heat pulse, a maximum, essentially constant deviation of approximately 100 percent is indicated. The differences in backside temperature rise are attributed principally to the effects of three dimensional heating occurring in the experimental facility; whereas, the computer program is based on a one-dimensional analysis. An analysis has shown that the temperature of a body exposed to three-dimensional heating responds more rapidly to environmental changes, by a factor of several magnitudes, than one affected by one-dimensional heating.

SERIES 9-EFFECTS OF UPSTREAM MASS INJECTION

PURPOSE. The purpose of these tests was to obtain and evaluate experimental data on the effect of stagnation region ablation and mass injection upon afterbody heat transfer and the ablation of "THERMO-LAG" T-500.

THEORETICAL DEVELOPMENT. To determine the upstream mass injection effect on downstream heat transfer for "THERMO-LAG" T-500, analytical expressions were used to derive correlation parameters by which to interpret experimental data (Reference 2). The method presents results in terms of similarity parameters for a given type of body configuration.

It can be assumed that the inviscid flow for two geometrically similar bodies expressed in terms of stagnation conditions, Pse, ρse, H_{se}, by means of the variables:

$$\bar{\rho} = \frac{\rho_e}{\rho_{se}}$$

$$\bar{u} = \frac{u_e}{u_{se}}$$

$$\mu = \frac{\mu_e}{\mu_{se}}$$

are identical functions of x/r_0 . These relations are satisfied when the boundaries of the specific heat ratios are $1.2 < \gamma < 1.4$, and if the pressure distribution is the same for the two bodies, $p = \rho e / \rho se$. It can also be assumed that the boundary conditions expressed in terms of modified stream functions at the wall $\bar{H}_c$, and $\bar{x}_w$ are identical in the two streams. This indicates that the velocity profiles of the two systems at various distances from the leading edges are similar. These assumptions permit the coolant mass flows to be related by the expression:

$$\left[\frac{\dot{m}_c}{r_0 \mu_{se}\sqrt{Re_N}}\right]_I = \left[\frac{\dot{m}_c}{r_0 \mu_{se}\sqrt{Re_N}}\right]_{II}$$

The only difference in the expression for laminar heat transfer between two bodies is the velocity gradients du/dx, and the characteristic parameter representing heat transfer $Nu/\sqrt{Re_N}$. As the velocity gradients were assumed to be similar for the case considered, the heat transfer on the impermeable surface will be related in the two

systems by:

$$\left[\frac{Nu_N}{\sqrt{Re_N}}\right]_I = \left[\frac{Nu_N}{\sqrt{Re_N}}\right]$$

The similarity parameters are expressed as:

$$N_1 = \frac{\dot{m}_c}{r_0 \mu_{se} \sqrt{Re_N}}$$

for the mass injection rate,

$$N_2 = \frac{Nu_N}{\sqrt{Re_N}}$$

for the heat transfer,

$$\bar{H}_c \text{ and } \bar{\psi}_w$$

and for the flow stream, so that:

$$N_2 = N_2 (N_1, \bar{H}_c, \bar{\psi}_w)$$

The sensitivity of the heat transfer on the aft body in terms of N_2 to the parameter ψ_w may not be significant if ψ_w is below a certain value. This is analogous to the wall-to-stagnation temperature ratio being less than approximately 0.4.

These mass injection similarity parameters were derived for a model with mass injection occurring at the stagnation region of a non-ablating body and an impermeable aft body surface. Such a model is little different from the represented case of a downstream surface with negligible mass flow as compared to that evaluated over the stagnation region of an ablating body.

CONDITIONS. The mass injection tests were performed for the test matrix given in Table 3-10. Two design aspects of the matrix are:

1. Test condition at which flight simulation was performed.
2. Types of models tested.

The selected test conditions were dictated by the design trajectory considered for manned spacecraft, entry. Heating rates and enthalpy values were used which characterize the materials mechanism. At low heat flux-enthalpy conditions, a chemically and physically stable debris layer forms. At moderate to high

high heat flux-enthalpy conditions, oxidation at the debris layer takes place.

TEST MODELS. Model types were selected which would provide a comparison of heat transfer and ablation of aft body surface with and without stagnation ablation. The models tested also provide an indication of cold wall heat flux versus hot wall heat flux.

Model geometry selection was based on minimization of adverse pressure effects at the test section. The location of thermocouples along the test section provide for uniform heat transfer distribution without mass injection.

The test was designed to provide backside temperature history, ablation panel surface temperature, and stagnation line recession data, to enable calculation of the mass injection similarity parameters. Complementary data used in the study was obtained from the gap test series and the three-dimensional models tested at test points 6, 12, and 24.

The models used in the mass injection tests were two-dimensional, with cylindrical leading edges of 1 inch radius, 4 inches wide. The overall length of each model was 4 inches. Three types of models were made for the tests. The models tested for the cold wall heat flux case were made of copper with a water-cooled leading edge. The models tested for the hot wall heat flux case were made of a high temperature capability graphite. The third type of model tested was made of "THERMO-LAG" T-500 material.

For the heat transfer phase of the test program, models of each design were instrumented with three identically designed calorimeter slugs to record the temperature responses. Cooper calorimeter slugs and base plates were used with the copper water-cooled models. Graphite calorimeter slugs and base plates were used with both the graphite and "THERMO-LAG" T-500 models. Relative locations of the calorimeter slugs are shown in Figure 3-52.

For the mass injection tests, each designed model had 0.100 - inch thick panels of "THERMO-LAG" T-500-6 sprayed over a 0.020-inch thick PH 7 steel substrate. Test panels were instrumented with three 28-gage chromel-alumel thermocouples spot-welded to the under body of the steel substrate. For each test panel, locations of the thermocouples were identical.

The three types of models used in both the heat transfer and ablation tests were the copper leading-edge, water-cooled, graphite, and "THERMO-LAG" T-500 models illustrated in Figures 3-49 through 3-51, respectively.

DISCUSSION OF RESULTS. The mass injection experiments were performed in the Mach 3 hyperthermal plasma arc facility of Giannini Scientific Corp., Santa Ana, California. The nonreduced temperature-time histories of the models tested are presented in Figures A-90 through A-107.

Experimental results of the performed tests are presented in Table 3-11. The recorded stagnation mass injection rates were calculated from integral stagnation region recession measurements. The integrated values account for the shape change along the leading edge geometry of the models tested. The calculated calorimeter heat fluxes give good correspondence to theoretical values using modified Newtonian pressure theory, which considers the effect of leading edge bluntness (Reference 3). The measured virgin material recession data presented in Table 3-11, is also presented in Figures 3-44 through 3-46 for ease of comparing results for given test conditions.

The measured thicknesses of gap series virgin material are given in Table 3-12. The measurements were made along one edge of the test specimens in order to be free of any gap mechanism influence.

Examination of the test results indicates that upstream mass injection provides a significant reduction in downstream heat transfer and ablation for "THERMO-LAG" T-500 materials. The reduction in heat transfer can be assessed from the results given in Table 3-11. The sidewall heat transfer rates for the "THERMO-LAG" T-500 leading edge bodies were reduced 25 to 45%, from the theoretical value for zero mass injection, while those of the graphite and water-cooled models showed only a 5 to 17 percent reduction.

The reduction in downstream ablation cuased by upstream mass injection is indicated by the measured virgin material recession data presented in Table 3-12 and Figures 3-44 through 3-46 for "THERMO-LAG" T-500. Figures 3-47 and 3-48 provide a means of assessing the upstream mass injection effect. Figure 3-47 shows the theoretical heat transfer with zero mass injection for the dimensionless ratio of distance along body geometry to leading edge radius, as predicted by other investigations (Reference 2). Indicated on the theoretical curve are the locations of the thermocouple stations. Figure 3-48 presents the tests results in terms of the similarity parameters N_1 and N_2 and functional relationships thereof with respect to the theoretical value for zero mass injection. The data indicates that the region of influence in the downstream direction progressively increases as the mass flow increases. Thus, for a

Examination of the test results indicates that upstream mass injection provides a significant reduction in downstream heat transfer and ablation for "THERMO-LAG" T-500 materials. The reduction in heat transfer can be assessed from the results given in Table 3-11. The sidewall heat transfer rates for the "THERMO-LAG" leading edge bodies were reduced 25 to 45 percent from the theoretical value for zero mass injection, while those of the graphite and water-cooled models showed only a 5 to 17 percent reduction.

The reduction in downstream ablation caused by upstream mass injection is indicated by the measured virgin material recession data presented in Table 3-12 and Figures 3-44 through 3-46 for "THERMO-LAG" T-500. Figures 3-47 and 3-48 provide a means of assessing the upstream mass injection effect. Figure 3-47 shows the theoretical heat transfer with zero mass injection for the dimensionless ratio of distance along body geometry to leading edge radius, as predicted by other investigations (Reference 2). Indicated on the theoretical curve are the locations of the thermocouple stations. Figure 3-48 presents the tests results in terms of the similarity parameters N_1 and N_2 and functional relationships thereof with respect to the theoretical value for zero mass injection. The data indicates that the region of influence in the downstream direction progressively increases as the mass flow increases. Thus, for a given mass flow, corresponding for example to test point 24, with an increase in downstream stations the heat transfer decreases by a factor of about 3 to 4. At more downstream stations corresponding to larger values of $\bar{x}$ than used in the test, indications are that the variation of heat transfer with rate of injection would probably approach some constant relation well below the theoretical value.

Comparison between the "THERMO-LAG" T-500 leading edge calorimeter and ablation models indicates that mass injection from the front part of the sidewall test panel, where the value of H_c is low, has some effect on downstream ablation. This effect, however, is not readily evident for the water-cooled leading edge models.

An indication of sidewall ablation for cooled wall leading edge models can be assessed from Figures 3-44 and 3-45. Figure 3-45 presents data also for material gap test models having corresponding test durations. The trend of the gap test data obtained from test point 12 conditions is in agreement with that of the water-cooled model for test point 24. It is not readily evident that the reduction in downstream ablation is due entirely to mass injection effects from the front part of the panel. Indications are that the reduction is due, in part, to the cooled layer of air coming off the cooled leading edge. This effect is indicated by examination of Figure 3-44, where the

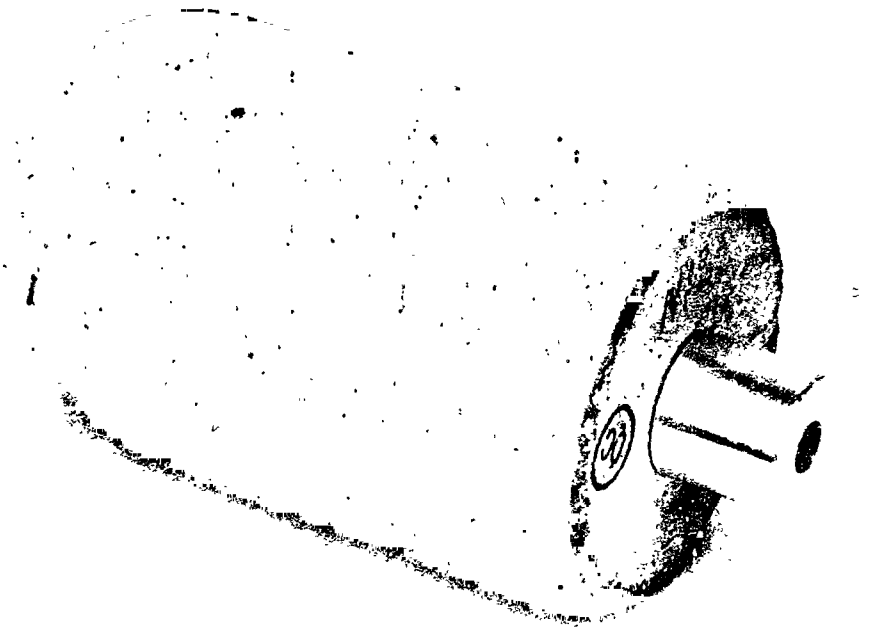


Figure 3-41. "THERMO-LAG" T-500 Model N-13 After Exposure to Vacuum

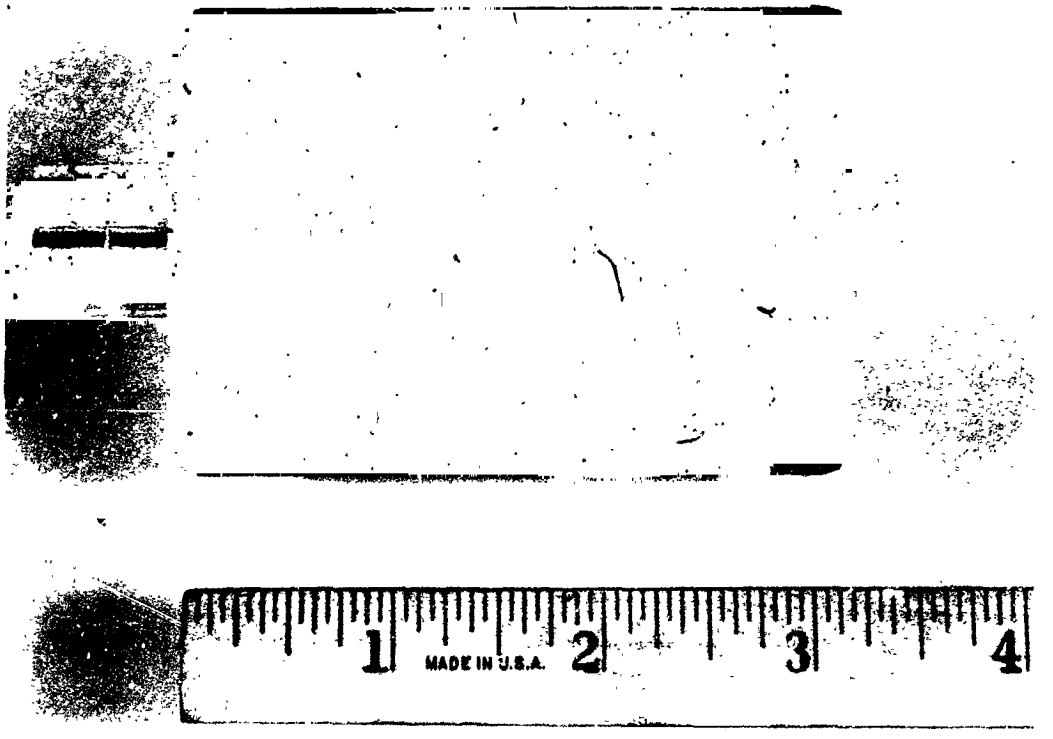


Figure 3-42. Plasma Jet Post Test Photograph of Vacuum Exposed "THERMO-LAG" T-500 Model N-13



Figure 3-43. Plasma Jet Post Test Photograph of "THERMO-LAG" T-500 Model N-41

coolant flow rate was the same as that for the models tested at conditions 12 and 24.

No comparisons of results of this study to other investigations were performed, due to the large differences in test conditions (Reference 2 and 4). The results of the tests are, however, in general agreement with that of other investigations. Due to insufficient transient history data on material recession from upstream mass injection, no evaluation of parameters for predicting sidewall heating could be made from this study.

The nonreduced temperature-time histories of the two-dimensional models tested are presented in Figures A-90 through A-107. Visual examination of the temperature traces indicated a departure from normal in the behavior of some models tested. Figure A-91 shows a sudden jump in temperature at about 450 seconds run time. This increase is due to a transition change from laminar to turbulent flow over the flat plate section of the water-cooled model. It is believed that this sudden transition from laminar to turbulent flow over the flat plate section of the water-cooled model. It is believed that this sudden transition from laminar to turbulent and back to laminar flow is due to a sudden drop in coolant pressure through the model. This behavior is not shown in the temperature traces of the other water-cooled models tested.

Figure A-104 shows the temperatures rising rapidly after 200 seconds test duration. This is due to the tendency of the test specimen to deform because of the large difference in thermal expansion properties of the graphite model and steel substrate of the test specimen at temperatures near 1800°F.

Due to the high enthalpy gradient that exists across the 3-inch test nozzel, test duration was controlled to minimize the effect that model leading edge shape change has on aft body heating.

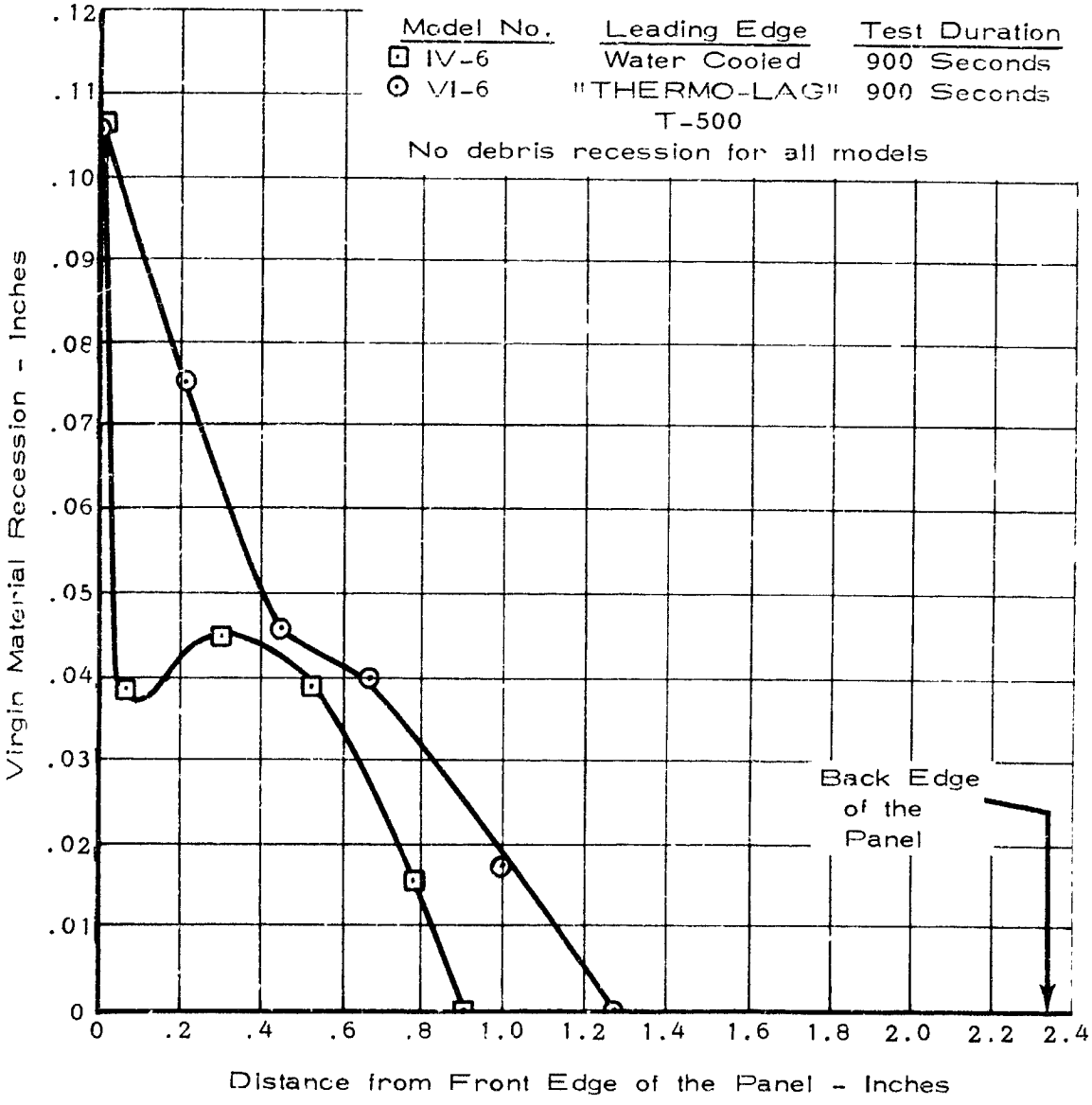


Figure 3-44. Virgin Material Recession Versus Distance from Front Edge of the Panel - Test Point 6.

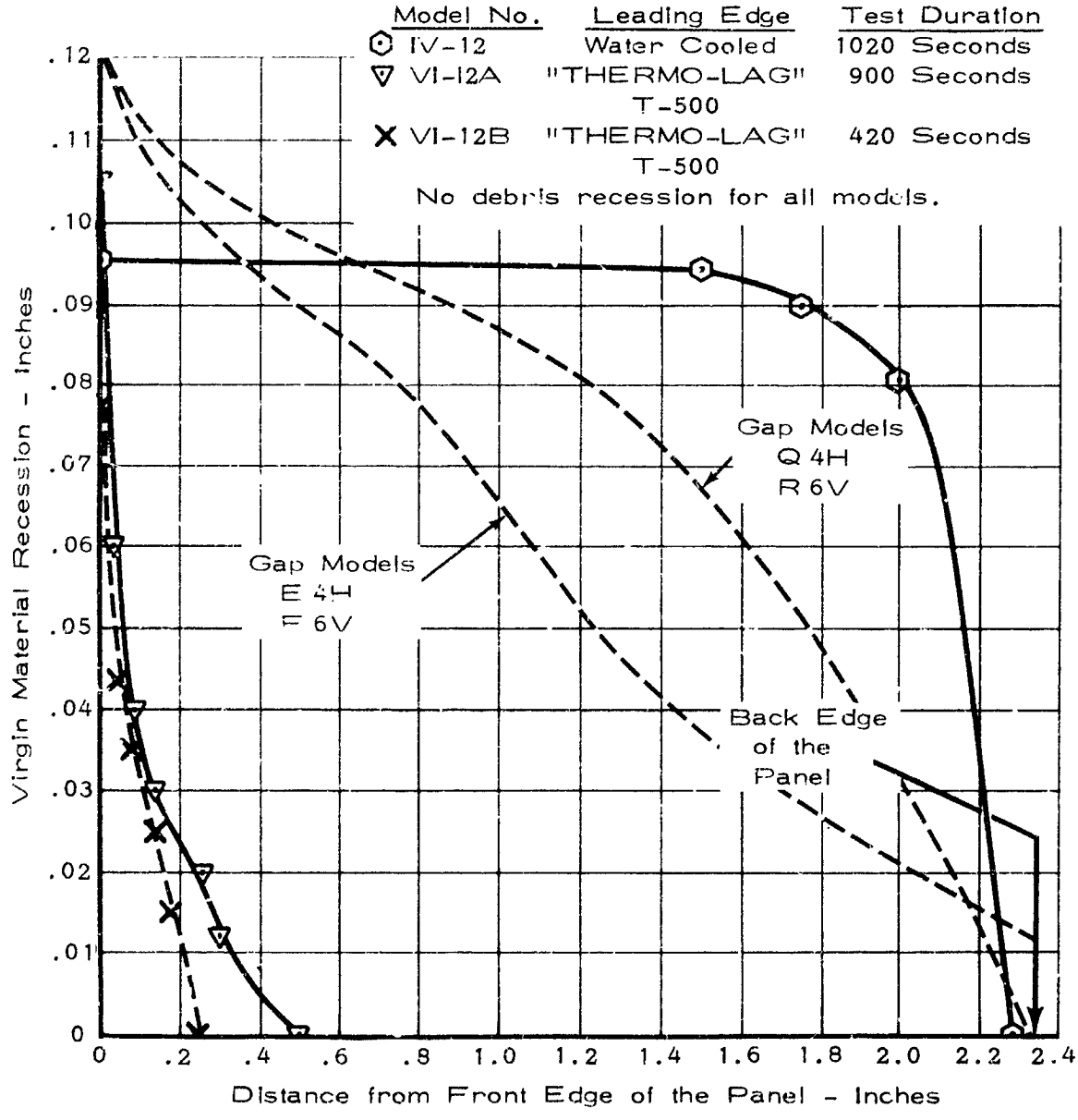


Figure 3-45. Virgin Material Recession Versus Distance from Front Edge of the Panel - Test Point 12.

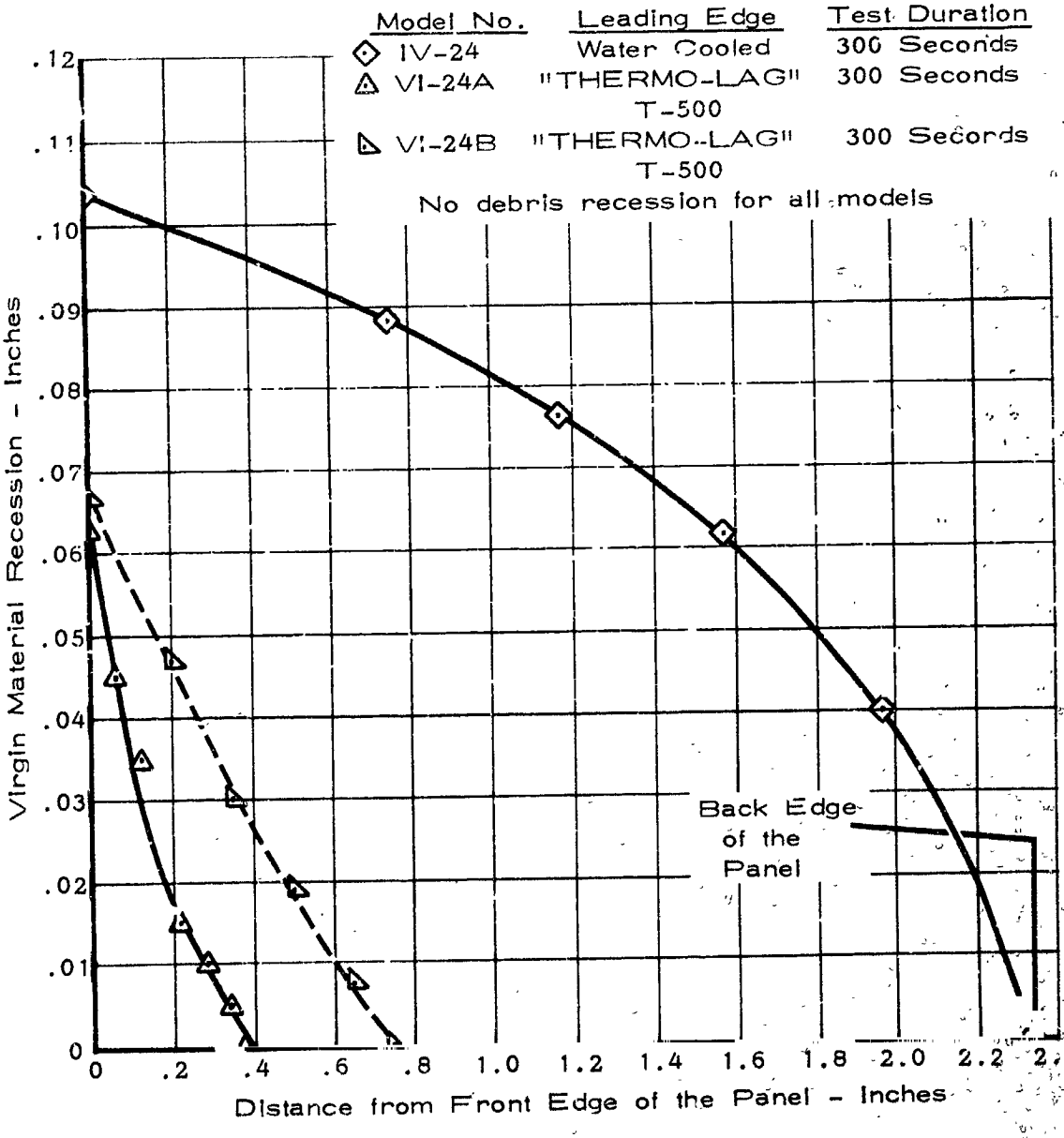


Figure 3-46. Virgin Material Recession Versus Distance from Front Edge of the Panel - Test Point 24.

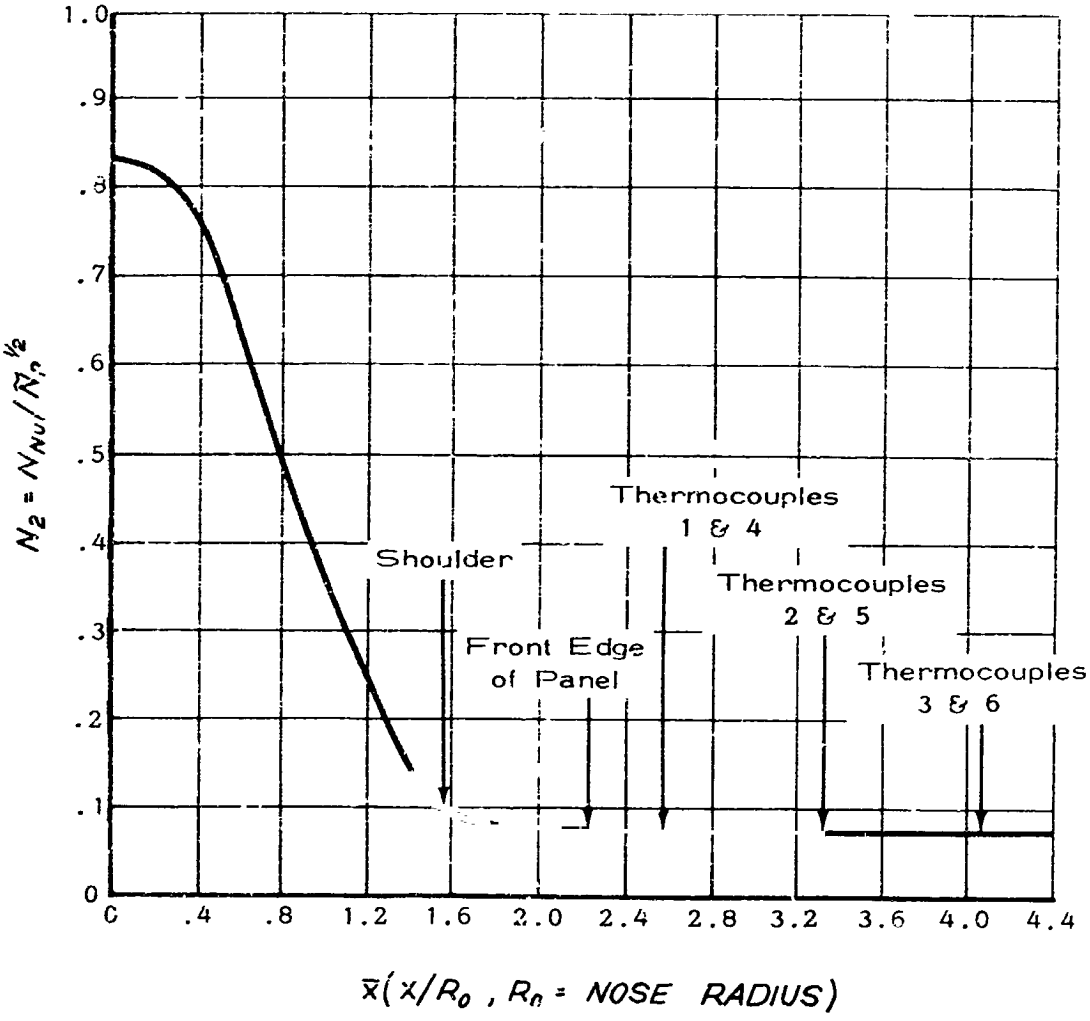


Figure 3-47. Theoretical Heat Transfer with Zero Injection.

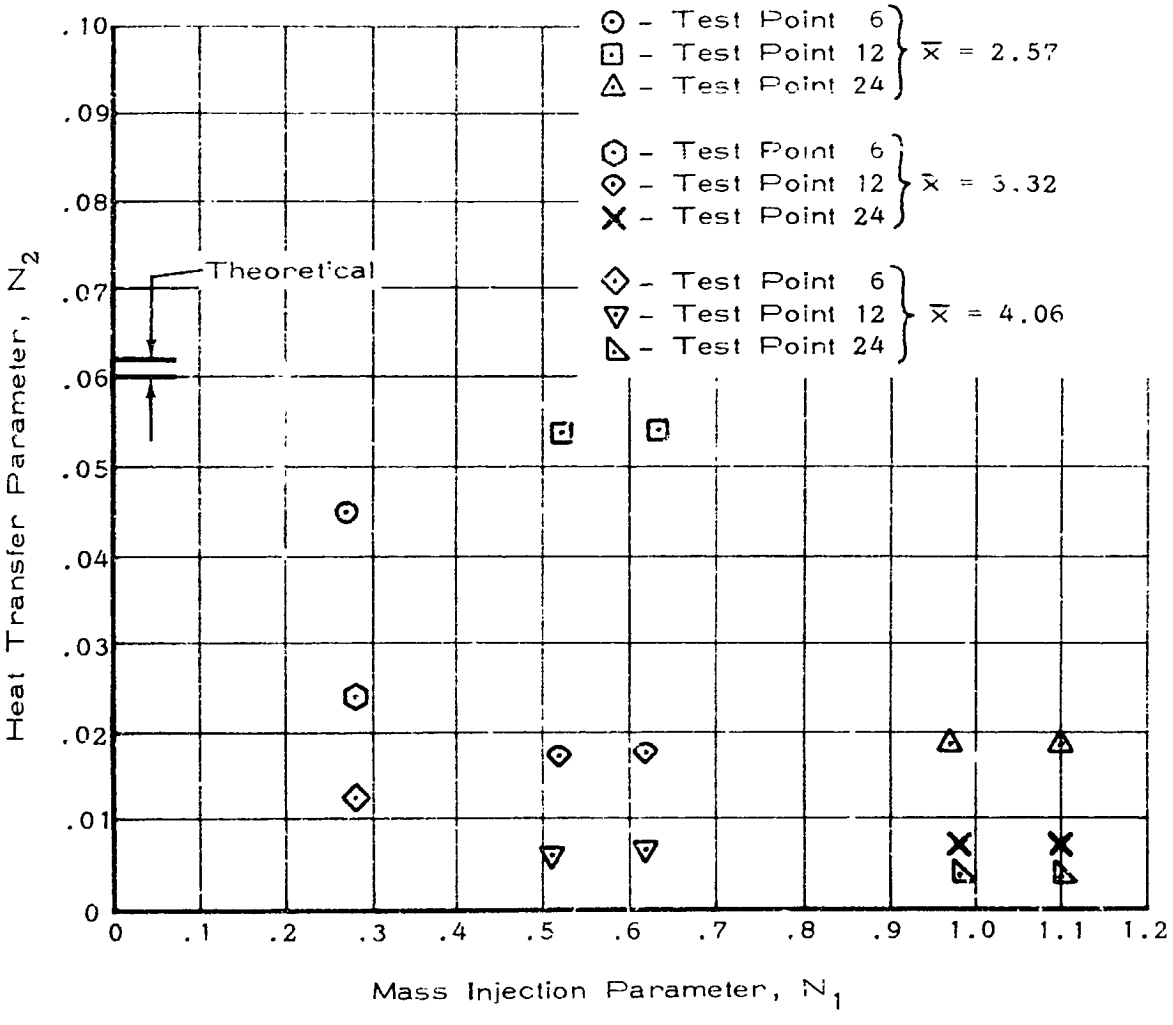


Figure 3-48. Variation of Heat Transfer with Mass Injection Parameter for "THERMO-LAG" T-500

* Model No.	Test Point	Test Conditions				
		Stagnation Heat Flux (Btu/ft^2-sec)	Stagnation Enthalpy (Btu/lbm)	Stagnation Pressure (atm)	Stream Mass Flow Rate (lbm/sec)	Test Duration (sec)
I-6	6	36	4.985	0.0077	1.80×10^{-3}	900
III-6	6	36	5.025	0.0077	1.80×10^{-3}	900
IV-6	6	36	5.000	0.0077	1.80×10^{-3}	900
VI-6	6	36	4.995	0.0077	1.80×10^{-3}	900
I-12	12	79.5	9.985	0.0063	1.42×10^{-3}	300
II-12	12	79.5	10.100	0.0063	1.42×10^{-3}	120
III-12	12	79.5	10.075	0.0063	1.42×10^{-3}	180
IV-12	12	79.5	10.050	0.0063	1.42×10^{-3}	1020
V-12	12	79.5	9.950	0.0063	1.42×10^{-3}	300
VI-12A	12	79.5	10.050	0.0063	1.42×10^{-3}	900
VI-12B	12	79.5	10.000	0.0063	1.42×10^{-3}	420
I-24	24	121.3	17.510	0.0050	8.71×10^{-4}	300
II-24	24	121.3	17.485	0.0050	8.71×10^{-4}	300
III-24	24	121.3	17.510	0.0050	8.71×10^{-4}	300
IV-24	24	121.3	17.450	0.0050	8.71×10^{-4}	300
V-24	24	121.3	17.465	0.0050	8.71×10^{-4}	300
VI-24A	24	121.3	17.550	0.0050	8.71×10^{-4}	300
VI-24B	24	121.3	17.505	0.0050	8.71×10^{-4}	300

*Note

I Water cooled leading edge with copper calorimeter
II Graphite leading edge with graphite calorimeter
III "THERMO-LAG" T-500 leading edge with graphite calorimeter
IV Water cooled leading edge with "THERMO-LAG" T-500 panel
V Graphite leading edge with "THERMO-LAG" T-500 panel
VI "THERMO-LAG" T-500 leading edge with "THERMO-LAG" T-500 panel

Table 3-10. Upstream Mass Injection Test Matrix

Model No.	Stagnation Mass Injection Rate (lbm/sec)	Calorimeter Heat Flux (BTU/ft^2-sec)			Ablation Panel Recession (Inch)					
		Front	Center	Back	F 0.0"	0.2"	0.4"	0.8"	1.0"	2.34"
*I-6		2.0	2.0	2.0						
*III-6	2.16×10^{-4}	1.5	1.5	1.5						
IV-6					0.015	0.043	0.045	0.120	0.000	0.000
VI-6	1.84×10^{-4}				0.013	0.077	0.064	0.035	0.018	0.000
*I-12		4.23	4.21	4.06						
*II-12		4.75	4.76	4.6						
*III-12	5.66×10^{-4}	4.6	4.38	3.42						
IV-12					0.095	0.095	0.095	0.095	0.095	0.000
V-12										
VI-12A	3.44×10^{-4}				0.100	0.024	0.005	0.0	0.0	0.0
VI-12B	4.14×10^{-4}				0.100	0.012	0.000	0.000	0.	0.0
*I-24		4.87	4.50	4.04						
*II-24		6.43	6.25	5.50						
*III-24		2.57	1.65	1.41						
IV-24					0.105	0.100	0.096	0.087	0.082	0.
V-24										
VI-24A	6.25×10^{-4}				0.064	0.017	0.0	0.0	0.0	0.0
VI-24B	5.45×10^{-4}				0.067	0.047	0.026	0.010	0.0	0.0

* Calorimeter Models
F At distance from front edge of test panel

Table 3-11. Results of Mass Injection Tests

Model No	Run Time (Sec.)	Test Panel Virgin Material Recession (Inches)				Material Thickness (in.)
		* 0.125	0.625	1.25	2.1875	
D-6-H	1320	0.068	.058	.05	.005	0.08
D-4-V		.08	.06	.05	0.0	.08
E-4-H	1000	.09	.075	.035	.002	.125
F-6-V		.12	.095	.065	.025	
K-6-V	1800		.092	.08	.07	.125
L-4-H			.075	.05	.065	.125
P-4-V	1280		.07	.065	.06	.08
Q-4-H	679	.102	.097	.08	0	.125
R-6-V		.115	.095	.08	.005	

* At distance from front of panel

Table 3-12. Material Gap Post-Test Data

Model	TP	Run Time (sec)	Sidewall Thickness avg. (in.)	Virgin Material Recession (in)		
				3/4" front Tc	Tc. No. 1 (1" from back)	3/4" Aft Tc.
GG-2	12	75	.030	char	.025	char
GG-4		150	0.100	.010	.025	.022
GG-5		90	.032	char	.033	char
-8		35	.029	.003	.011	.012
-1A		140	.101	.012	.025	.025
-11		390	.102	.090	.107	char
N-35	6	90	.102	0.0	0.0	0.0
N-36		420	.102	.04	.027	0.0
N-82		900	.102	.052	.105	.092
N-13	13	300	.102	.062	.082	.075
-34		300	.102	.020	.038	.020
-41		300	.102	.070	.082	.070

Table 3-13. Mass Injection Study - 3-Dimensional Models Tested

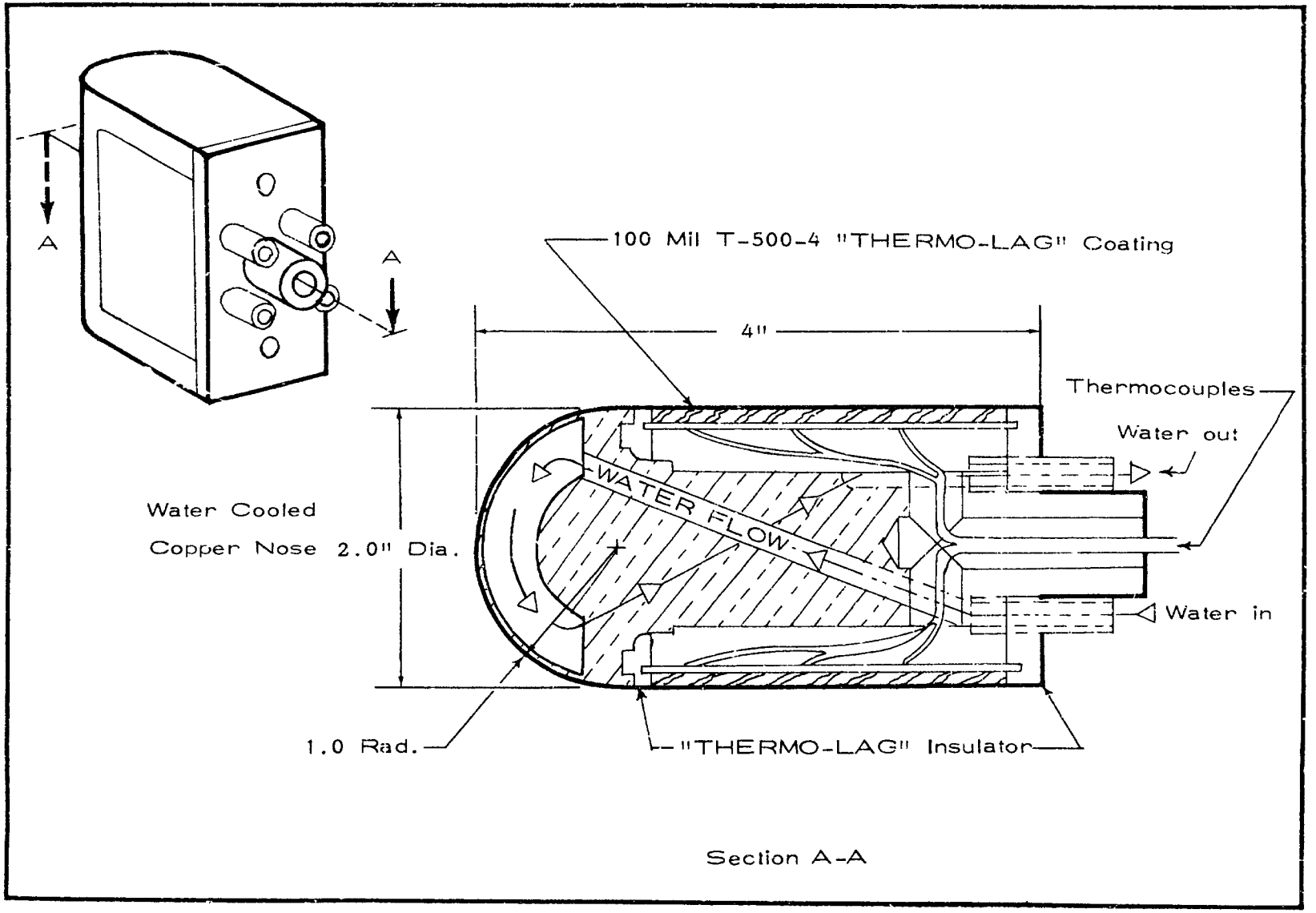


Figure 3-49. Simulated Flight Test Model (Type N)
Water Cooled Copper Nose, "THERMO-LAG" Body

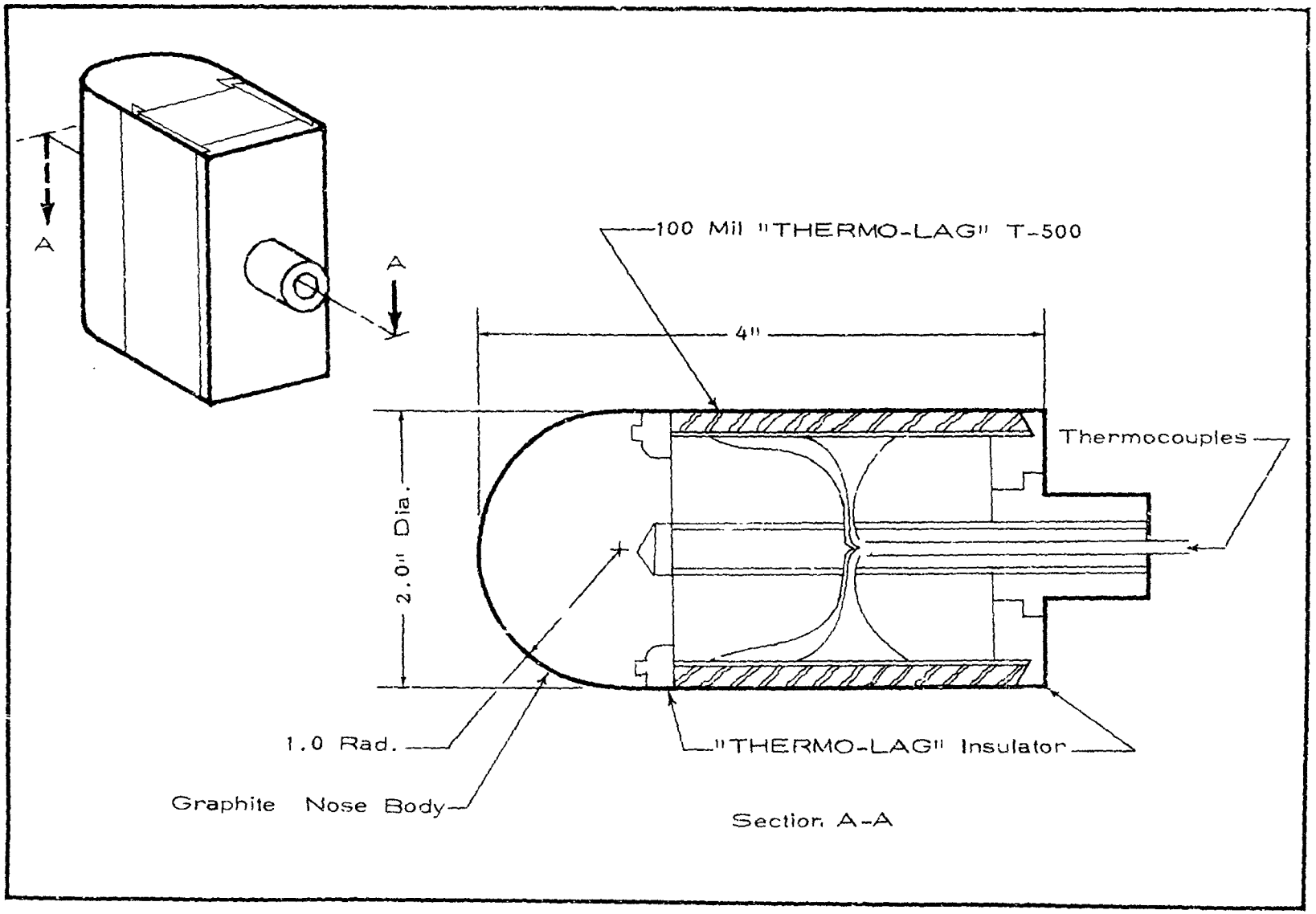


Figure 3-50. Simulated Flight Test Model (Type V)
Graphite Nose, "THERMO-LAG" Body

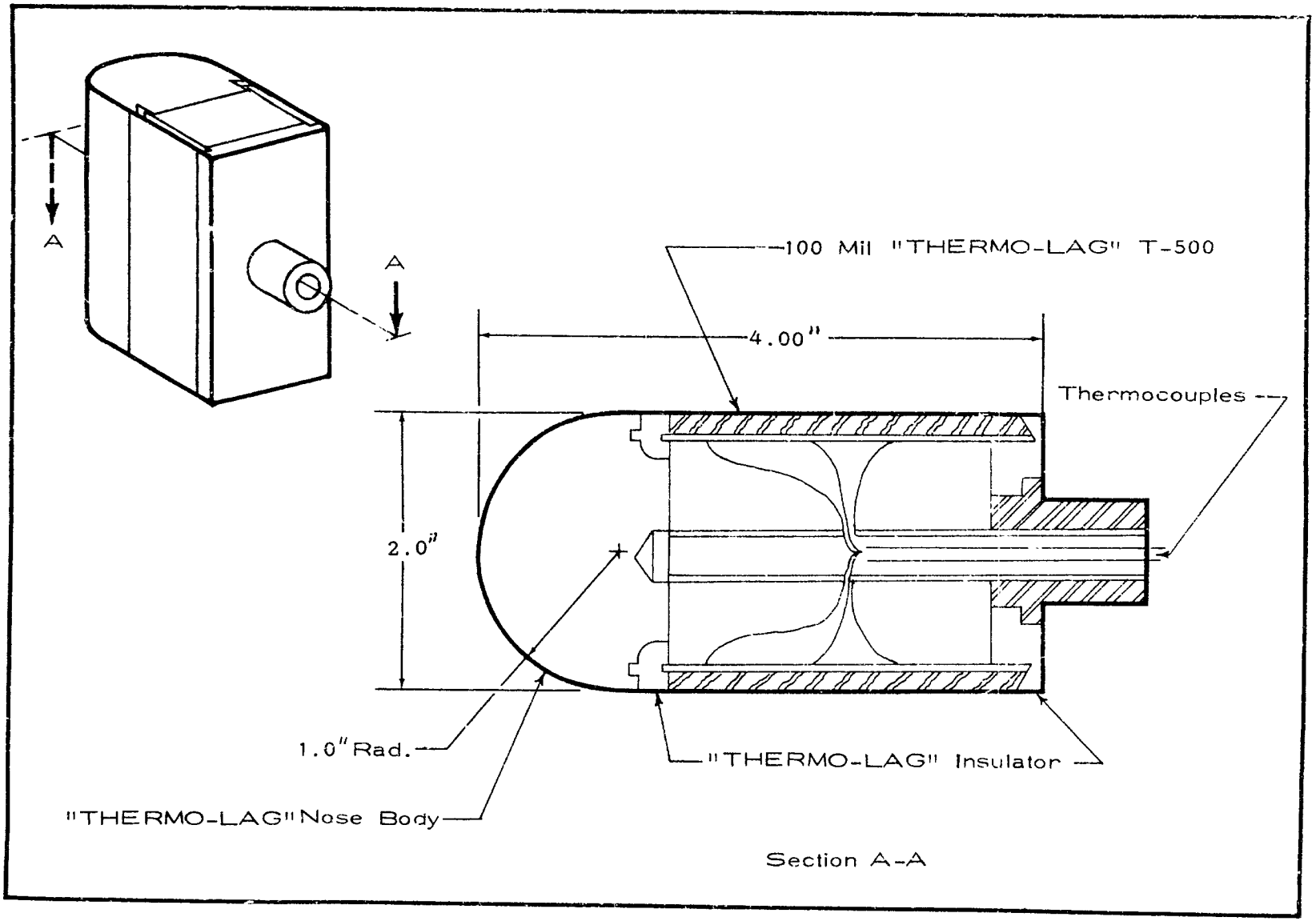


Figure 3-51. Simulated Flight Test Model (Type VI)
"THERMO-LAG" Nose, "THERMO-LAG" Body

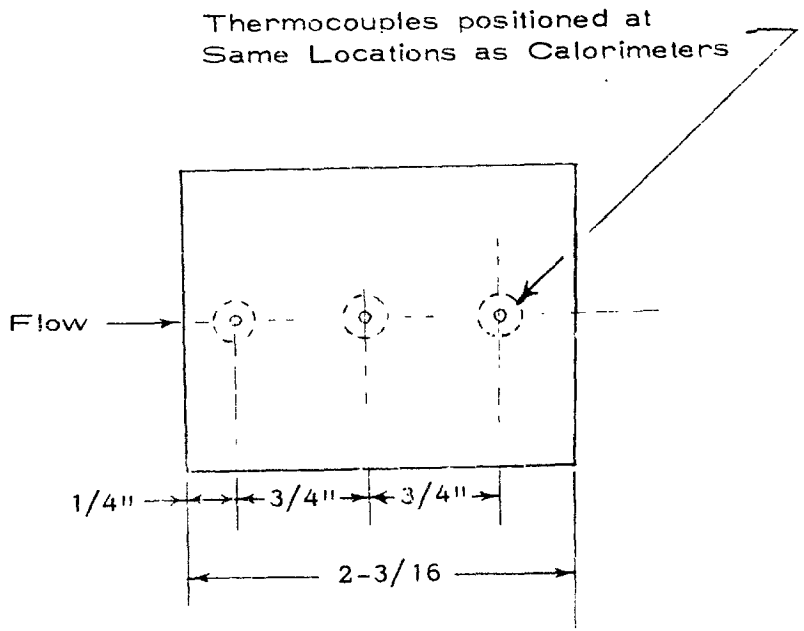


Figure 3-52. Test Plate Dimensions for Calorimeters and Thermocouples

RADIATION ABLATION TESTS

An investigation was made to evaluate the actual contribution to material performance resulting from energy transferred to the gaseous ablation products during passage through the porous debris in the absence of boundary layer phenomena. The data resulting from these tests was reduced and analyzed to obtain several parameters required by the numerical ablation program. These parameters are enumerated as follows:

1. The specific energy of chemical reaction of gaseous ablation products within the debris layer (β)
2. Heat capacity term for the gaseous ablation products (Cp)
3. Effective thermal conductivity of the debris, K_{eff}

The tests were performed in a 70 kw radiation facility in accordance with the test matrix shown in Table 3-14.

This series of tests used models of two different thicknesses as indicated in Table 3-14. The models were fabricated from spray deposited sheets of "THERMO-LAG" T-500. Each model was a 1-3/4 inch diameter cylinder instrumented with four 28-gage Chromel-Alumel thermocouples. A 1/4-inch thick, 2-inch diameter disk of the same material served as a mounting for the model proper while at the same time insulating it from the water-cooled holder used in the test. Of the four thermocouples, one was located at the surface of the model, another 0.015 inch from the surface, and the remaining were two at known depths within the model. The purpose of the thermocouples was to obtain temperature histories throughout the material during the ablation process from which the temperature-time derivatives could be established.

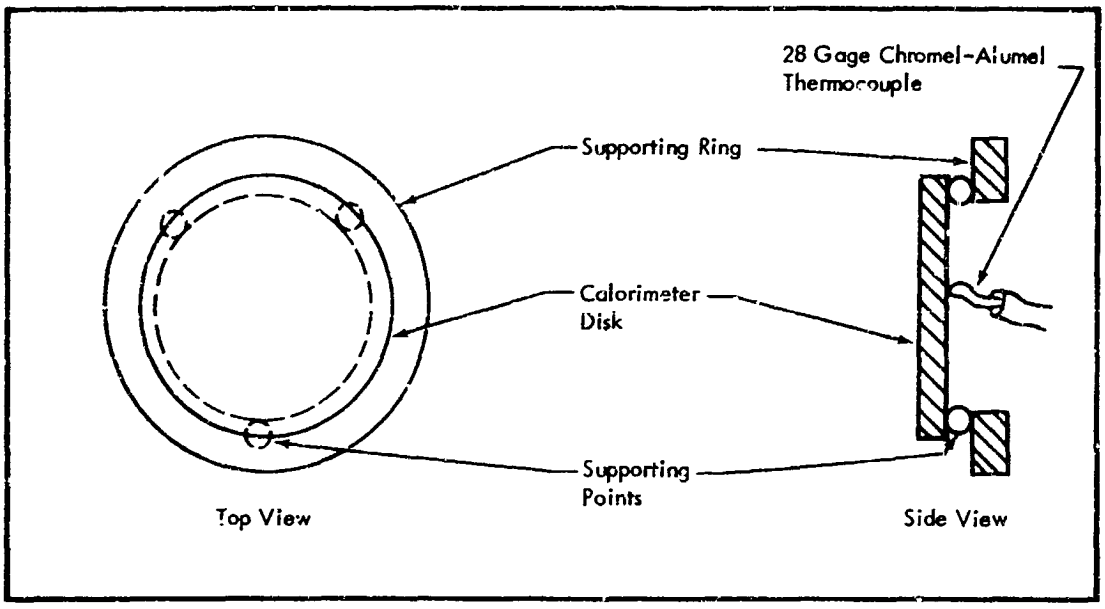
The results obtained were:

1. Virgin material recessions at several exposure times
2. Temperature-time histories from thermocouples placed at known locations throughout the material.

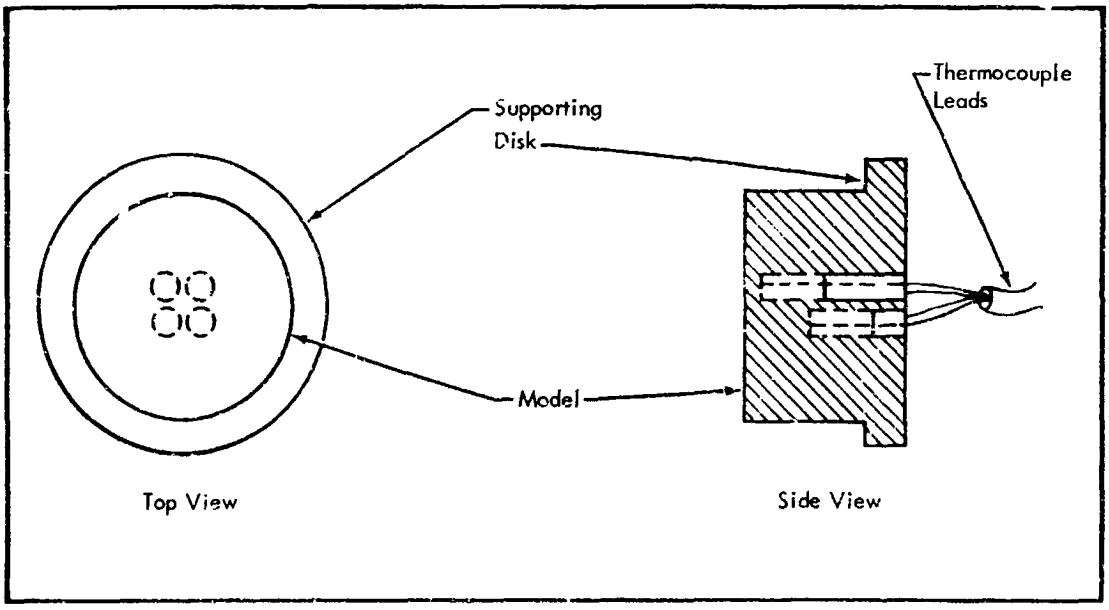
Typical nonreduced data are shown in Figures 3-54 and 3-55. The analysis of the radiation ablation tests is given under "Analytical Evaluation of Ablation Parameters".

Number of Tests	Specimen Thickness (In)	Distance from Lamp (In)	Lamps Voltage (Volts)	Cold Wall Heat Flux (Btu/Ft^2 - Sec)
3	0.31	1.5	129	55
3	0.31	1.5	185	10
3	0.31	1.5	235	15
3	0.46	0.625	225	20
3	0.46	0.625	255	25
3	0.46	0.625	287	30

Table 3-14. Radiation Ablation Test

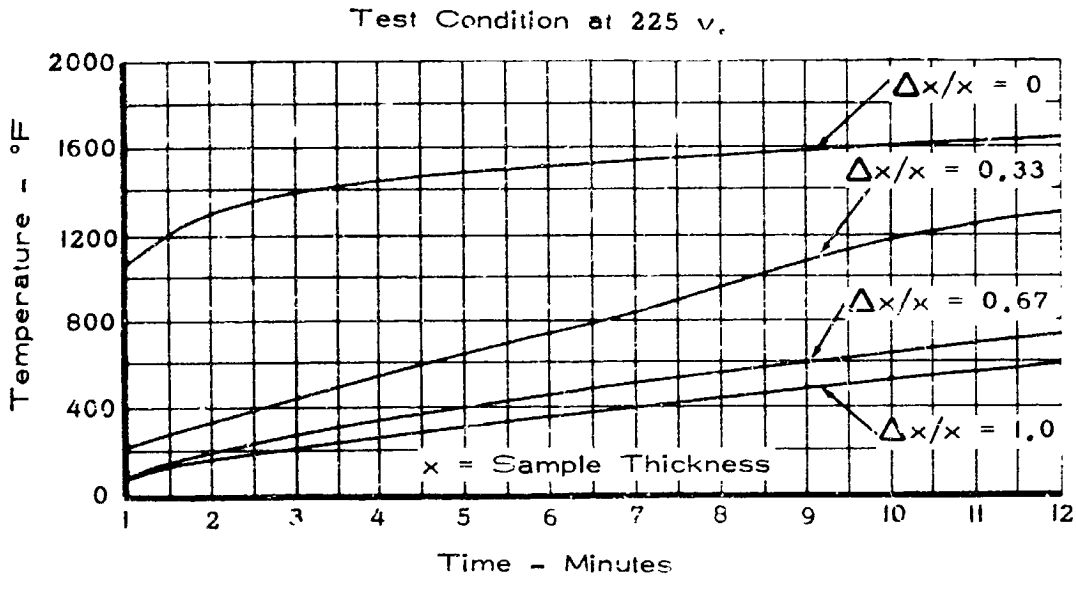


Molybdenum Calorimeter

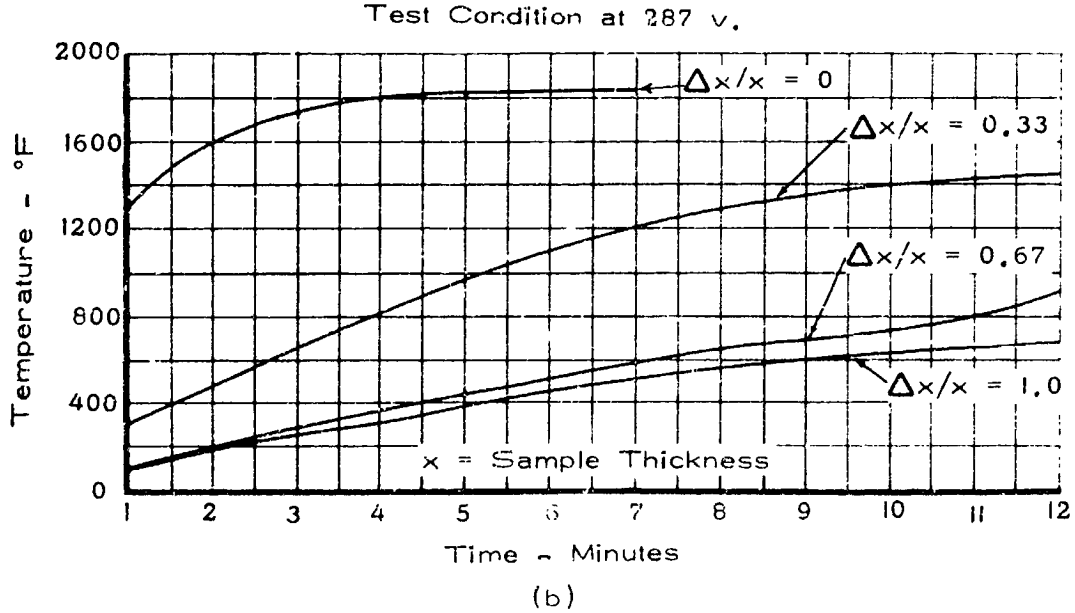


Radiation Ablation Model

Figure 3-53. Schematic Diagrams of Molybdenum Calorimeter and Radiation Ablation Model



(a)



(b)

Figure 3-54. Temperature Traces For Test Conditions at 225 v. And 287 v.

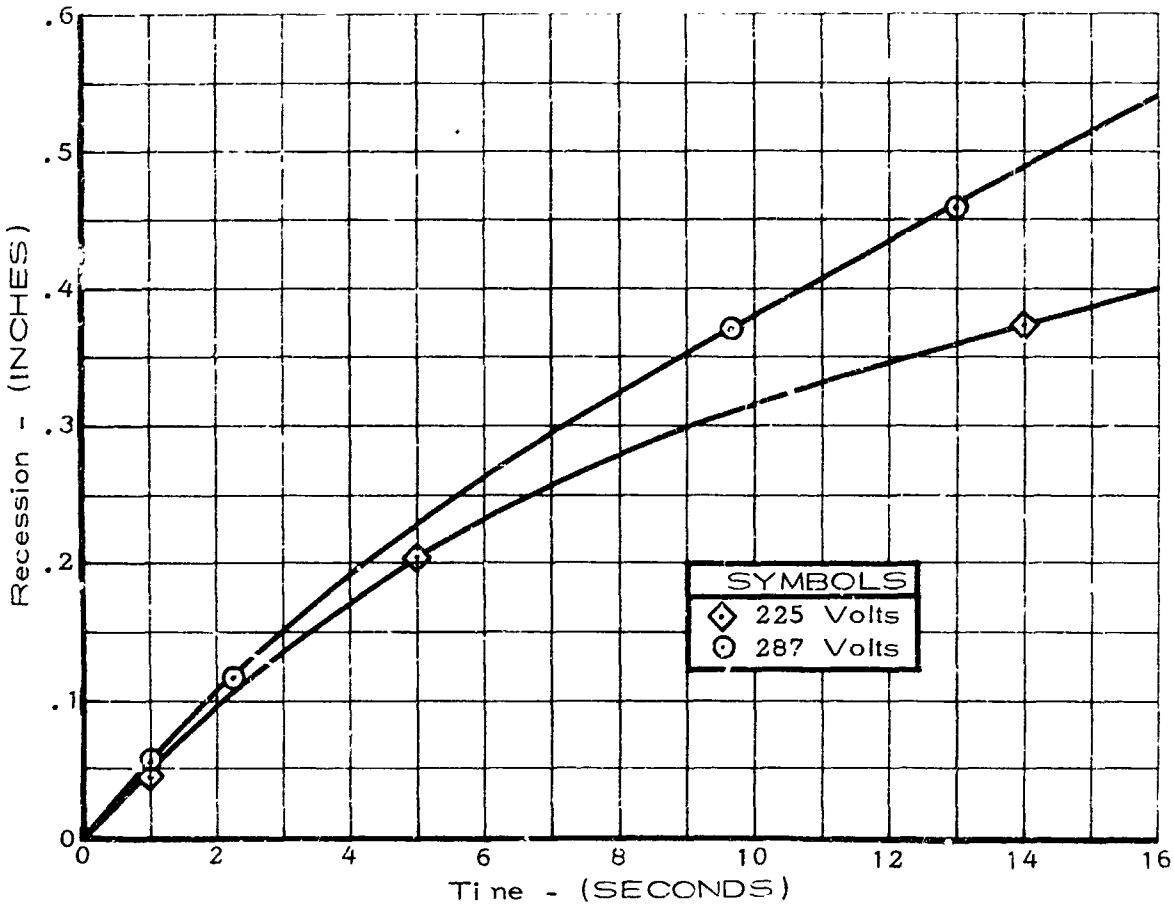


Figure 3-55. Recession Histories for Test Conditions at 225 Volts and 287 Volts.

PART B - ANALYTICAL EVALUATION OF ABLATION PARAMETERS

GENERAL APPROACH

An evaluation of the ablation energy transfer parameters was obtained in a systematic manner from the arc-plasma and radiation - ablation test results. First, a transpiration cooling parameter was derived and the energy liberated through combustion was computed. Secondly, the energy transferred within the debris layer was computed and the parameters required for the numerical ablation program were obtained.

Specifically, the arc plasma results were evaluated in terms of ablation efficiency, using the performance data obtained from the transient ablation test series. The dependence of efficiency on boundary layer enthalpy difference was utilized to define a transpiration cooling parameter. A difference in ablation performance was noted between ablation tests conducted at moderate and high enthalpy levels and those conducted at low enthalpy levels.

The efficiency at low enthalpies was considerably greater than anticipated. At these conditions the debris layer recession rate was reaction rate-controlled for heat fluxes of 100 Btu/Ft^2-sec or less. The difference in efficiency at the low and moderate enthalpies was obtained at a given total enthalpy; thus giving a measure of the exothermic effects resulting from oxidation reactions.

A gross energy balance for the ablation system was written and the energy transferred to the gaseous ablation products within the porous debris layer was represented in terms of a specific energy factor. At this point sufficient information existed from arc-plasma test results to compute the specific energy factor for a temperature range of 2200°R to 4750°R.

The remaining unknown parameter was the effective thermal conductivity of the porous debris layer. This was obtained from the arc plasma data for the temperature range of 2200°R to 4750°R by means of an approximate solution to the energy balance across the entire boundary layer.

For temperatures below 2200°R, radiation ablation data were utilized. For this environment, the gross energy balance technique of parameter evaluation was not sufficiently accurate. The method chosen involved the simultaneous solution of the differential energy balance taken at several locations within the debris at a given temperature. The required derivatives for the energy balance were obtained from temperature histories of thermocouples placed

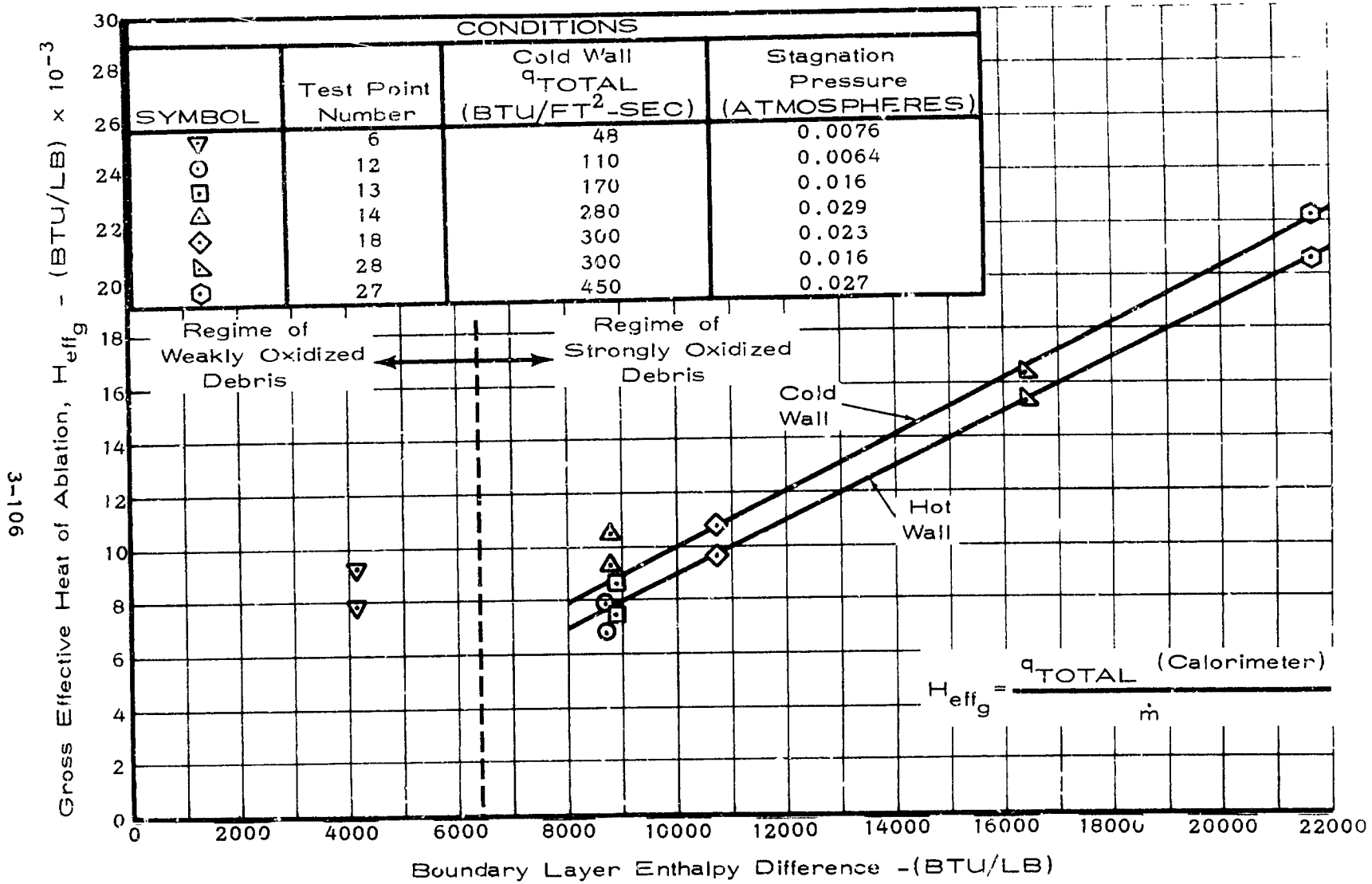


Figure 3-56. Variation of Gross Effective Heat of Ablation with Boundary Layer Enthalpy Difference

at known locations within the debris.

BOUNDARY LAYER THERMAL EFFECTS

TRANSPIRATION COOLING PARAMETER. The results of the transient ablation test series were utilized to obtain an accurate measure of material recession rate at any desired exposure time. Knowledge of the nose radius at one exposure time permitted a radius correction of the measured heat flux and the resulting computation of ablation efficiency. The measured heat fluxes were obtained with a water-cooled copper calorimeter and therefore excluded the effects of mass injection and chemical reactions between the external fluid and ablation products. The cold wall heat fluxes were adjusted to hot wall conditions through an enthalpy difference correction. The resulting ablation efficiency histories showed transient performance until the debris layer attained maximum thickness. For constant model shape the transient performance would have been followed by steady state behavior characterized by a linear recession history and constant efficiency. It was noted that some of the performance histories attained a maximum value which then decreased with increasing exposure time. Evidently the heating rate to the blunt models was greater than the radius-corrected hot wall calorimeter measured value. This finding was consistent with the results obtained from tests of the effect of model geometry on ablation performance. In these tests, the blunt models were found to indicate less efficiency than the hemisphere-nosed models where efficiency was based on the measured total heat flux.

The maximum values of cold and hot wall gross efficiency for the various test conditions were plotted versus the boundary layer enthalpy difference (Figure 3-56). This maximum value was attained before measurable model nose shape change was observed; thus the data of the transient test series were compared on a constant shape basis. To complement data where required, the results from test points 14 and 18, not included in the transient series, were utilized. Certain data from these runs did not reflect model geometry change and were therefore valid for comparison in Figure 3-56. The net heat flux into the debris surface excluding the effects of mass injection and chemical reactions at the surface and in the boundary layer was obtained by subtracting the reradiation flux from the calorimeter measured total heat flux (Figure 3-57). These results yield an apparent transpiration cooling parameter, giving a quantitative measure of the effect of enthalpy on sensible heating within the boundary layer of the injected gases, and, also, the resulting energy transfer due to chemical reactions between the

ablation products and the plasma stream. At this point, however, the data could not be correlated on the same basis since the various test conditions did not all exhibit the same stagnation pressure, which variable affects efficiency. Furthermore, surface temperature was found to be dependent upon pressure at a given total enthalpy. The data of Figure 3-57 were corrected to a constant pressure of 0.027 atmospheres and the corresponding surface temperatures obtained by means of Figures 3-23 and 3-25. At a constant pressure, the surface temperature was found to increase with increasing enthalpy difference giving a greater slope to the efficiency curve than warranted by the enthalpy difference dependency. The explanation involves consideration of additional energy absorbed within the debris layer at higher surface temperatures, the magnitude of which is discussed in the analysis of the radiation ablation tests. A gross energy balance was written as follows:

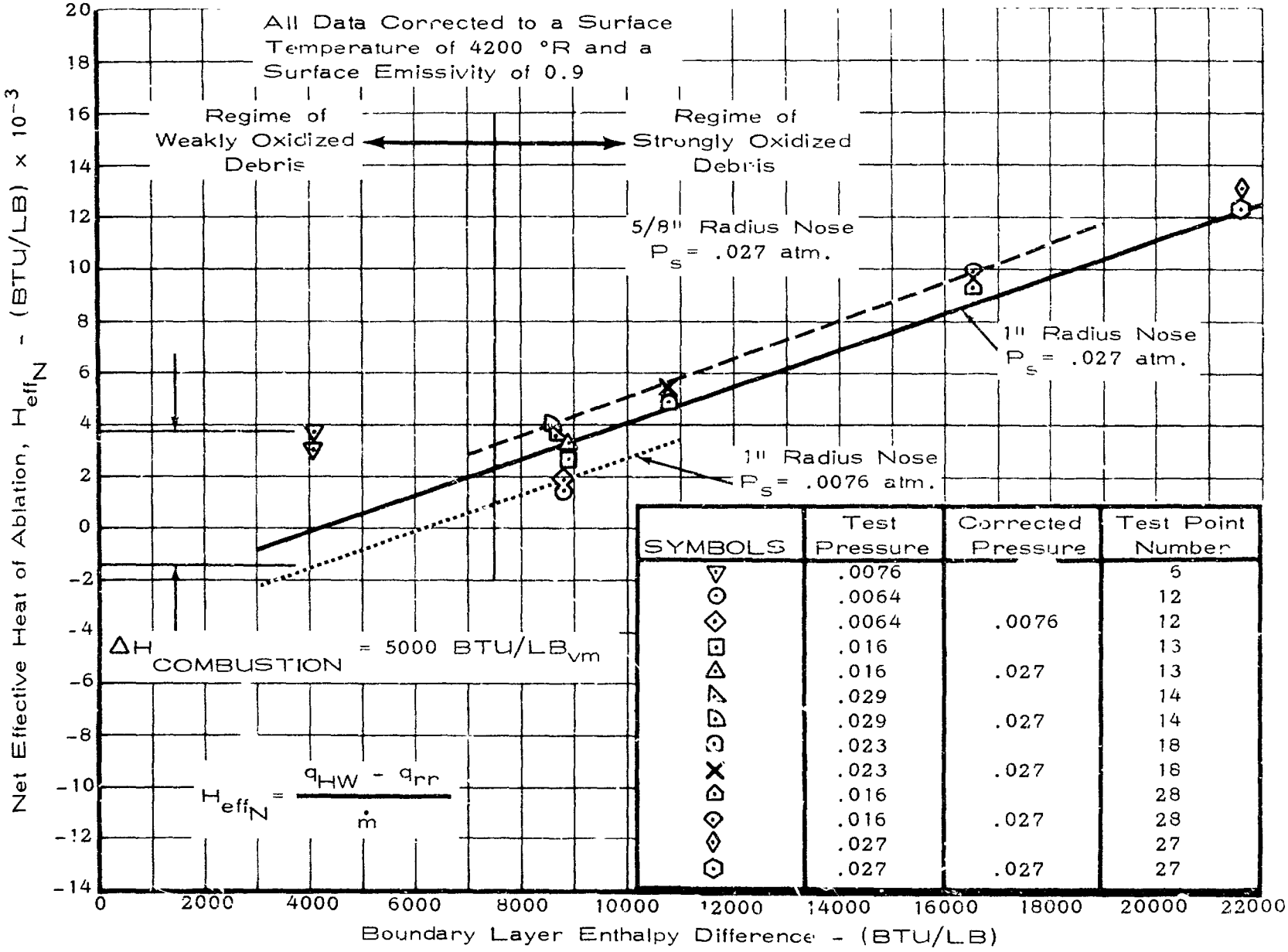
$$q_{TOTAL} - q_{rr} - \dot{m}_1 \bar{C}_p \left[\overline{T_w} - 4200^{\circ}R\right] = \dot{m}_1 \bar{C}_p (4200 - T_{sub}) + \ldots$$

$$\ldots + \dot{m}_2 \alpha (H_T - H_w) + \frac{K}{\dot{m}} \frac{dT}{dx}\bigg|_{\substack{VIRGIN \\ SURFACE}} + \Delta H_{combustion} \qquad (3-1)$$

$$\text{WHERE } q_{rr} = \sigma \epsilon F (T_w^4 - T_e^4)$$

In this expression, the net efficiency was corrected to a surface temperature of 4200°R. The transpiration cooling parameter was taken as the slope of the temperature and pressure-corrected experimental curves of Figure 3-57. The data were correlated for constant model configuration where the 5/8-inch and 1-inch radius hemisphere-nosed models gave a transpiration cooling parameter value of 0.78 and 0.73 respectively for an enthalpy difference range of 8600 Btu/Lb. to 21600 Btu/Lb. As discussed in previous sections, total enthalpies of 5000 Btu/Lb and lower produced an essentially nonoxidizing debris layer. A study of the 500 Btu/LB_m enthalpy transient test series and several isolated tests at 3500 Btu/Lb_m and 2500 Btu/Lb_m enthalpies showed no clearly defined dependence of efficiency upon enthalpy difference at these total enthalpies.

The results give a range of α which reflects the experimental accuracy of the data, particularly in view of the nonsymmetrical model geometries produced at the high enthalpy condition (test point 27). However, the ablation performance at test point 27 was evaluated before the appearance of measureable geometry change, using models N-6, N-11, and N-22.



SYMBOLS	Test Pressure	Corrected Pressure	Test Point Number
▽	.0076		6
⊙	.0064		12
◇	.0064	.0076	12
⊡	.016		13
△	.016	.027	13
◿	.029		14
◱	.029	.027	14
◌	.023		18
✕	.023	.027	18
⊡	.016		28
◇	.016	.027	28
◇	.027		27
⬡	.027	.027	27

Figure 3-57. Variation of Net Effective Heat of Ablation with Boundary Layer Enthalpy Difference.

A further possible reason for the variation of α may be associated with the smaller nose radius producing a lower residence time within the boundary layer such that the degree of completion of the oxidation reactions at the stagnation region has diminished with respect to that found for the larger models.

HEAT ADDITION PRODUCED BY OXIDATION

For the purpose of estimating the thermal effects upon ablation performance of the oxidation reactions occurring at the 10,000 Btu/Lb_m total enthalpy condition, the 1.0-inch radius models were compared for the oxidizing and nonoxidizing ablation regimes. The efficiency results of test point 6 were corrected for surface omittance from a value of 0/6 to 0/9, and the surface temperature corrected to 4200°R to permit a comparison with the results of test point 12, at which a comparable pressure existed. A slight difference in pressure was accounted for through Figure 3-25. The efficiency curve of Figure 3-57 was extrapolated through the results of test point 12 at the 8600 Btu/Lb_m enthalpy difference level to an enthalpy difference of 150 Btu/Lb_m. The difference in efficiency for the test point 6 results and the extrapolated curve at the same enthalpy difference was taken as the exothermic effect of combustion for the conditions of test point 12 and was found to be about 5000 Btu/Lb of virgin material.

Considering the primary product of surface oxidation to be carbon monoxide at the low pressures tested and at total enthalpies of 10,000 Btu/Lb and greater, where surface temperatures exceed 4000°R the heat of combustion at the surface was taken to be 4000 Btu per pound of carbon. An estimate of additional stagnation region heating due to surface combustion was made for the different test conditions and is given in Table 3-15. The average debris surface density of 22 Lb/Ft^3 was used in the computations. The heat addition in the boundary layer was taken as the difference between the total energy liberated and the heat of surface combustion. These values are also listed in Table 3-15. It is seen that the additional heating expressed as a percentage of the hot wall convective heating rate is considerable at the 10,000 Btu/Lb enthalpy level but is of lesser magnitude at the high enthalpies.

			Hemisphere-Nosed Models					
H_T (Btu/Lb)	Radius Corrected (Calorimeter) (Btu/Ft^2-Sec)	P_s (atm)	Configuration & Model No.	Total Mass Loss Rate (Lb/Ft^2-Sec)	q-Surface Combustion (Btu/Ft^2-Sec.)	q-S.C. q_{HW} (Percent)	q-Boundary Layer (Btu/Ft^2-Sec.)	q-B.L. q_{HW} %
10,000	82.7	.0064	GG-5, 1" Cylinder	$1.23(10)^{-2}$	12.8	15.5	46.7	56.5
10,000	148.5	.016	N-46, 1" Cylinder	$1.84(10)^{-2}$	19.1	12.9	70	47
12,000	214	.023	M-19, 5/8" Cone	$2.22(10)^{-2}$	23.0	10.7	84.4	39.4
10,000	168	.029	N-105, 5/8" Cylinder	$1.83(10)^{-2}$	19.0	11.3	69.6	41.5
17,500	268	.016	M-21, 5/8" Cone	$1.91(10)^{-2}$	19.8	7.4	72.5	27
23,000	425	.027	N-6, 1" Cylinder	$2.1\ (10)^{-2}$	21.8	5.1	80	18.8
			Flat-Faced Models					
12,000	137	.023	N-112, 5/8" Cylinder	$1.84(10)^{-2}$	19.1	14	73	53.2
12,500	159	.020	N-71, 1" Cylinder	$1.71(10)^{-2}$	17.7	11.2	65	41
23,000	251	.027	N-73, 1"	$1.13(10)^{-2}$	11.7	4.65	43	17.2

Table 3-15. Additional Heating Due To Oxidation Reactions

DEBRIS LAYER ENERGY TRANSFER

DISCUSSION OF PHYSICAL BEHAVIOR. An evaluation of the performance characteristics of the porous carbonaceous debris layer was approached by the correlation of surface temperature, debris layer recession, and virgin material recession for all ablation tests. These data were compared at constant exposure times using the average surface temperature to eliminate to a considerable extent variations between tests due to the existence of nonequilibrium debris thicknesses and varying nose geometries. Figure 3-58 presents these data for constant exposure times of 150, 300, and 420 seconds. It was noted that a definite relationship exists between the surface temperature, debris thickness, and virgin material recession with a slight variation for different nose radii and oxygen concentrations.

As noted in Figure 3-21, obtained from ablation histories, the virgin material and debris layer recession rates increase with increasing temperature. The debris thickness decreases with increasing surface temperature above 3000°R, and exhibits almost no recession at temperatures below 3000°R.

This correlation of debris surface temperature and total recession gave a criterion used to qualify the arc plasma test data as to reproducibility of material performance. It is apparent that the material behavior followed a consistent pattern for a given oxygen concentration.

Having established the relationship of Figure 3-58, it was noted that one variable, such as surface temperature is sufficient to determine the physical state of the ablation system. These curves and the ablation histories of Figures 3-11 through 3-16 were used to evaluate the relationship between surface temperature and virgin mass loss rate (Figure 3-59).

EVALUATION OF ENERGY TRANSFER PARAMETERS

ARC-PLASMA DATA. An energy balance for an element within the debris was derived and is the basis upon which the numerical ablation program was developed:

$$(\rho c)_{DEBRIS} \frac{\partial T}{\partial \theta} = K_{eff} \frac{\partial^2 T}{\partial x^2} + \dot{m} \xi_1 (c_p + \beta) \frac{\partial T}{\partial x} \qquad \text{(B-2)}$$

This relation states that the time rate of energy storage within the solid debris matrix is equal to the difference between the heat conducted in and out of the element and the energy transferred to

the gaseous ablation products transpiring through the element. Upon application of the boundary conditions, (B-3) and (B-4), several simplifying assumptions were made and a steady state solution obtained.

$$T \text{ (Debris Backside)} = T(\text{Sublimation}) \qquad \text{(B-3)}$$

$$K\frac{\partial T}{\partial x}\Big|_{\substack{\text{INTO}\\ \text{SUBLIMING}\\ \text{SURFACE}}} = \dot{m}\,\bar{\xi}_{e_1} Q_L + K\frac{\partial T}{\partial x}\Big|_{\substack{\text{FROM}\\ \text{SUBLIMING}\\ \text{SURFACE}}} \qquad \text{(B-4)}$$

It was found that energy stored in the solid debris matrix involved less than 1 percent of the total energy transferred and therefore, its omission from the energy balance was justified for the steady state ablation case. The energy stored in the virgin material was assumed to be the amount necessary to heat the material from room temperature to the sublimation temperature for the arc plasma tests of high ablation rates. The resulting solution considering the total debris layer is given as:

$$T_{SURFACE} = T_{SUB} + \frac{Q_L + \frac{C_{VM}}{\bar{\xi}_{e_1}}(T_{SUB} - T_o)}{(\overline{C_p + \beta})}\left[e^{\bar{\xi}_{e_1}(\overline{C_p+\beta})\frac{\dot{m}\bar{x}\rho}{\bar{K}_{eff}}} - 1\right] \qquad \text{(B-5)}$$

Two unknowns in this relation were $(\overline{C_p + \beta})$ and $\overline{K_{eff.}}$ The total energy balance (B-1) was used to evaluate $(\overline{C_p + \beta})$; however, acknowledgement of this term was necessary to accurately evaluate the transpiration cooling parameter (B-2) on a constant surface temperature basis. An estimate of $(\overline{C_p + \beta})$ at surface temperatures between 4000 and 4500°F was obtained from the radiation - ablation data of reference 5. This value was used in the preliminary evaluation of (B-2) and $(\overline{C_p + \beta})$ was obtained from relation (B-1) using data from the transient test series where the mass loss rates are well defined (Figure 3-60). The results obtained from the reference 5 data and those derived from (B-1) were within reasonable agreement; however, a final correction in the determination of (α) was made.

The mean effective specific heat of the gaseous products was found to behave differently in the two ablation performance regimes. As shown in Figure 3-60, the strongly oxidized debris regime produced a $(\overline{C_p + \beta})$ dependency upon mass loss rate and surface temperature. Mass loss rate was the predominant independent variable, giving a significant increase in $(\overline{C_p + \beta})$ for a small increase in mass loss rate (Figure 3-61).

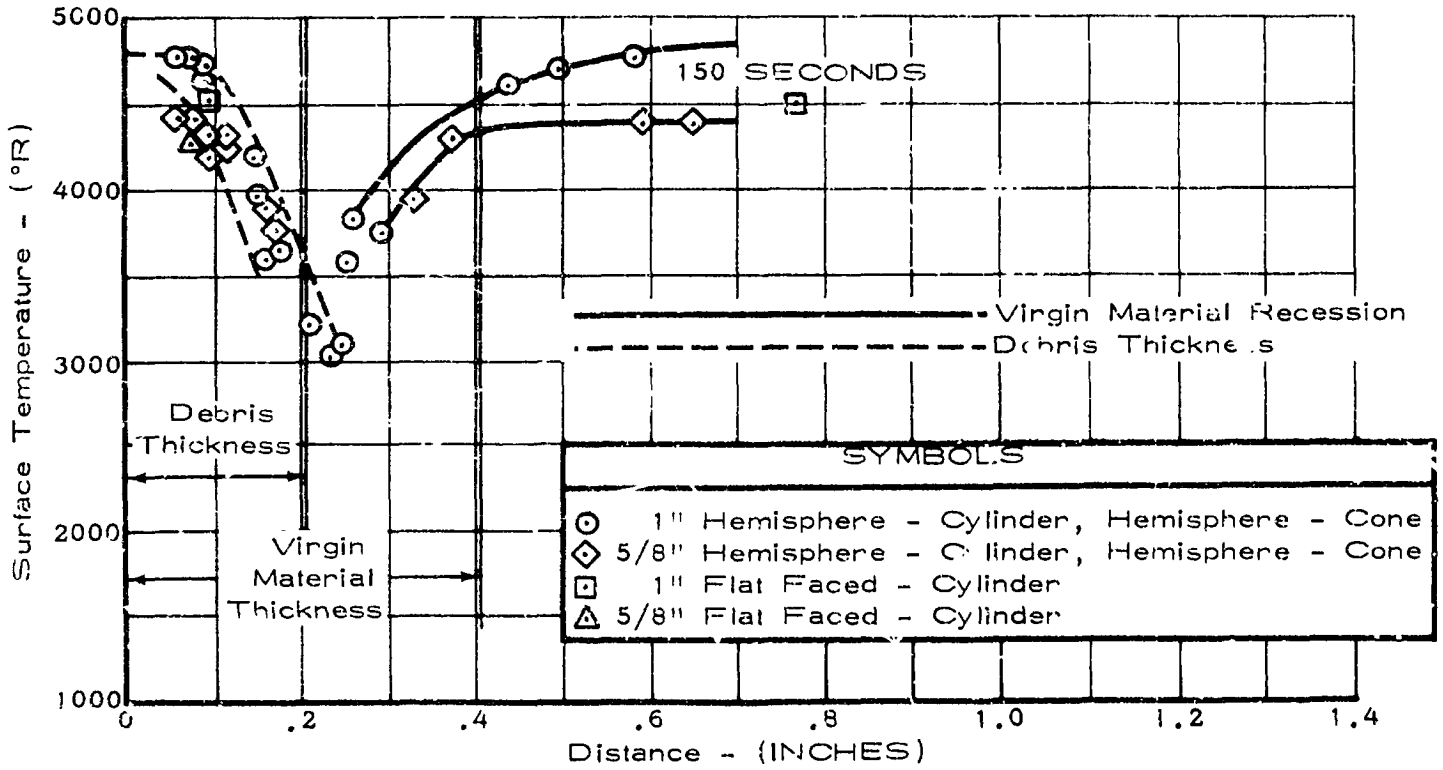


Figure 3-58. Relationship Between Debris Thickness, Virgin Material Recession, Surface Temperature, and 21 Percent of Oxygen Concentration for Several Constant Values of Exposure Time (Sheet 1 of 2).

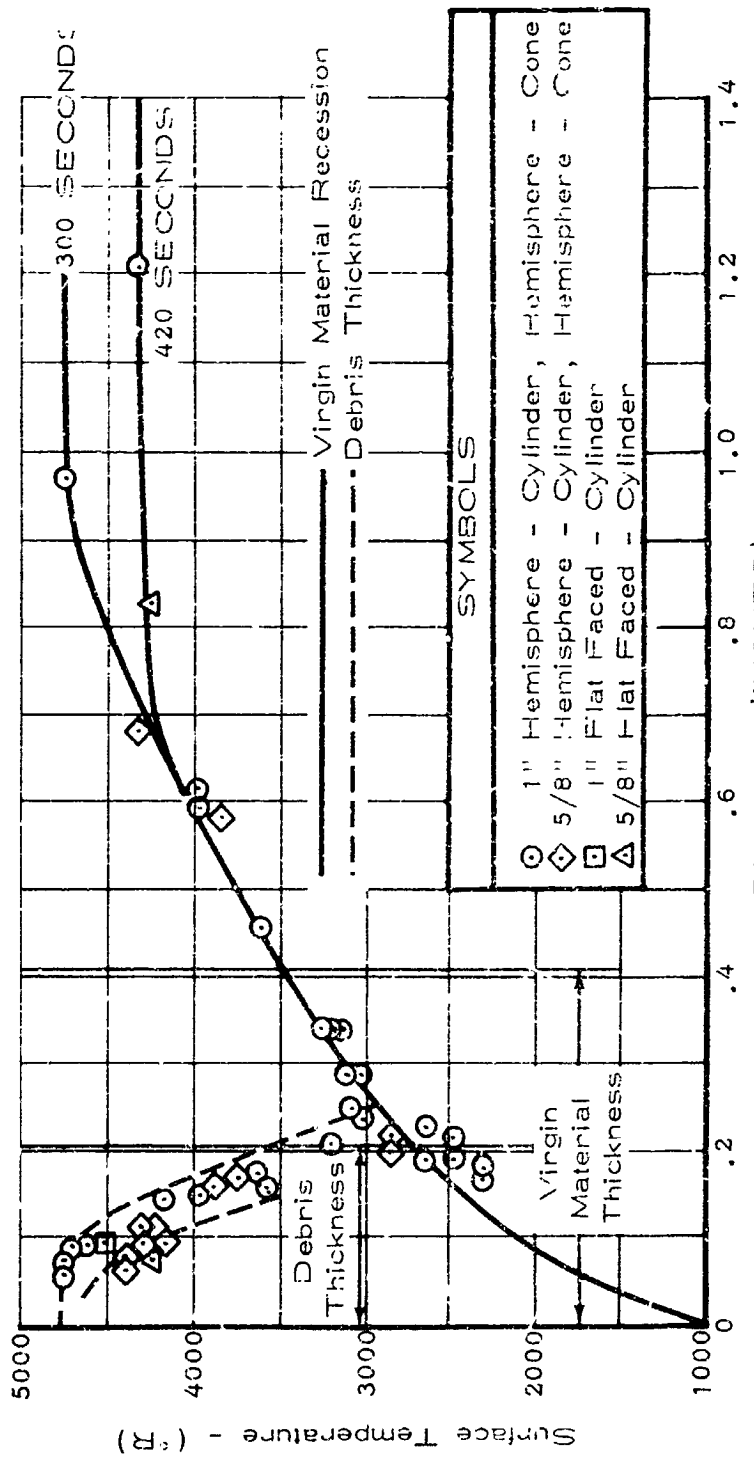


Figure 3-58. Relationship Between Debris Thickness, Virgin Material Recession, Surface Temperature, and 21 Percent of Oxygen Concentration for Several Constant Values of Exposure Time (Sheet 2 of 2).

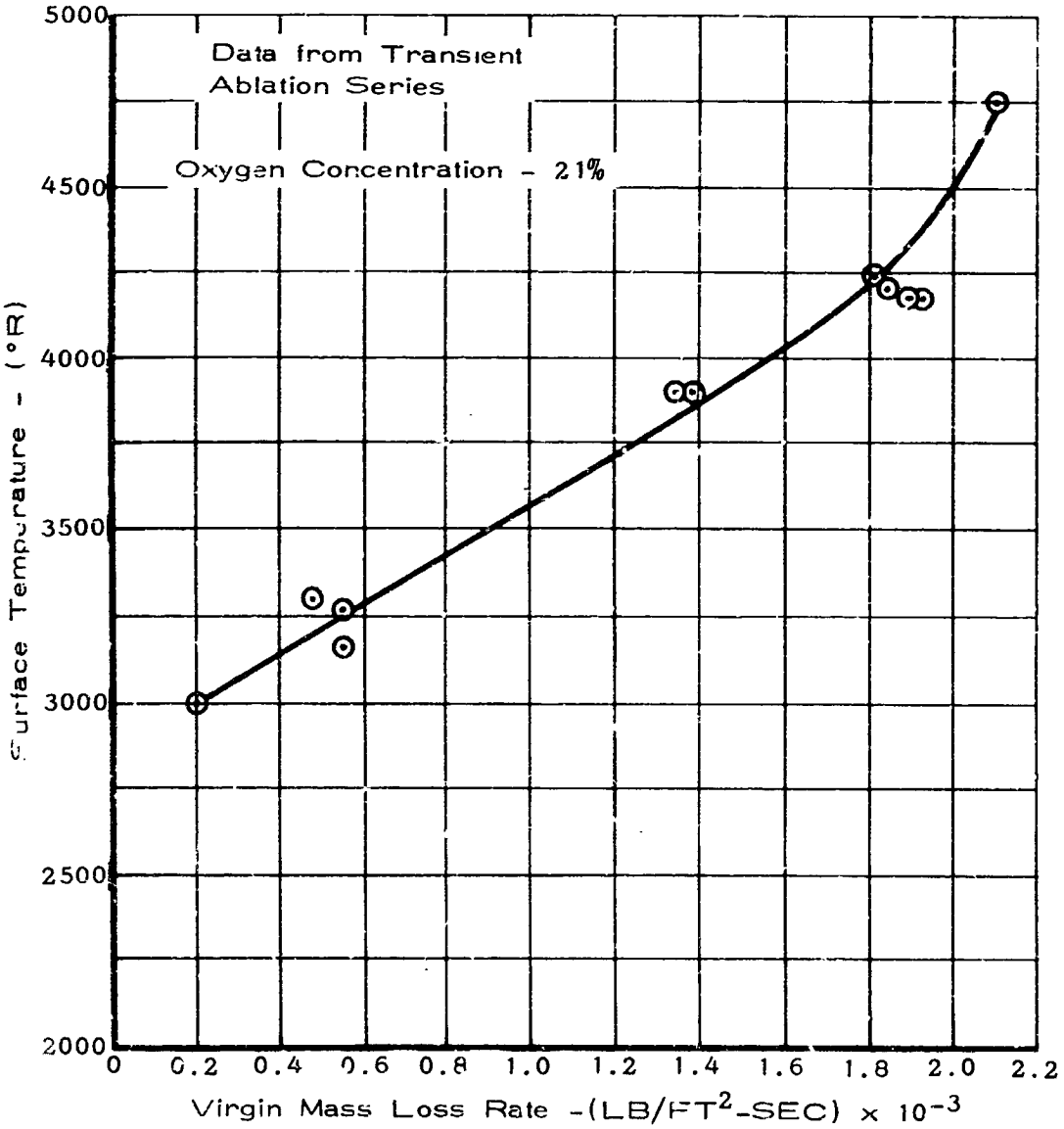


Figure 3-59. Variation of Virign Mass Loss Rate with Debris Surface Temperature

In the regime of the relatively inert debris surface shown in Figure 3-60, total enthalpy was found to be the main independent variable, giving a 300 percent increase in $(\overline{Cp + \beta})$ for a decrease in total anthalpy from 5000 Btu/Lb_m (Figure 3-62). Cold wall heat flux was maintained constant in Figure 3-62, and the measured average mass loss rate was found to be relatively constant.

Figure 3-63 shows the variation of $(\overline{Cp + \beta})$ with stream oxygen concentration for constant test conditions at a total enthalpy of 5000 Btu/Lb_m and cold wall heat flux of 110 Btu/Ft^2-sec. The importance of oxygen diffusion into the debris layer upon the $(\overline{Cp + \beta})$ term is noted by the significant increase in $(\overline{Cp + \beta})$ as the oxygen concentration is reduced from 21 percent to a stream of pure nitrogen.

The debris layer mean effective thermal conductivity was then obtained from (B-5) and Figure 3-61, and the above method used to estimate the actual thermal conductivity variation with temperature as shown in Figure 3-64.

A result of the above arc-plasma ablation analyses was the quantitative evaluation of the energy transfer parameters required by the numerical ablation program for surface temperatures ranging from 3300°R to 4800°R and total enthalpies ranging from 2500 Btu/Lb_m to 23000 Btu/Lb_m. The evaluation of these parameters at lower temperatures was necessary for an understanding of material behavior at vehicle aft body locations. This was achieved in the Emerson radiation facility for temperatures from 1000°R to 2000°R through analysis of the debris on a differential element basis discussed in the following section.

ANALYSIS OF RADIATION ABLATION TESTS. The effective thermal conductivity, $\bar{K}_{eff}$, of the debris layer and the specific energy parameter $(\overline{Cp + \beta})$ of the gaseous ablation products were determined for a temperature range of 550°F to 1500°F from the radiation-ablation test data. This was accomplished from temperature histories obtained at known locations within the ablation model. The basic energy relation upon which the numerical ablation program is based is given for an element of debris matrix as:

$$\rho C \frac{\partial T}{\partial t} = K_{eff} \frac{\partial^2 T}{\partial x^2} + \dot{m} \xi (C_p + \beta) \frac{\partial T}{\partial x}$$

The relation states that the time rate of energy storage within the solid debris matrix is equal to the difference between the heat conducted in and out of the element and the energy transferred to the gaseous ablation products transpiring through the debris layer.

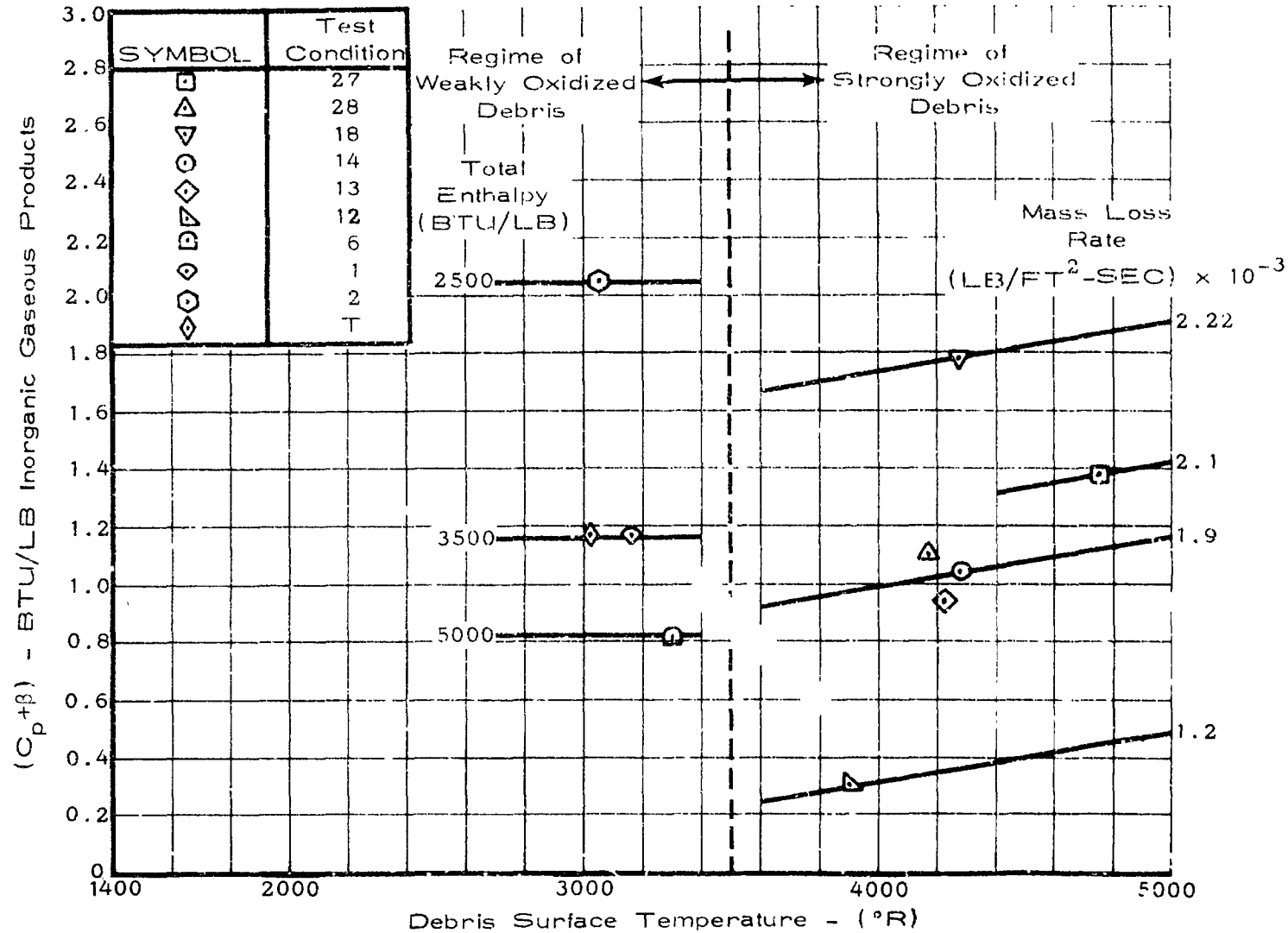


Figure 3-60. Variation of Mean Effective Specific Heat of Gaseous Ablation Products with Debris Surface Temperature.

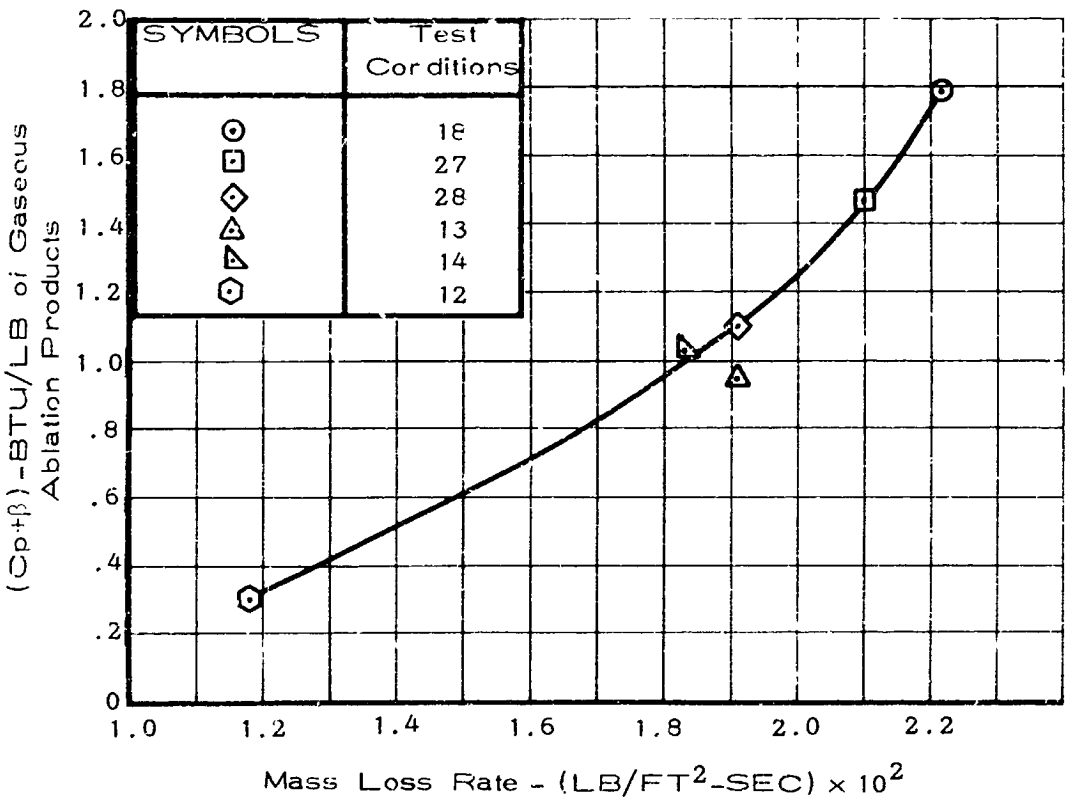


Figure 3-61. Variation of Mean Effective Specific Heat of Gaseous Ablation Products with Mass Loss Rate for a Range of Total Enthalpy from 10,000 BTU/LB to 23,000 BTU/LB

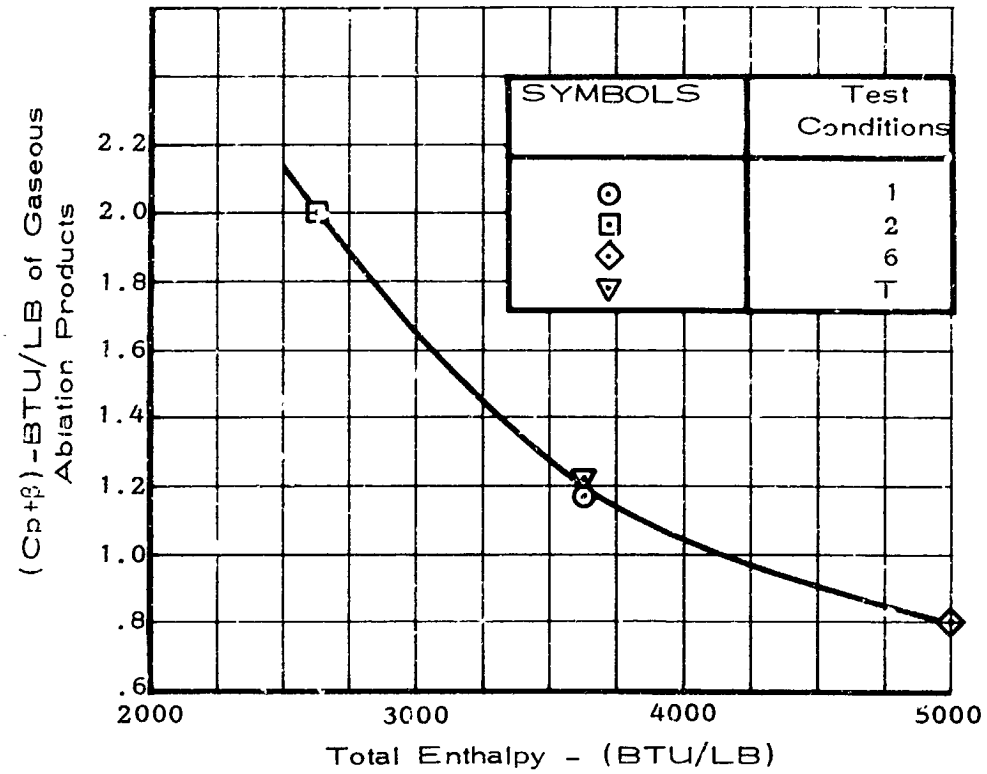


Figure 3-62. Variation of Mean Effective Specific Heat of Gaseous Ablation Products with Total Enthalpy for the Weakly Oxidized Debris Regime

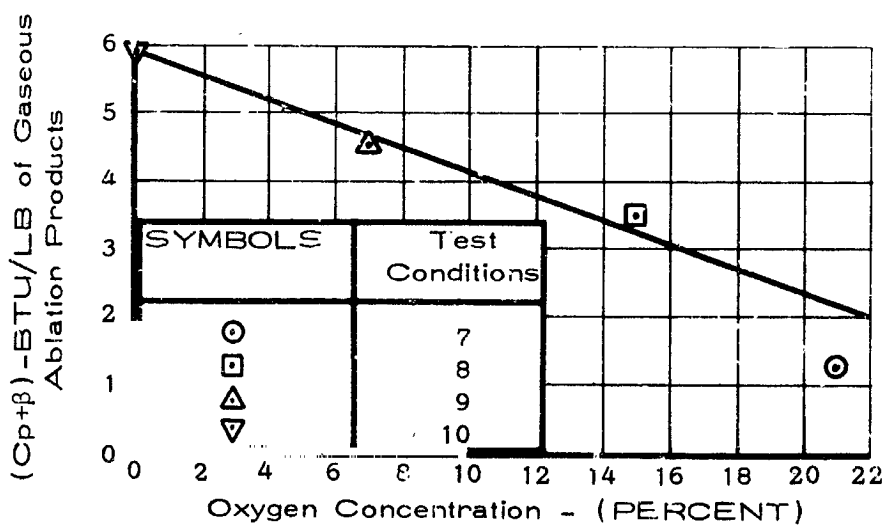


Figure 3-63. Effect of Oxygen on the Mean Specific Heat of Gaseous Ablation Products

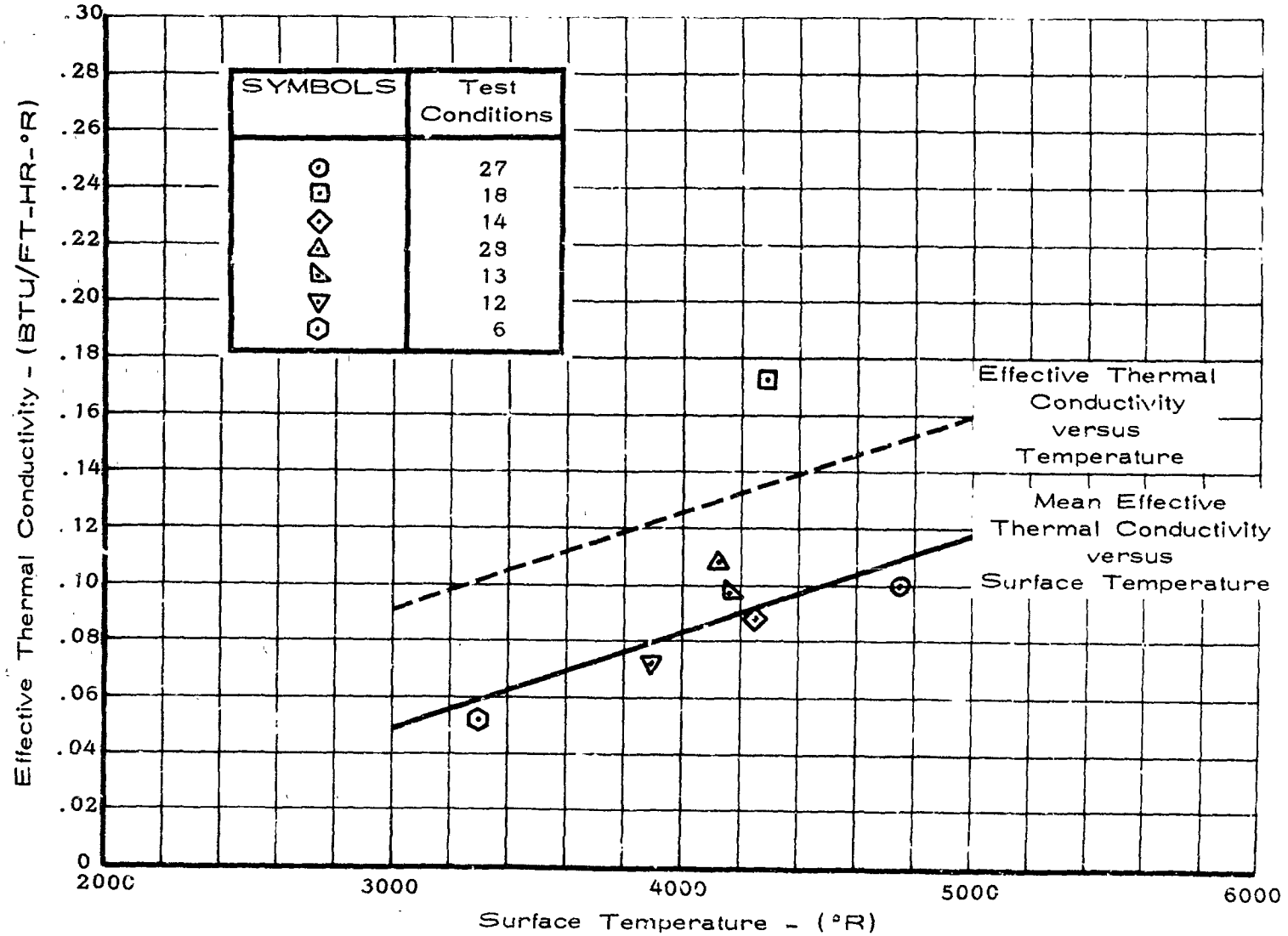


Figure 3-64. Variation of Debris Layer Effective Thermal Conductivity with Temperature

In view of the small pore size of the debris, the gaseous products were assumed to be at a temperature equilibrium with the porous matrix throughout the debris layer. This assumption has been confirmed by calculations of heat conducted at the test conditions.

The unknown quantities $(\overline{Cp + \beta})$ and $\bar{K}_{eff}$ were determined through the simultaneous solution of the energy relation developed at several different exposure times for a constant temperature. Typical thermocouple traces giving the temperature histories at known locations within the debris layer are shown in Figure 3-54. A cross-plot of these traces gave temperature distributions through the ablation model for given values of exposure time. From these two curves the derivatives required in the energy relation were evaluated at the desired time and temperature. The mass loss rate histories were computed from recession history curves. The recession history curves were contracted from the measured recessions of several ablation tests conducted at a constant power setting, each having a different exposure time. The quantities Cp and β were evaluated as a sum coefficient which satisfies the input data requirement of the numerical ablation program. Results of this data reduction scheme are given in Figure 3-65. The value of effective thermal conductivity was verified at the sublimation temperature through the numerical evaluation of a boundary condition to the energy relation taken at the subliming surface:

$$-K_{eff}\frac{dT}{dt}\Big|_{\substack{INTO\\SURFACE}} = \dot{m}\,\bar{\xi}Q_L - K_{VIR}\frac{dT}{dt}\Big|_{\substack{FROM\\SURFACE}}$$

In the initial phase of the radiation ablation test program, indications were that modification of the in-house radiation facility would enable acquisition of the data to determine the ablation performance parameters required for aft body thermal analysis. It was later determined that the use of test data from an outside source (B-5) would be required to determine the performance parameters for the entire temperature range of interest up to that expected at the stagnation point of a re-entry capsule. The in-house radiation tests permitted evaluation of $\bar{K}_{eff}$ and $(\overline{Cp + \beta})$ for the temperature range 550°F to 1500°F. The effective thermal conductivity showed a smooth consistent variation with temperature; however, the specific temperature gave a complex energy parameter relationship which was not discernable from arc-plasma data. This parameter was computed to be positive at the sublimation temperature, 550°F, and to pass through a negative transition phase at about 1,000°F. The data indicate the occurence of an exothermic chemical reaction commencing just above the sublimation temperature and liberating

the maximum amount of energy at about 1100°F.

Prediction of $(\overline{Cp + \beta})$ from the arc-plasma test data using an energy balance technique indicated positive values of the specific gross energy term for temperatures from 2200°R to 4750°R. Arc-plasma model stagnation region surface temperatures were not sufficiently low to substantiate the $(\overline{Cp})$ calculations from the radiation-ablation data. Temperatures at the arc-plasma model sidewalls were of the desired value; however, the magnitude reduction in convective heating due to upstream mass injection was not known with sufficient accuracy.

There are several factors to be considered when comparing the $(\overline{Cp})$ values obtained from arc-plasma results using a gross energy balance, with the radiation-ablation results using internal temperature traces.

1. The gross energy balance method of determining the Cp term from the air-arc plasma test data yielded an approximate determination of the mean value, where the achievement of an accurate energy balance in the arc-plasma facility is difficult.

2. It is probable that $(Cp + \beta)$ is dependent upon pressure. The radiation ablation tests were conducted at a pressure of one atmosphere while the arc-plasma runs were conducted at very low pressures.

Radiation ablation tests performed in an arc-image furnace at a pressure of one atmosphere (B-5) indicated that $(Cp + \beta)$ has an approximate actual mean value of 2.0 for a surface temperature of 4500°F. The magnitude of $(Cp + \beta)$ must therefore increase rapidly with increased temperature from the small negative value found at 1500°F to a positive value in excess of 2.0 at some temperature above 1500°F. Arc plasma ablation tests at low flux levels and one atmosphere pressure using models instrumented with thermocouples at small intervals throughout the material, would verify the in-house radiation ablation results or indicate a behavior dependency of thermal performance upon thermal environment within the debris layer.

Similar to the results in a fluid flow environment, there was strong evidence that the magnitude of $(Cp + \beta)$ is dependent upon the rate of stream oxygen diffusion into the debris layer. The diffusion rate is reduced with increased mass rate of the counterflowing ablation products, such that greater values of $(Cp + \beta)$ would be

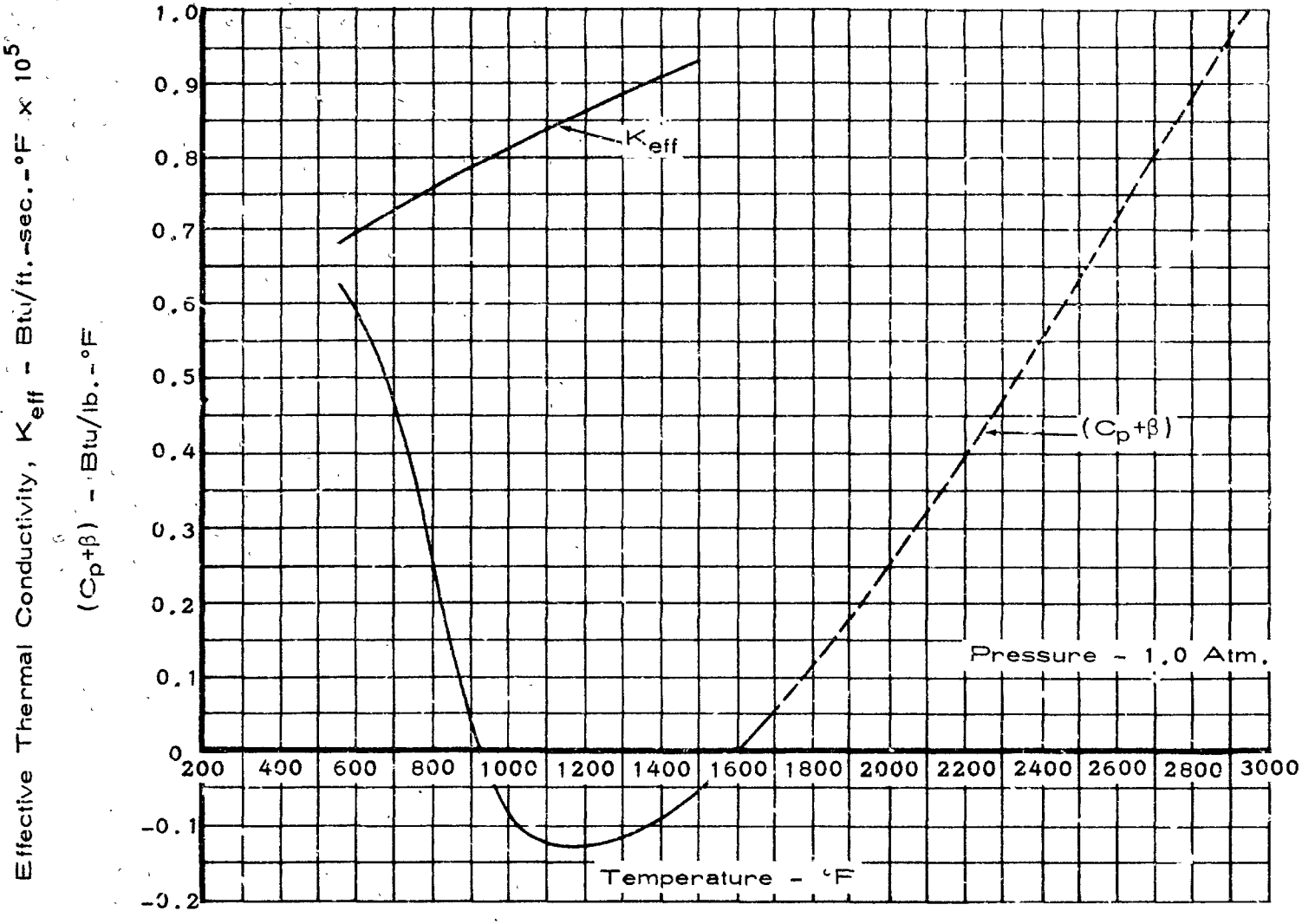


Figure 3-65. Effective Thermal Conductivity of the Debris Layer and the Specific Energy of the Gaseous Ablation Products

realized at large mass ablation rates where the exothermic oxygen reactions in the debris are lessened. This mass transfer effect explains material performance in the pure radiation environments of the Emerson facility and that of reference 5

In a flow environment; $(Cp + \beta)$ was found to be mainly dependent upon surface temperature at the moderate and high enthalpies. At low enthalpies giving surface temperatures of 3200°R and less, $(Cp + \beta)$ was found to increase with decreasing total enthalpy at a constant surface temperature.

ANALYSIS OF BASIC AIR-ARC PERFORMANCE PARAMETERS

In view of the importance of the heating rate to the model surface relative to the determination of ablation performance, the experimentally determined air-arc tunnel stagnation point heat flux levels were correlated with theory. The Fay and Riddell stagnation point heat transfer method was used, assuming no recombination of gas species at the wall. The plasma stream properties were assumed to be those of equilibrium air and were obtained from NASA Technical Report R-50. This comparison of experiment and theory was performed over the entire range of heat flux levels comprising the air-arc plasma jet test matrix. Further confidence in the facility calibration was obtained by correlating transient hot wall copper and graphite calorimeter data with the theoretical results.

The results are plotted in Figure 3-66 as the ratio of experimental heat flux to theoretical heat flux versus stagnation enthalpy. A comparison of the experimental heat flux as obtained from water-cooled calorimeter data showed a maximum scatter of +6 to -20 percent from the theoretical heat flux for stagnation enthalpies ranging from 5000 to 23,000 Btu/Lb. The hot wall transient calorimeter data compared with theory also falls within this deviation. Assuming the validity of the theoretical predication technique for this application the conclusion of this comparison is that the heat flux levels reported by the air-arc facility are reliable for data reduction purposes within limits of +6 to -20 percent.

PARAMETRIC STUDY

The establishment of the reliability of the air-arc facility calibrations permitted resolution of material performance in terms of basic thermodynamic parameters. A parametric study to determine the effect of the endothermic reaction parameter, effective debris layer thermal conductivity, and debris surface temperature on ablation performance was accomplished using the plasma jet test data

obtained under NASA Contract NAS 9-877. The objective of the study was to determine if the experimental temperature and recession histories obtained from the tests could be predicted analytically using reasonable values of these thermodynamic properties.

A numerical analysis technique was used to simultaneously solve the experimentally correlated approximate solution to the ablation model, given in Figure 3-67 and an energy balance at the surface of the model for a given set of test conditions (stagnation enthalpy and convective heat flux specified). A transpiration cooling factor $\alpha = 0.6$ and heat sublimation $Q_L = 500$ Btu/Lb were used in the study.

These parameters were kept constant throughout the analysis. The results of the parametric study are plotted as total material recession and debris surface temperature versus plasma jet exposure time. The results appear in Figures 3-68 through 3-72.

Figure 3-68 shows the material response to a stagnation enthalpy of 5110 Btu/Lb_m and a net hot wall heat flux to the model surface, excluding mass injection, of 60 Btu/Ft^2-sec. The specific heat ratio or endothermic reaction parameter was maintained constant at $Cp/Cpo = 0.57$ and the debris thermal conductivity ratio, k/ko, was varied from 0.5 to 1.5. Decreasing the thermal conductivity threefold resulted in a reduction of the material recession of approximately 36 percent at 300 seconds exposure but increased the debris surface temperature only 3 percent. Thus, it is apparent that the virgin material recession is strongly dependent upon the debris thermal conductivity but the surface temperature is not appreciably affected by change in thermal conductivity.

Figures 3-69 and 3-70 provide a comparison of the effect of the net heat flux to the model surface on debris layer surface temperature. The parametric effects shown in Figure 3-69 represent the experimental conditions of test point No. 10. Examination of Figure 3-69 shows that the total recession curve (solid line, $Cp/Cpo = 1$) obtained from the parametric study reproduced the experimental recession data point for 300 seconds exposure, but the predicted surface temperature is approximately 600°F higher than the measured temperature. Figure 3-70 presents the theoretical analysis for the same conditions with the exception that the net heat flux to the model surface is 60 Btu/Ft^2-sec. It is noted in Figure 3-70 that the debris layer surface temperature predicted by the simplified theoretical analysis corresponds to the actual surface temperature obtained by experiment. The predicted recession, however, is 15 percent low.

The surface temperature was found to be relatively independent of the debris layer thermal conductivity and the specific heat factor but the total recession was not. Therefore, a reduction in Cp/Cpo, and increase in k/ko or a combination of both will increase the recession to correspond to the experimental value without showing any appreciable effect on the surface temperature. The data presented in Figure 3-71 indicates that both surface temperature and total recession can be predicted by changing k/ko to 1.5 and keeping other factors constant. This represents one combination of the specific heat factor and effective thermal conductivity ratio which can be used to predict the experimental recession and temperature history. Experimental determination of the endothermic reaction parameter and debris thermal conductivity establishes the limiting values of these parameters.

Comparison of the theoretical temperature histories of Figures 3-69 and 3-70 indicates that the net heat flux to the model surface is critical in determining the debris layer surface temperature, or conversely, the surface temperature is predicted upon the actual heat flux to the model surface for a given enthalpy level and material properties. The study indicates that the heat flux to the model surface for the environmental conditions of test point No. 10 is of the order of 60 Btu/Ft^2-sec. rather than 110 Btu/Ft^2-sec. The cold wall heat flux measured by the water-cooled calorimeter is the sum of the pure convective heat flux to the calorimeter and the heat flux due to recombination of gas species at the wall. The heat flux to the "THERMO-LAG" test model surface is less than the cold wall calorimeter heat flux. The fact that gas species do not recombine at the debris surface and the occurrence of endothermic reactions within the boundary layer reduces the heat flux for this point.

The material response to a cold wall heat flux of 110 Btu/Ft^2-sec. and a 15,052 Btu/Lb enthalpy level as predicted by theory is shown in Figure 3-72. These conditions correspond to test point Number 23 of the air arc test matrix. To perform the analysis the following material properties were used:

Transpiration Cooling Factor	0.6
Debris Layer Thermal Conductivity Ratio	1.0
Heat of Sublimation	500 Btu/Lb
Endothermic Reactior Parameter Ratio	1.0

The predicted recession history and temperature history agree well with the experimental data point obtained at 300 seconds exposure time. For this test point, the basic mode of heat transfer has changed. The surface temperature which was shown to be critically dependent

upon the net heat flux to the model surface is consistent with that predicted by theory. Indications are that the endothermic effects of boundary layer reactions and sublimation of the carbonaceous debris surface are being overshadowed by undetermined exothermic reactions occurring at the debris surface or within the boundary layer. The study indicates that a comprehensive experimental and theoretical program should be performed to obtain a better understanding of the actual change in heat transfer mechanism associated with the low enthalpy to high enthalpy transition for constant heat flux conditions.

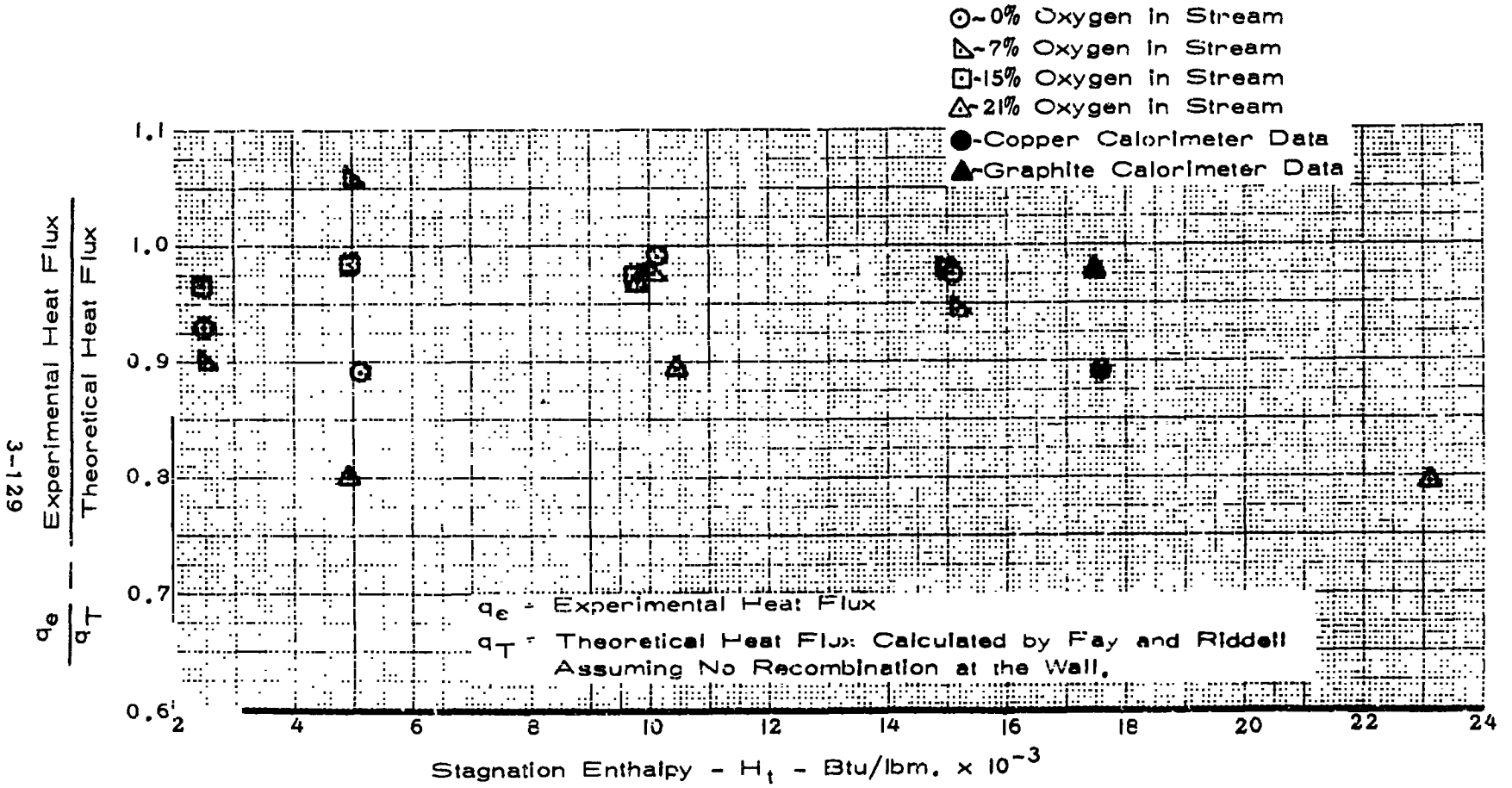


Figure 3-66. Comparison of Experimental and Theoretical Heat Flux

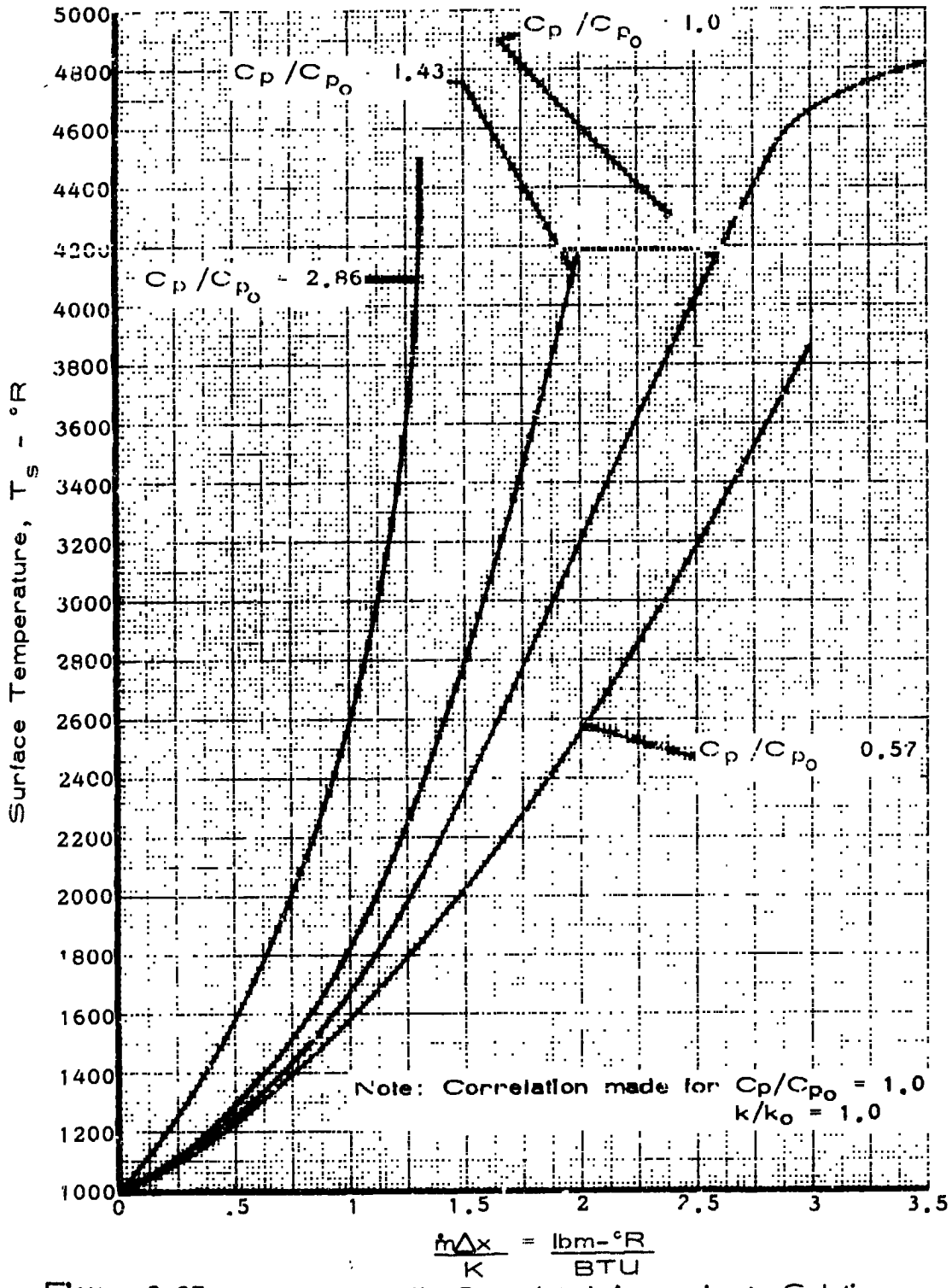


Figure 3-67. Experimentally Correlated Approximate Solution To the Ablation Model and the Effect of C_p/C_{p_o} on Correlation Parameter $\dot{m}$ x/K.

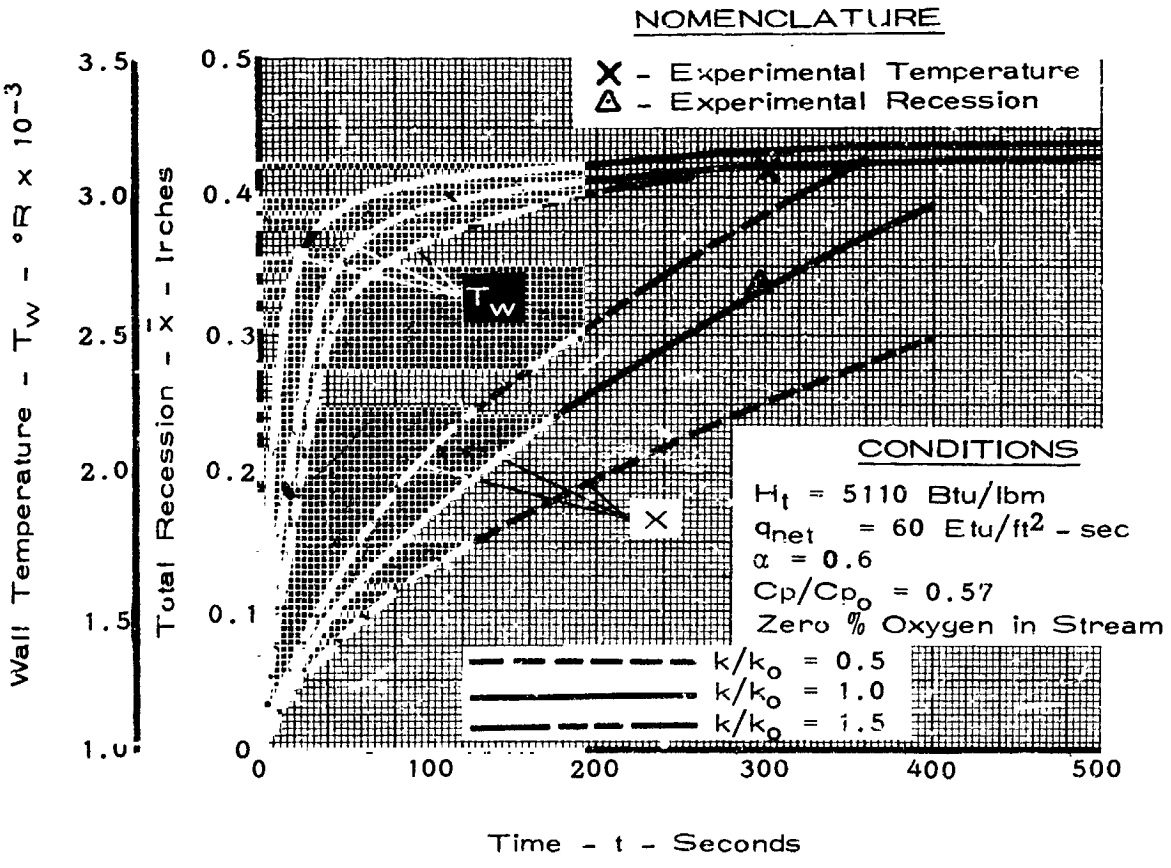


Figure 3-68. Results of Ablation Performance Parametric Study

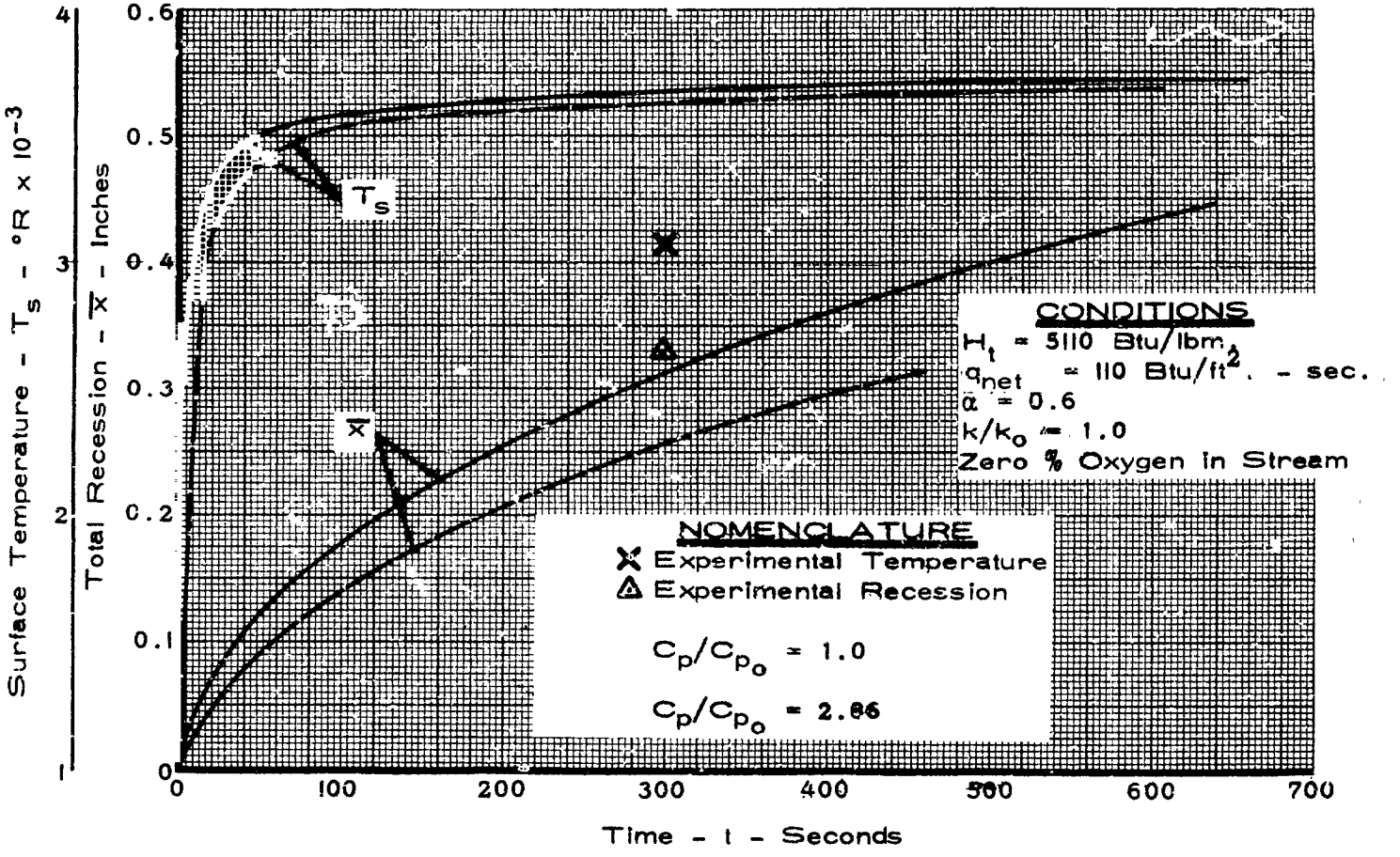


Figure 3-69. Results of Ablation Performance Parametric Study.

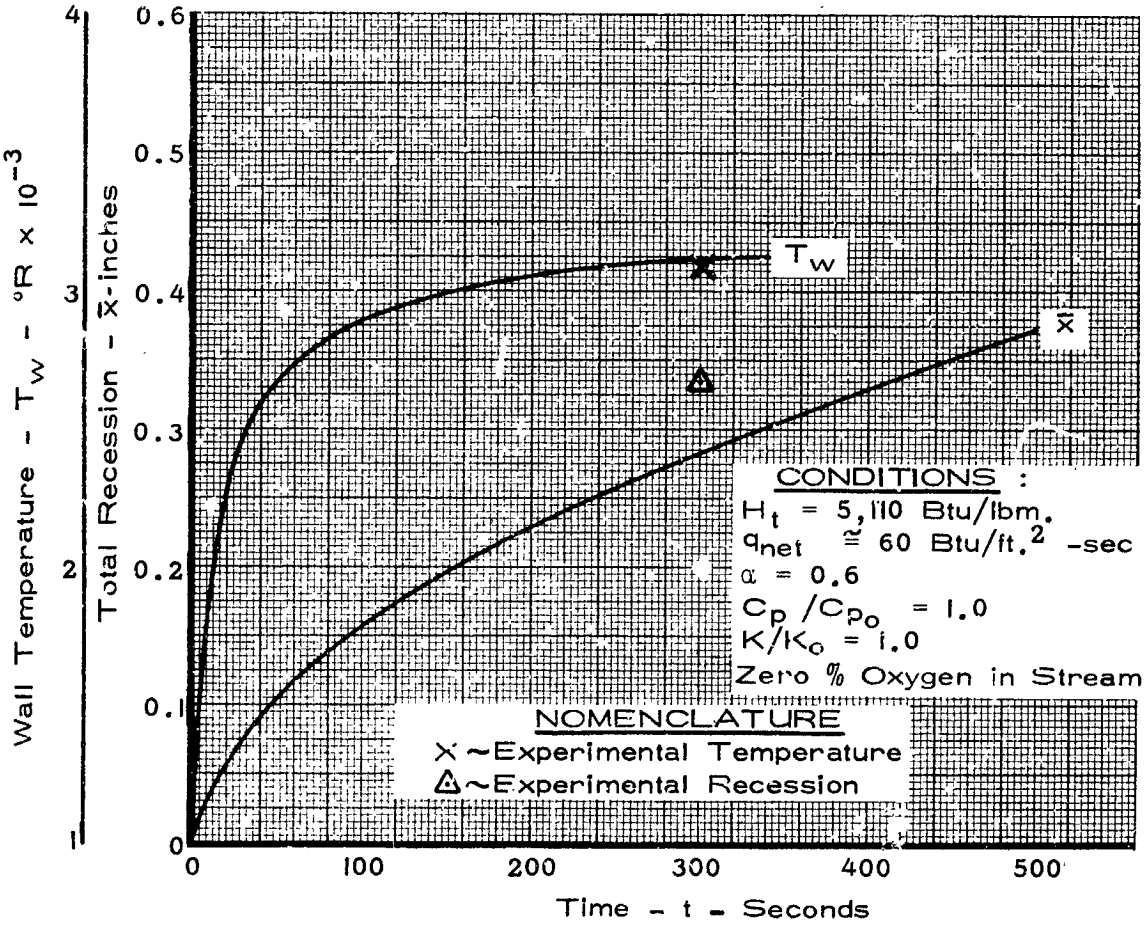


Figure 3-70. Results of Ablation Performance Parametric Study

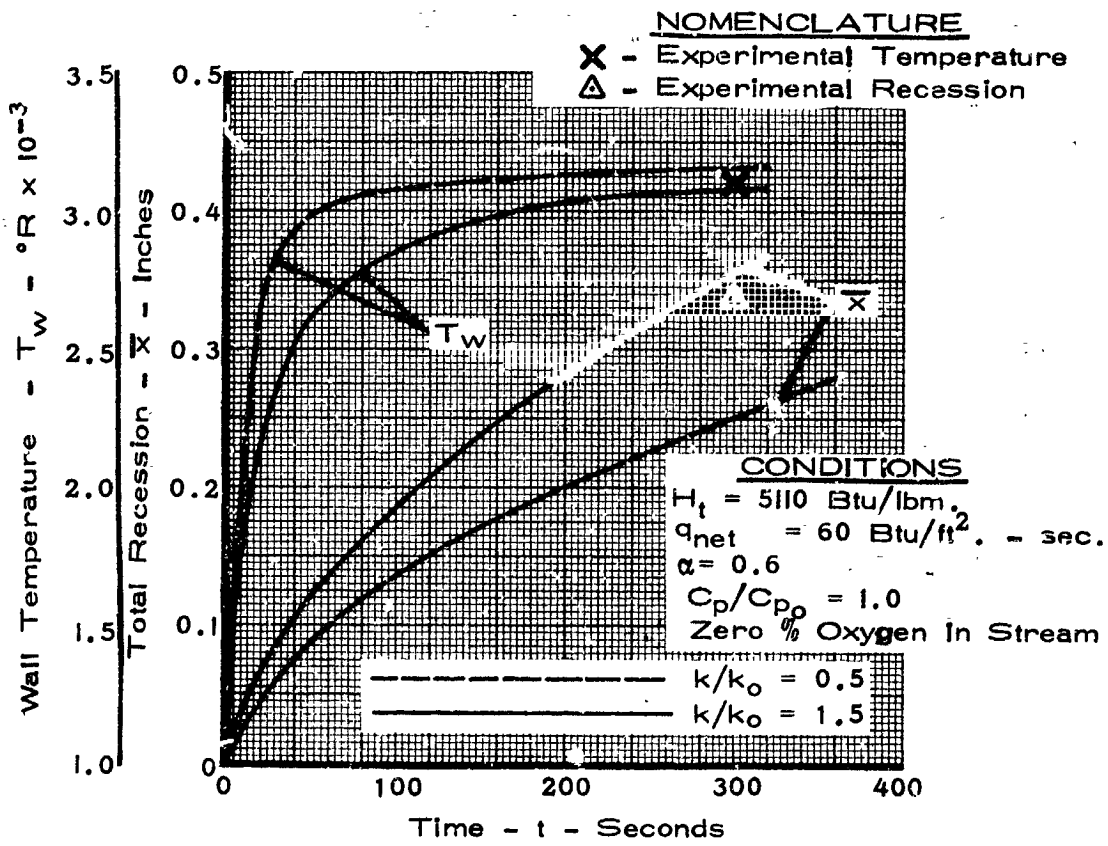


Figure 3-71. Results of Ablation Performance Parametric Study

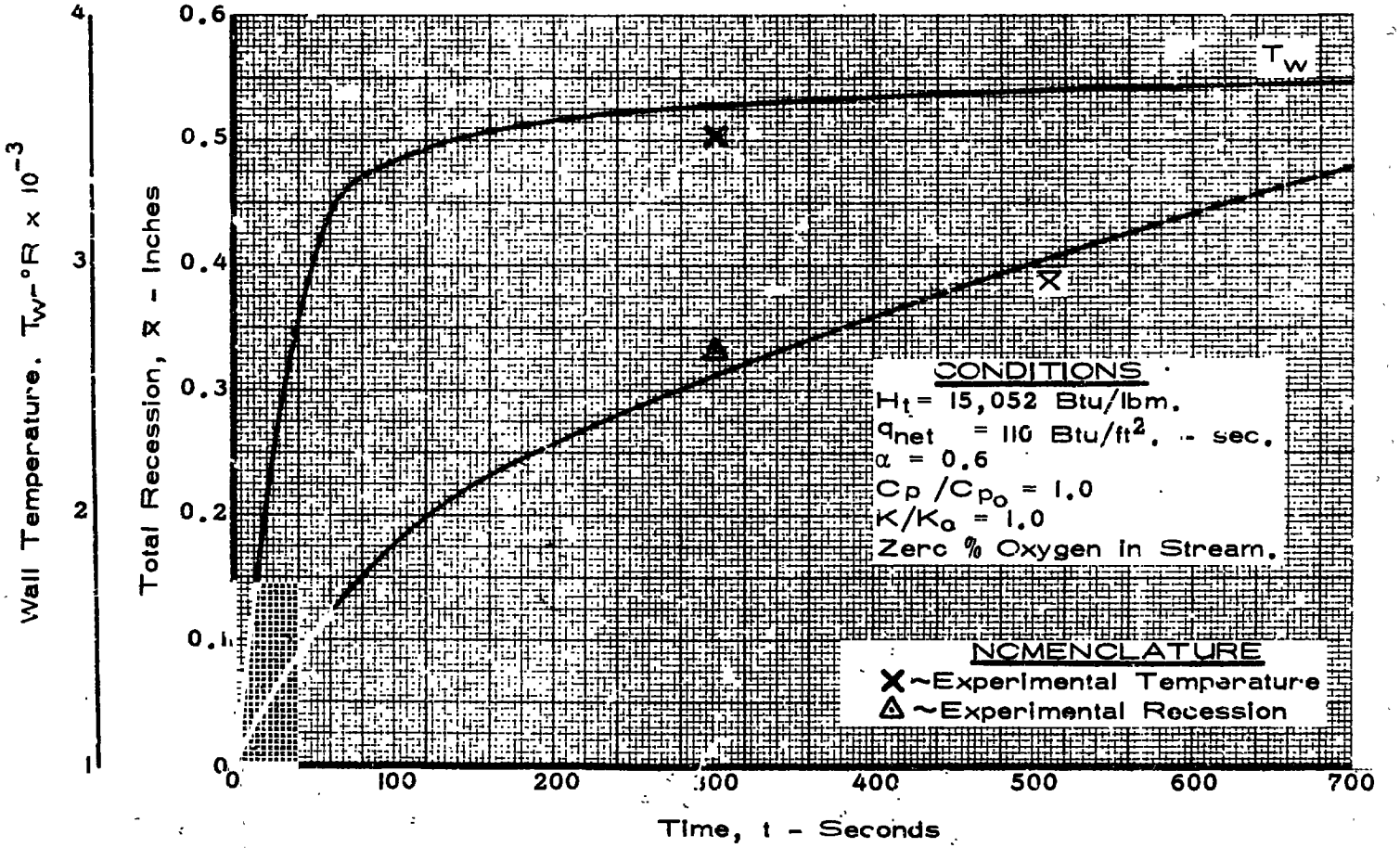


Figure 3-72. Results of Ablation Performance Parametric Study

SECTION IV
NOMENCLATURE

C_p Specific Heat, a constant pressure (Btu/Lb °R)

H Enthalpy, (Btu/Lb)

$\overline{Hi}$ H_l/H_{se}, static enthalpy ratio of species I, (Dimensionless)

h Coefficient of heat transfer (Btu/Ft^2-Sec-°F)

k Coefficient of thermal conductivity (Btu/Ft-Sec-°F)

$\dot{m}_c$ Mass flow rate of injected coolant (Lbs/Sec)

N_{uN} Nusset No, defined by $\frac{hx}{k}$, (Dimensionless)

N_1 Mass transfer similarity parameter, defined by Equation (3), (Dimensionless)

N_2 Heat transfer similarity parameter defined by Equation (4), (Dimensionless)

q Surface heat transfer rate (Btu/Ft^2-Sec)

r_o Stagnation body nose radius (Inches)

Re_N Reynolds No, $\left(\frac{\rho_u r_o}{\mu}\right)$, (Dimensionless)

T Temperature (°F)

u Velocity component parallel to surface (Ft/Sec)

$\overline{u}$ u_e/u_{se}, Velocity ratio, (Dimensionless)

x Distance along body geometry (Ft)

$\bar{x}$ Nondimensionalized space coordinate along surface (Dimensionless)

α Transpiration cooling factor (Dimensionless)

γ Ratio of specific heats (Dimensionless)

μ Absolute viscosity (Lb/Ft-Sec)

$\bar{\mu}$ μ_e/μ_{se} , Viscosity ratio (Dimensionless)

ρ Density, (Lb/Ft^3)

$\bar{\rho}$ ρ_e/ρ_{se}, Density Ratio, (Dimensionless)

ϕ Real gas parameter ($\rho_{se}/\rho_{se}\, H_{se}$)

ψ Temperature ratio, T_e/T_{se} (Dimensionless)

SUBSCRIPTS

C Denotes flow characteristic prior to mass injection

e Local conditions external to the boundary layer

se Conditions external to the boundary layer at stagnation point

w Conditions evaluated at the wall

SECTION V
REFERENCES

1. Charwatt, A.F., et. al., "An Investigation of Separated Flows" Part II, Journal of the Aerospace Sciences, Volume 28, page 513, July 1961.

2. Libby, P. A., and Cresci, R.J., "Experimental Investigation of the Downstream Influence of Stagnation-Point Mass Transfer" Journal of the Aerospace Sciences, Volume 28, No. 1, pages 51 through 64, January 1961.

3. Lees, L., "Laminar Heat Transfer Over Blunt-Nosed Bodies at Hypersonic Flow Speeds, "Jet Propulsion, Volume 26, No. 4, April 1956.

4. Hoshizaki, H., and Smith, H. J., "Axisymmetric Stagnation Point Mass Transfer Cooling" Lockheed Missiles and Space Division, LMSD - 48379, 17 December 1958.

5. Radiation - Ablation Tests, Southwestern Research Institue, Structural Meeting Unit Research Memorandum Number 43, 10 May 1962.

APPENDIX A

TEMPERATURE-TIME HISTORIES OF AIR-ARC SIMULATION TESTS

The nonreduced air-arc plasmajet substrate temperature-time history data for all "THERMO-LAG" T-500 models tested under NASA Contract 9-877 are presented in Figures A-1 through A-88.

The data presented in Figures A-1 through A-77 can be related to any model tested, the prefix letter of the model. The O series are the surface oxidation tests. The D, E, GG, and HH series are the material investigation tests. The M and N series, constituting the bulk of the performed tests, fulfill the required low pressure, oxidation, transient and pressure effect test matrices.

Figures A-78 through A-87 present data from the material gap tests. The post script letter identifies the orientation of the gap with respect to the flow stream. The letter H indicates that the gap was aligned parallel to the flow stream, while the letter V indicates a gap was aligned normal to the flow stream. Thermocouples numbered 2 and 6 measured temperatures at the bare substrate metal in the gap. Thermocouples numbered 3 and 7 measured temperatures 0.125 inch from the gap. Thermocouples numbered 4 and 8 measured temperatures at positions 0.50 inch from the gap.

The data for the trajectory simulation tests are presented in Figures A-88 and A-89.

Figures A-90 through A-107 present the nonreduced temperature-time histories for the upstream mass injection effect tests.

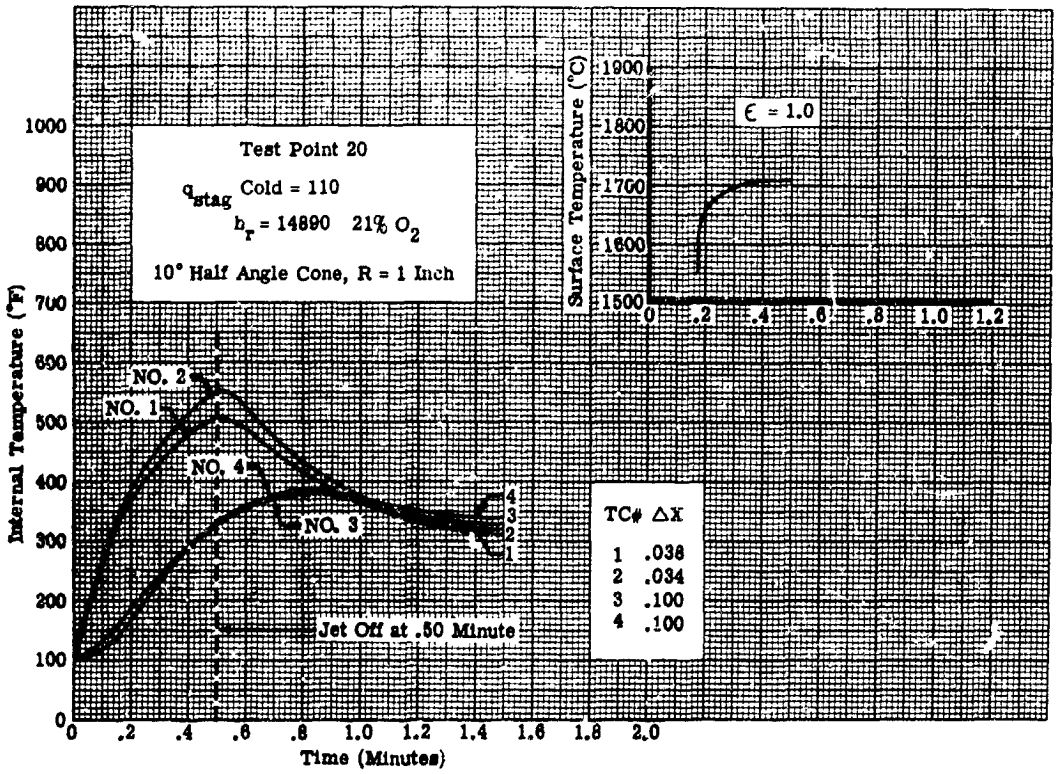


Figure A-1. Temperature-Time History of Model M-6

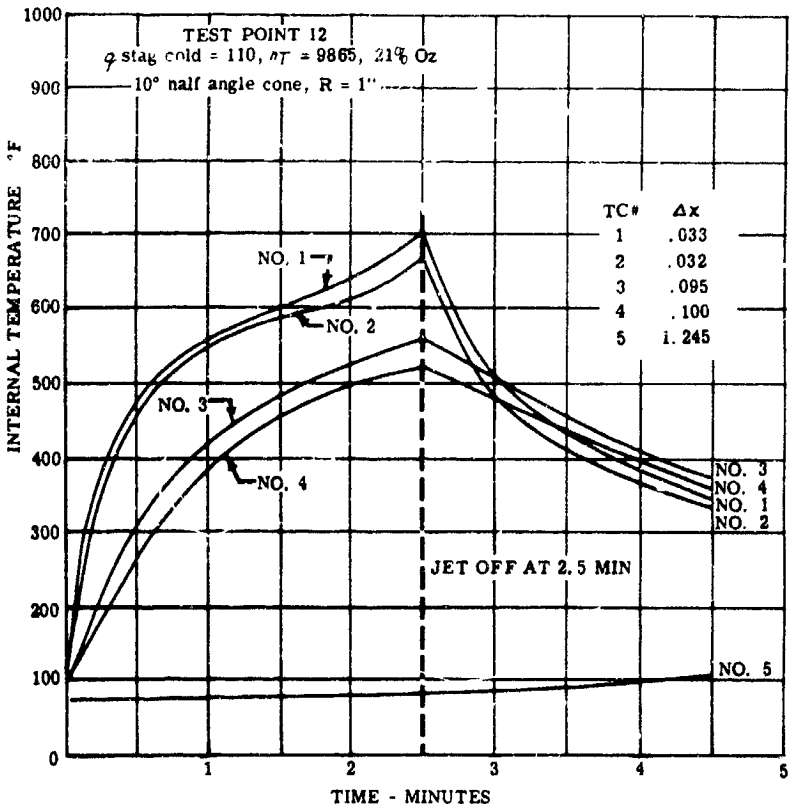


Figure A-2. Temperature-Time History of Model M-9

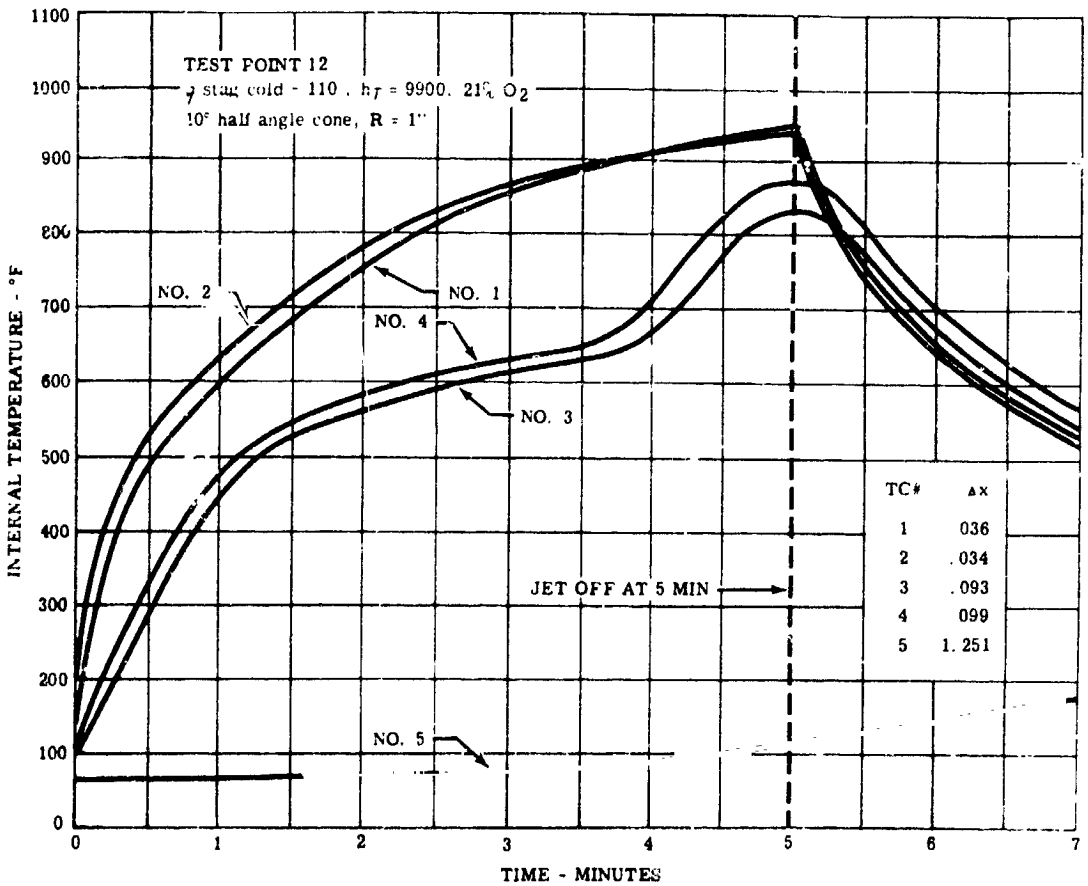


Figure A-3. Temperature-Time History of Model M-10

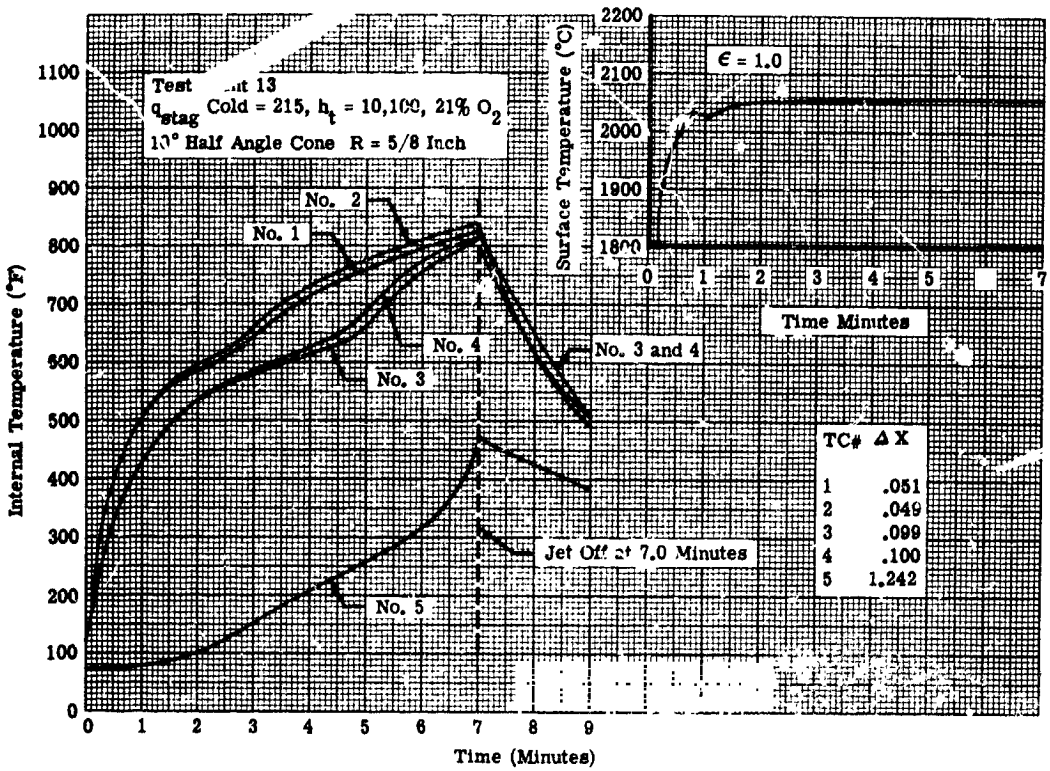


Figure A-4. Temperature-Time History of Model M-18

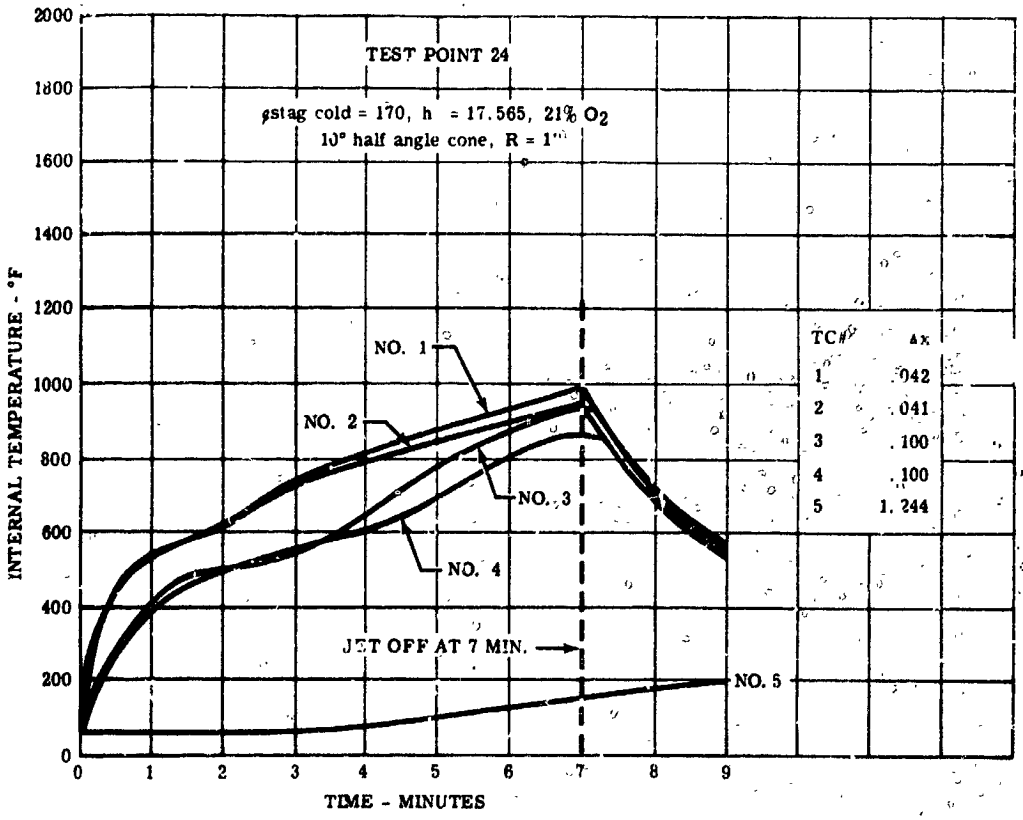


Figure A-5. Temperature-Time History of Model M-16

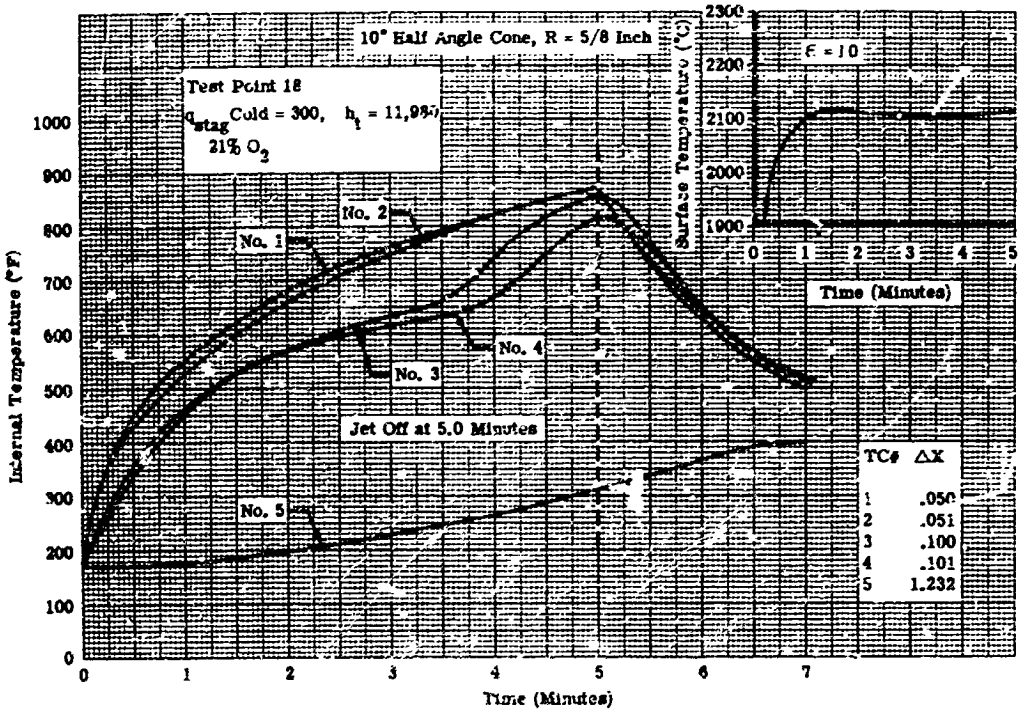


Figure A-6. Temperature-Time History of Model M-19

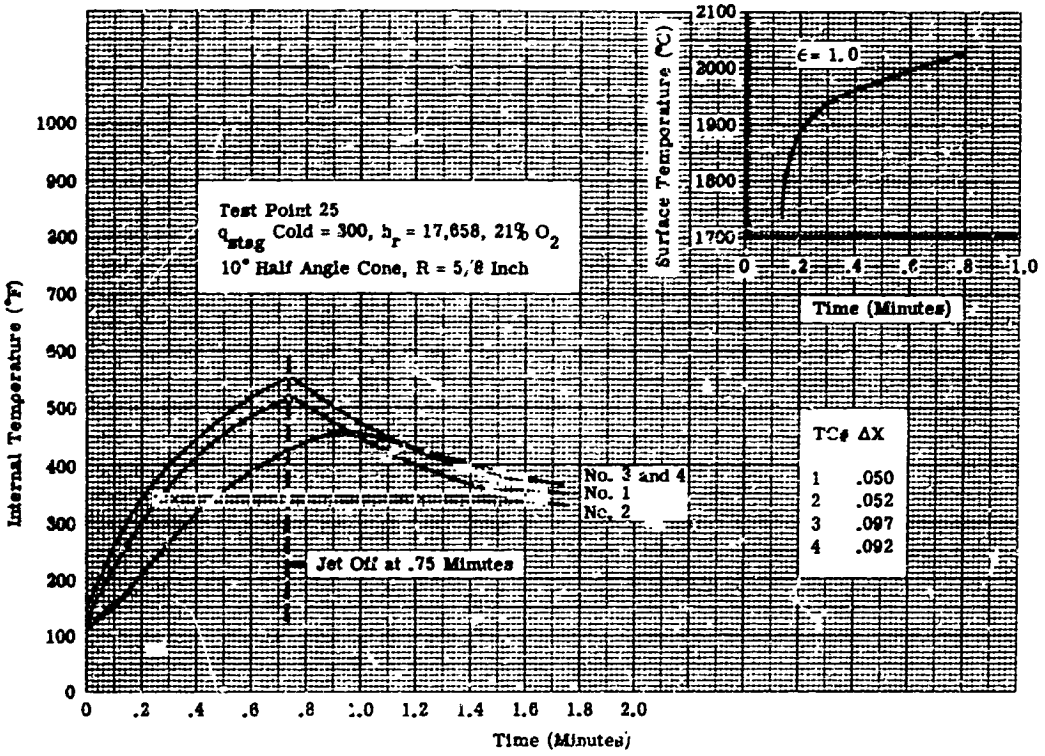


Figure A-7. Temperature-Time History of Model M-21

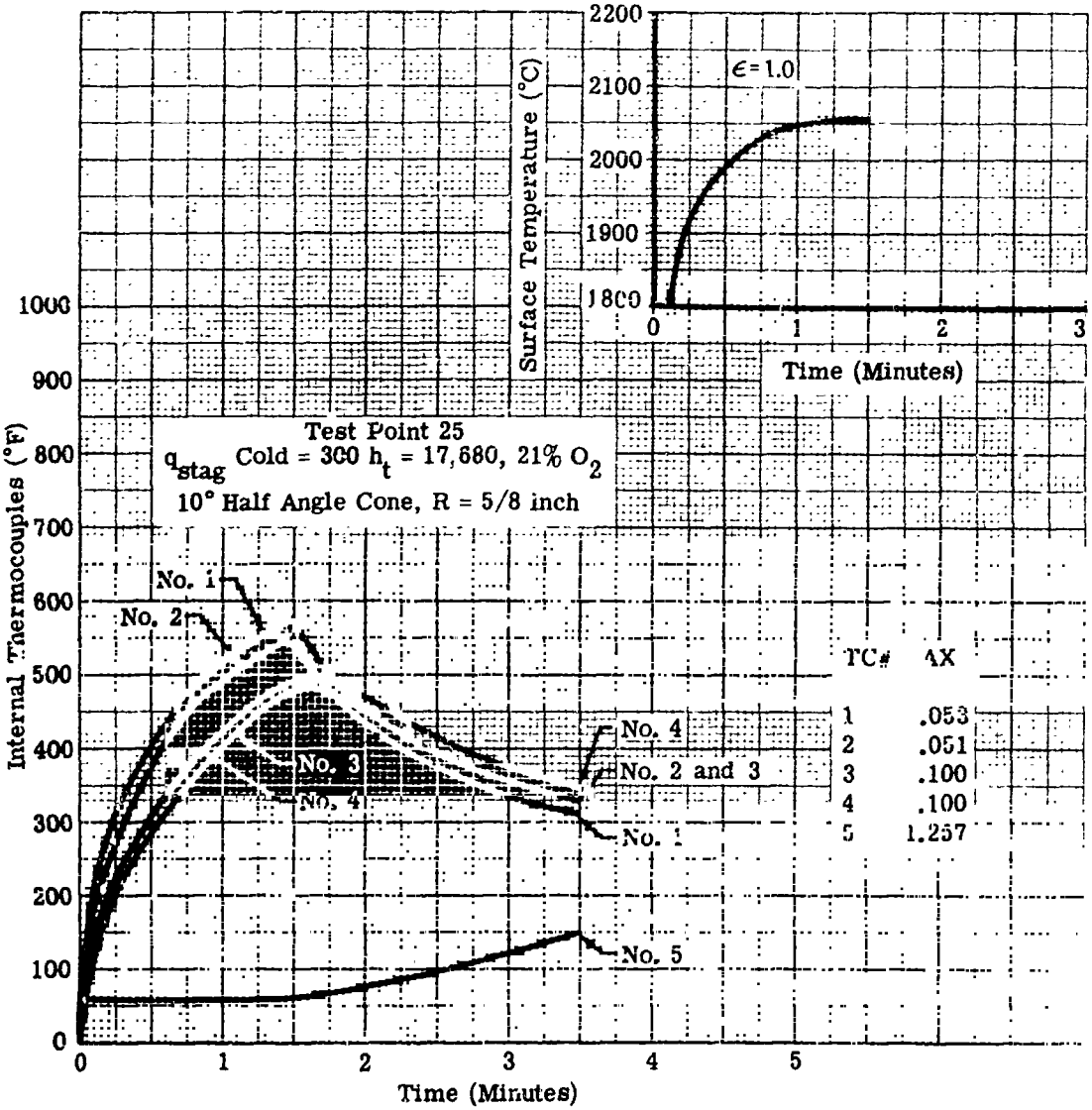


Figure A-8. Temperature-Time History of Model M-22

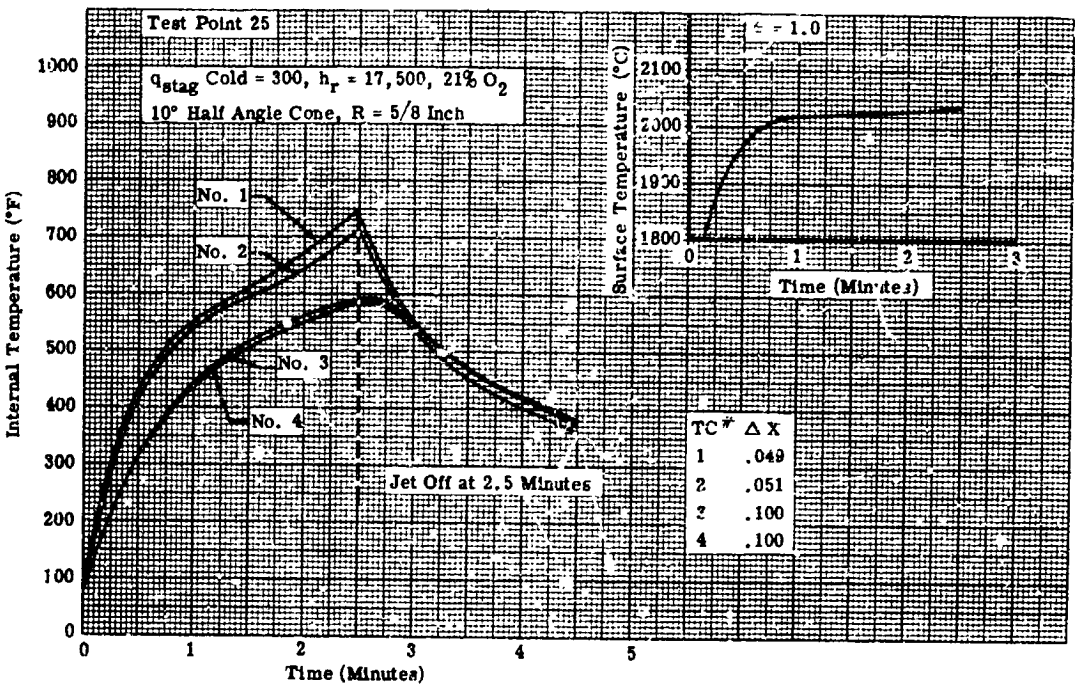


Figure A-9. Temperature-Time History of Model M-23

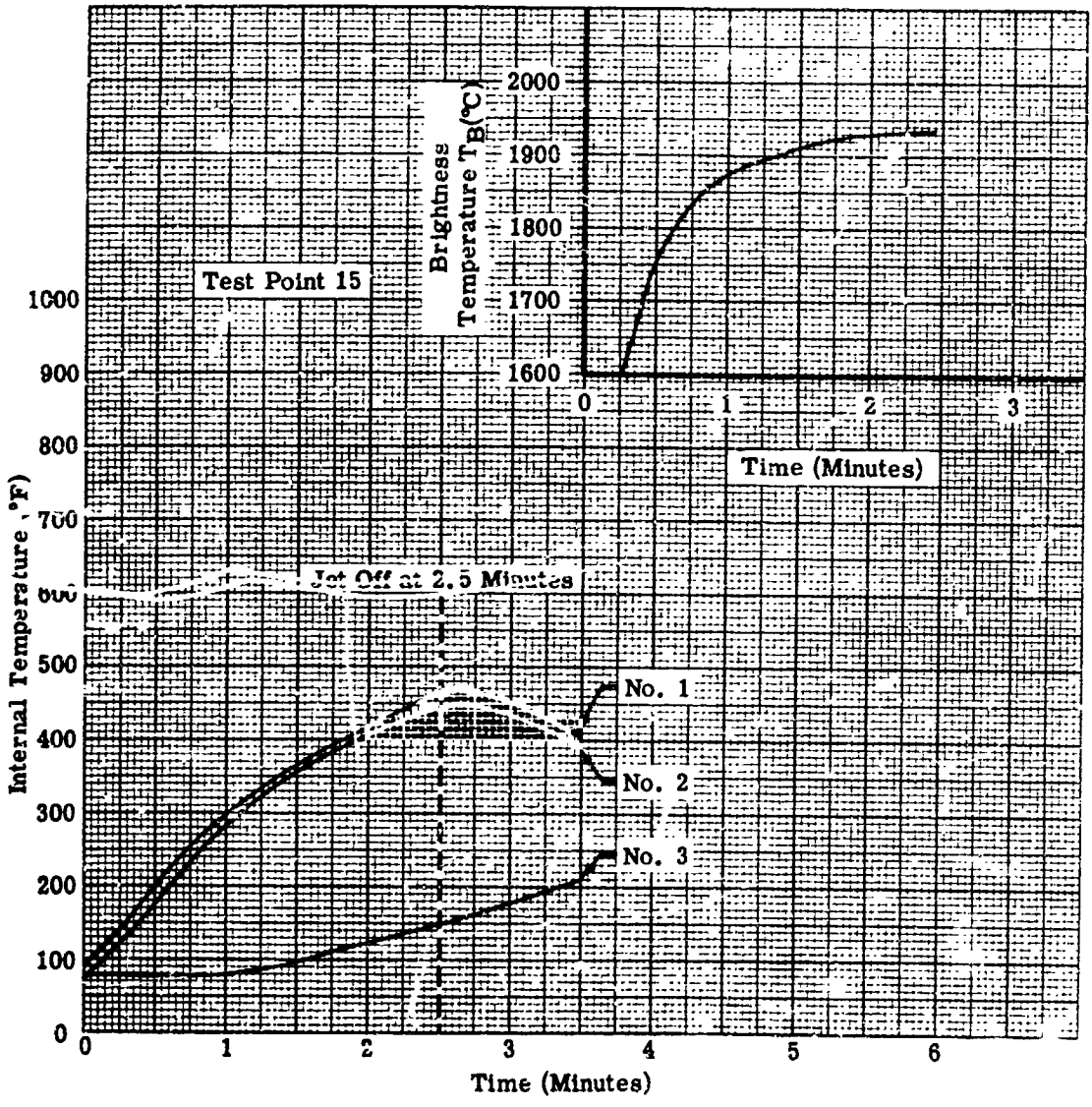


Figure A-10. Temperature-Time History of Model O-1

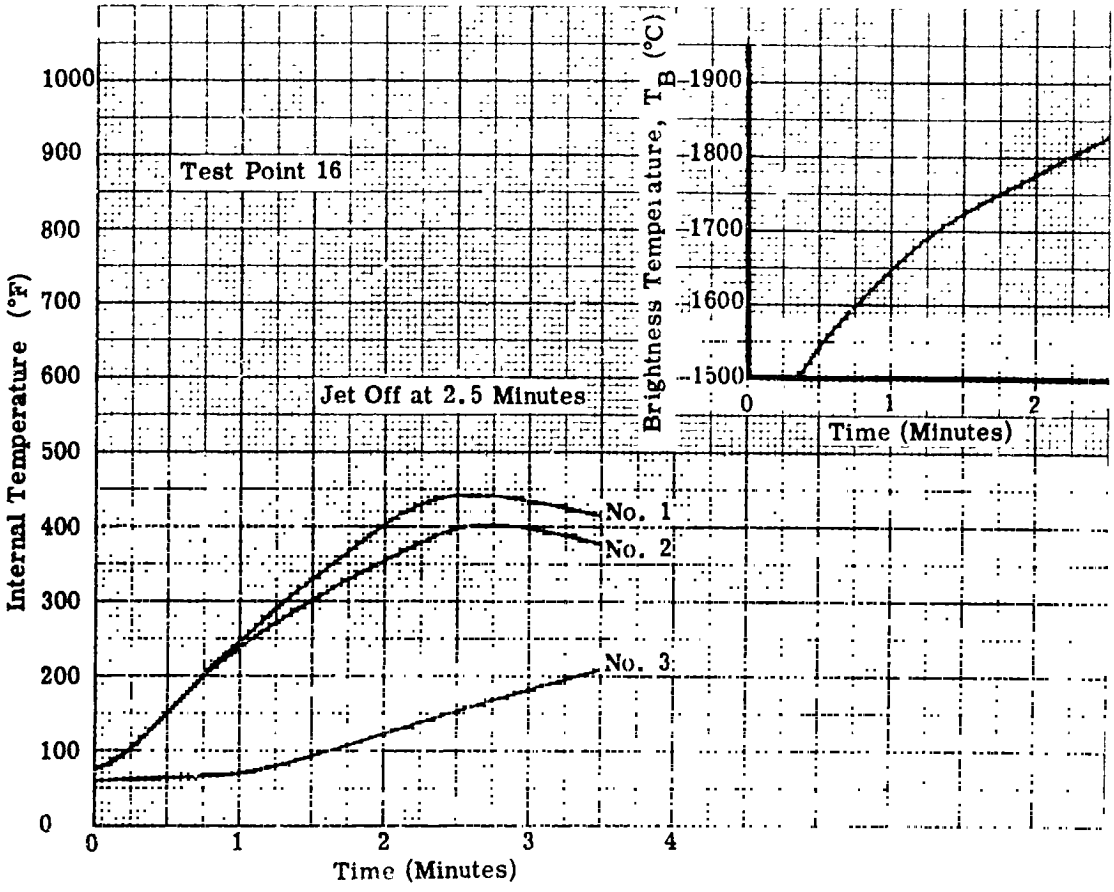


Figure A-11. Temperature-Time History of Model O-2

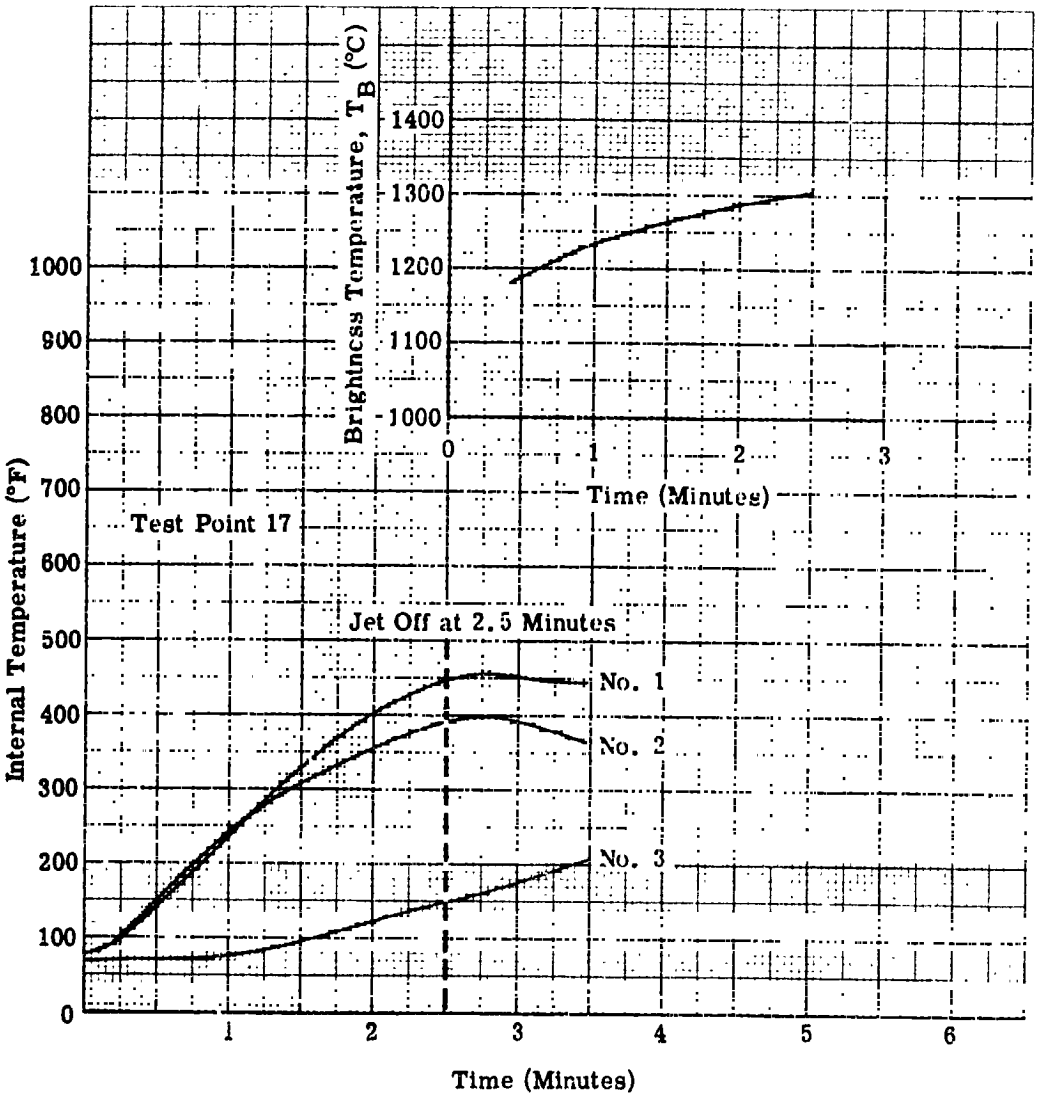


Figure A-12. Temperature-Time History of Model O-3

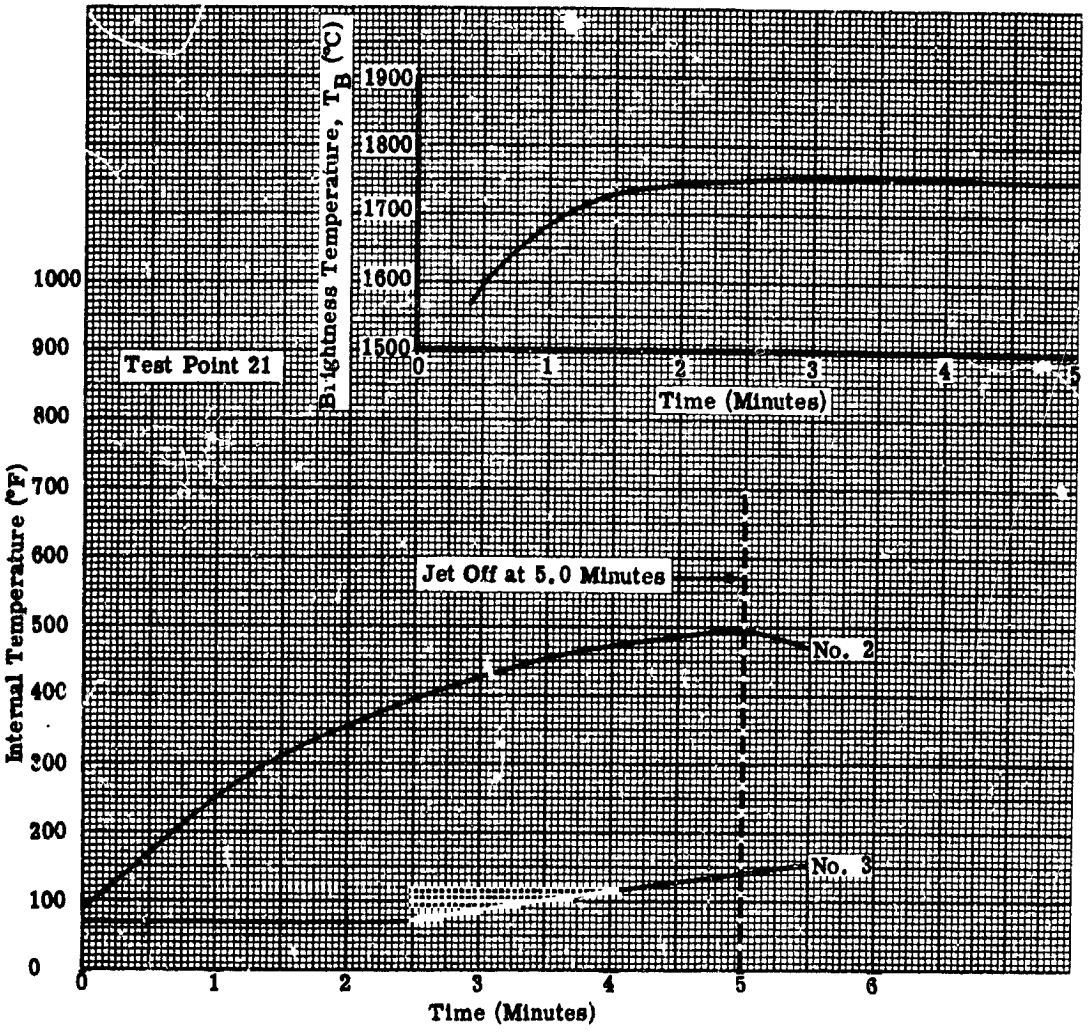


Figure A-13. Temperature-Time History of Model O-6

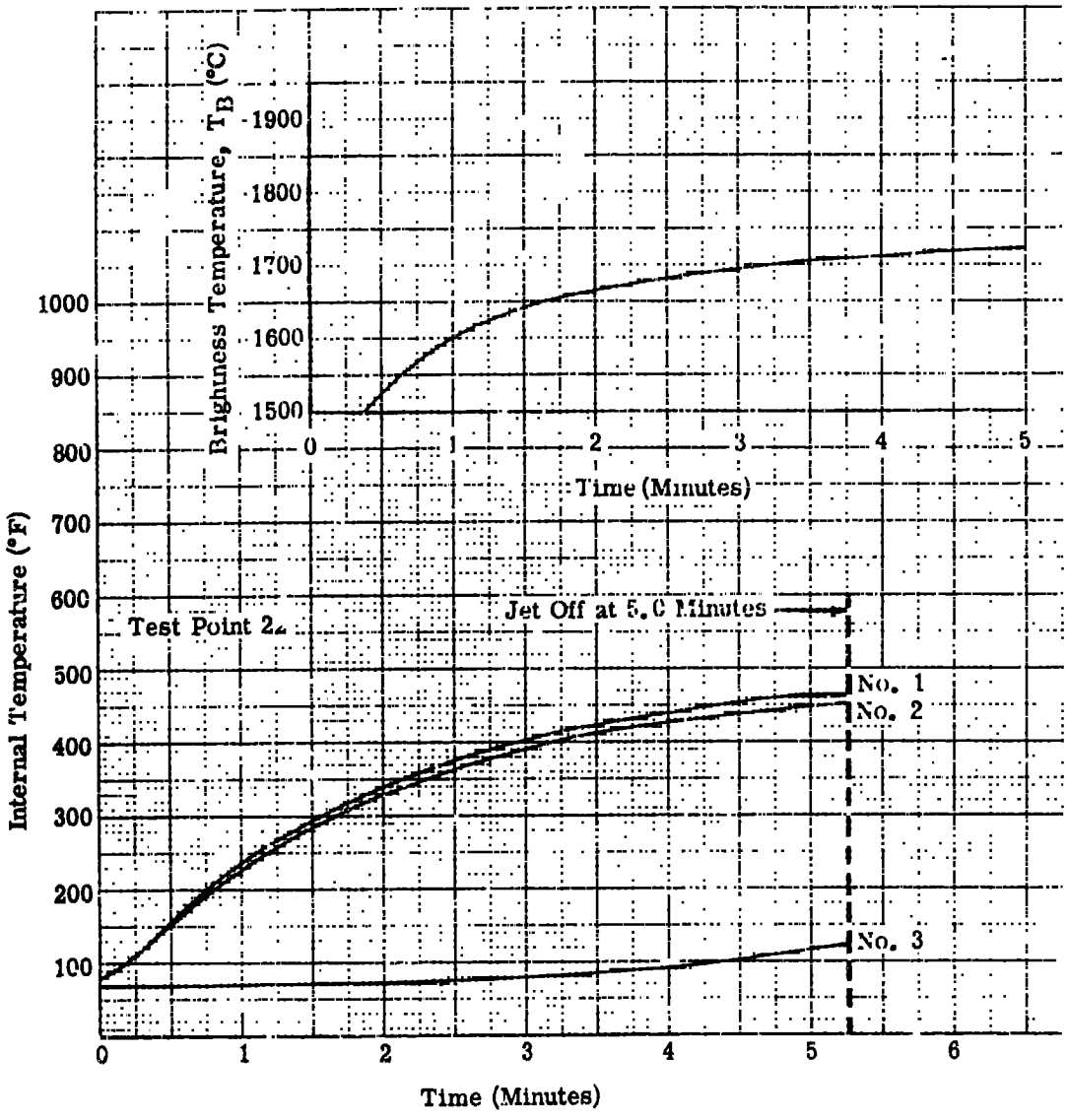


Figure A-14. Temperature-Time History of Model O-7

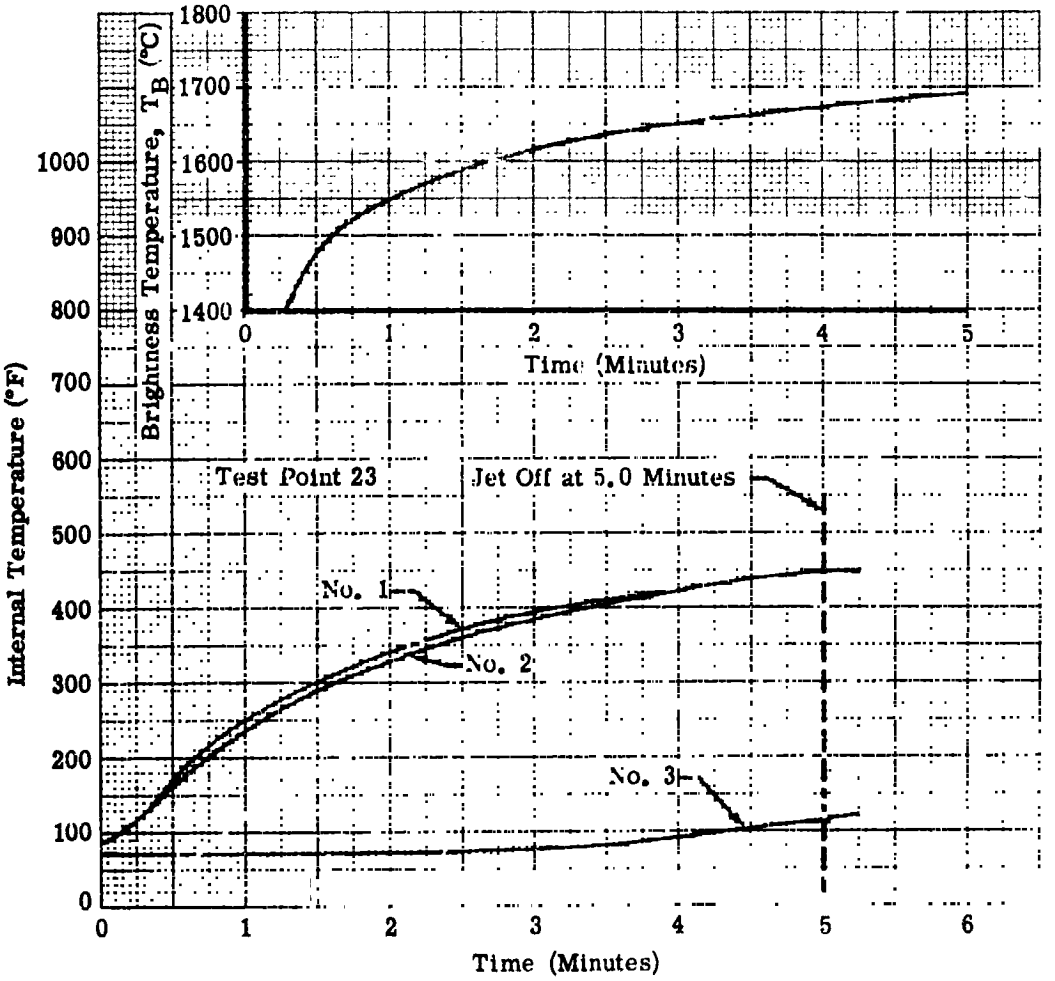


Figure A-15. Temperature-Time History of Model C-8

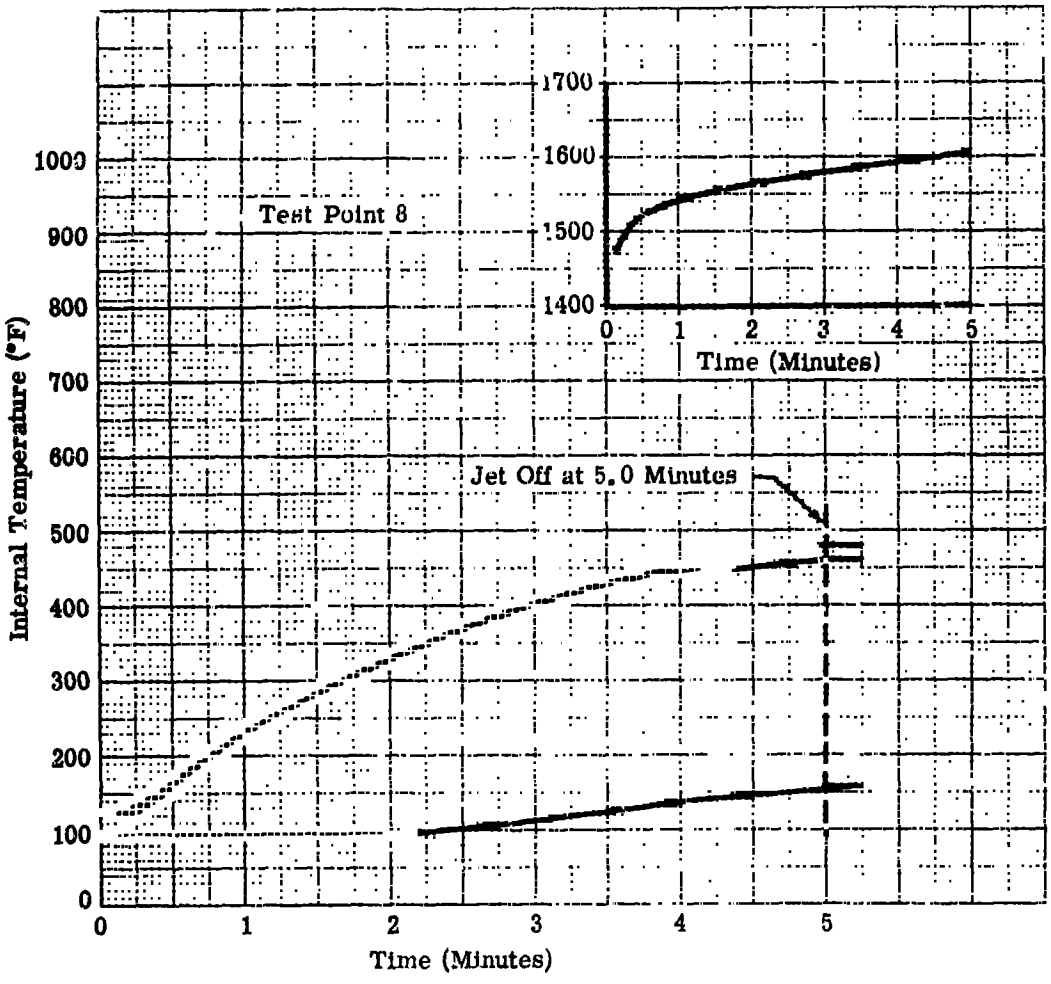


Figure A-16. Temperature-Time History of Model O-9

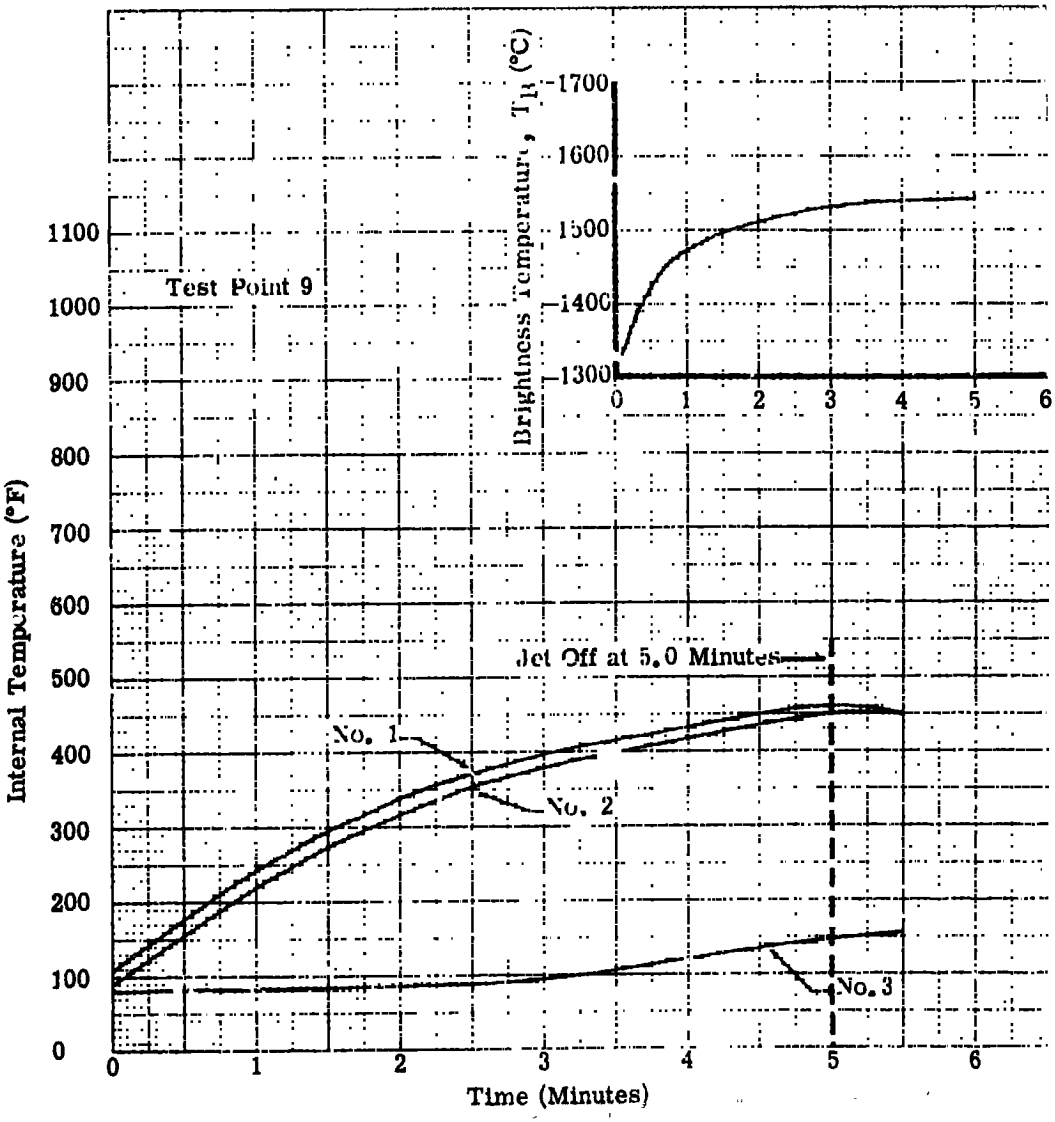


Figure A-17. Temperature-Time History of Model O-11

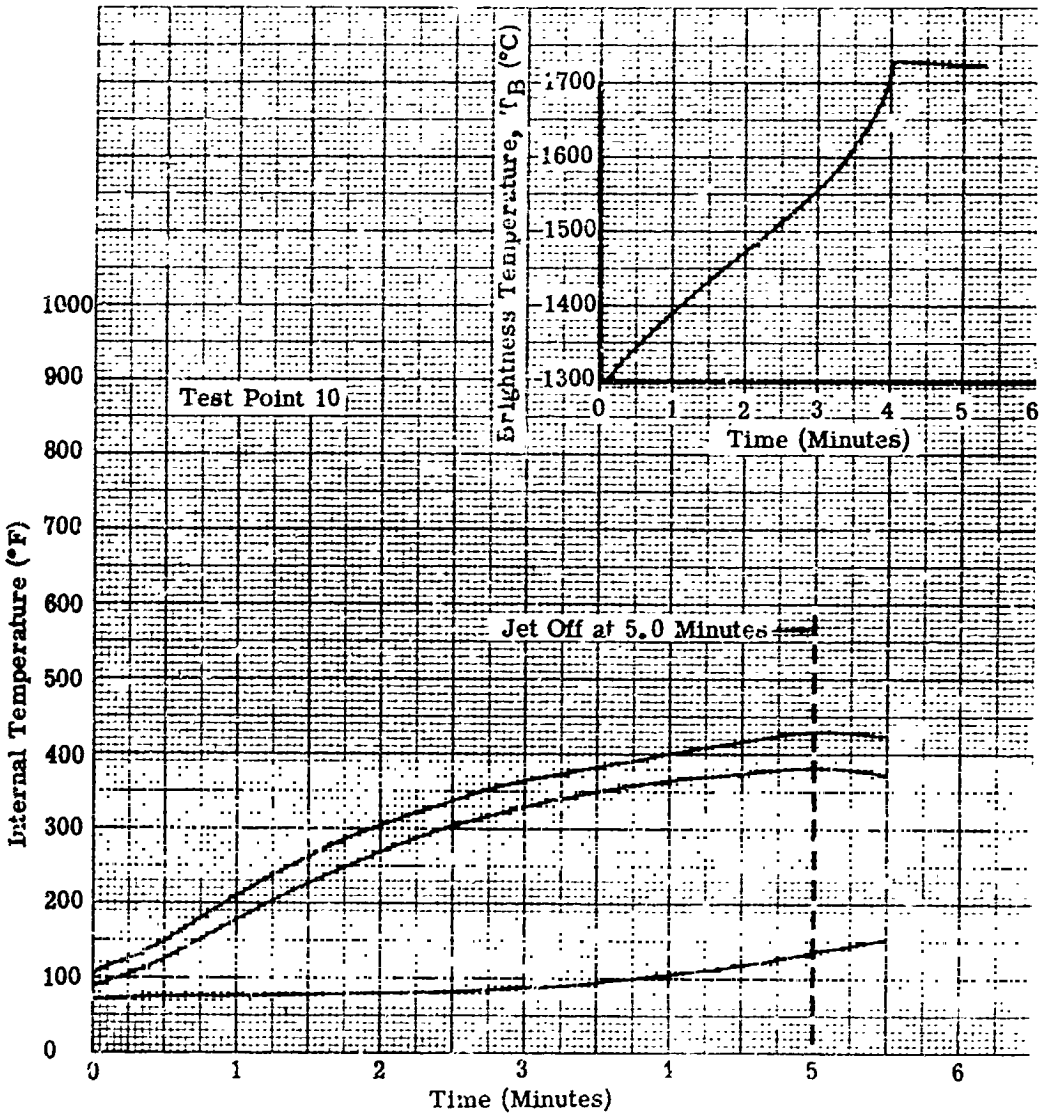


Figure A-18. Temperature-Time History of Model O-13

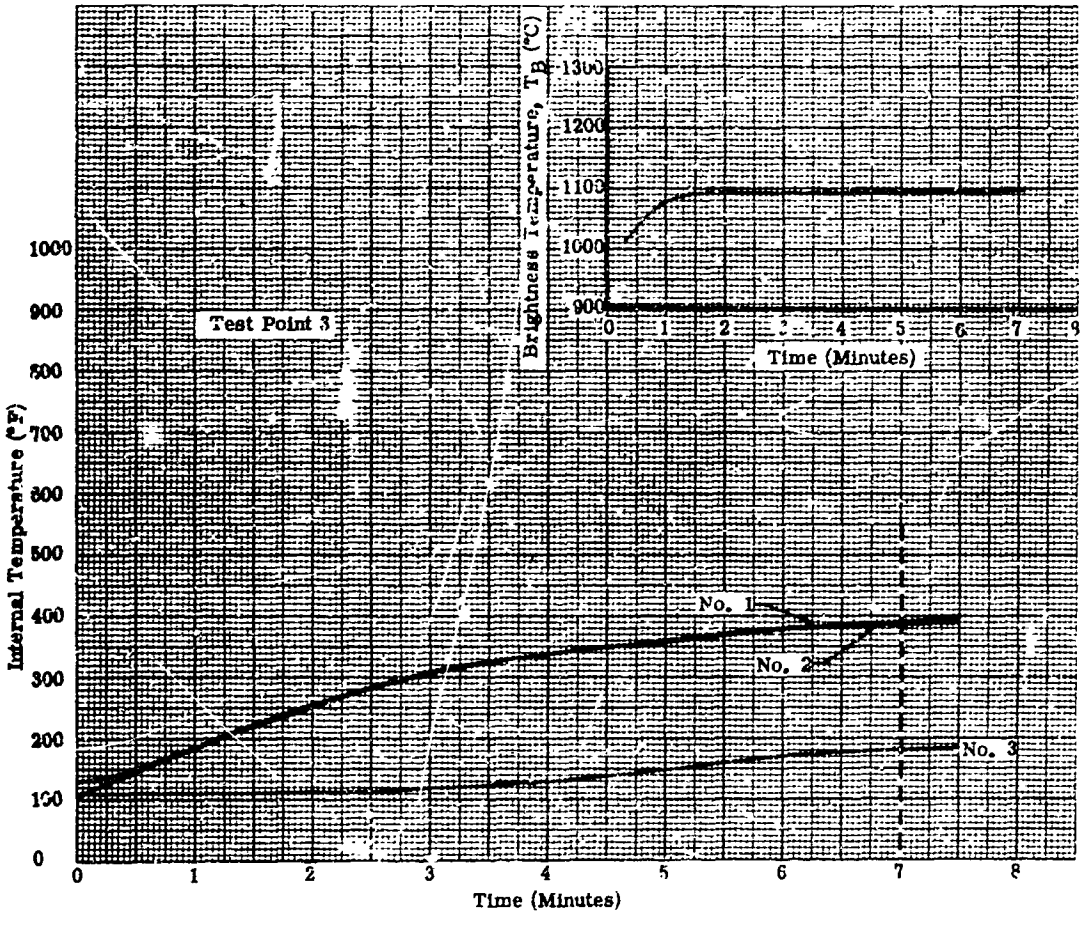


Figure A-19. Temperature-Time History of Model O-14

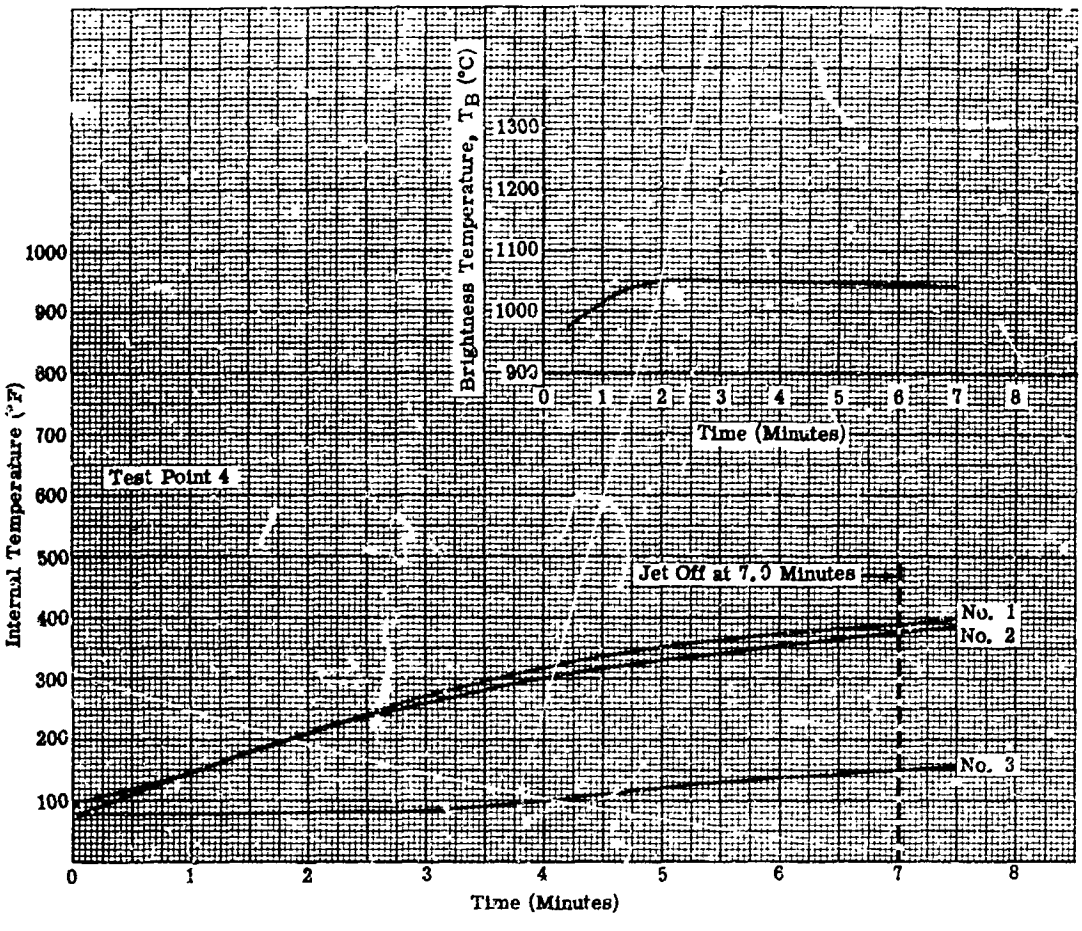


Figure A-20. Temperature-Time History of Model O-15

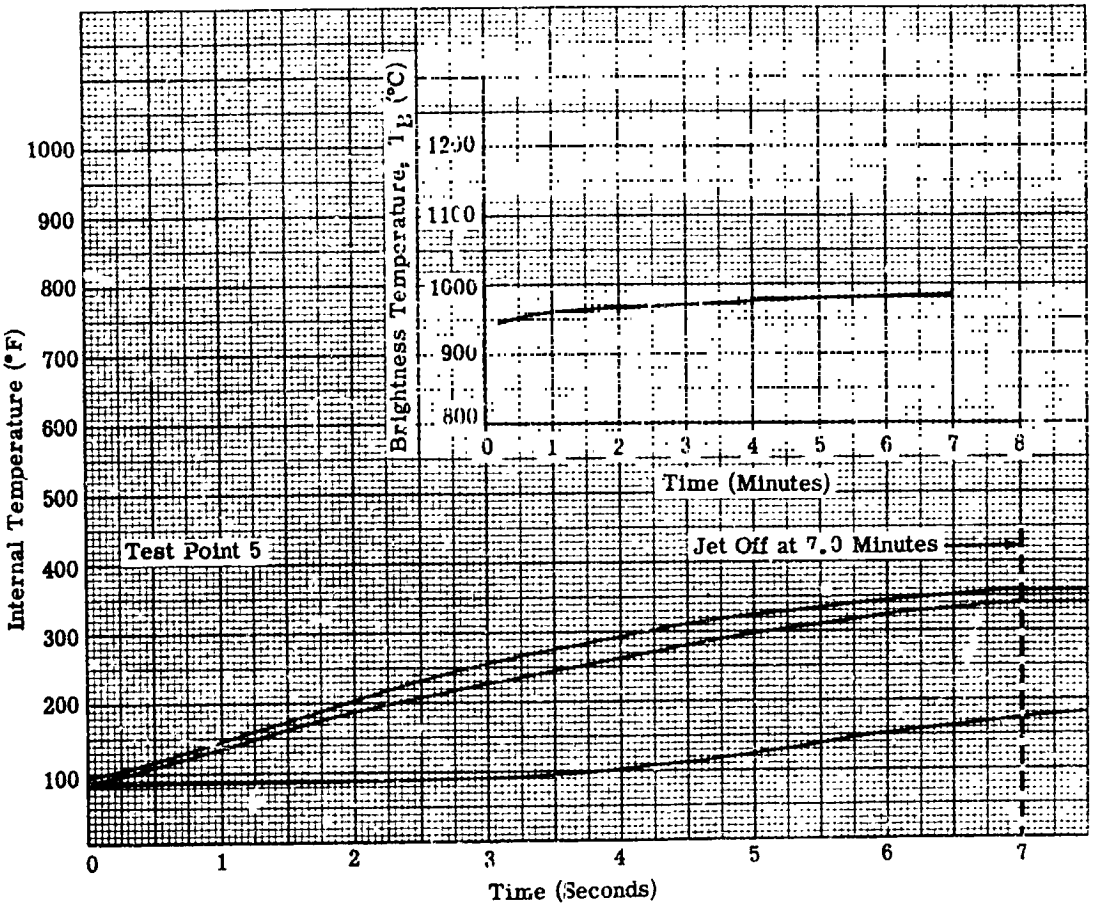


Figure A-21. Temperature-Time History of Model O-16

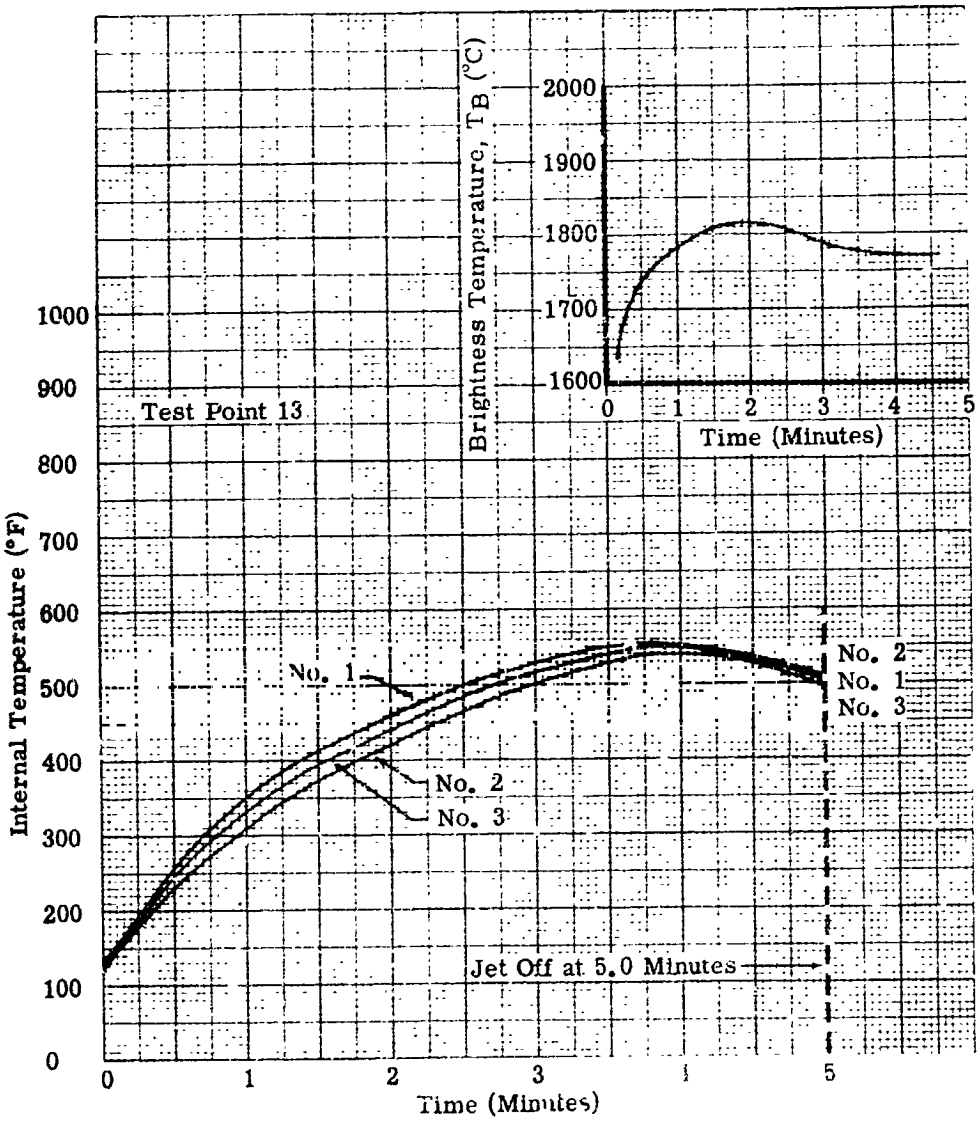


Figure A-22. Temperature-Time History of Model D-12

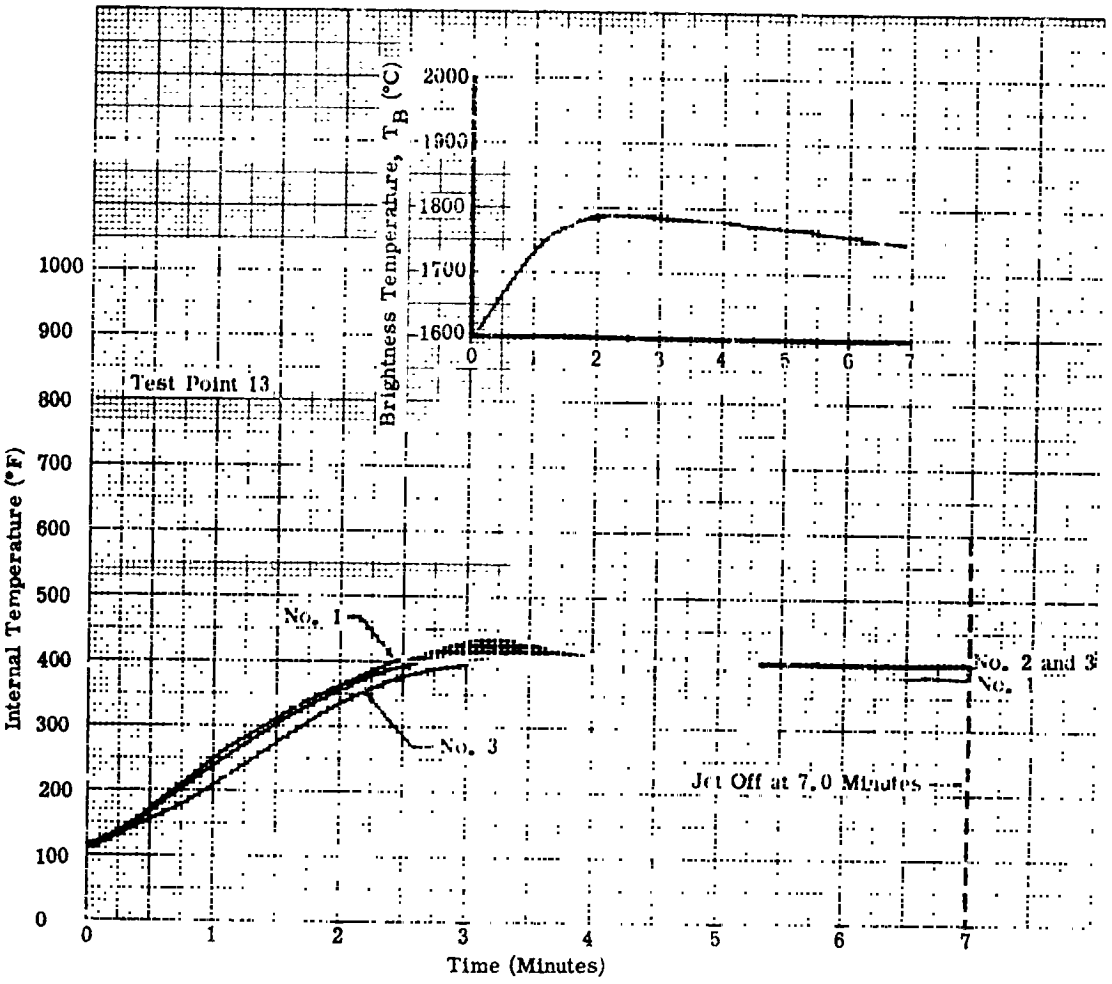


Figure A-23. Temperature-Time History of Model D-2-2

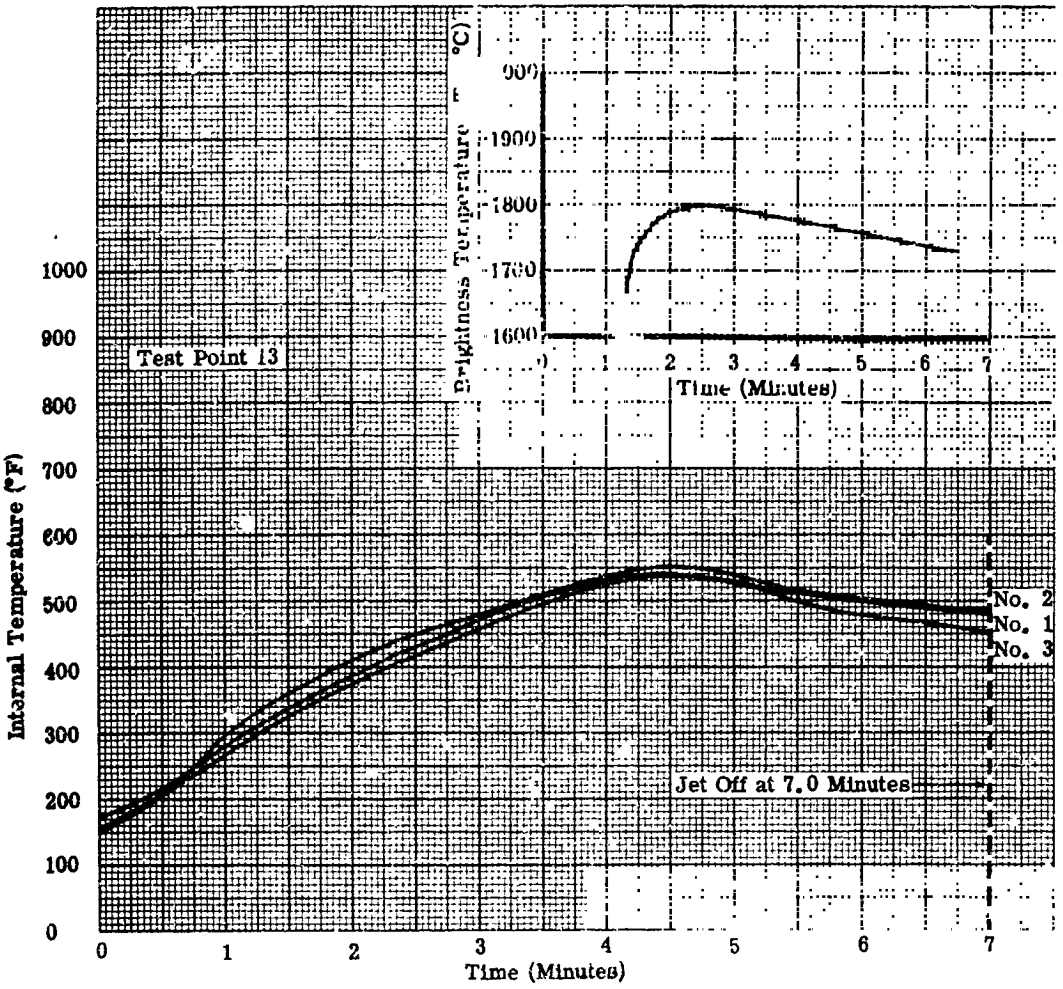


Figure A-24. Temperature-Time History of Model E-12

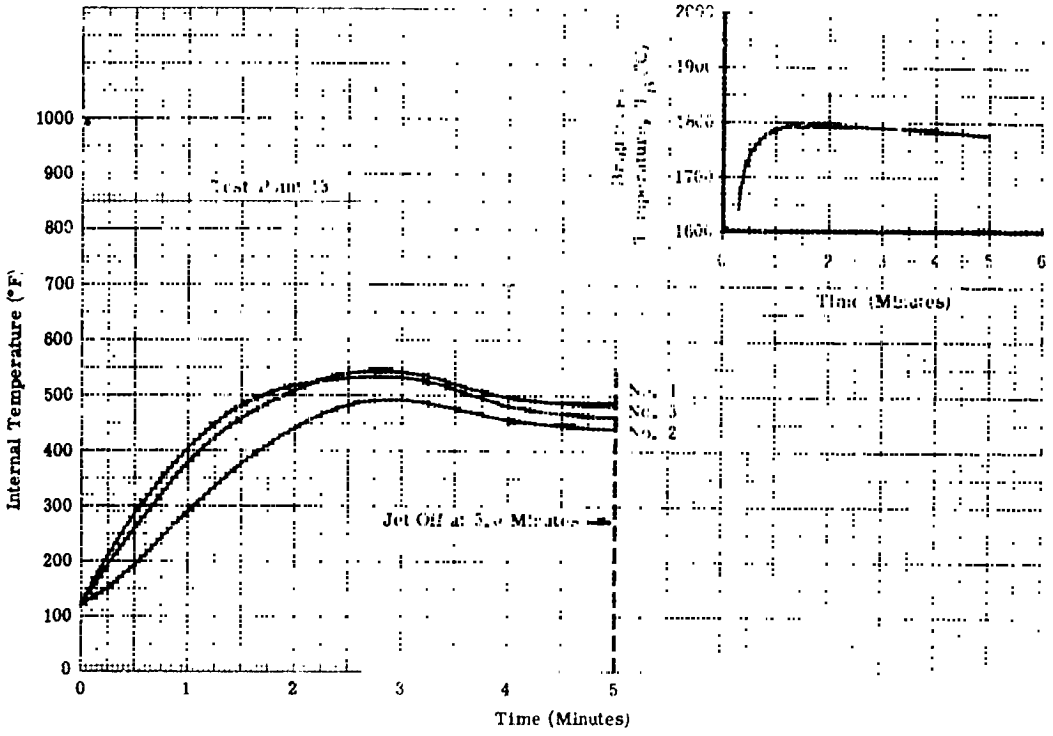


Figure A-25. Temperature-Time History of Model E-22

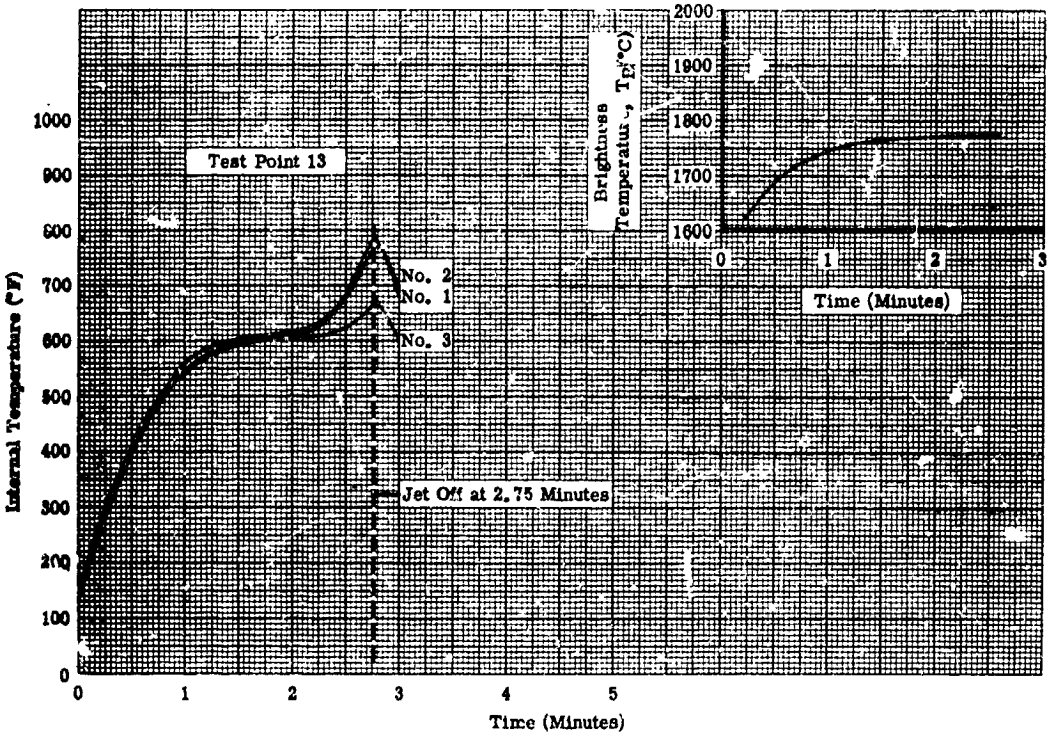


Figure A-26. Temperature-Time History of Model GG-1

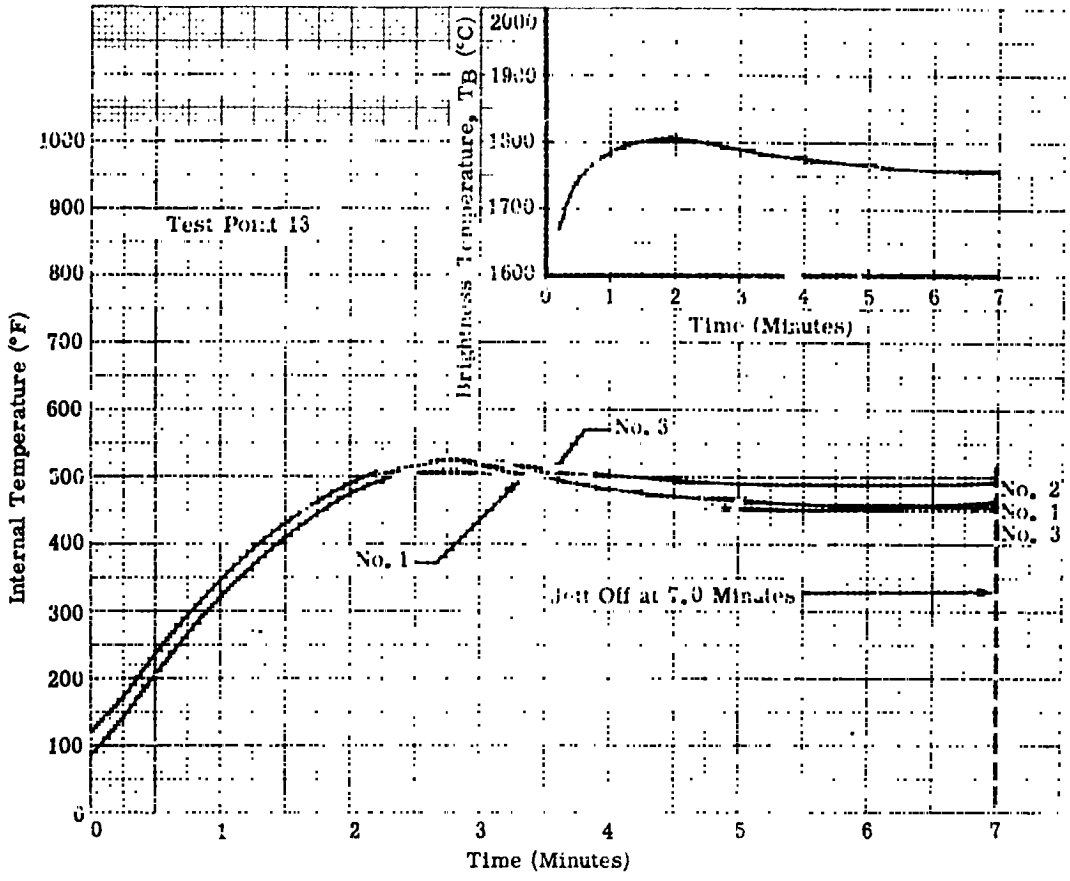


Figure A-27. Temperature-Time History of Model GG-3

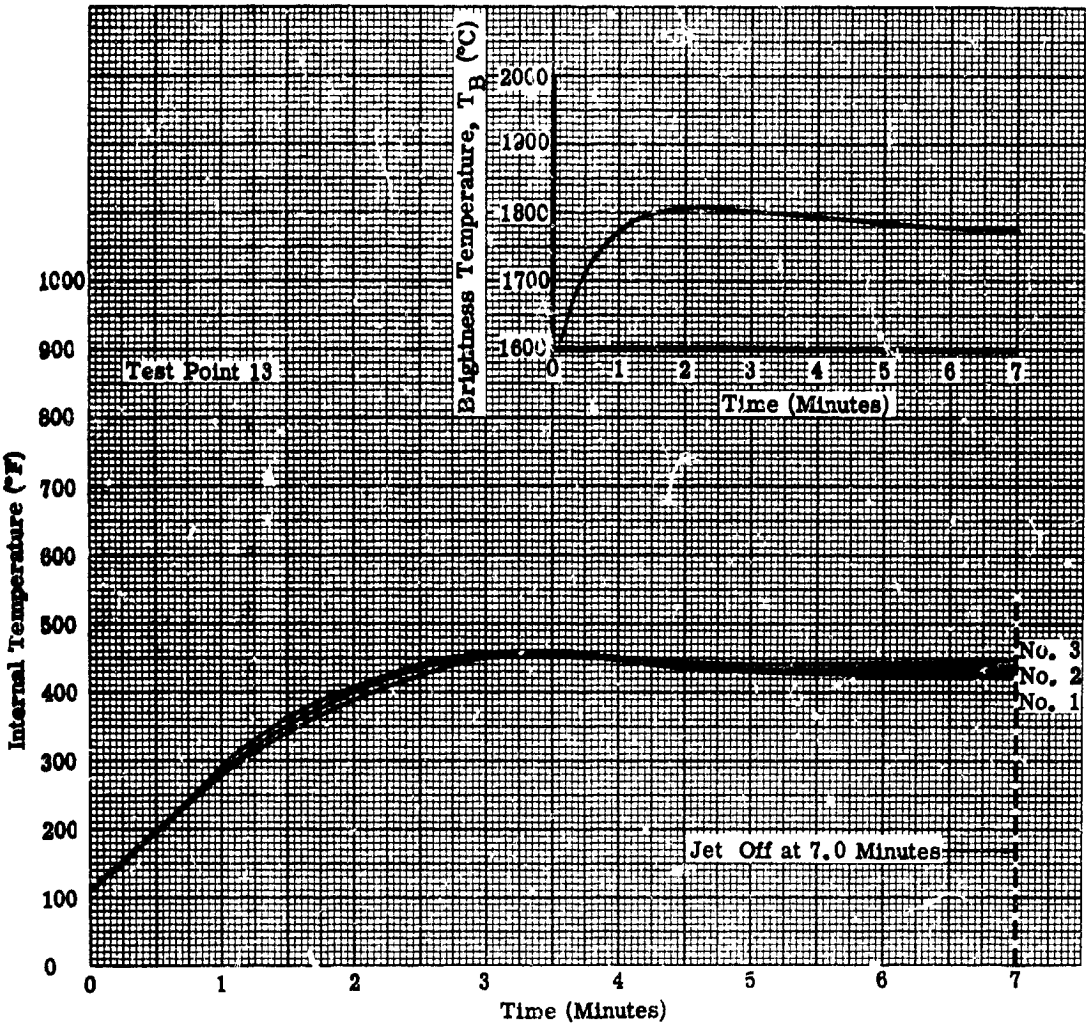


Figure A-28. Temperature-Time History of Model HH-1

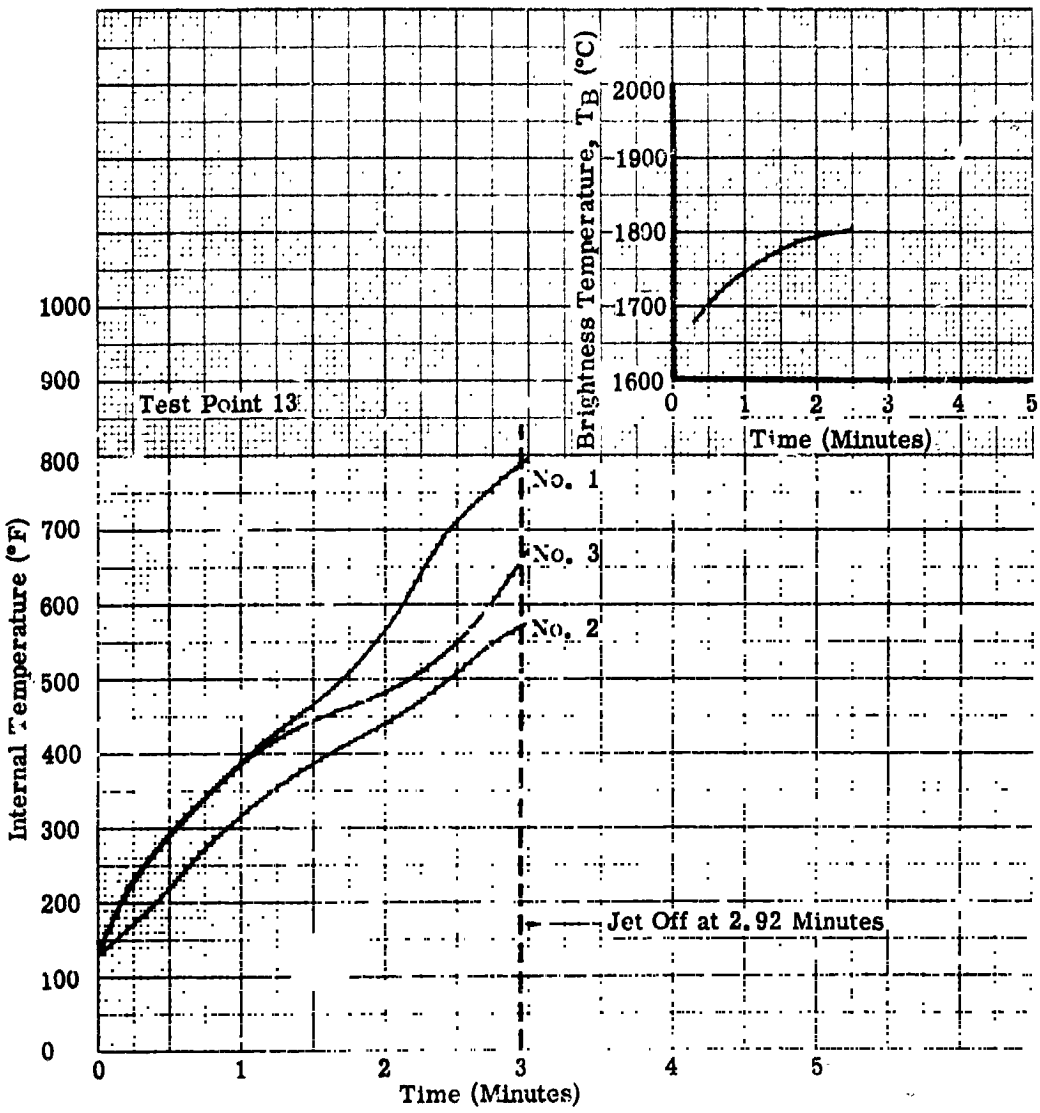


Figure A-29. Temperature-Time History of Model HH-2

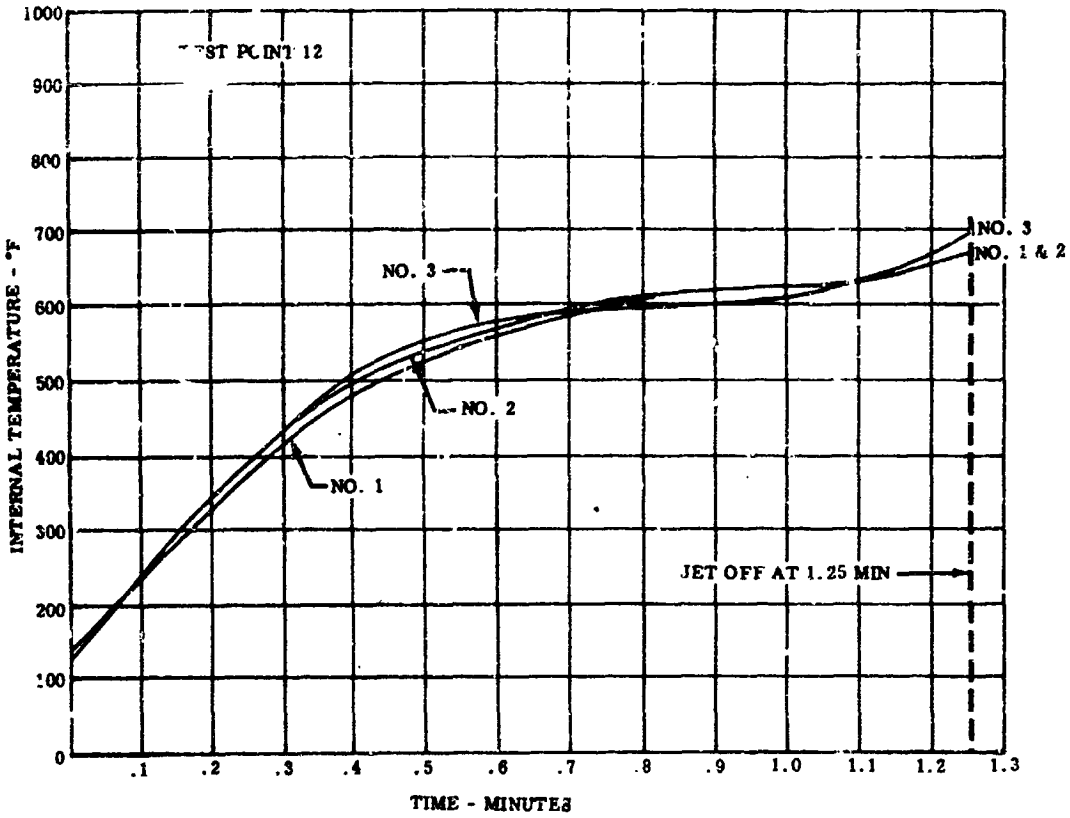


Figure A-30. Temperature-Time History of Model D-1

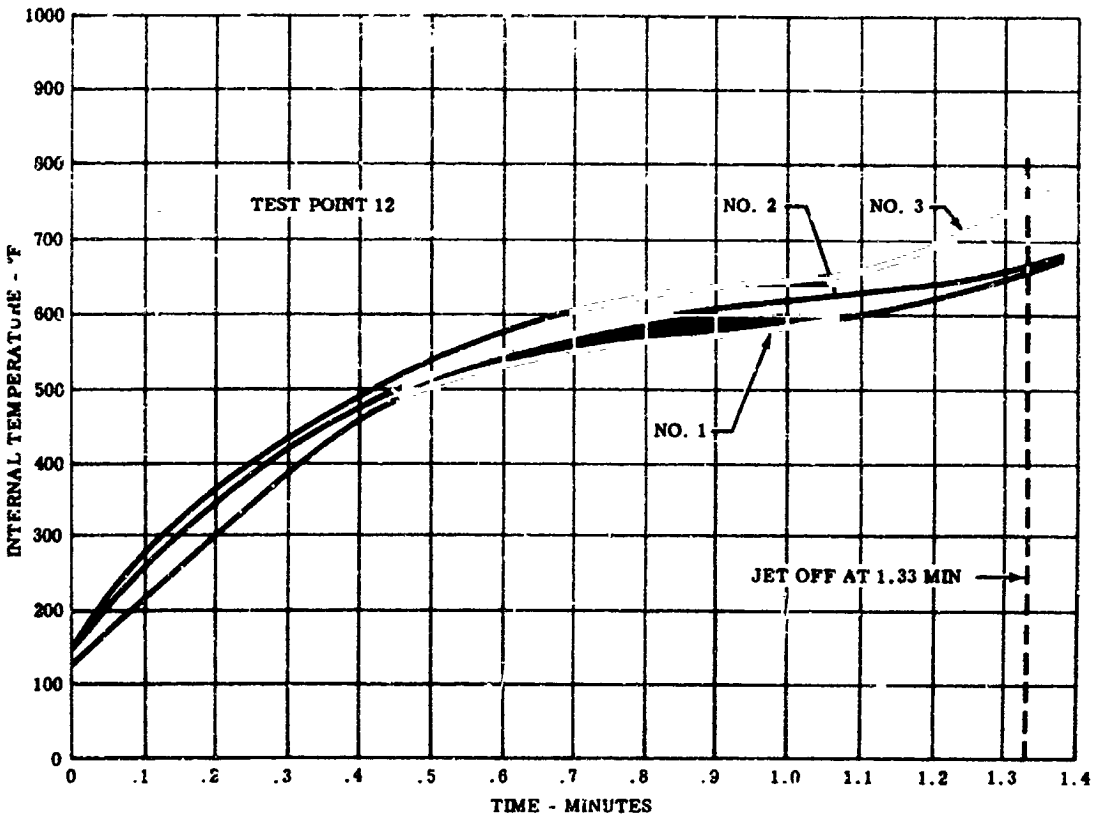


Figure A-31. Temperature-Time History of Model D-2

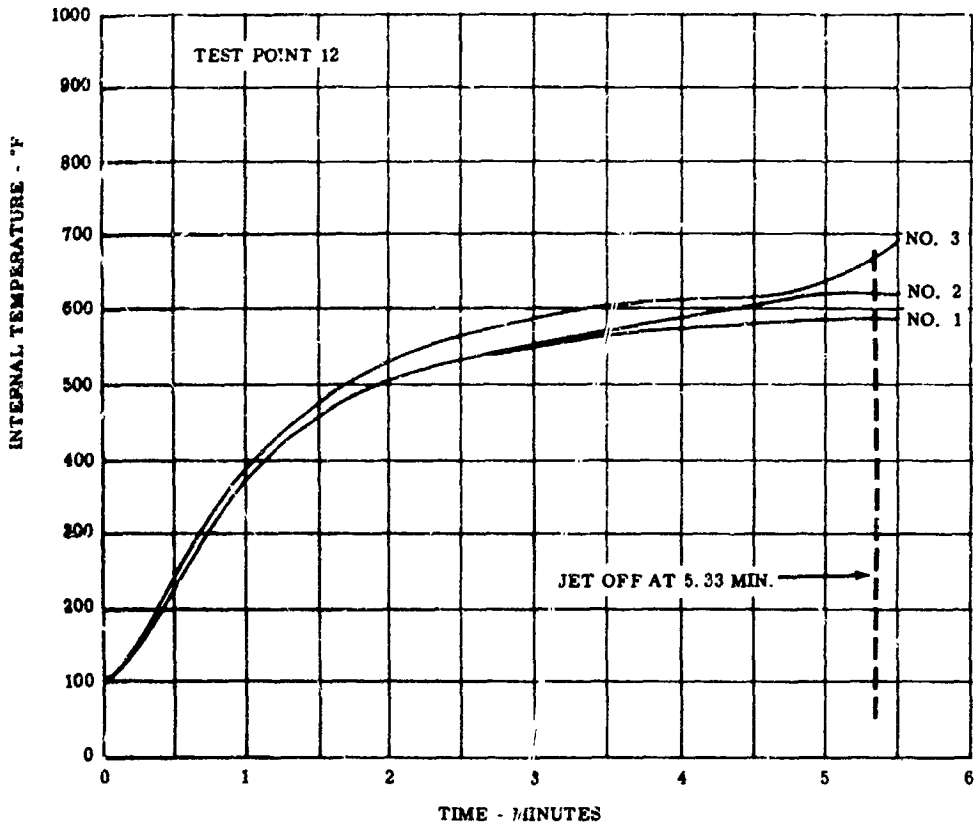


Figure A-32. Temperature-Time History of Model D-9

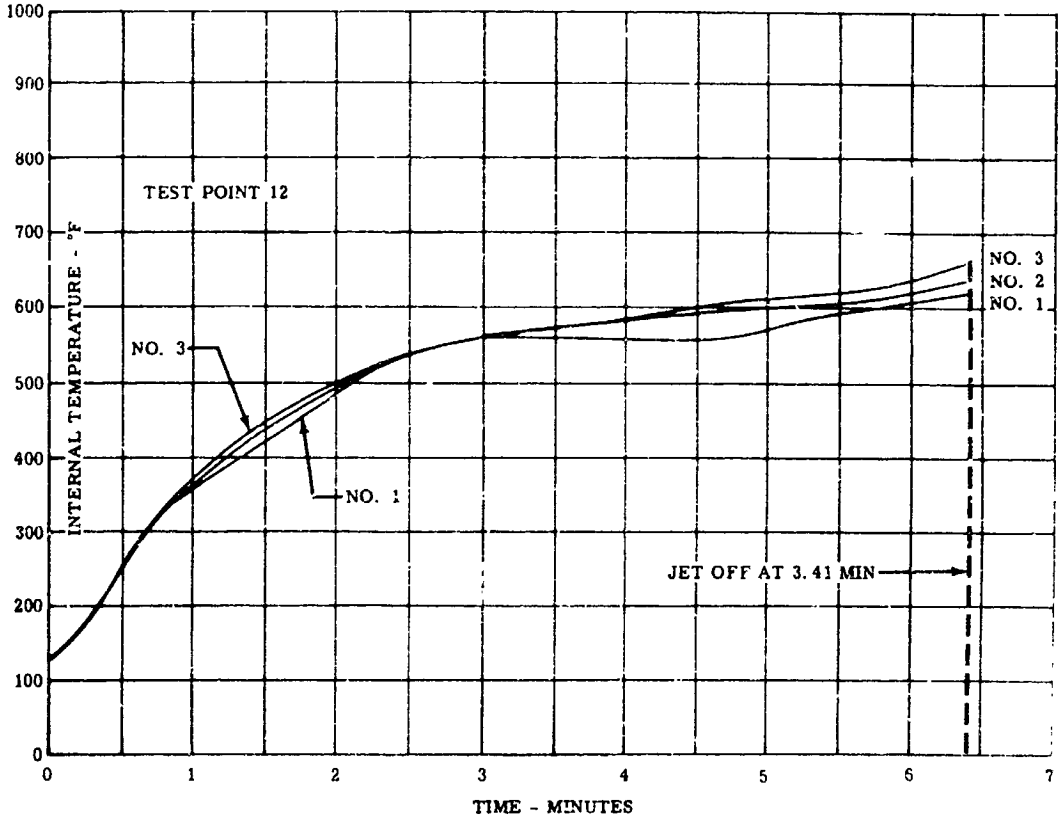


Figure A-33. Temperature-Time History of Model D-10

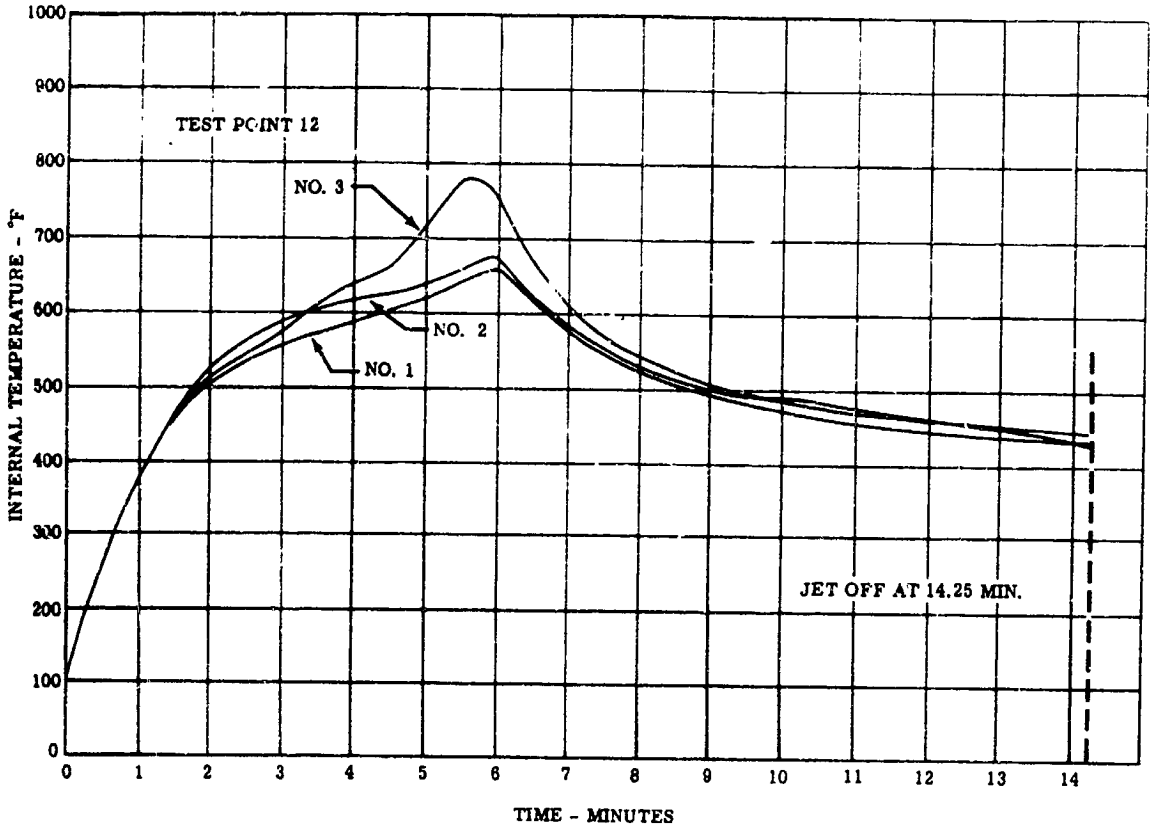


Figure A-34. Temperature-Time History of Model D-11

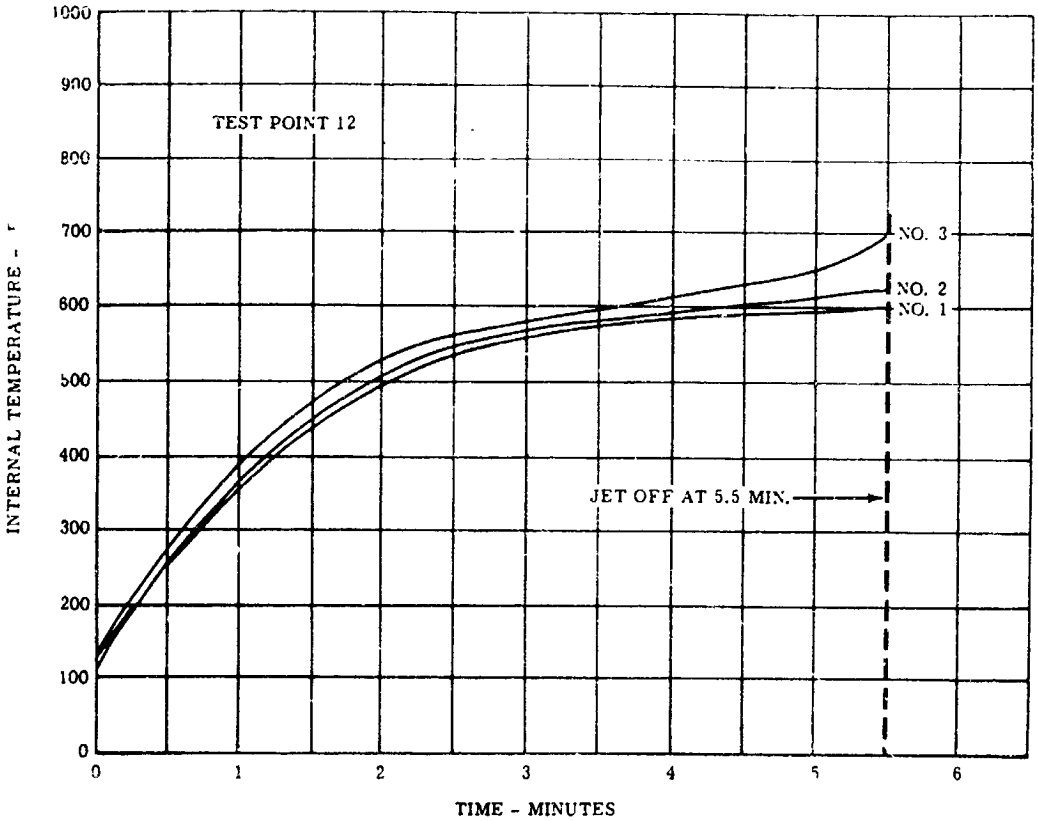


Figure A-35. Temperature-Time History of Model D-12

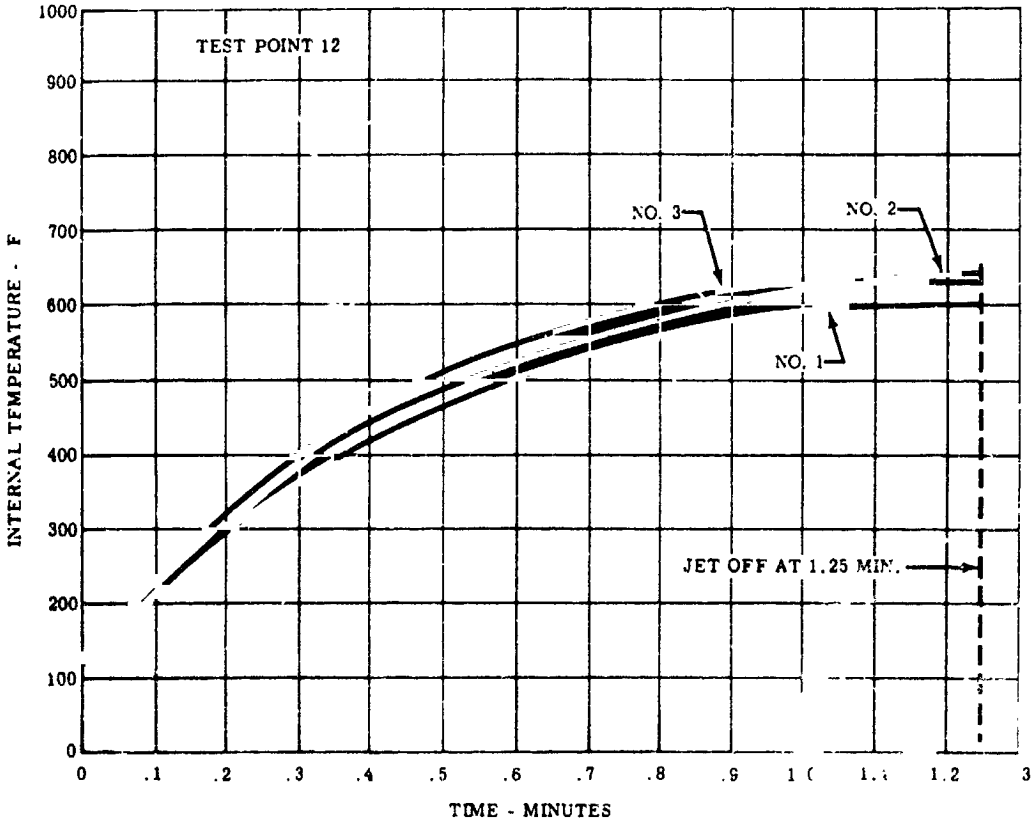


Figure A-36. Temperature-Time History of Model E-15

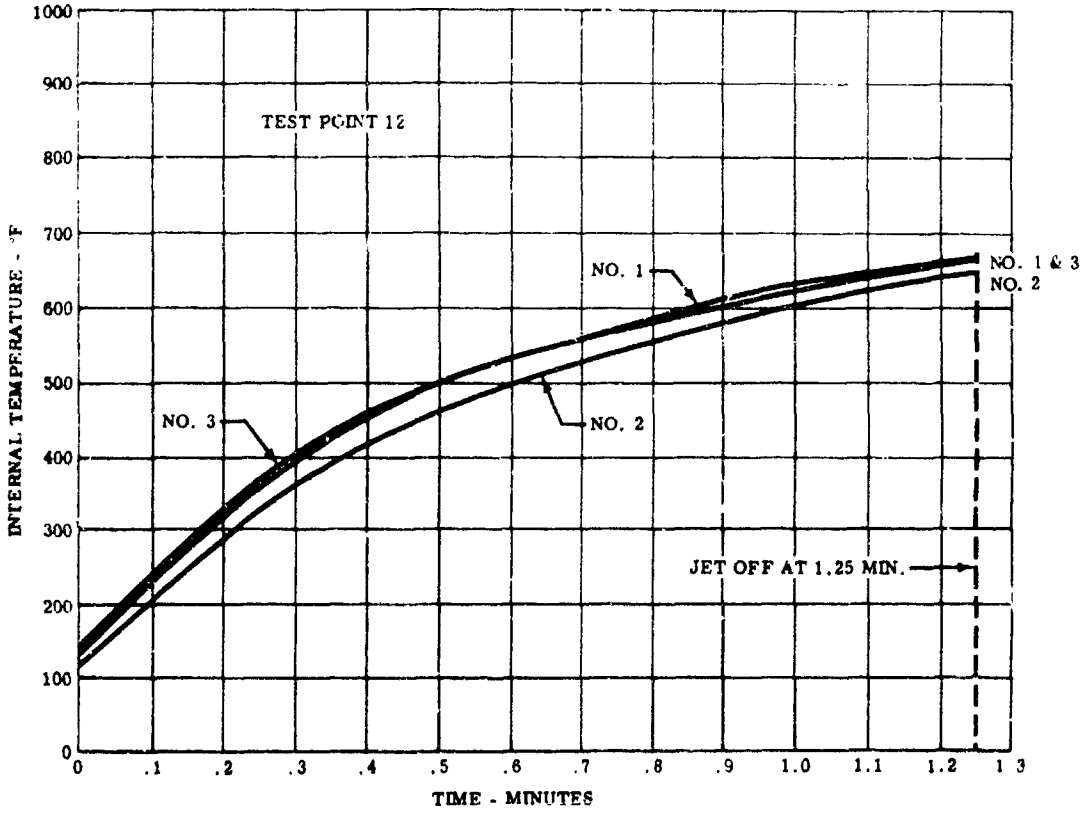


Figure A-37. Temperature-Time History of Model E-16

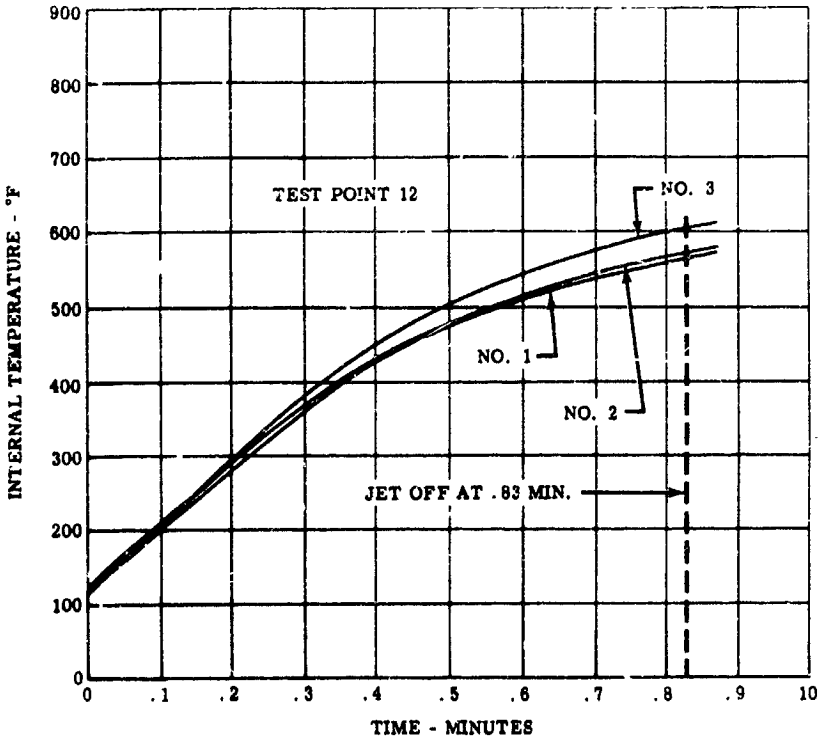


Figure A-38. Temperature-Time History of Model E-17

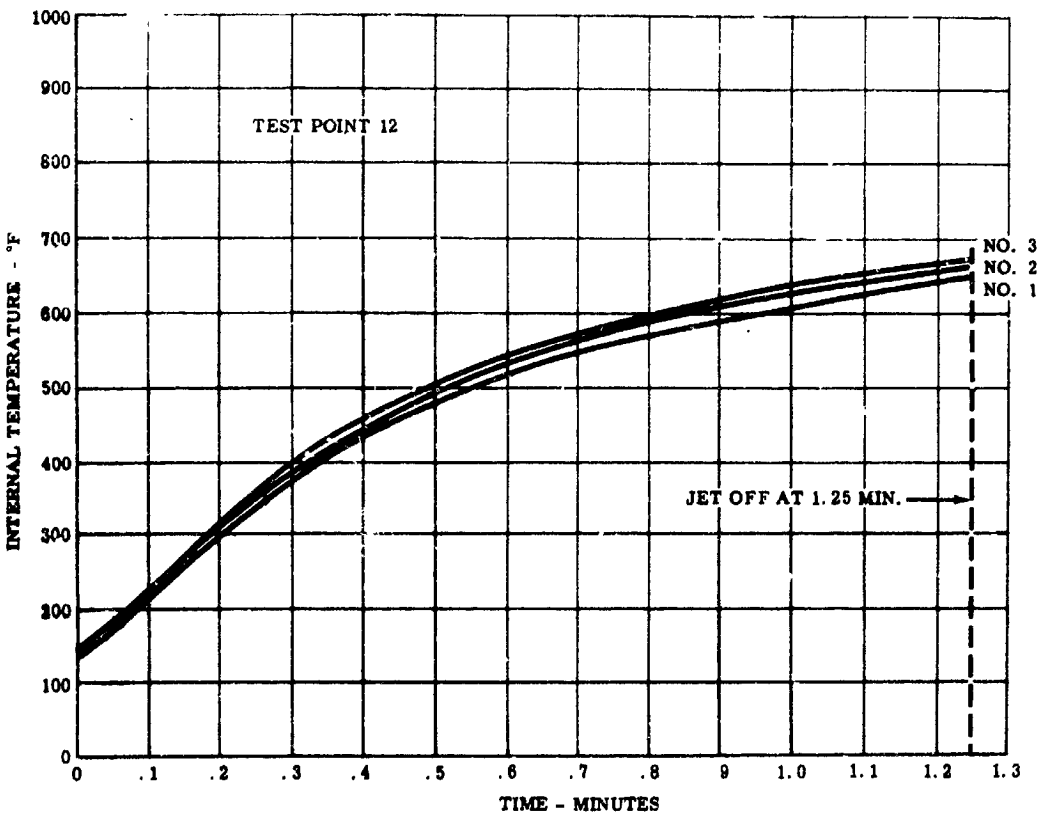


Figure A-39. Temperature-Time History of Model E-18

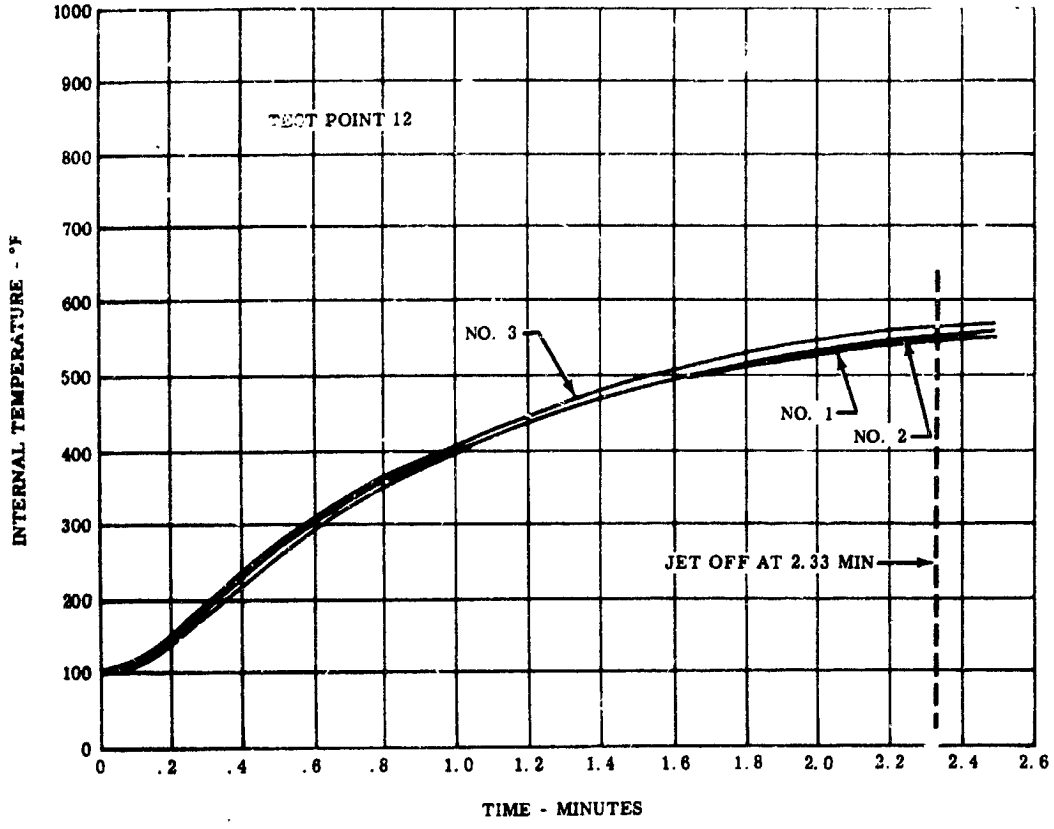


Figure A-40. Temperature-Time History of Model GG-1A

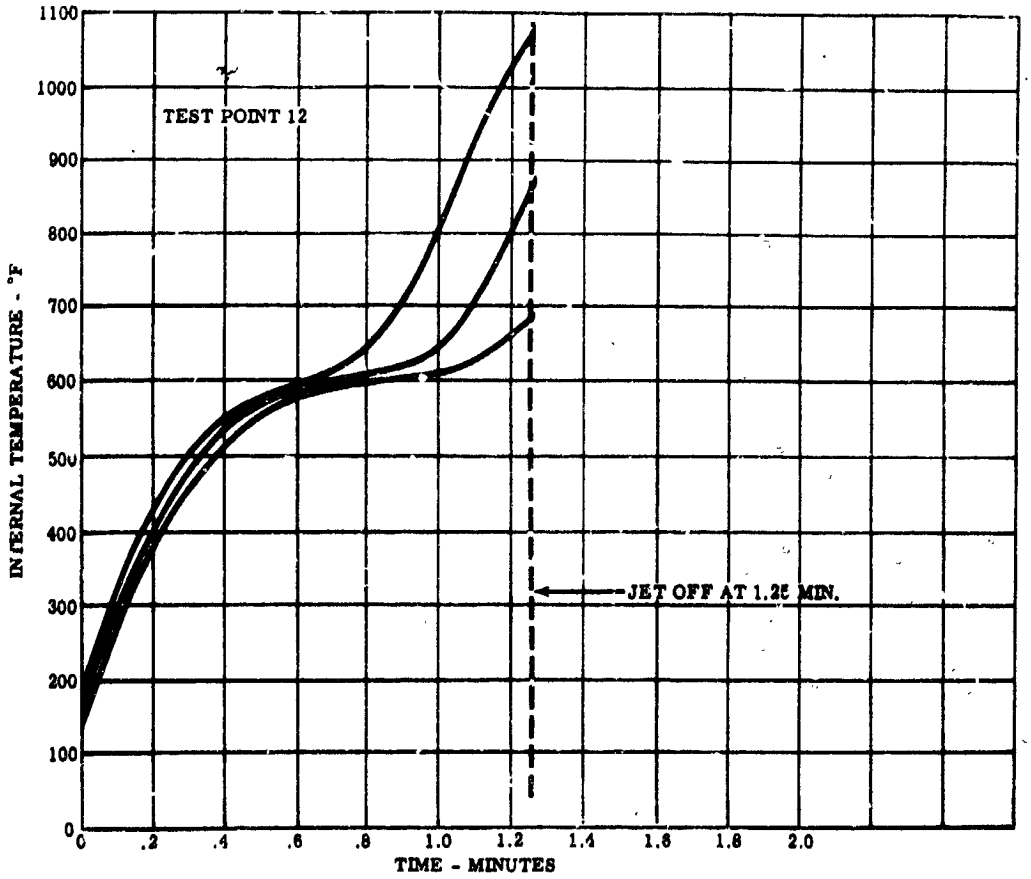


Figure A-41. Temperature-Time History of Model GG-2

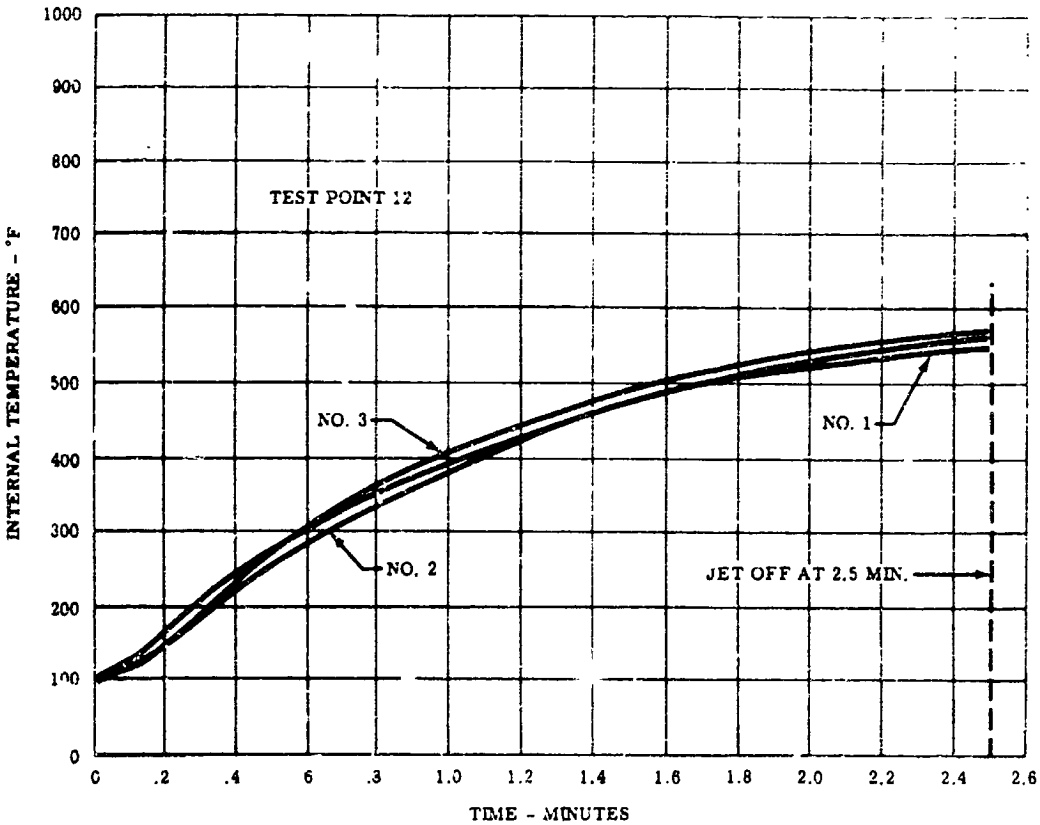


Figure A-42. Temperature-Time History of Model GG-4

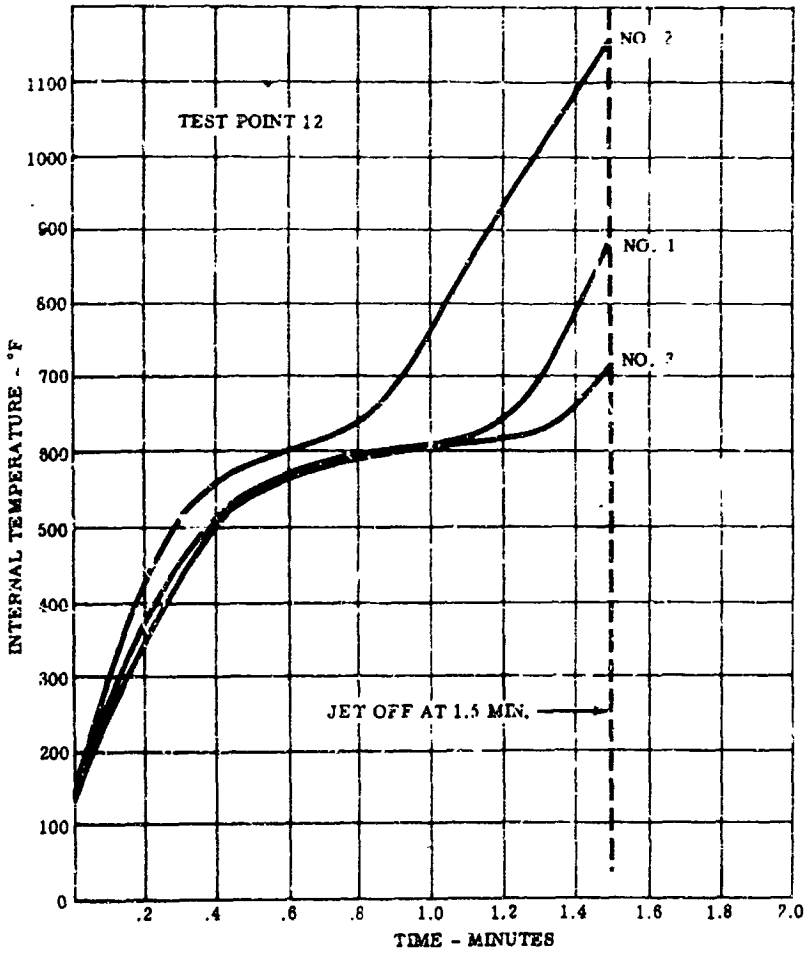


Figure A-43. Temperature-Time History of Model GG-5

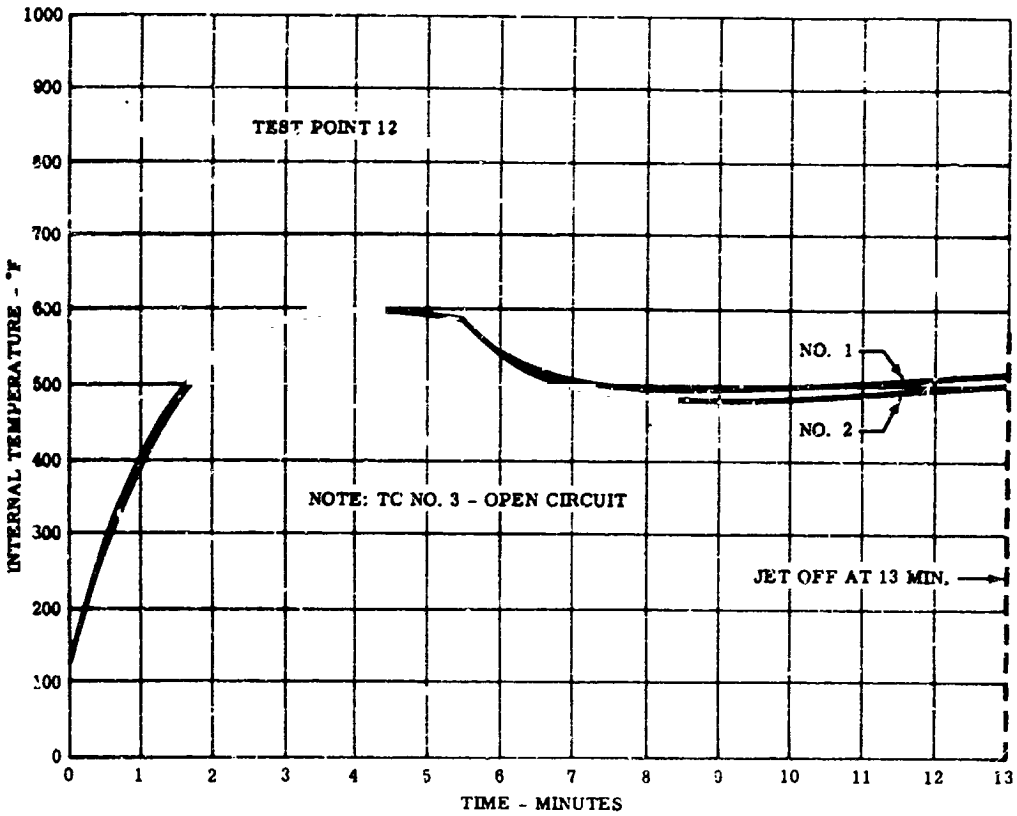


Figure A-44. Temperature-Time History of Model GG-7

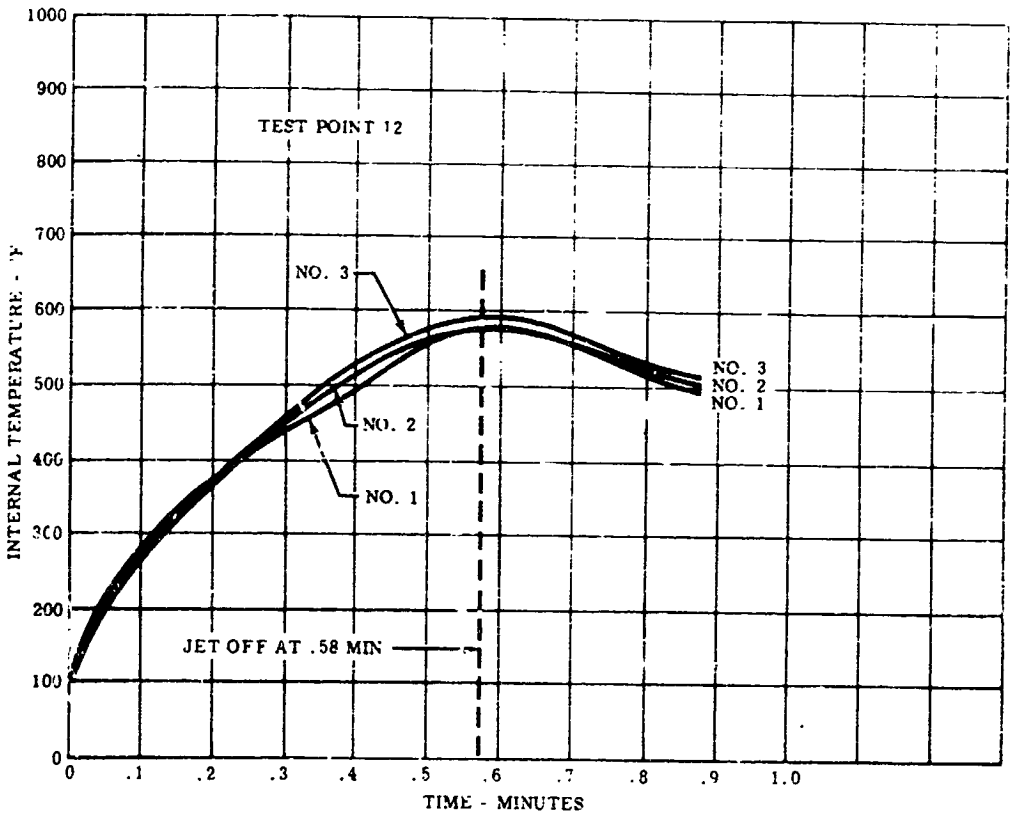


Figure A-45. Temperature-Time History of Model GG-8

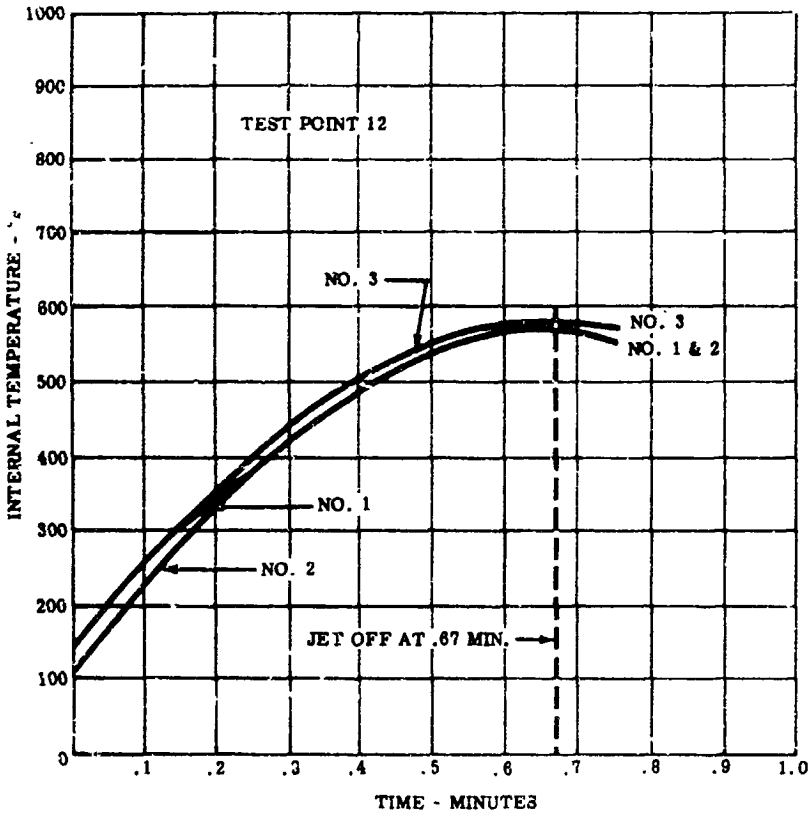


Figure A-46. Temperature-Time History of Model GG-9

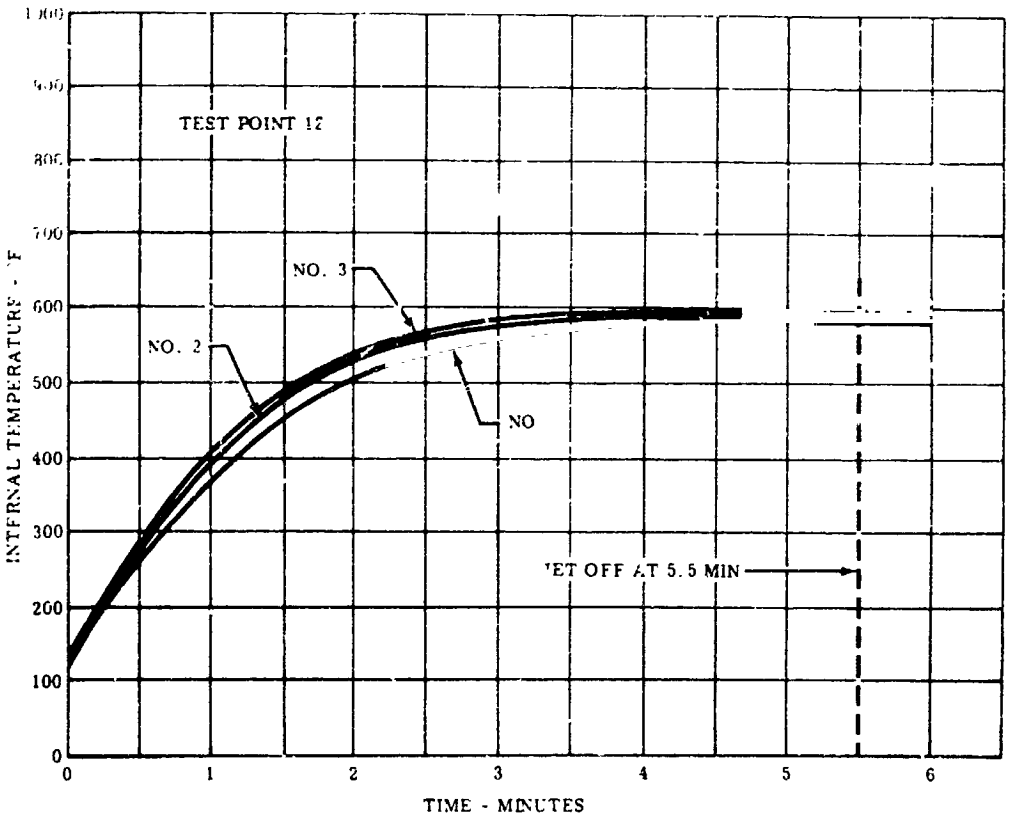


Figure A-47. Temperature-Time History of Model GG-11

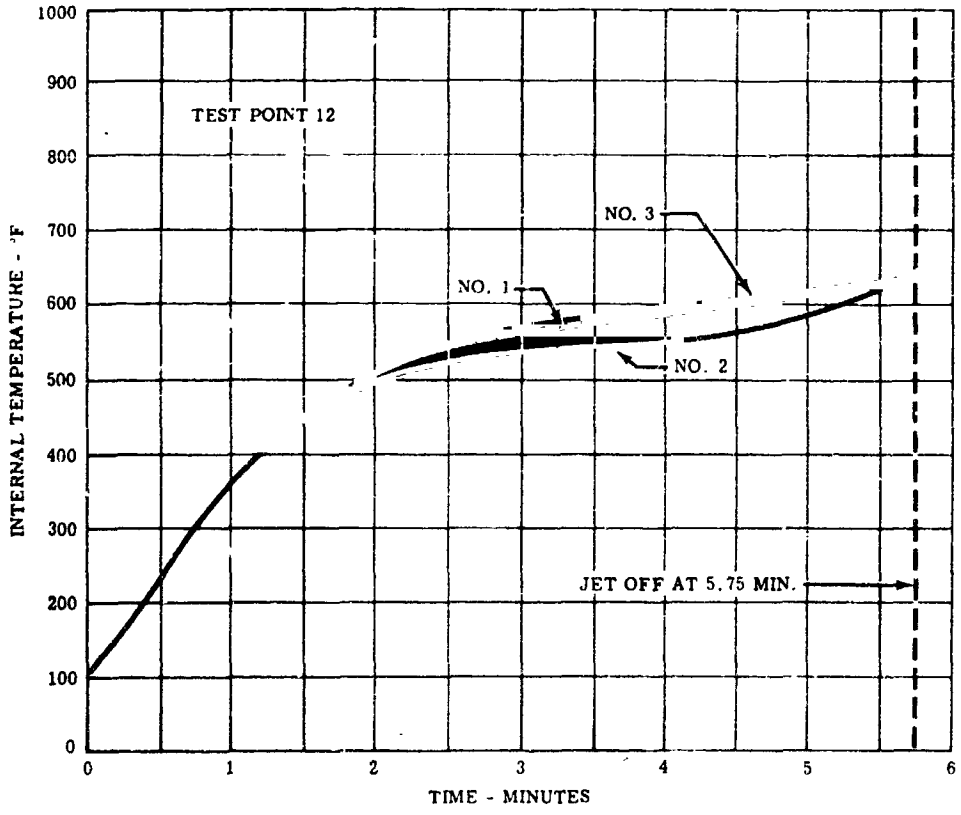


Figure A-48. Temperature-Time History of Model D-2-4

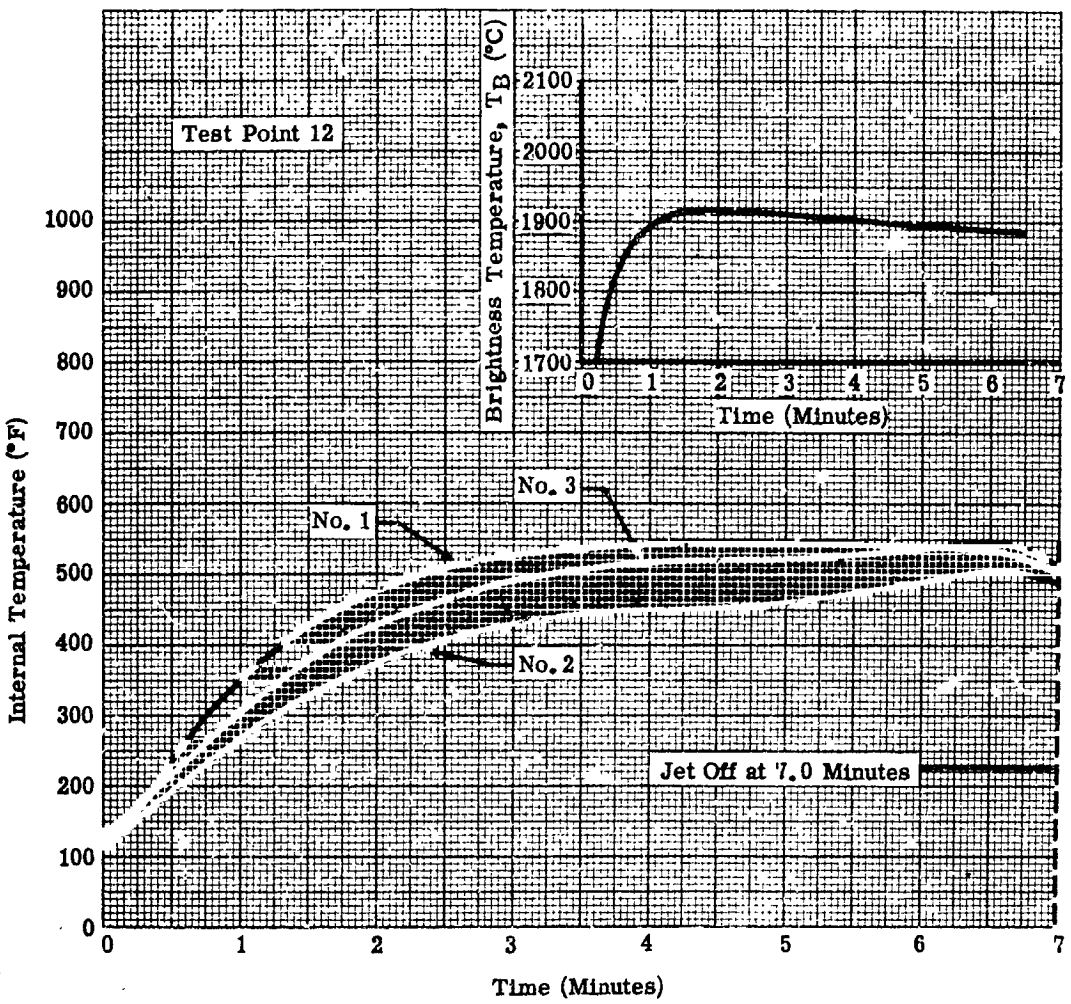


Figure A-49. Temperature-Time History of Model D-2-5

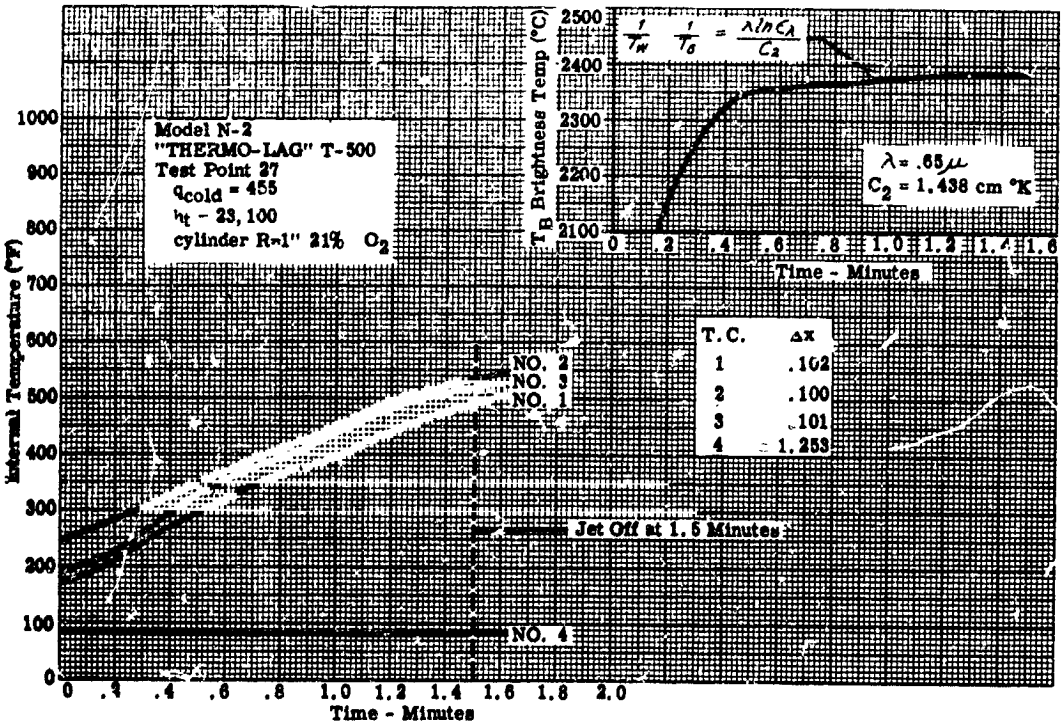


Figure A-50. Temperature-Time History of Model N-2

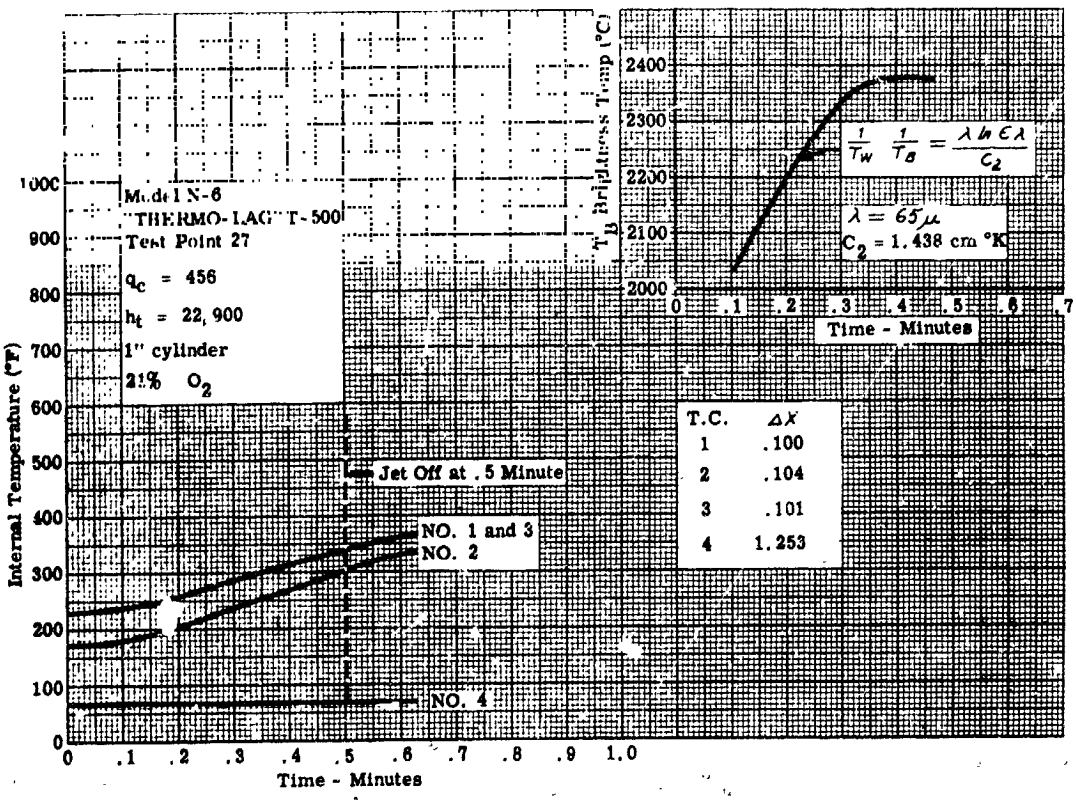


Figure A-51. Temperature-Time History of Model N-6

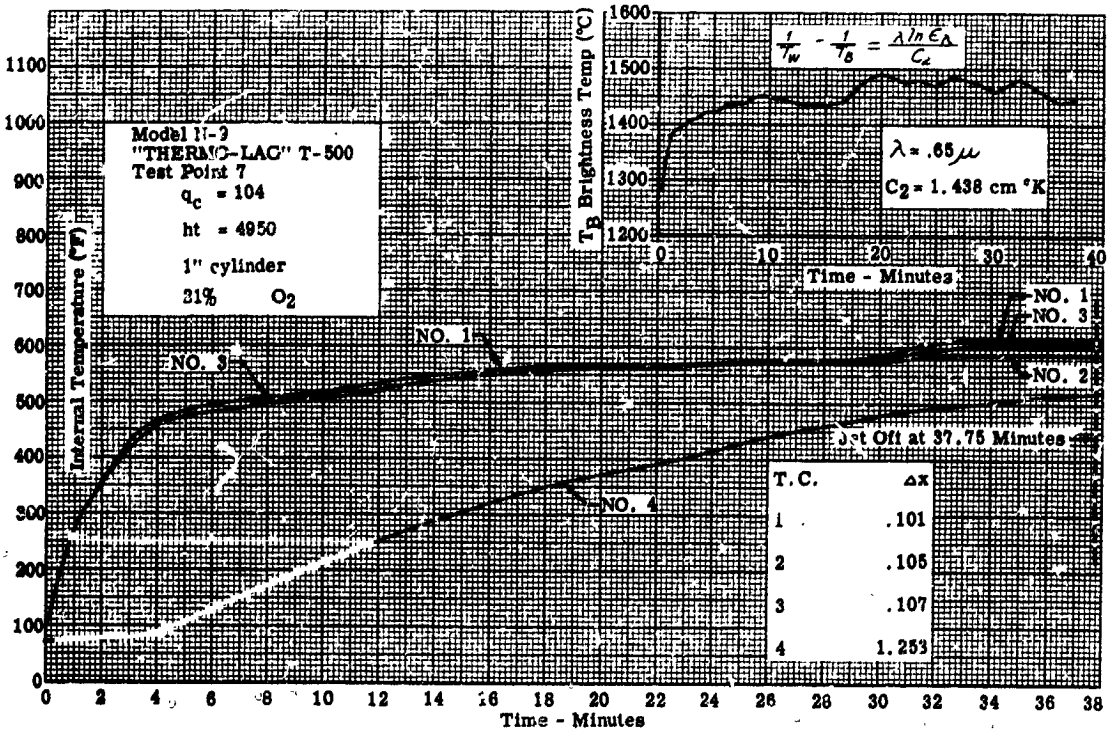


Figure A-52. Temperature-Time History of Model N-9

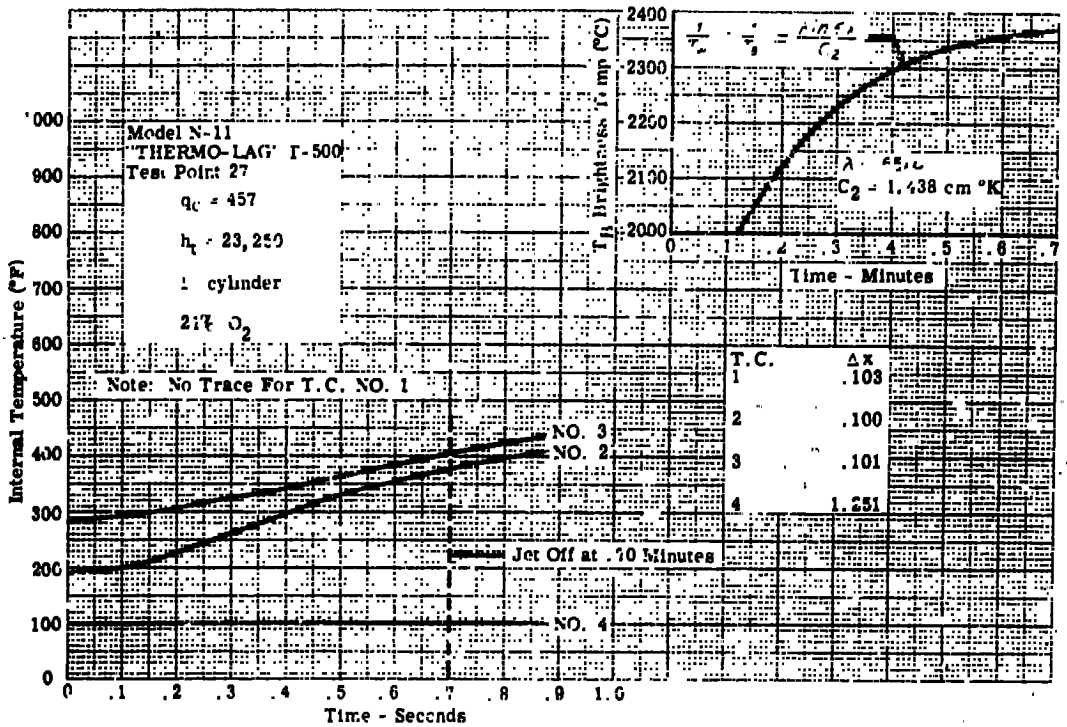


Figure A-53. Temperature-Time History of Model N-11

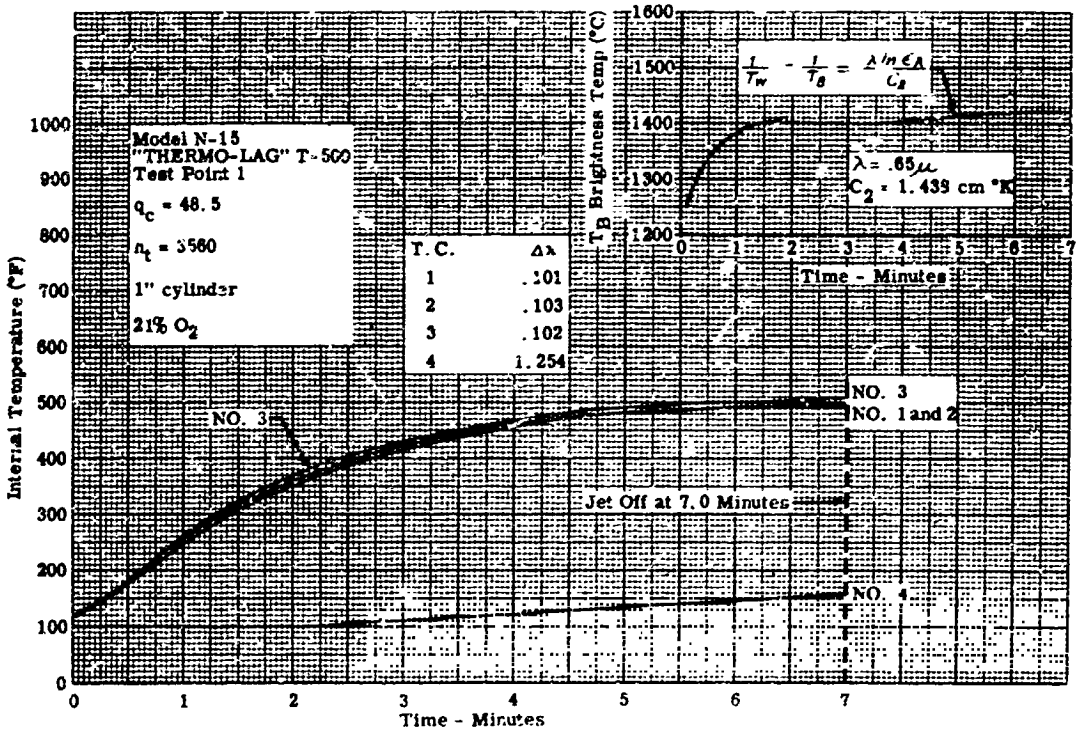


Figure A-54. Temperature-Time History of Model N-15

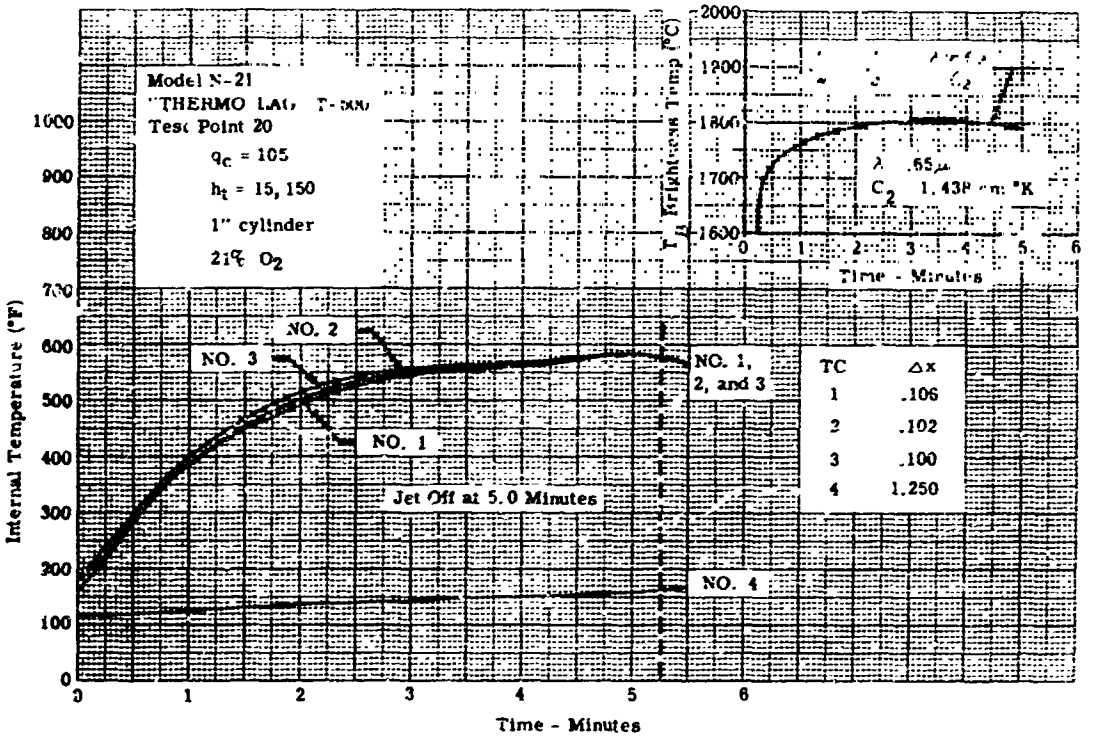


Figure A-55. Temperature-Time History of Model N-21

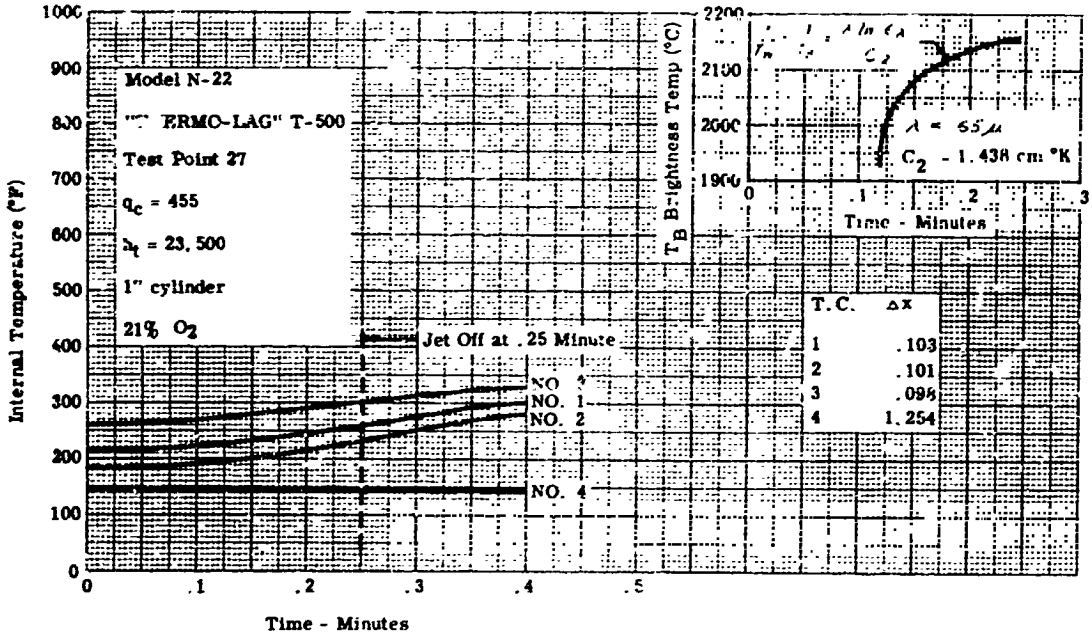


Figure A-56. Temperature-Time History of Model N-22

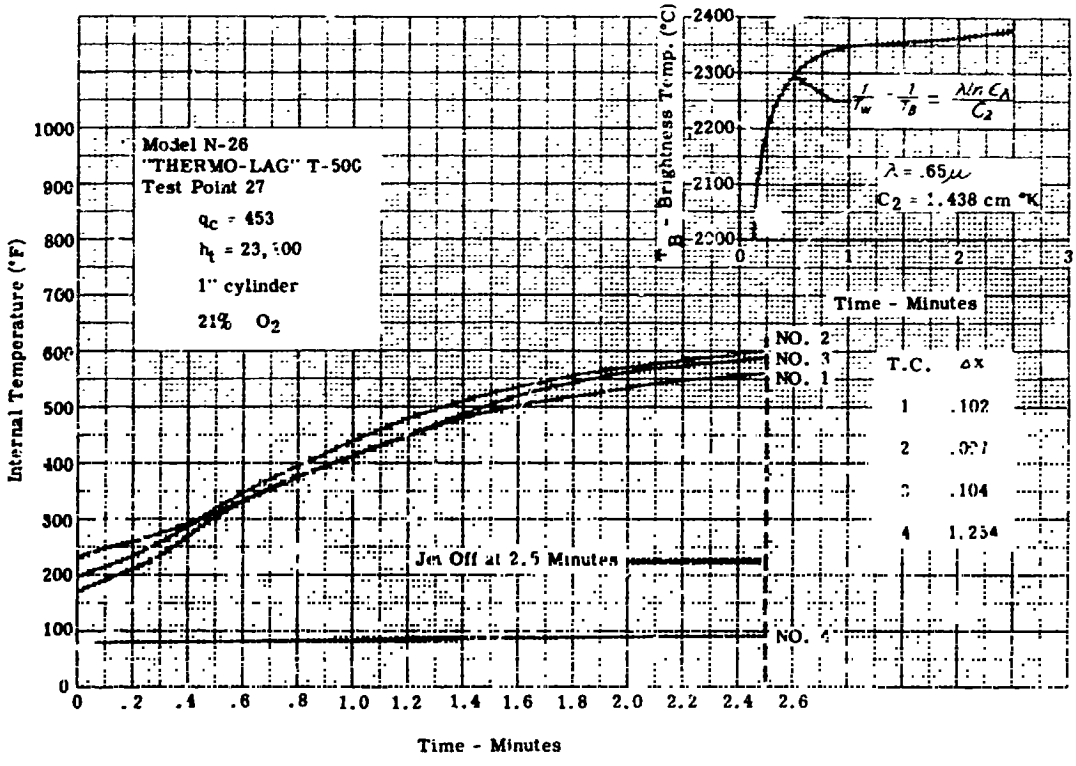


Figure A-57. Temperature-Time History of Model N-26

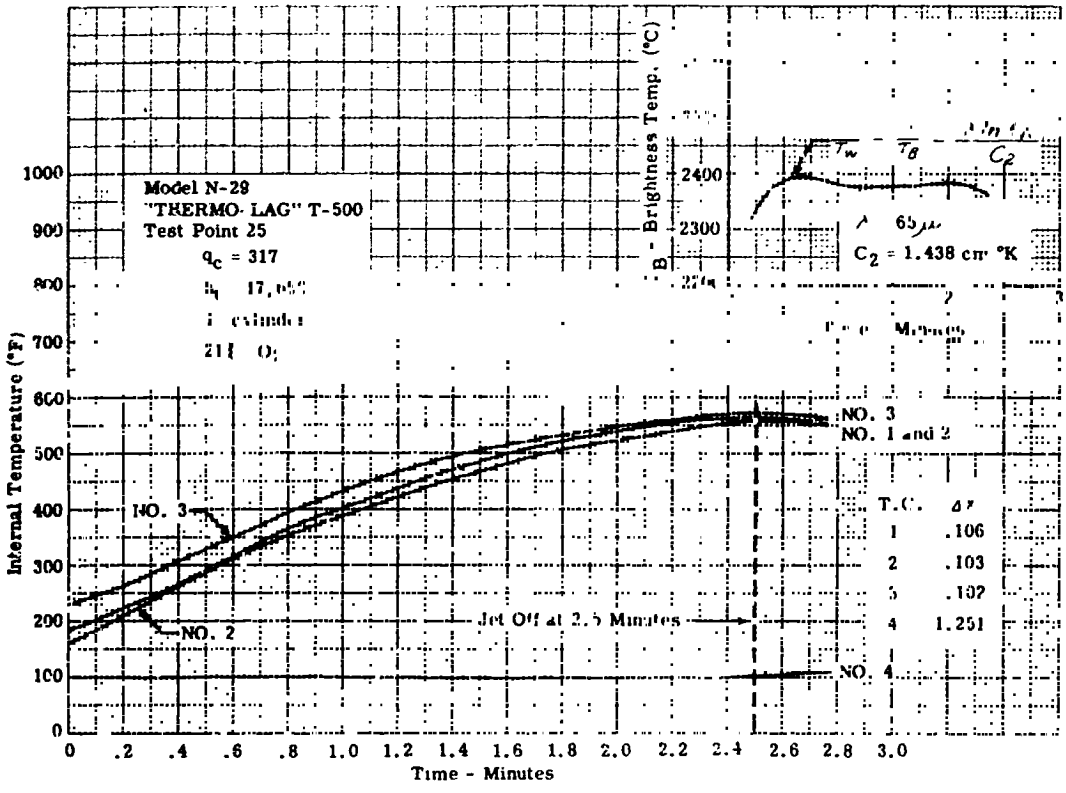


Figure A-58. Temperature-Time History of Model N-29

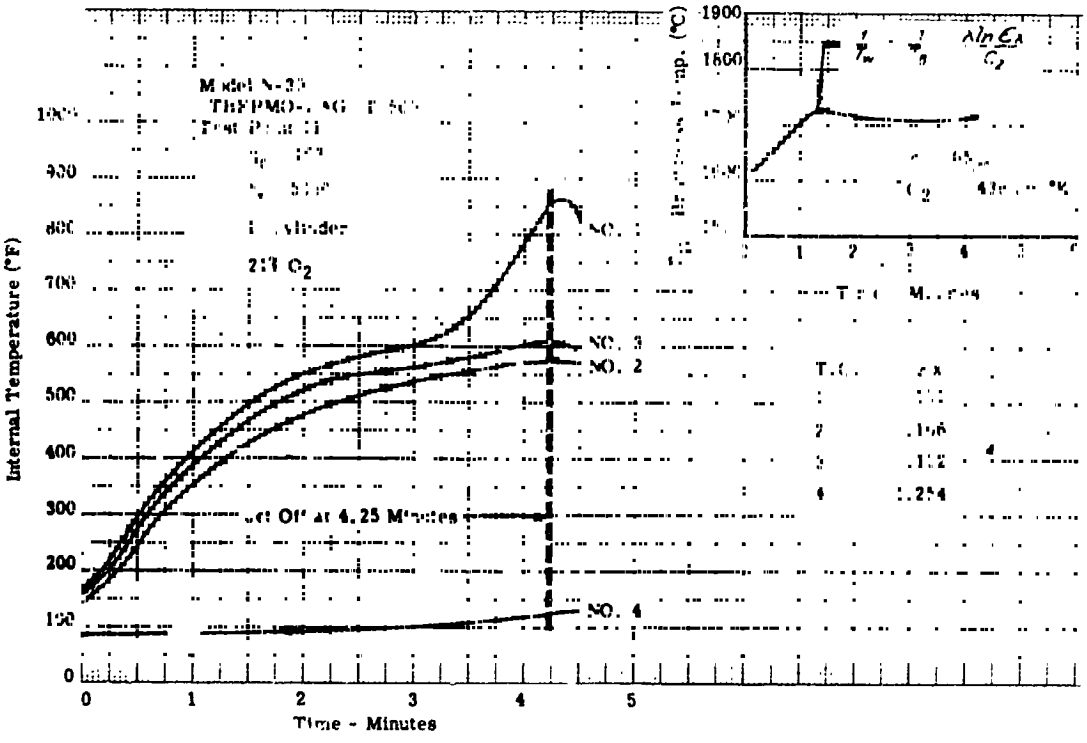


Figure A-59. Temperature-Time History of Model N-30

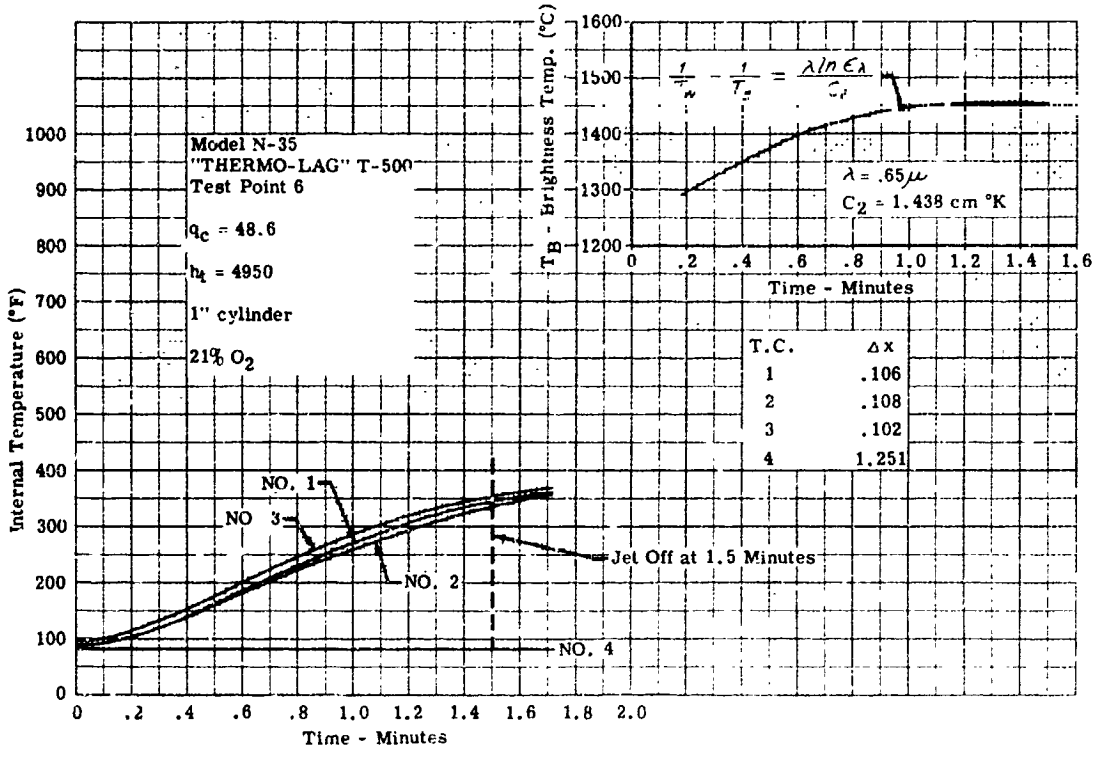


Figure A-60. Temperature-Time History of Model N-35

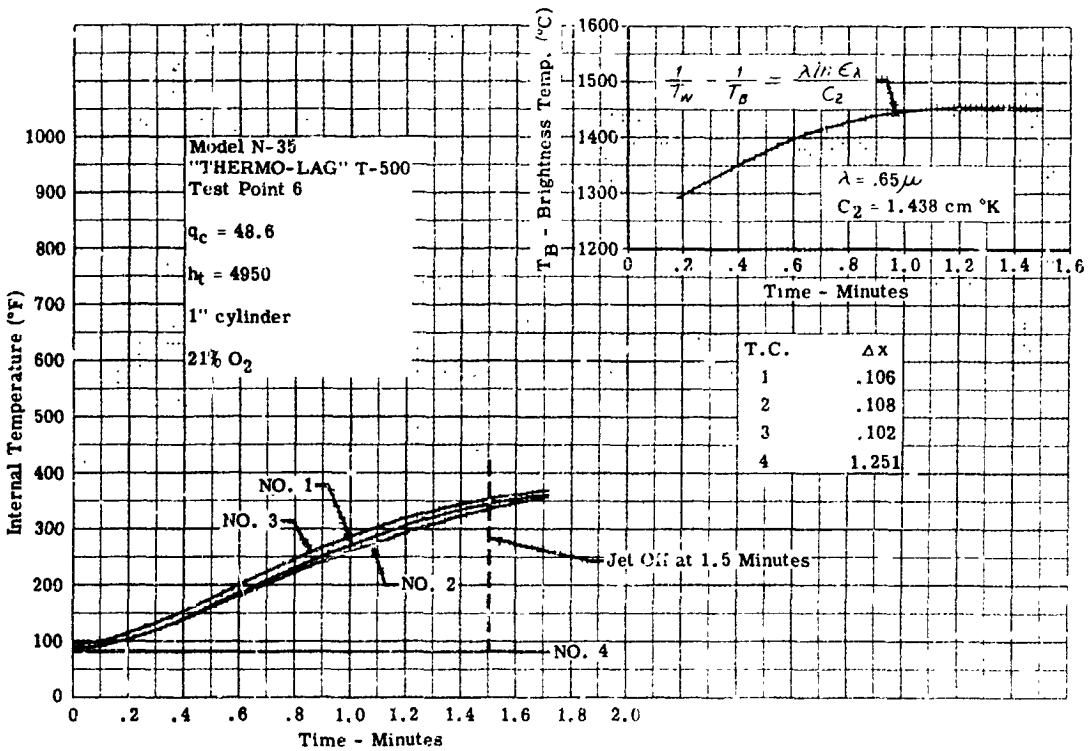


Figure A-61. Temperature-Time History of Model N-35

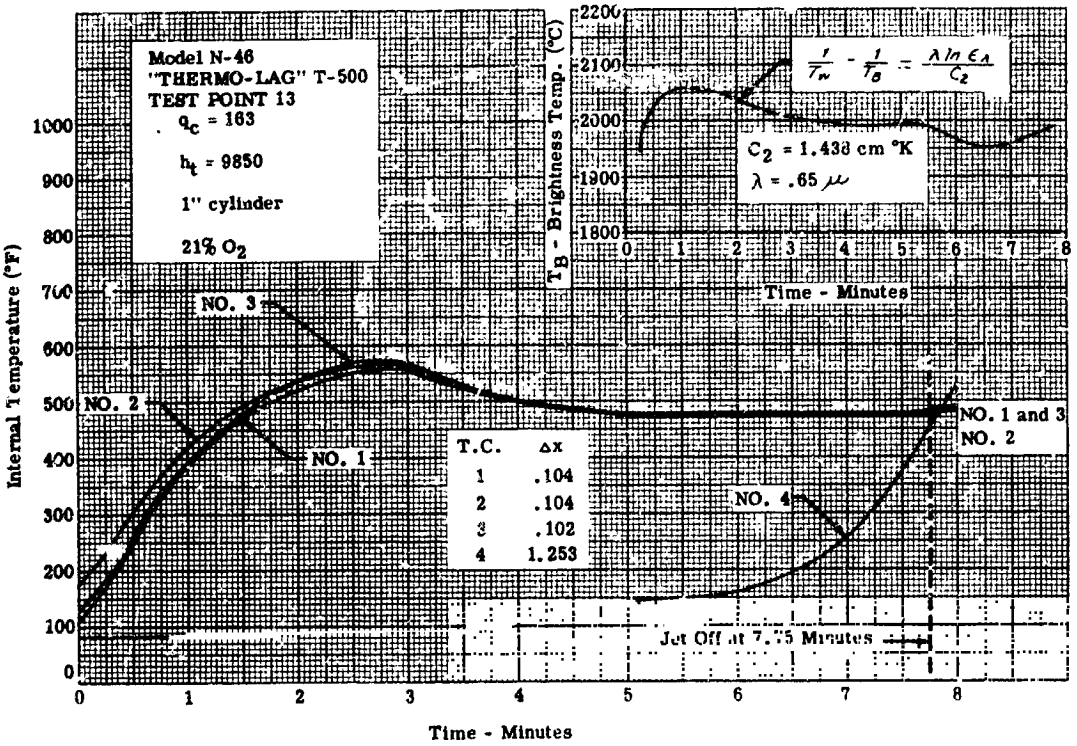


Figure A-62. Temperature-Time History of Model N-46

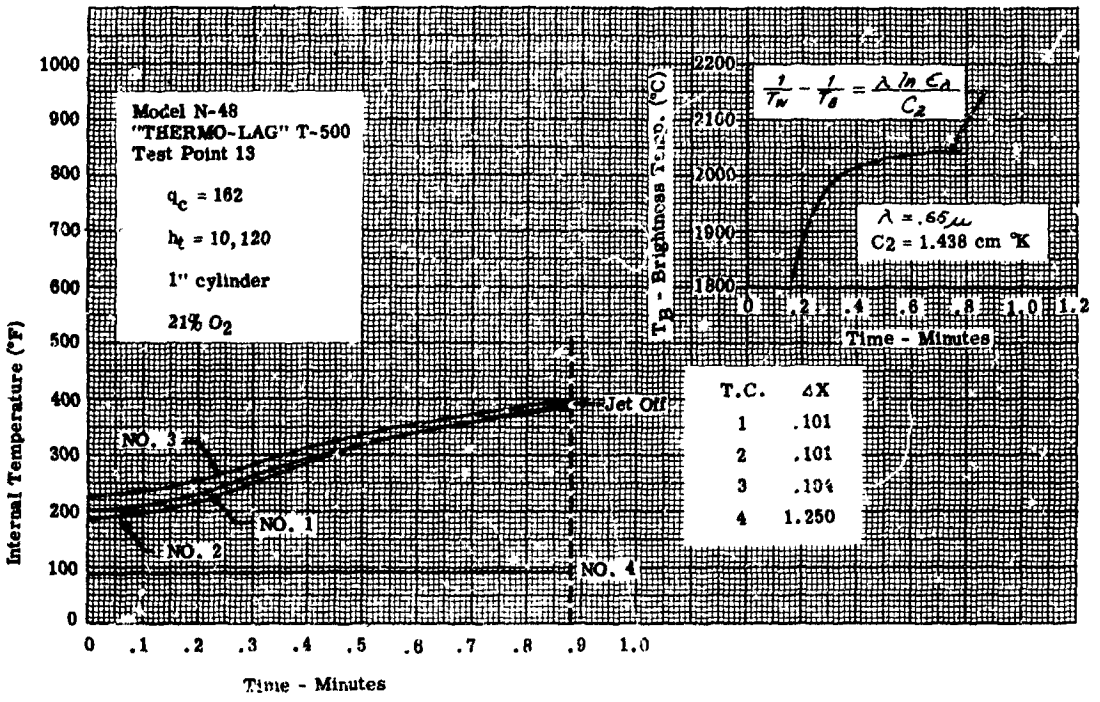


Figure A-63. Temperature-Time History of Model N-48

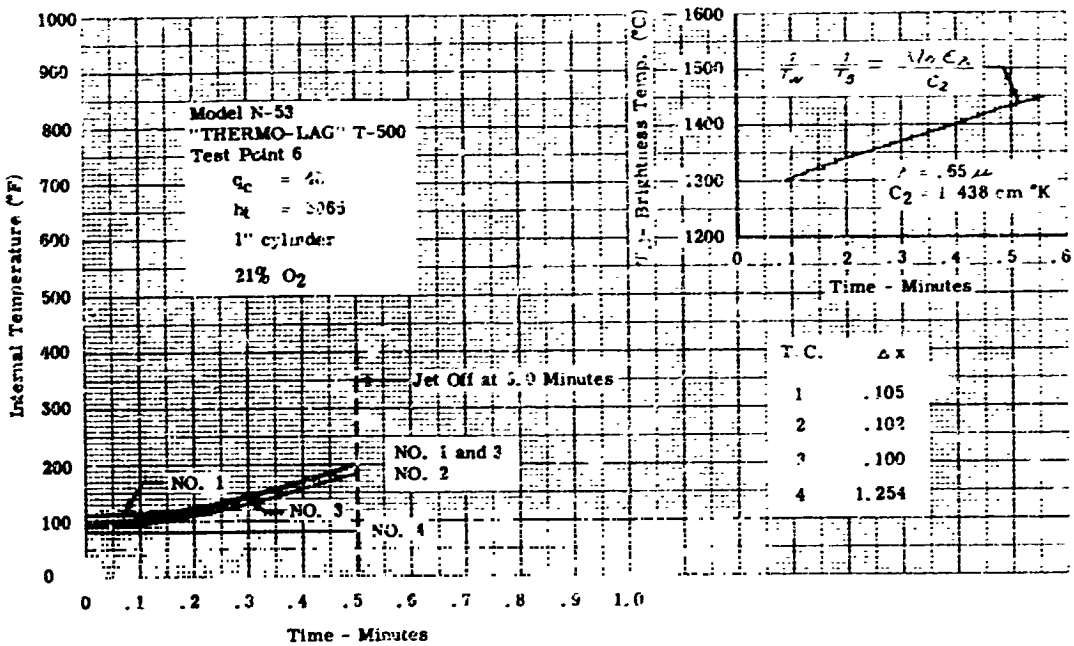


Figure A-64. Temperature-Time Histoyr of Model N-53

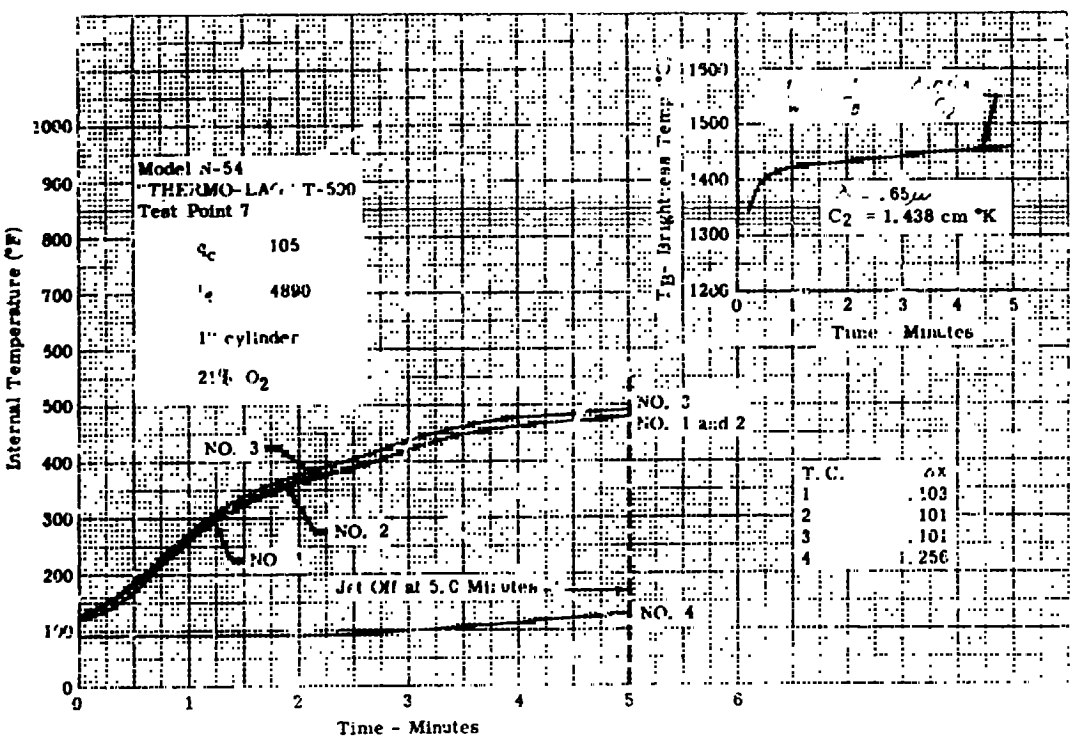


Figure A-65. Temperature-Time History of Model N-54

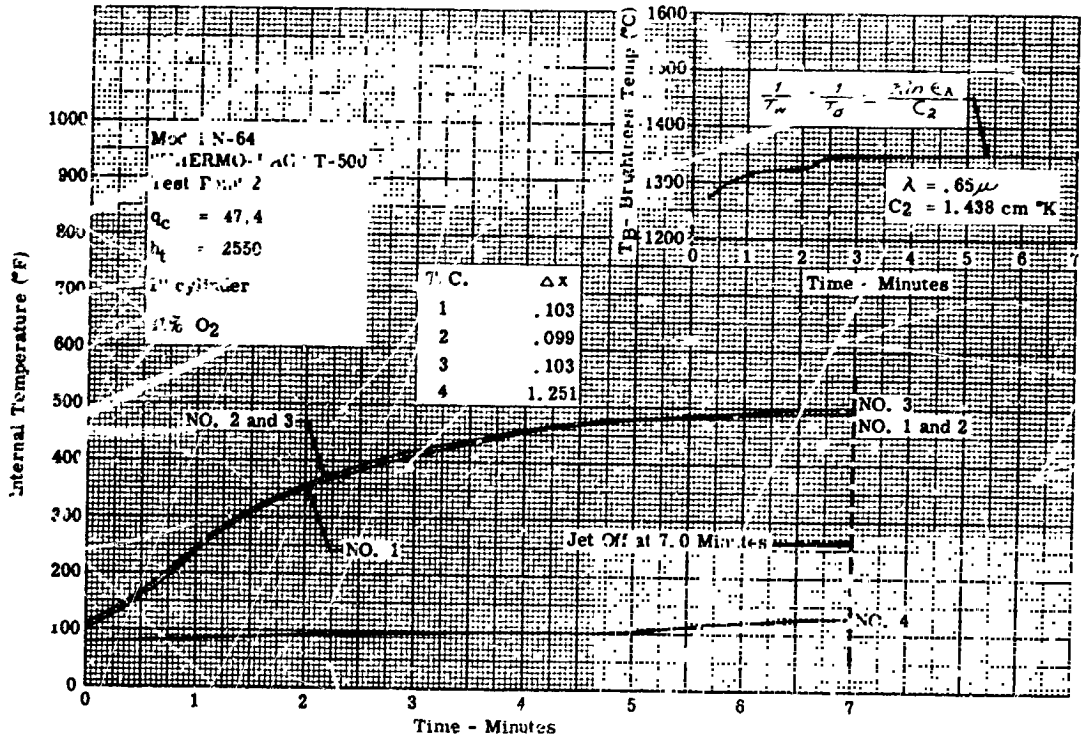


Figure A-66. Temperature-Time History of Model N-64

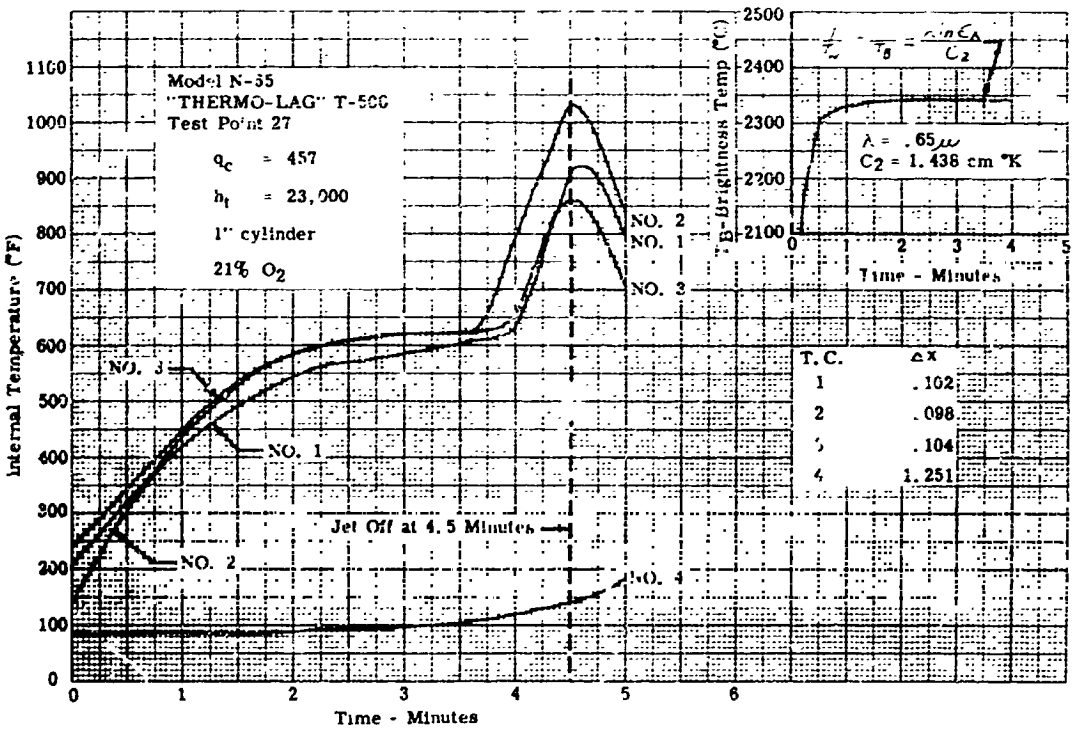


Figure A-67. Temperature-Time History of Model N-65

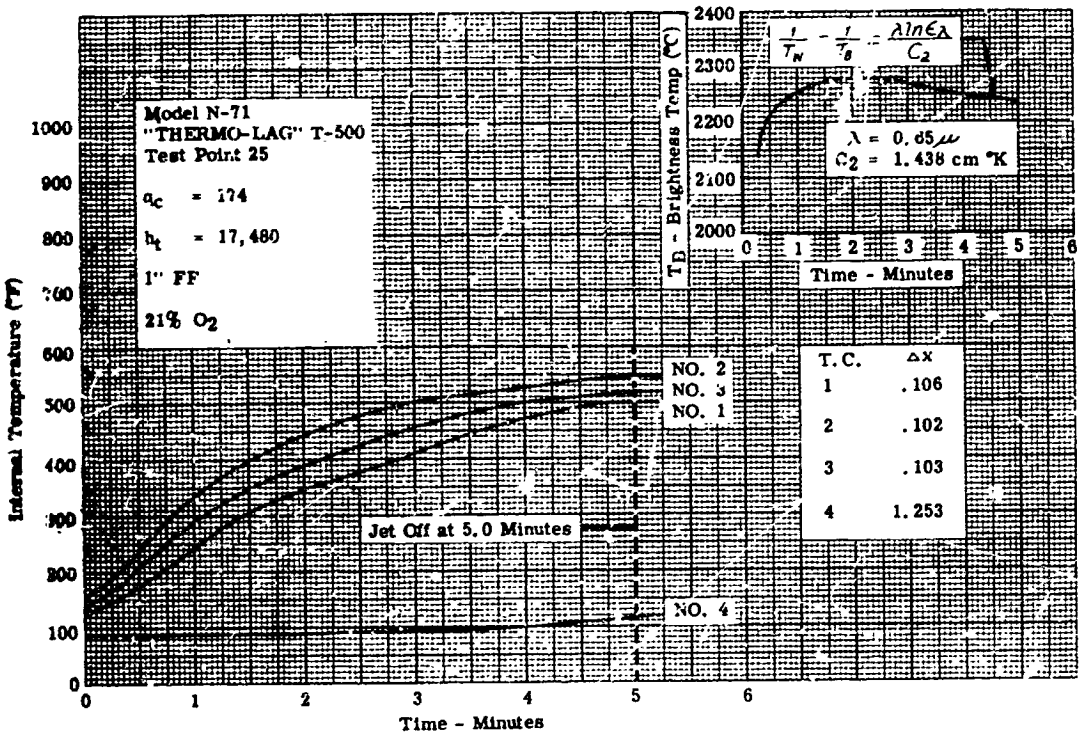


Figure A-68. Temperature-Time History of Model N-71

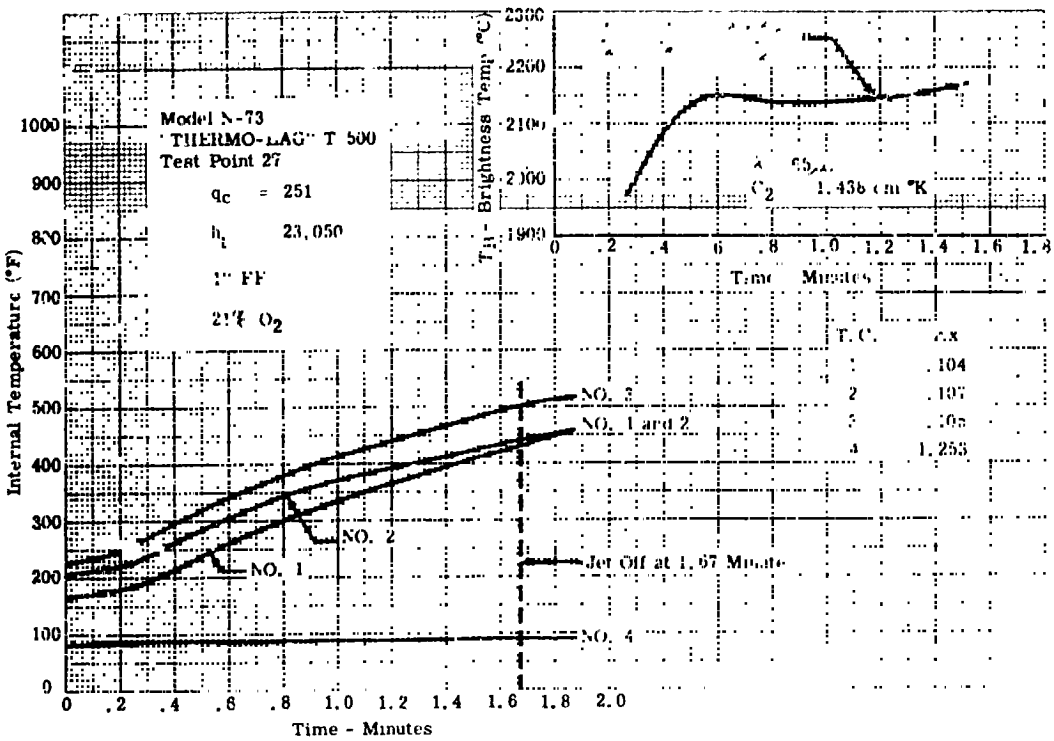


Figure A-69. Temperature-Time History of Model N-73

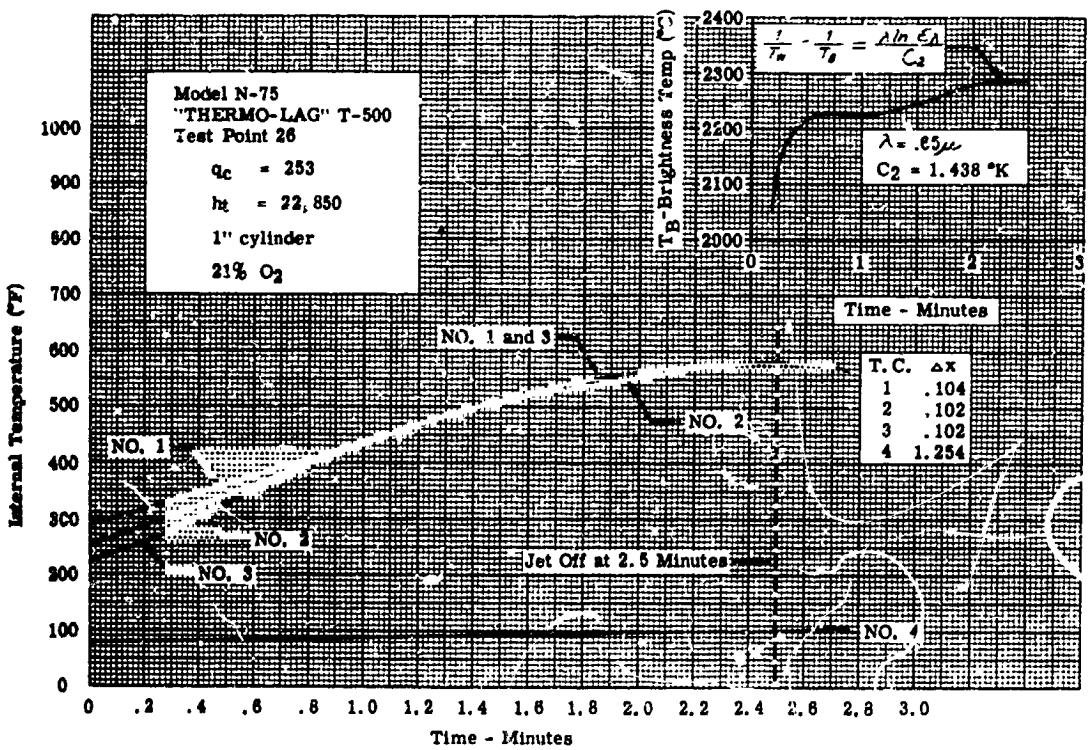


Figure A-70. Temperature-Time History of Model N-75

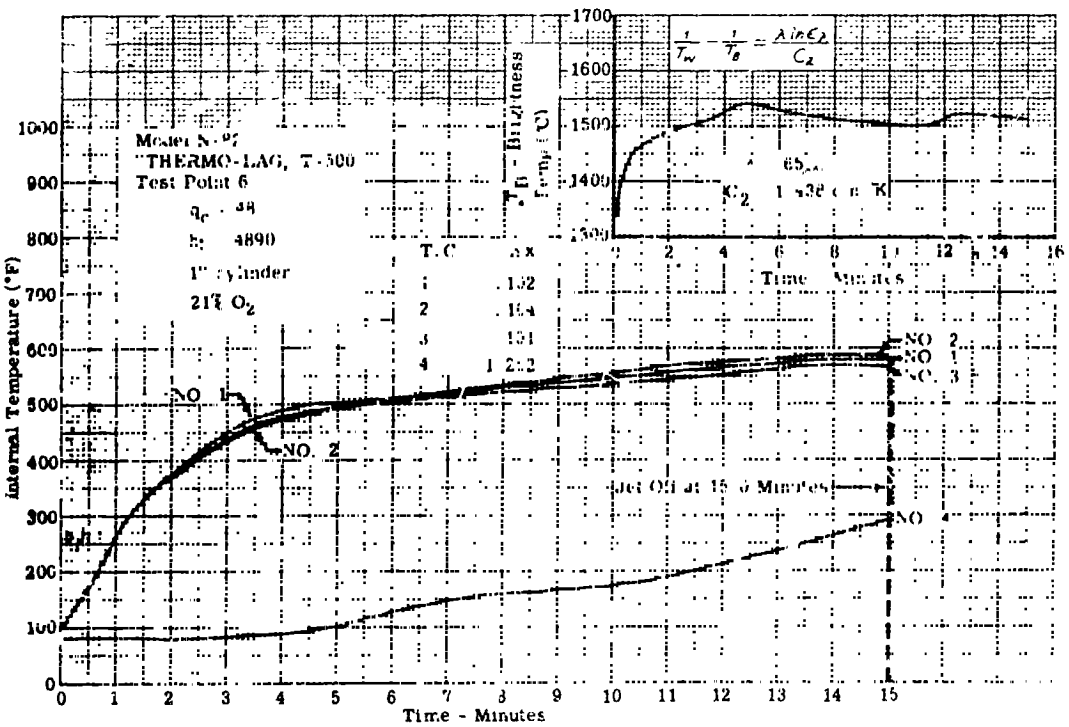


Figure A-71. Temperature-Time History of Model N-82

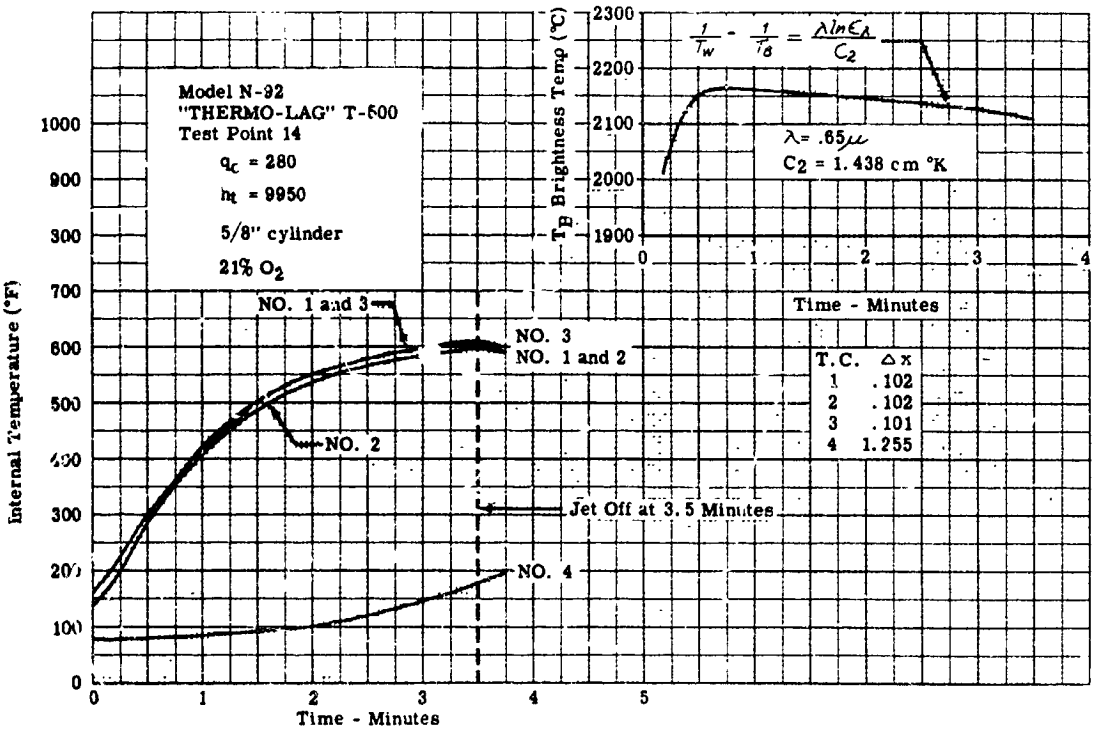


Figure A-72. Temperature-Time History of Model N-92

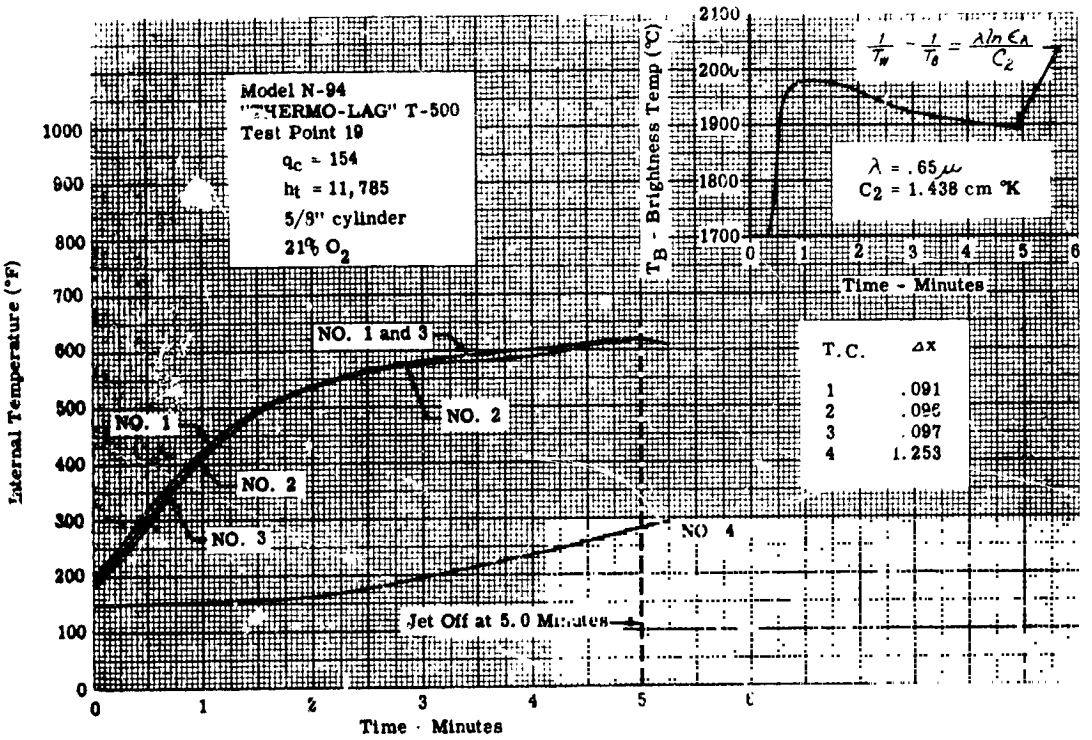


Figure A-73. Temperature-Time History of Model N-94

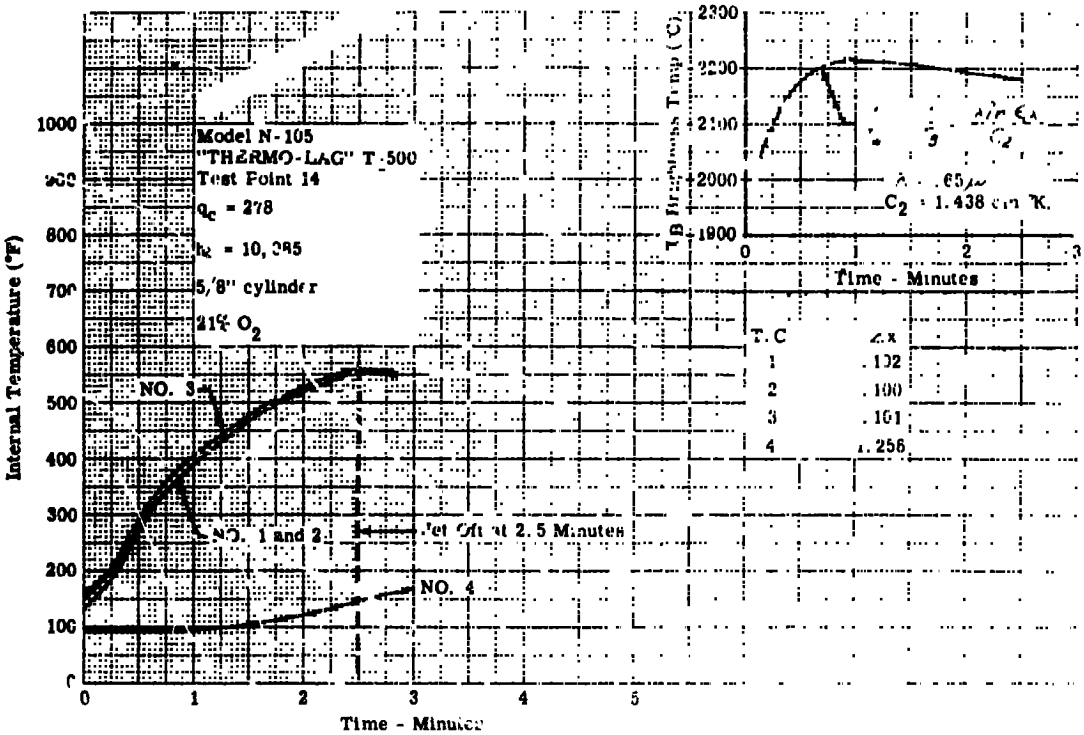


Figure A-74. Temperature-Time History of Model N-105

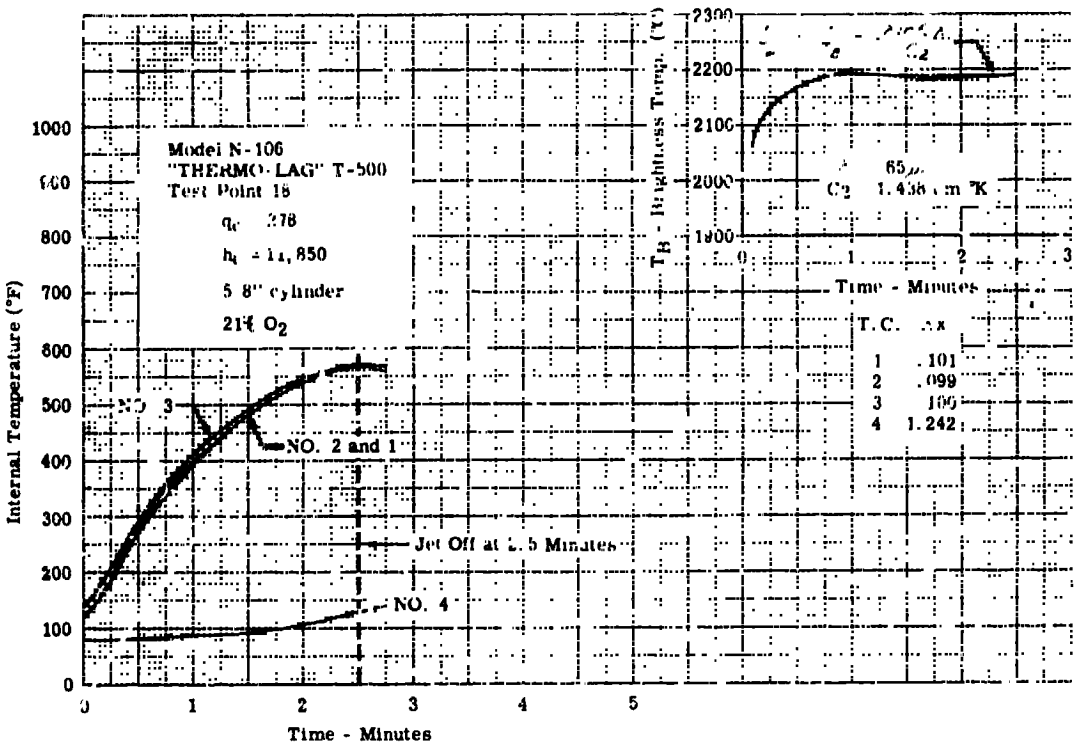


Figure A-75. Temperature-Time History of Model N-106

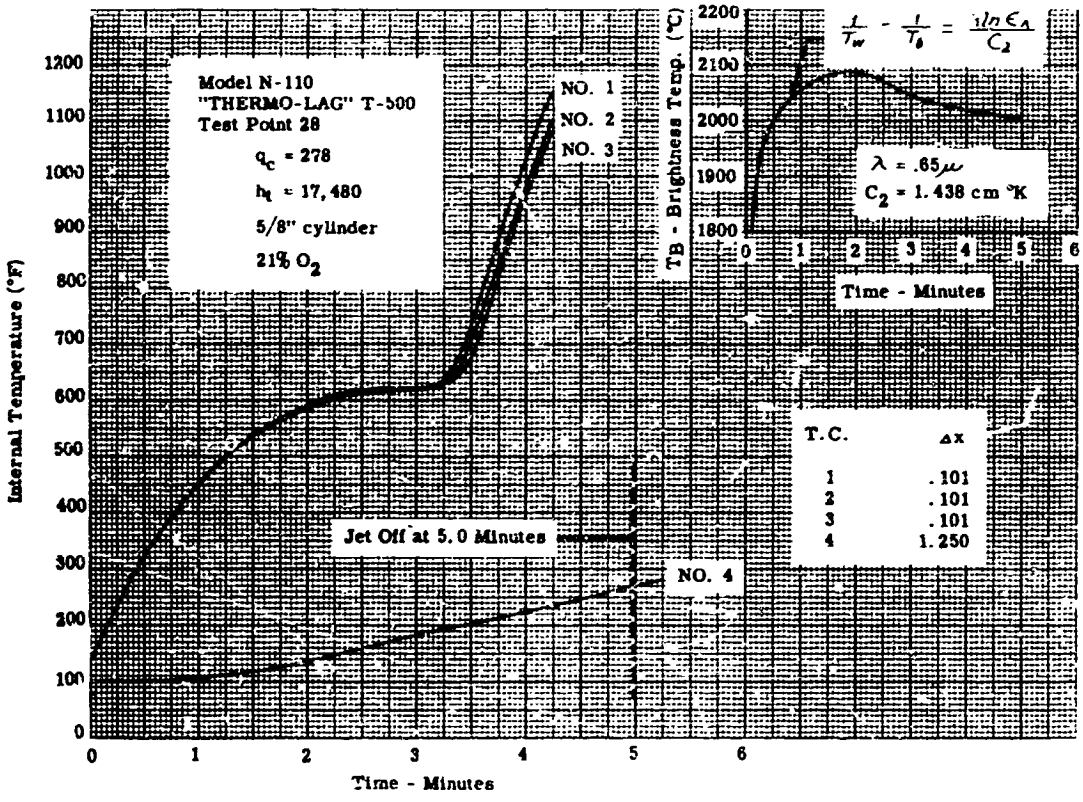


Figure A-76. Temperature-Time History of Model N-110

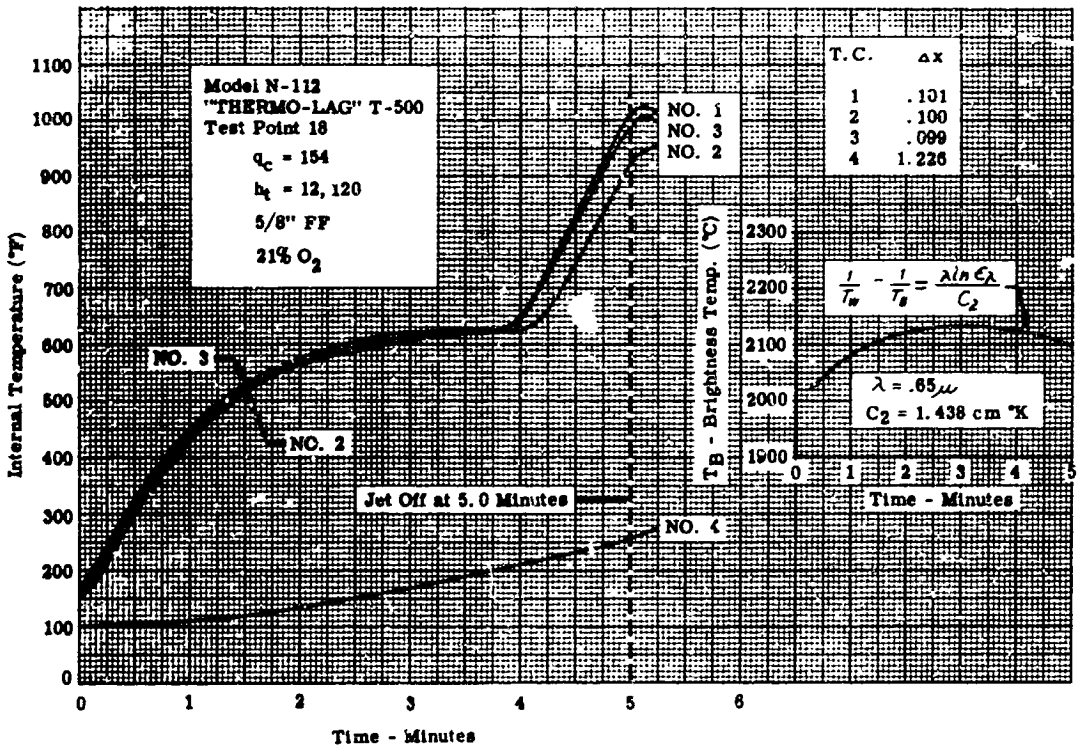


Figure A-77. Temperature-Time History of Model N-112

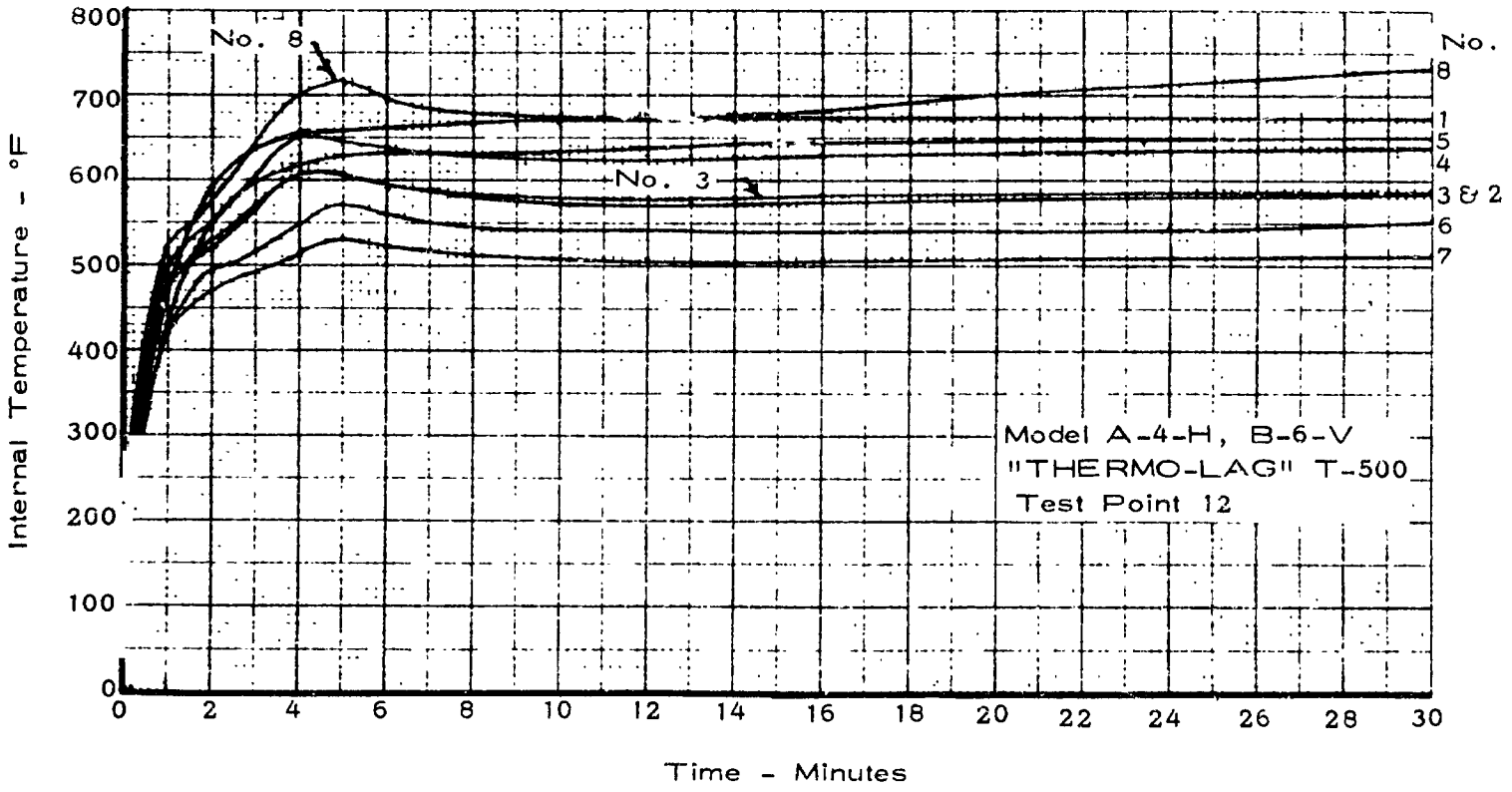


Figure A-78. Temperature-Time History for Material Gap Test

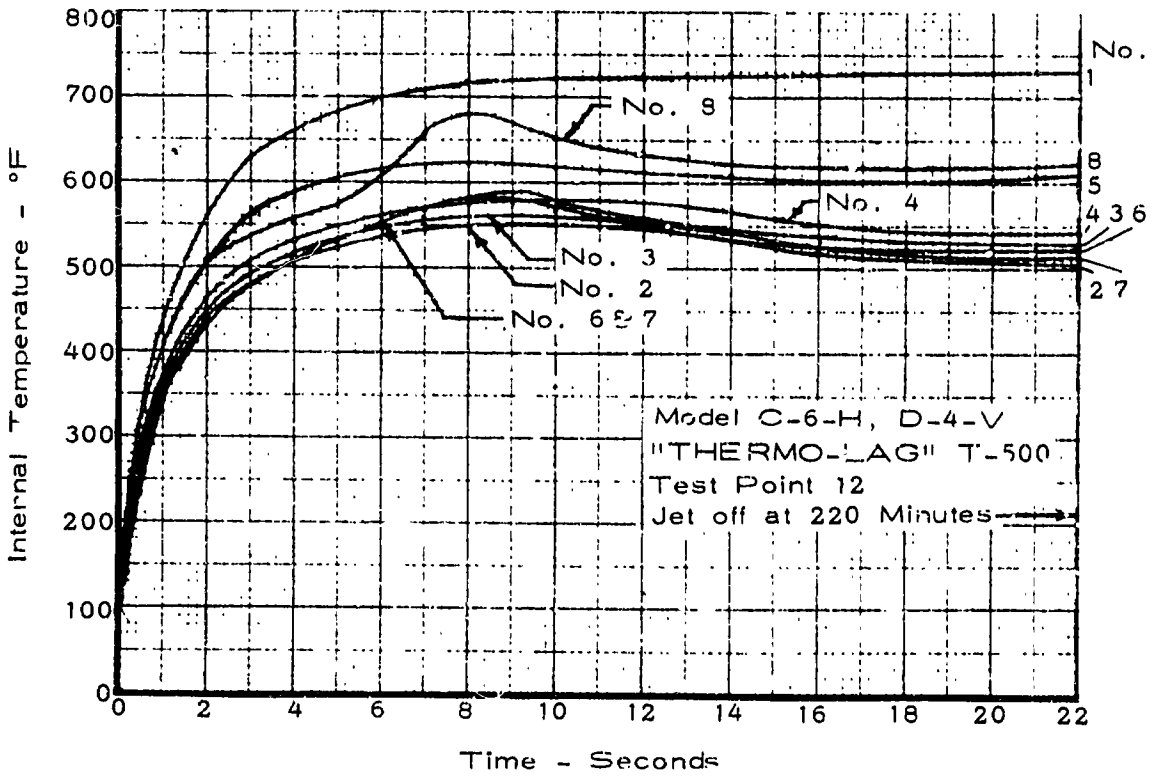


Figure A-79. Temperature-Time History for Material Gap Test

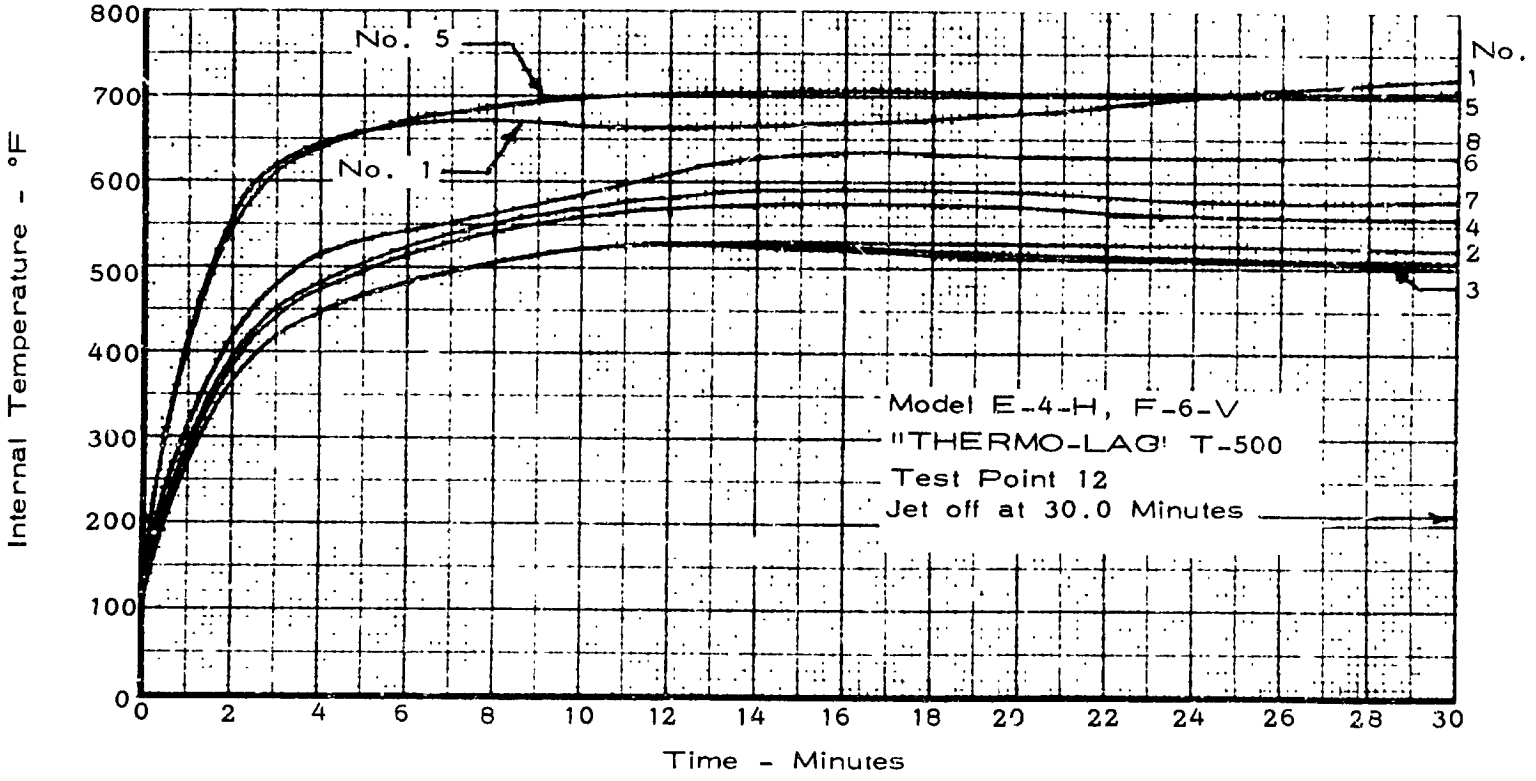


Figure A-80. Temperature-Time History For Material Gap Test

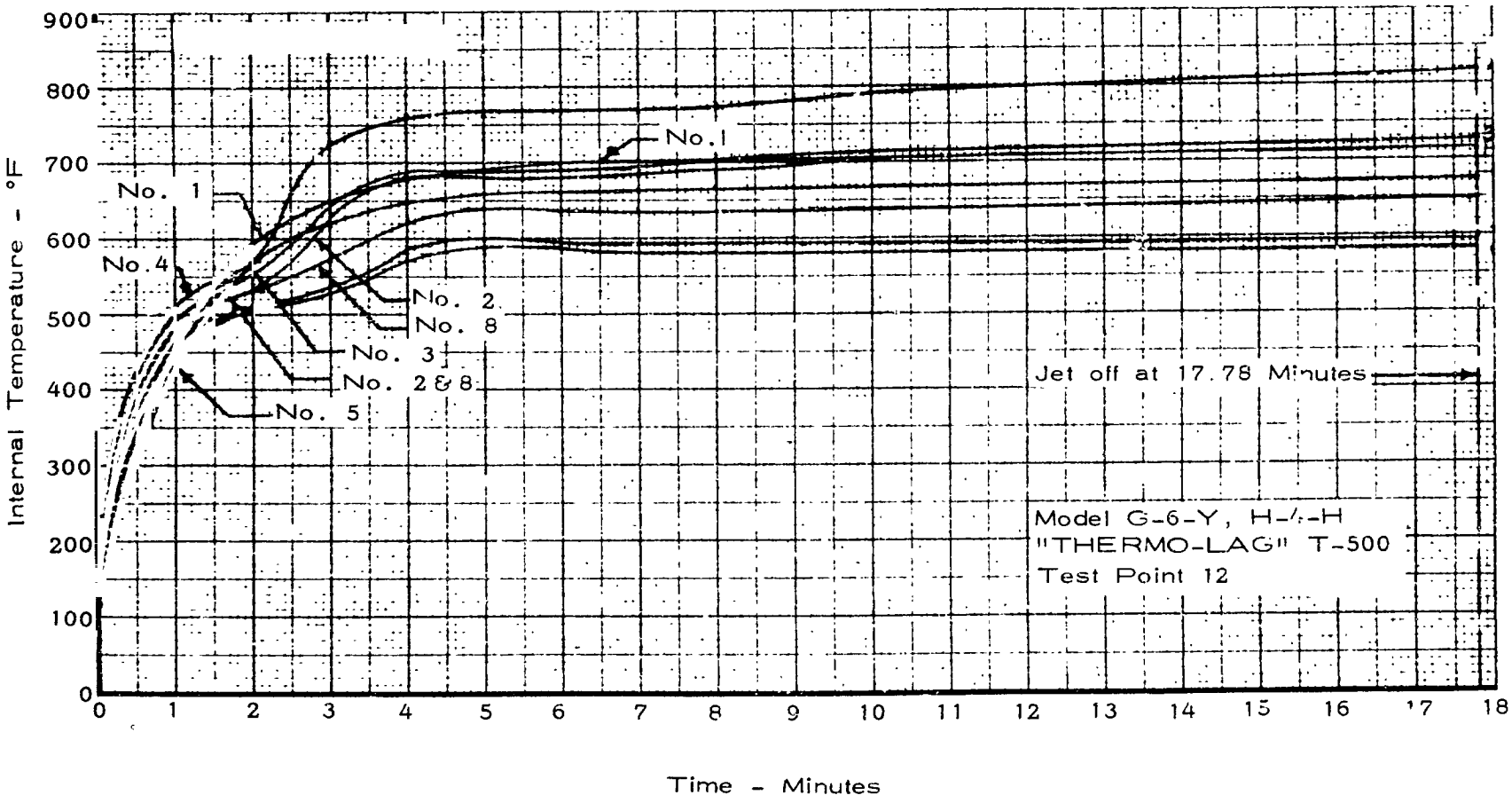


Figure A-81. Temperature-Time History For Material Gap Test

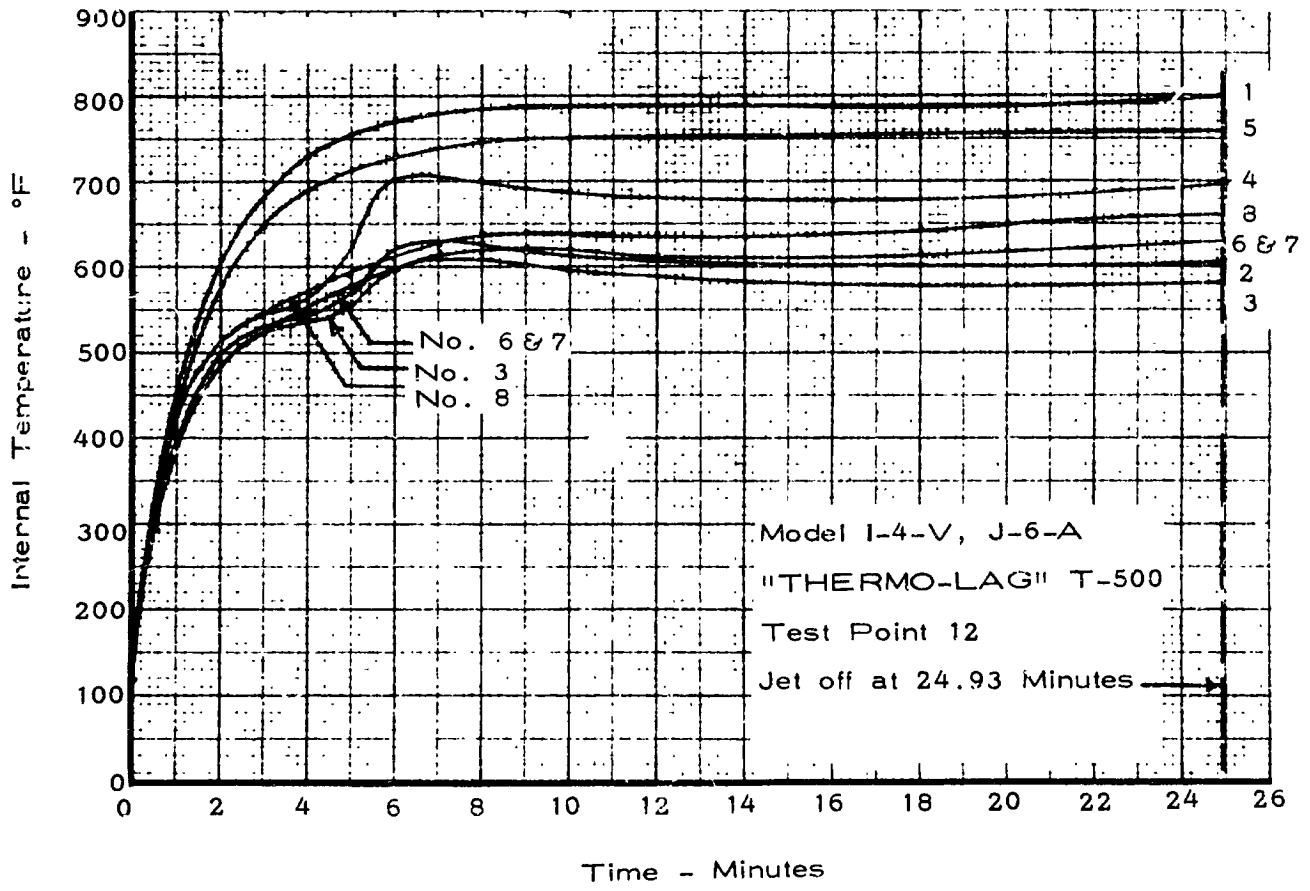


Figure A-82. Temperature-Time History For Material Gap Test

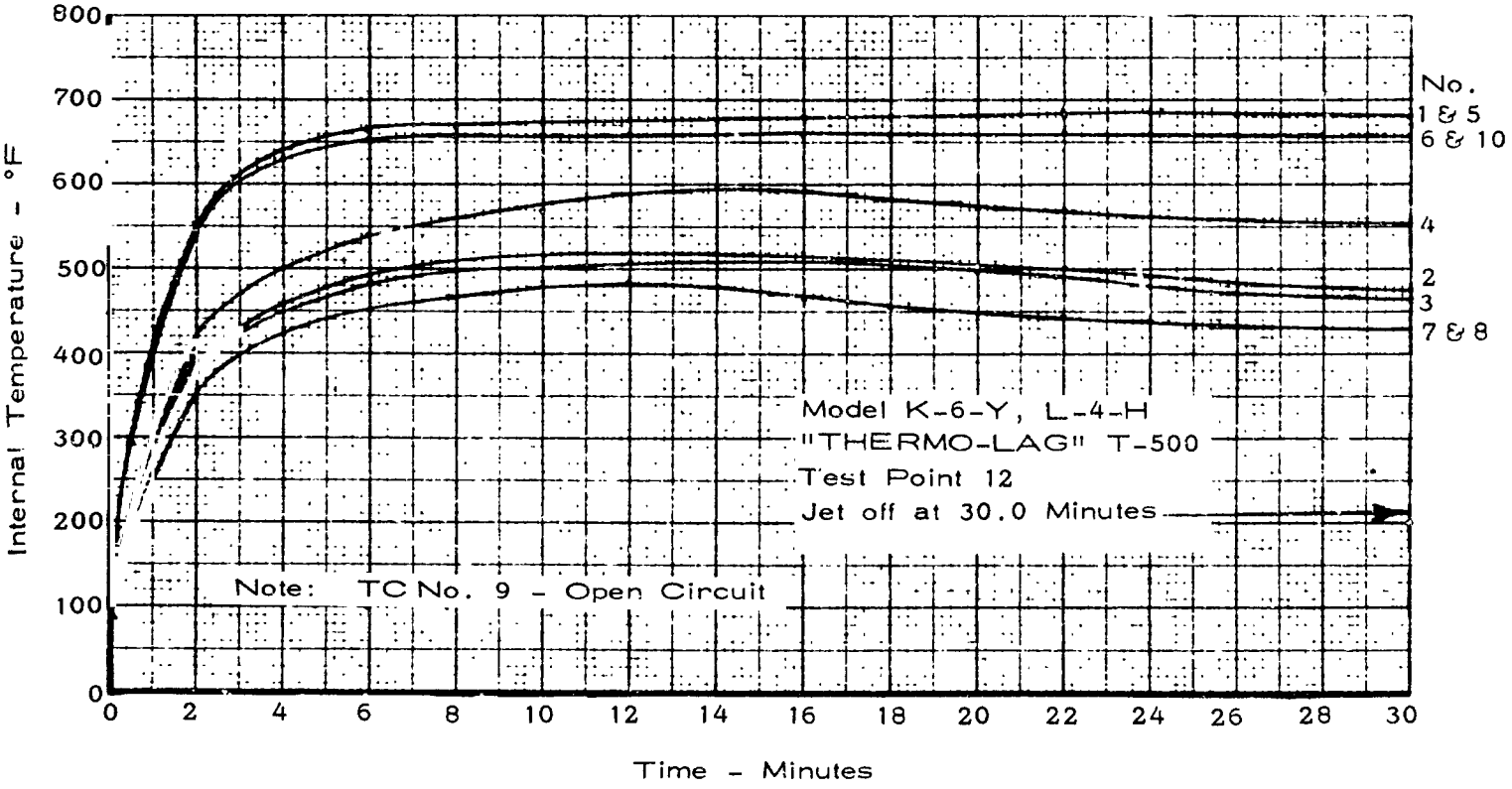


Figure A-83. Temperature-Time History For Material Gap Test

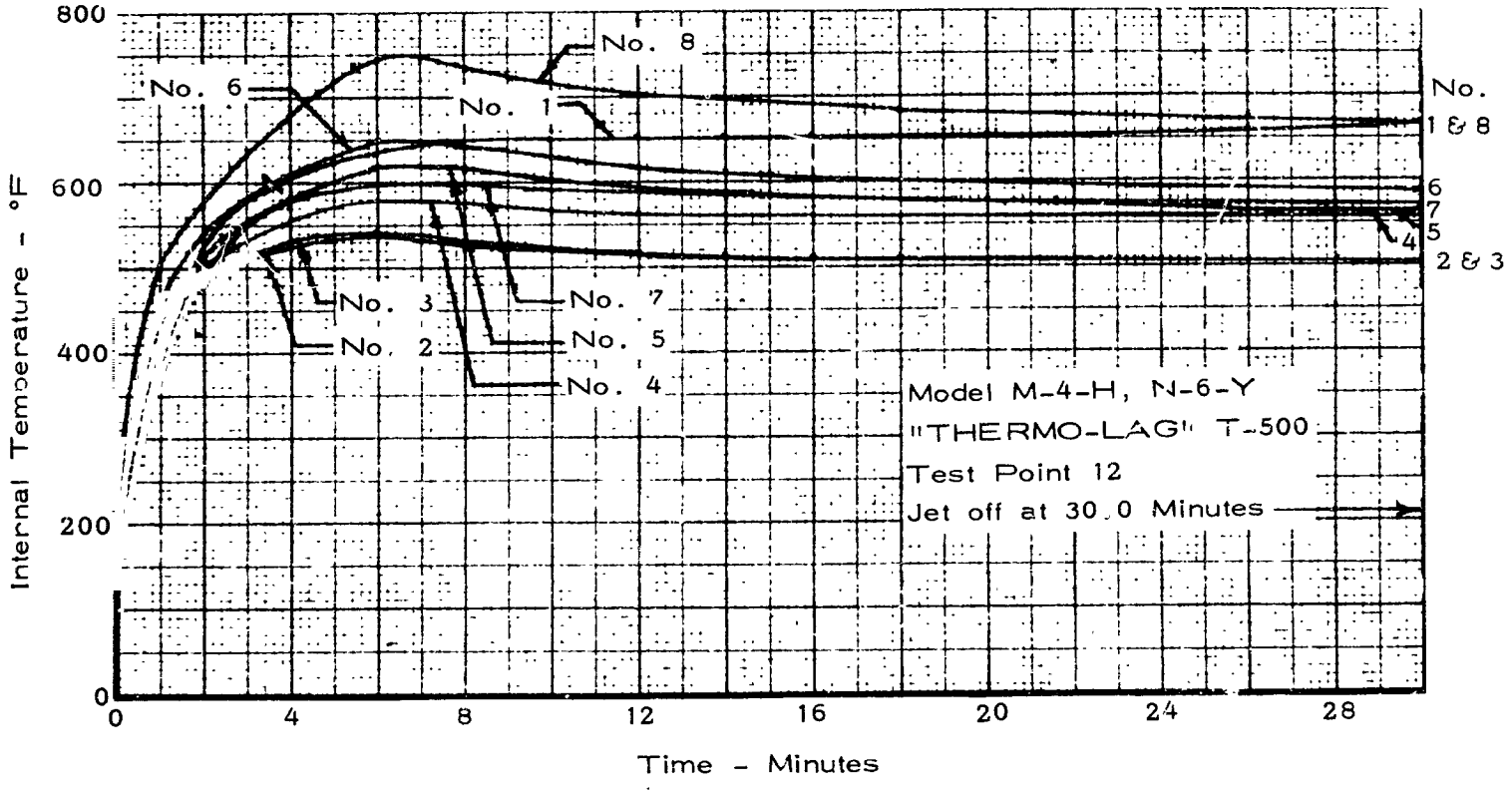


Figure A-84. Temperature-Time History For Material Gap Test

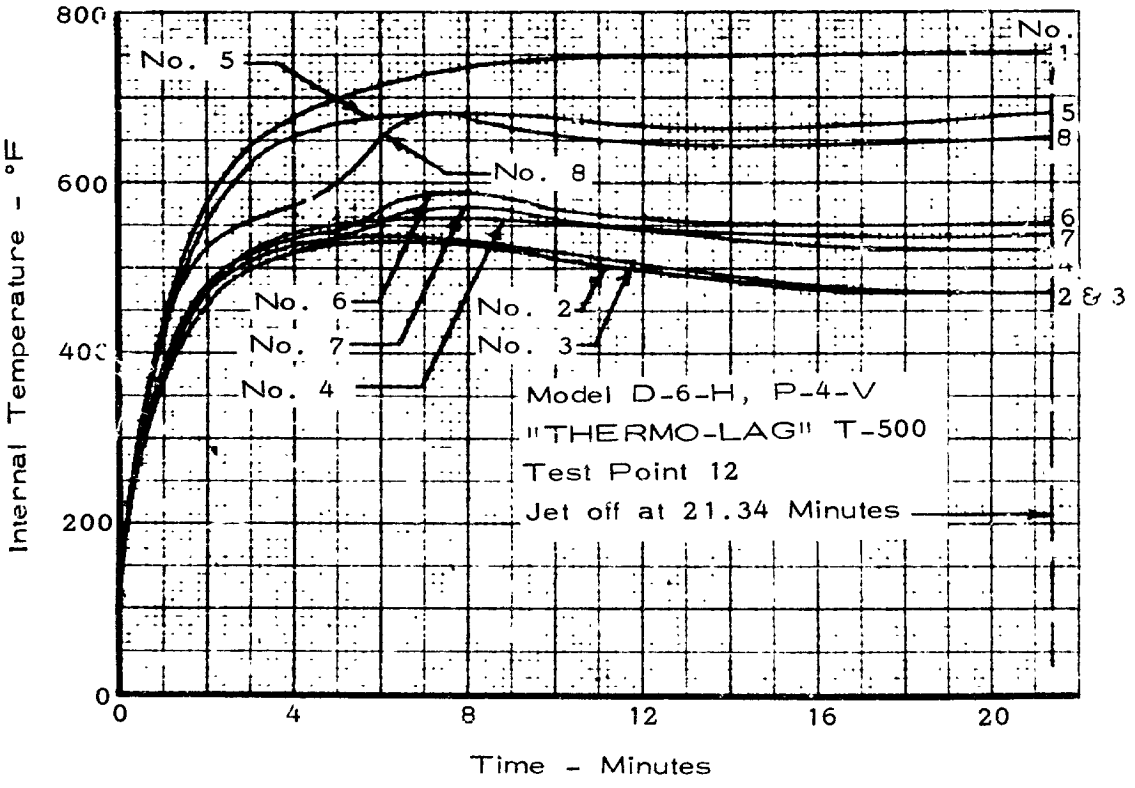


Figure A-85. Temperature-Time History For Material Gap Test

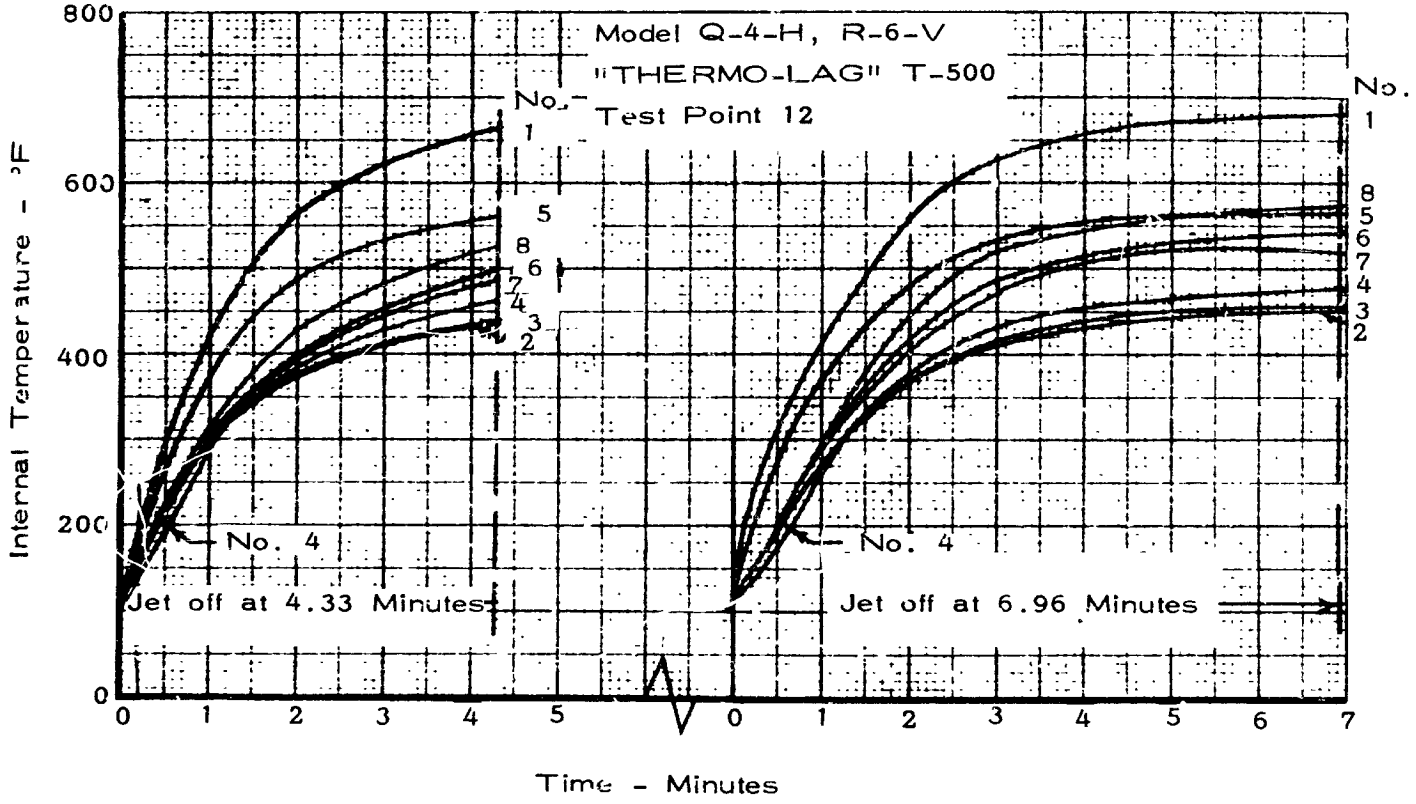


Figure A-86. Temperature-Time History For Material Gap Test

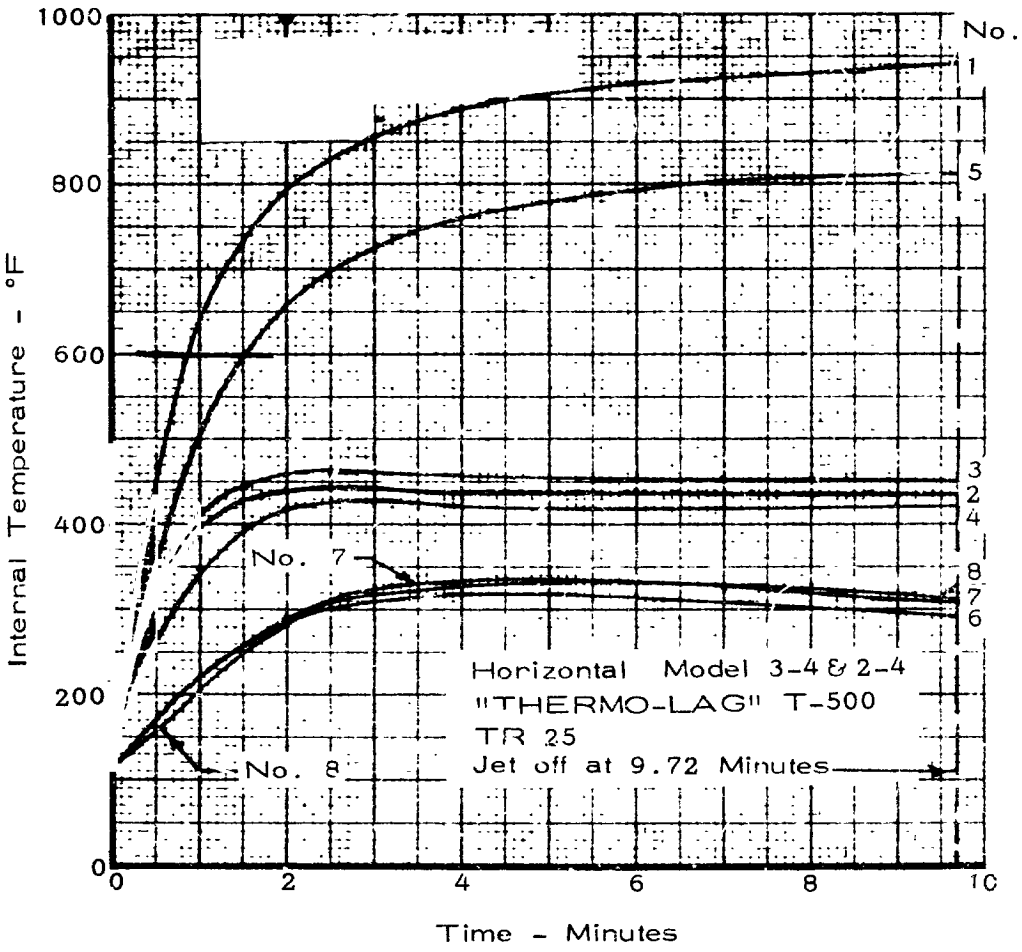


Figure A-87. Temperature-Time History For Material Gap Test

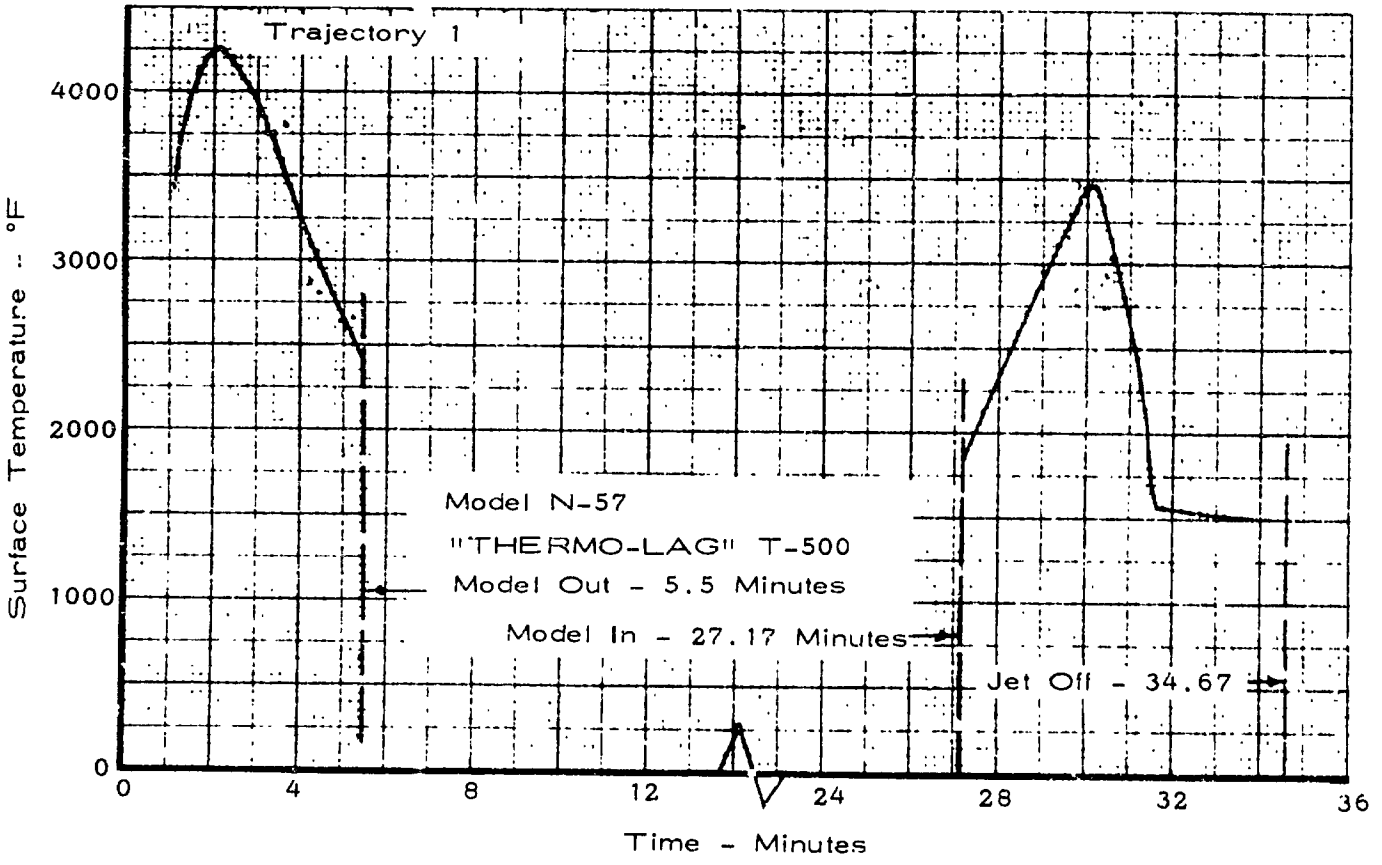


Figure A-88. Trajectory No. 1 Temperature-Time History

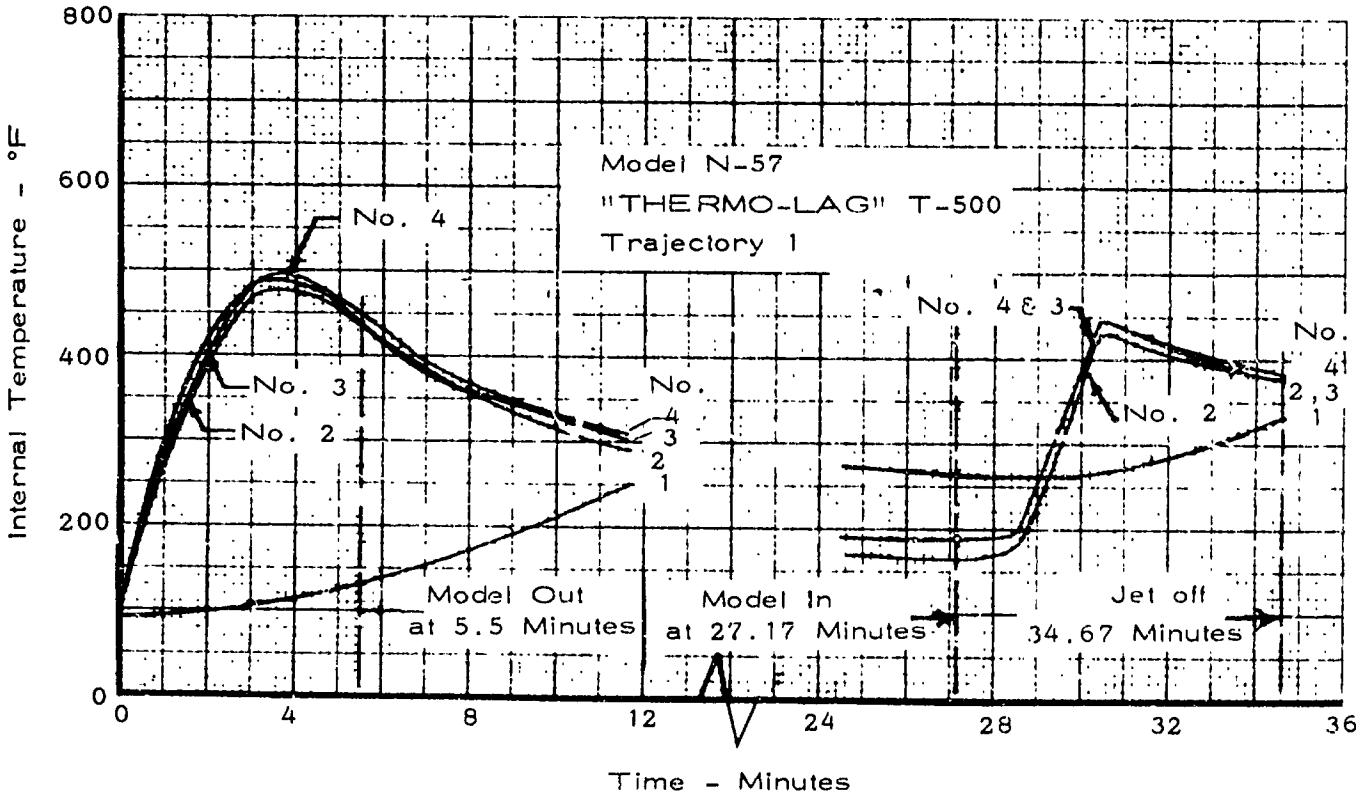


Figure A-89. Trajectory No. 1 Temperature-Time History

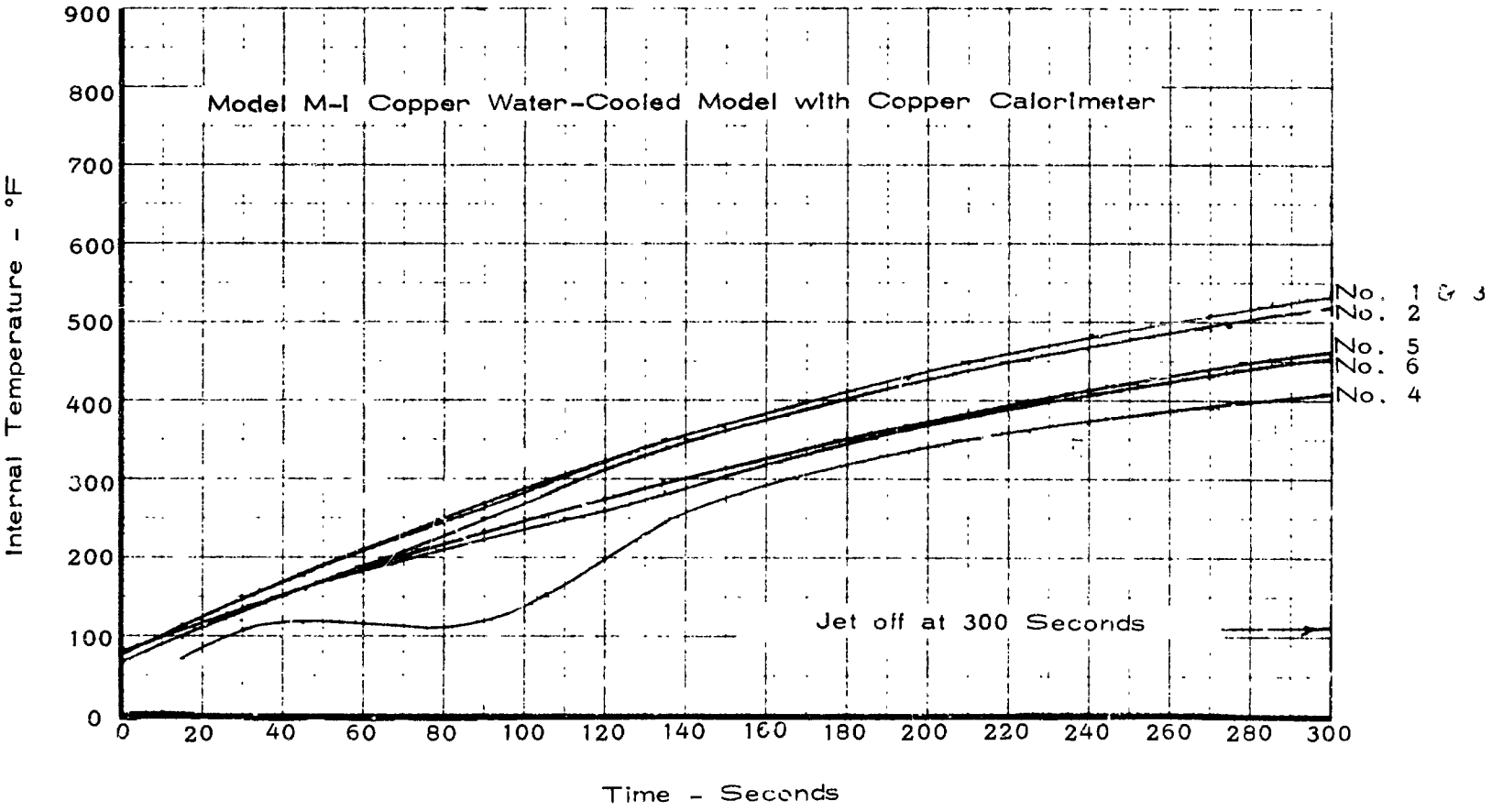


Figure A-90. Temperature-Time History of Mass Injection Test Model M-1

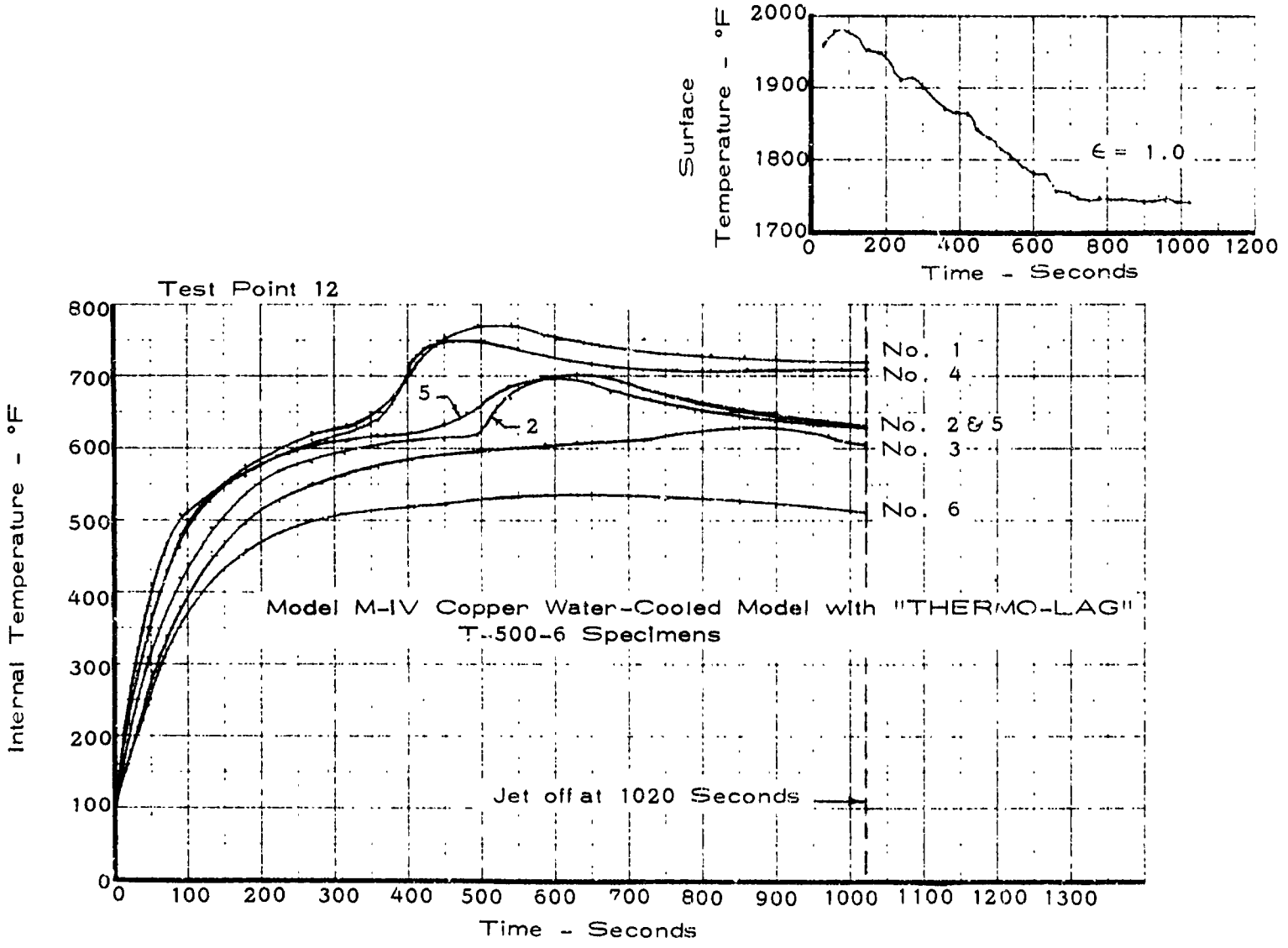


Figure A-91. Temperature-Time History of Mass Injection Test Model M-IV

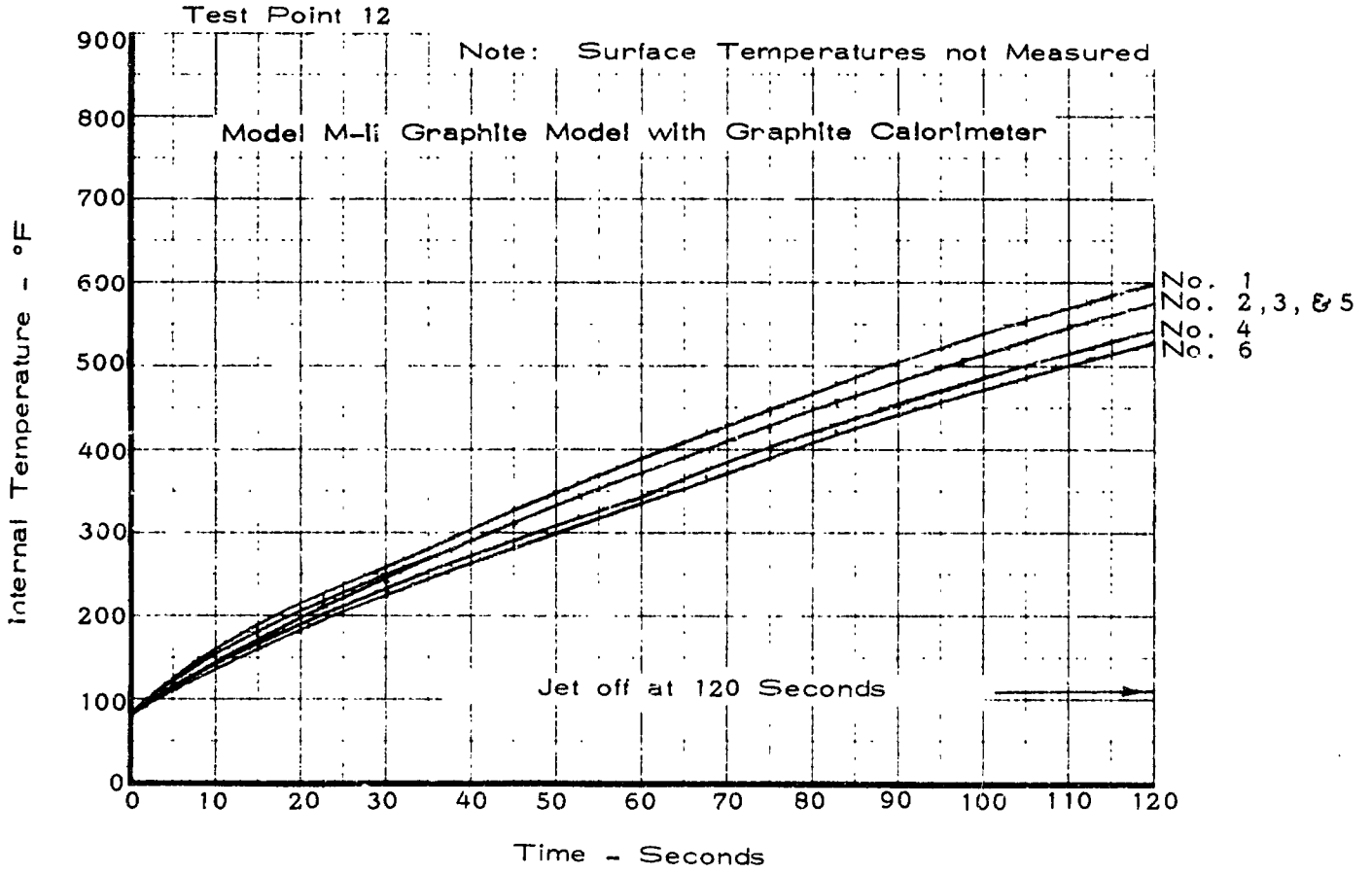


Figure A-92. Temperature-Time History of Mass Injection Test Model M-II

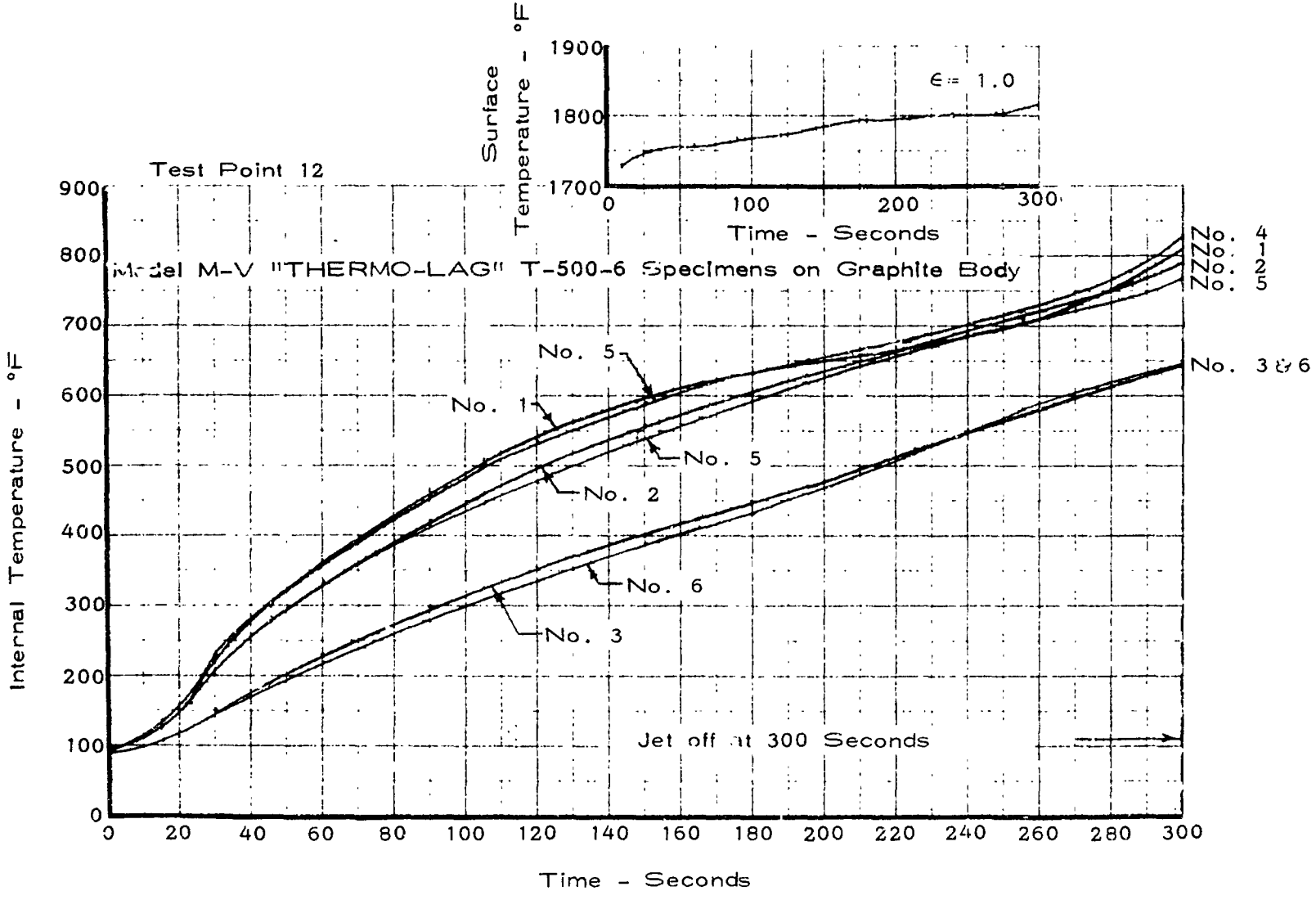


Figure A-93. Temperature-Time History of Mass Injection Test Model M-V

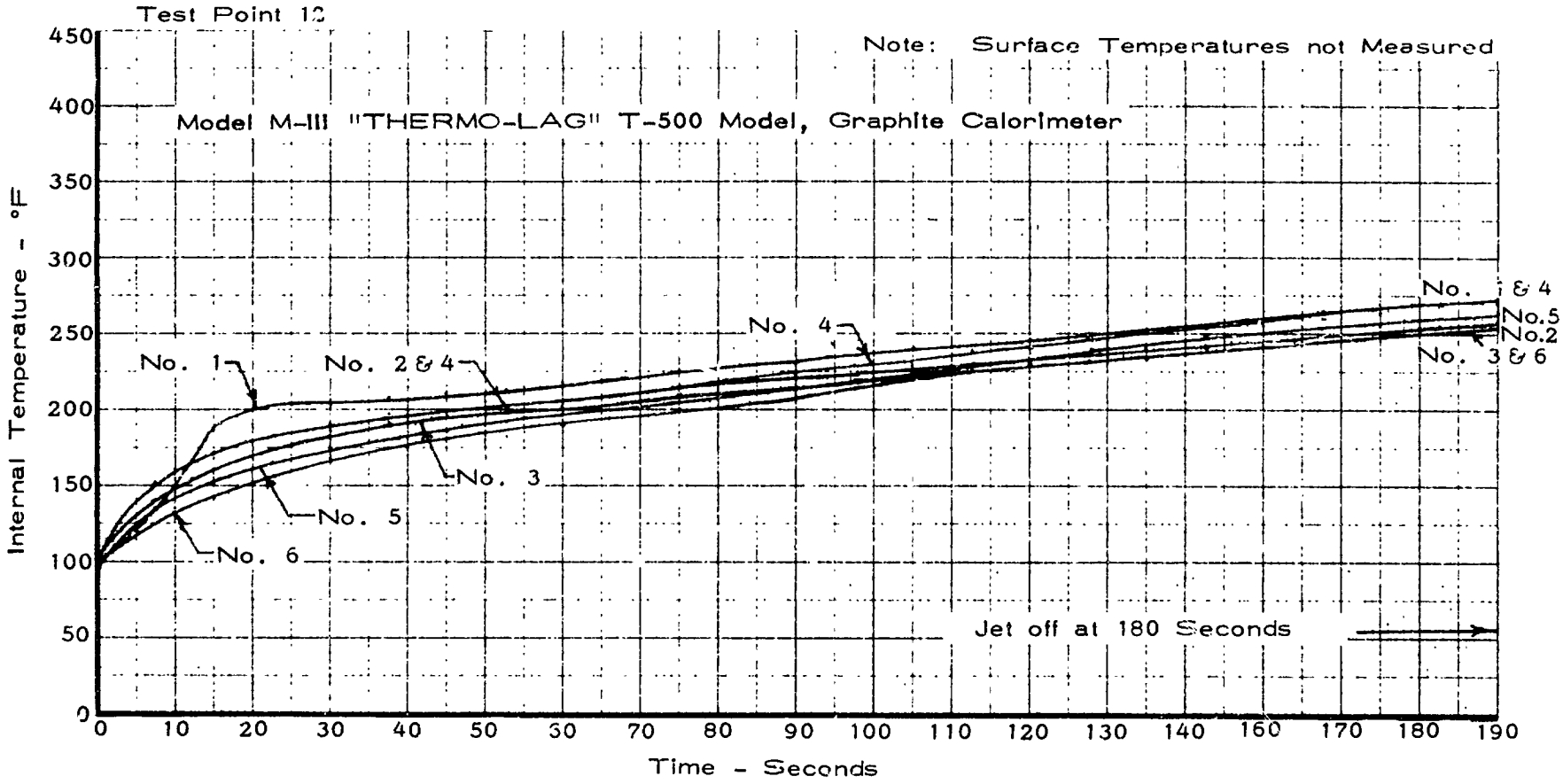


Figure A-94. Temperature-Time History of Mass Injection Test Model M-III

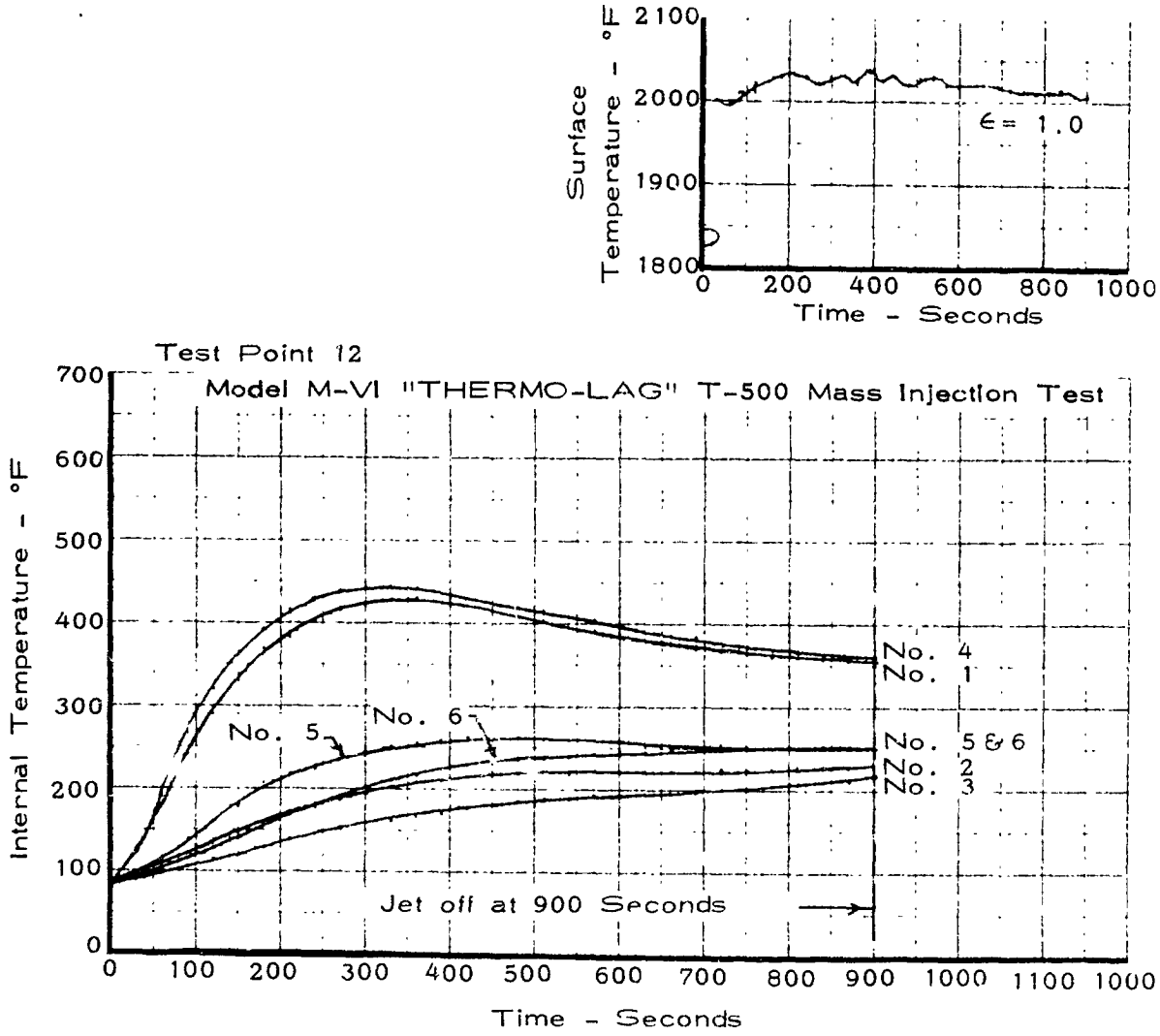
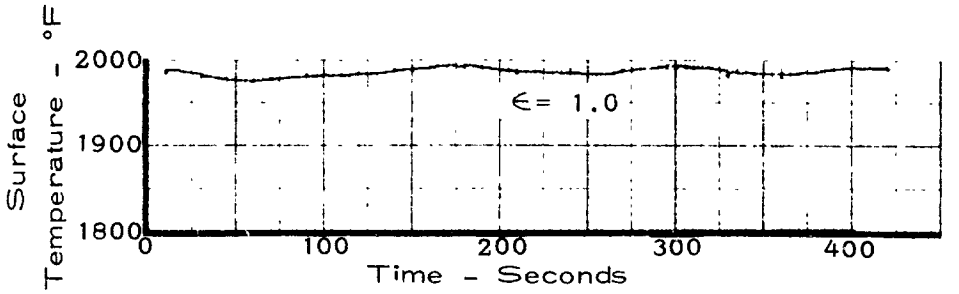


Figure A-95. Temperature-Time History of Mass Injection Test Model M-VI-1



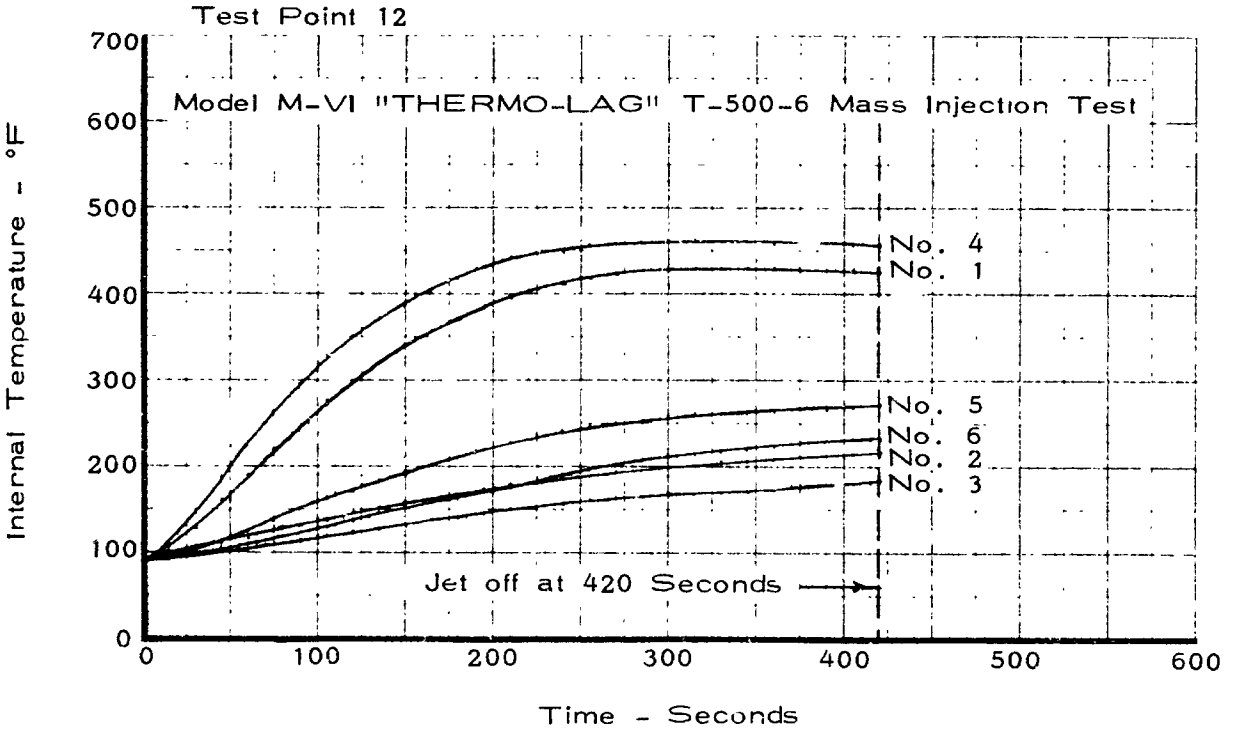
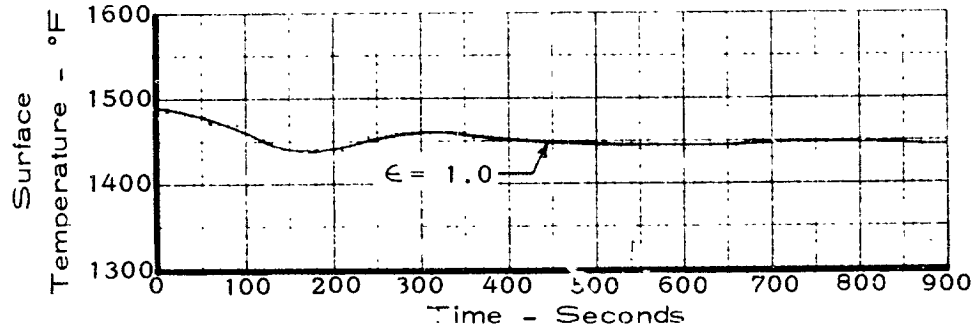


Figure A-96. Temperature-Time History of Mass Injection Test Model M-VI-2



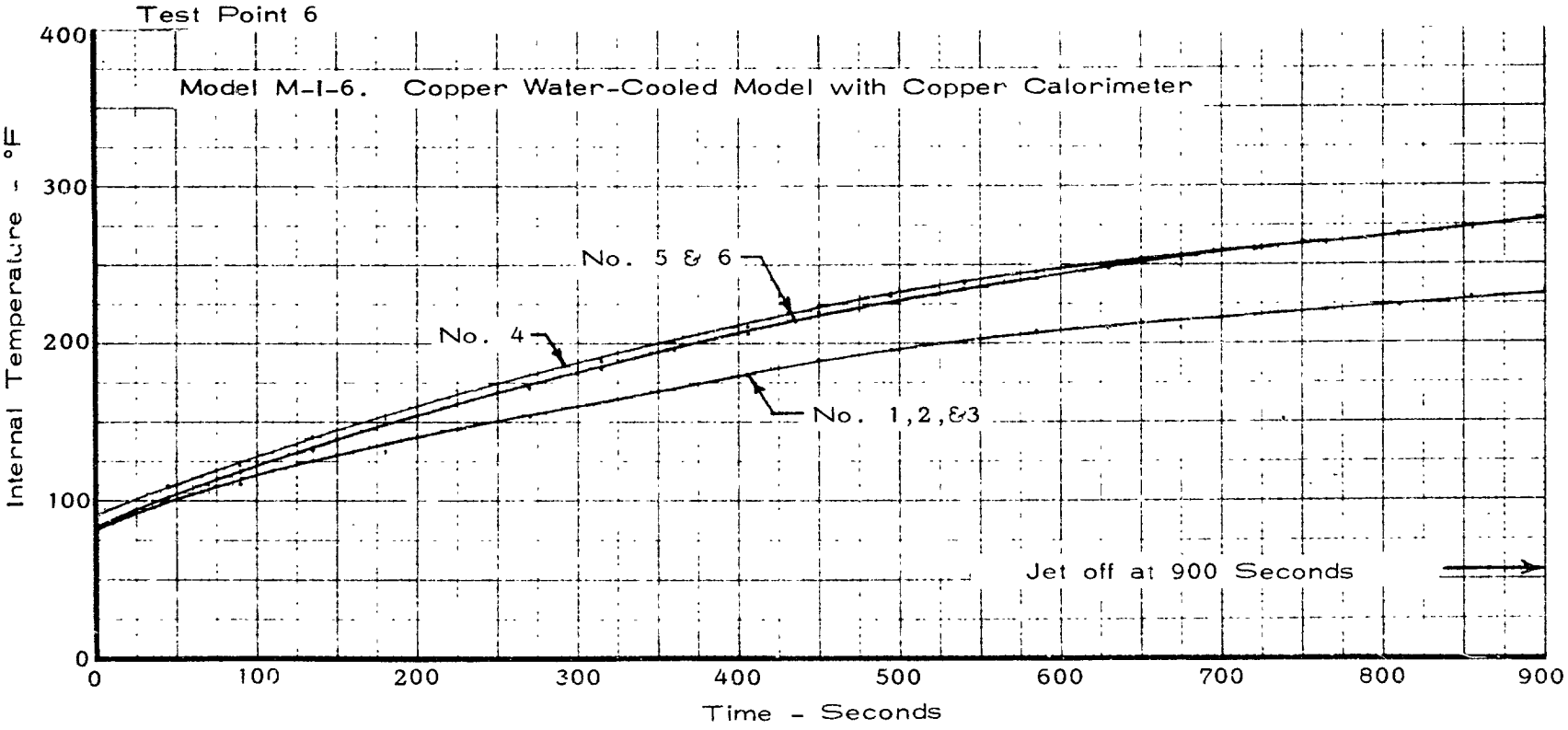
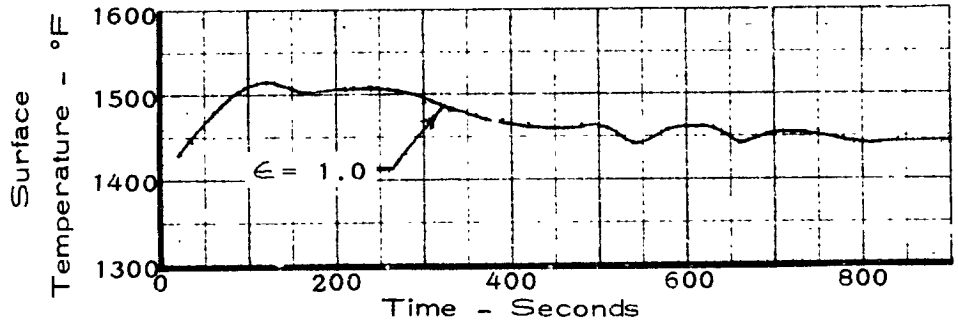


Figure A-97. Temperature-Time History of Model M-I-6



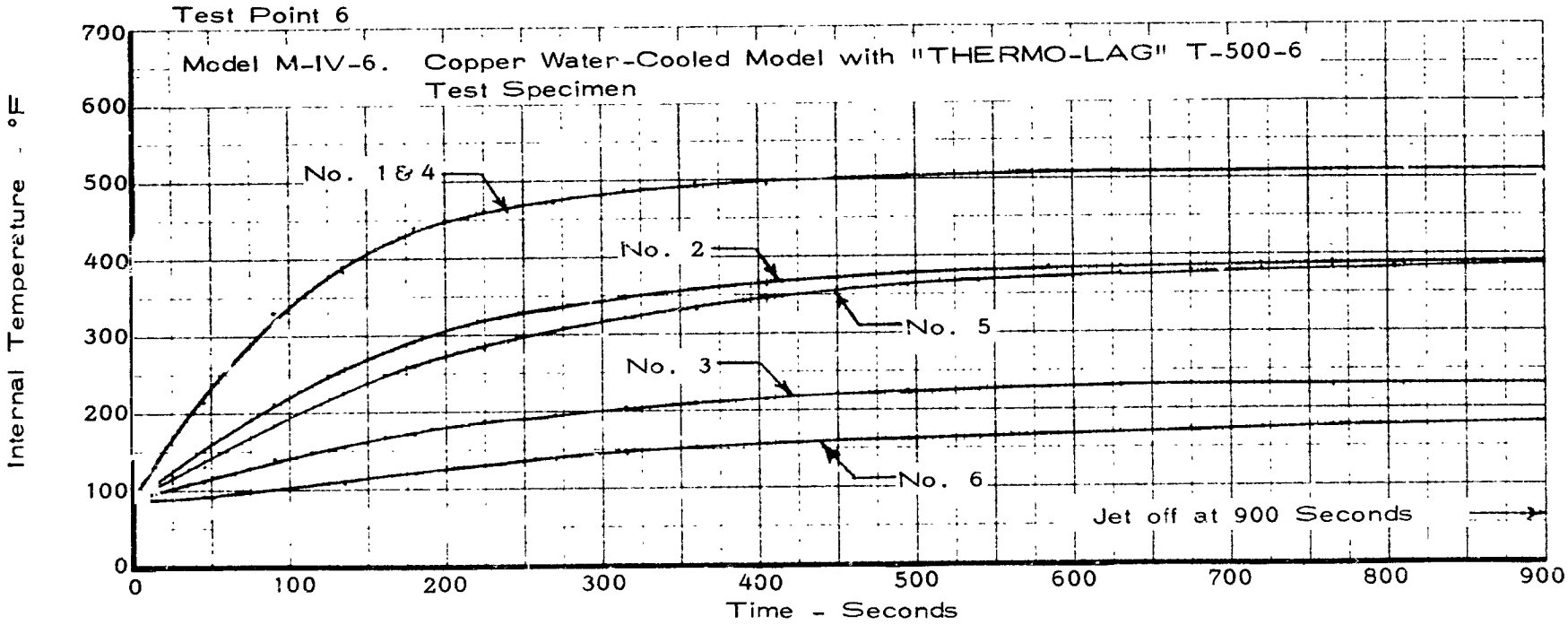
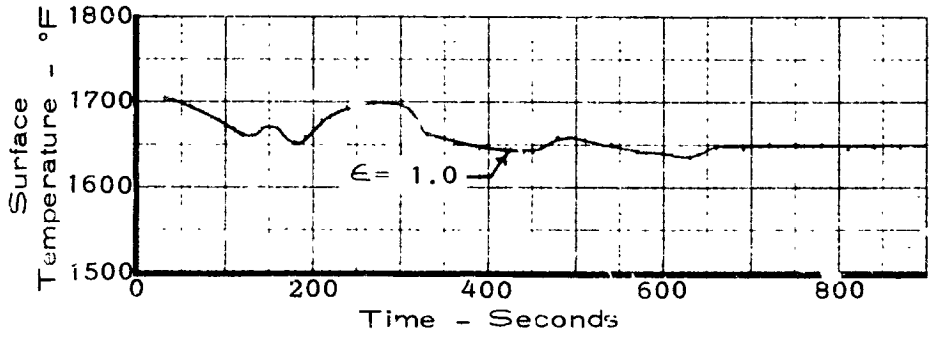


Figure A-98. Temperature-Time History of Model M-IV-6



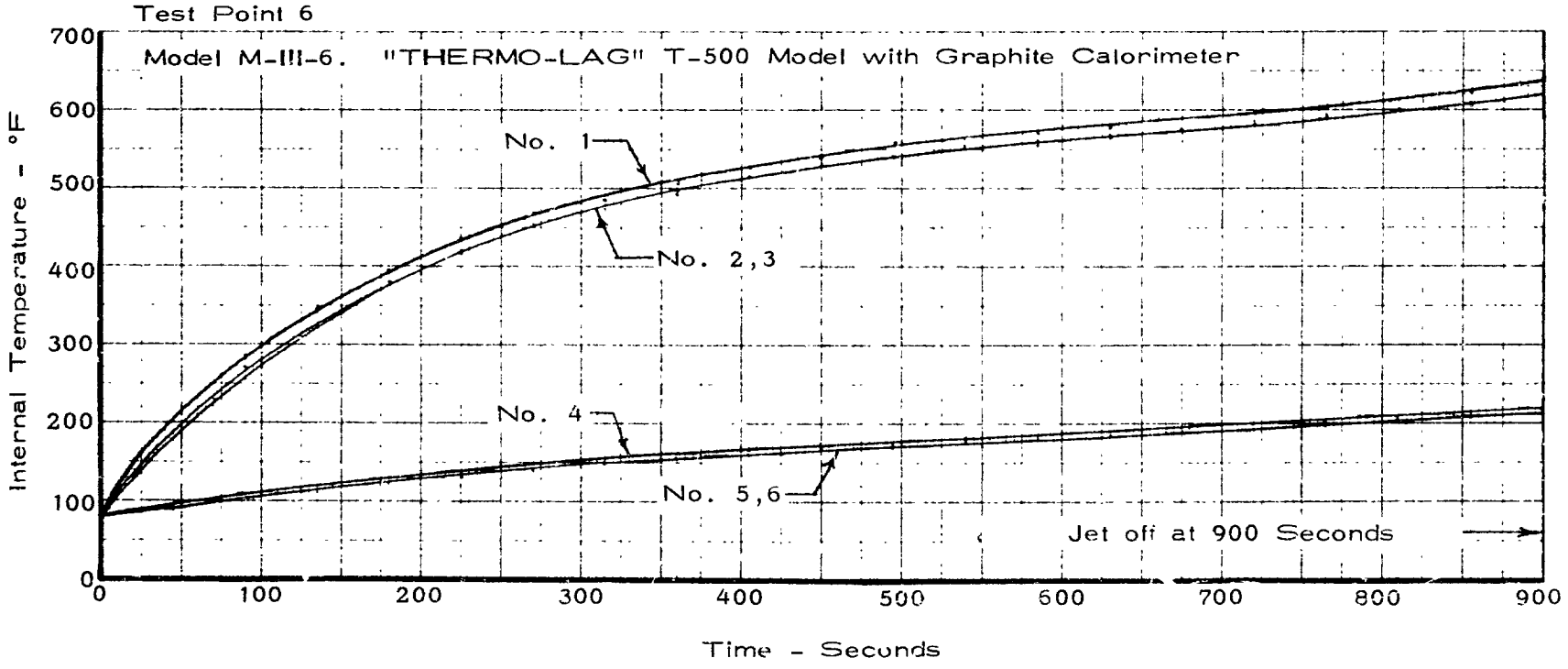


Figure A-99. Temperature-Time History of Model M-III-6

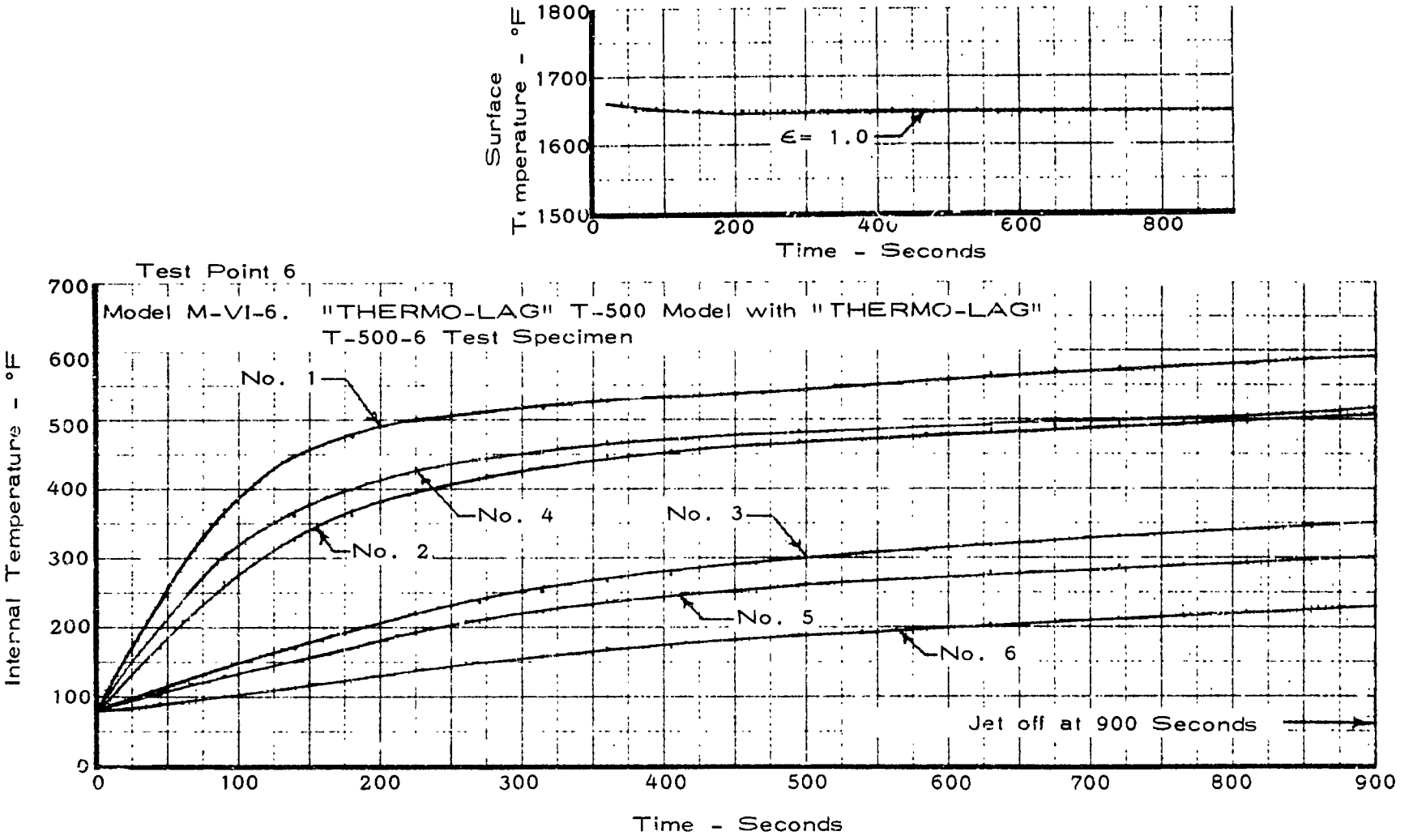
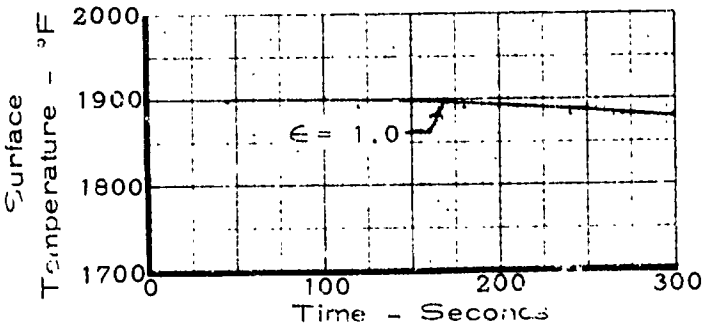


Figure A-100. Temperature-Time History of Model M-VI-6



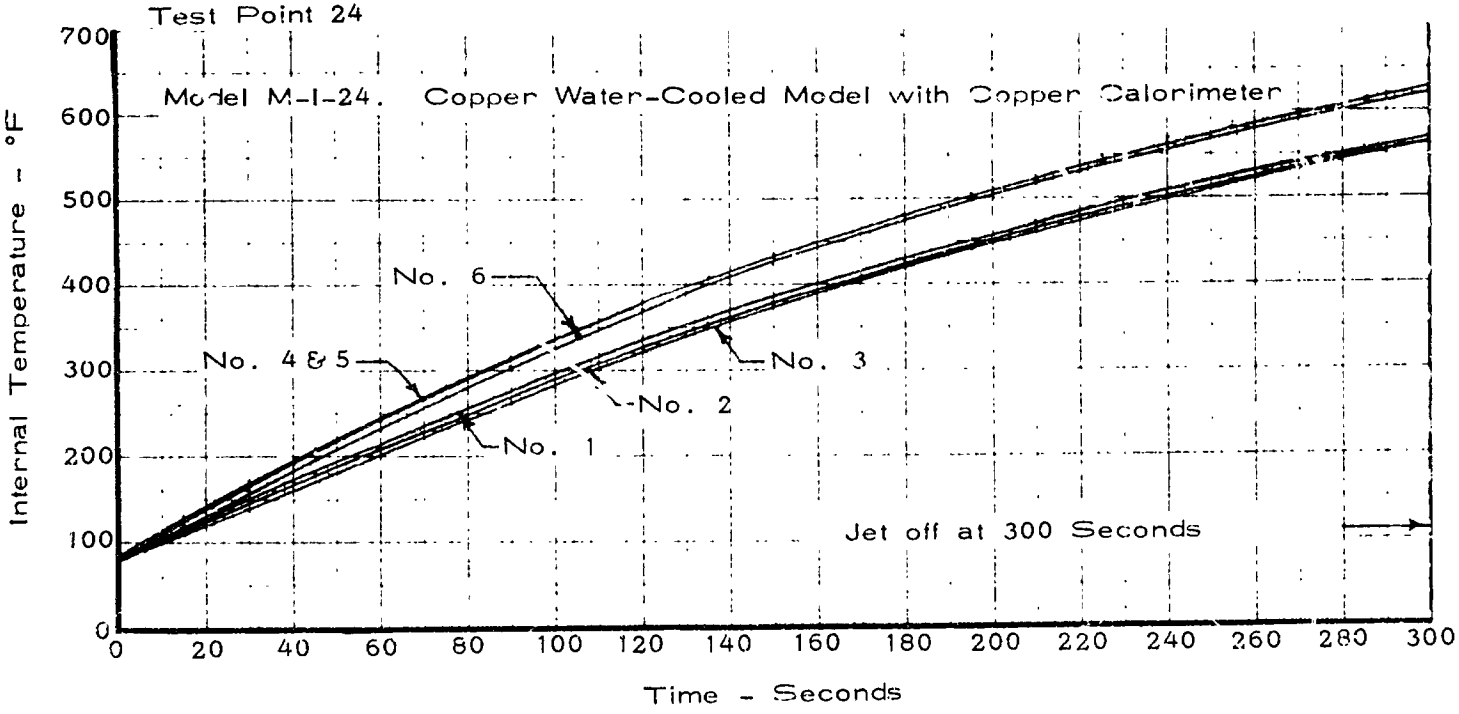


Figure A-101. Temperature-Time History of Model M-I-24

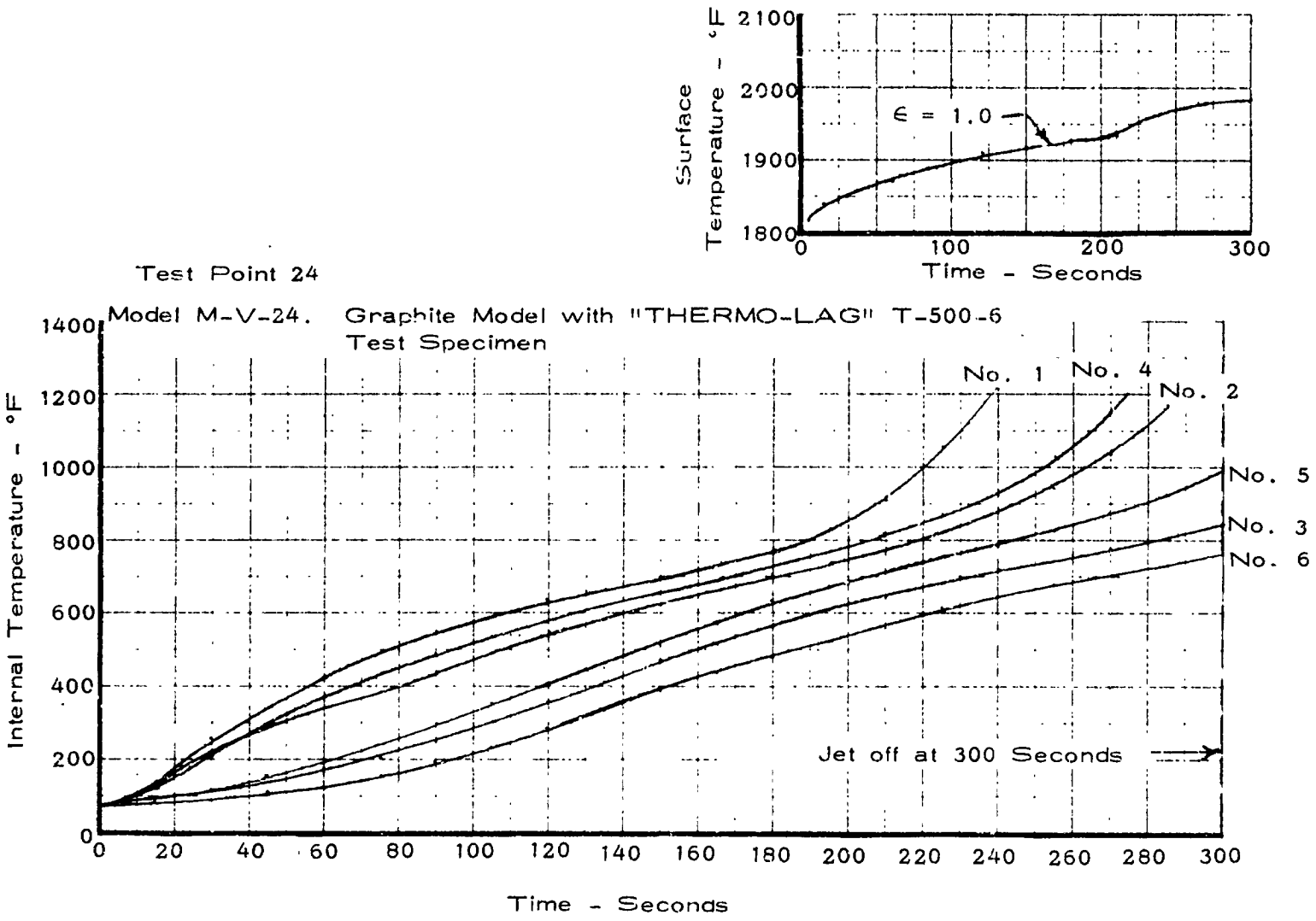


Figure A-102. Temperature-Time History of Model M-V-24

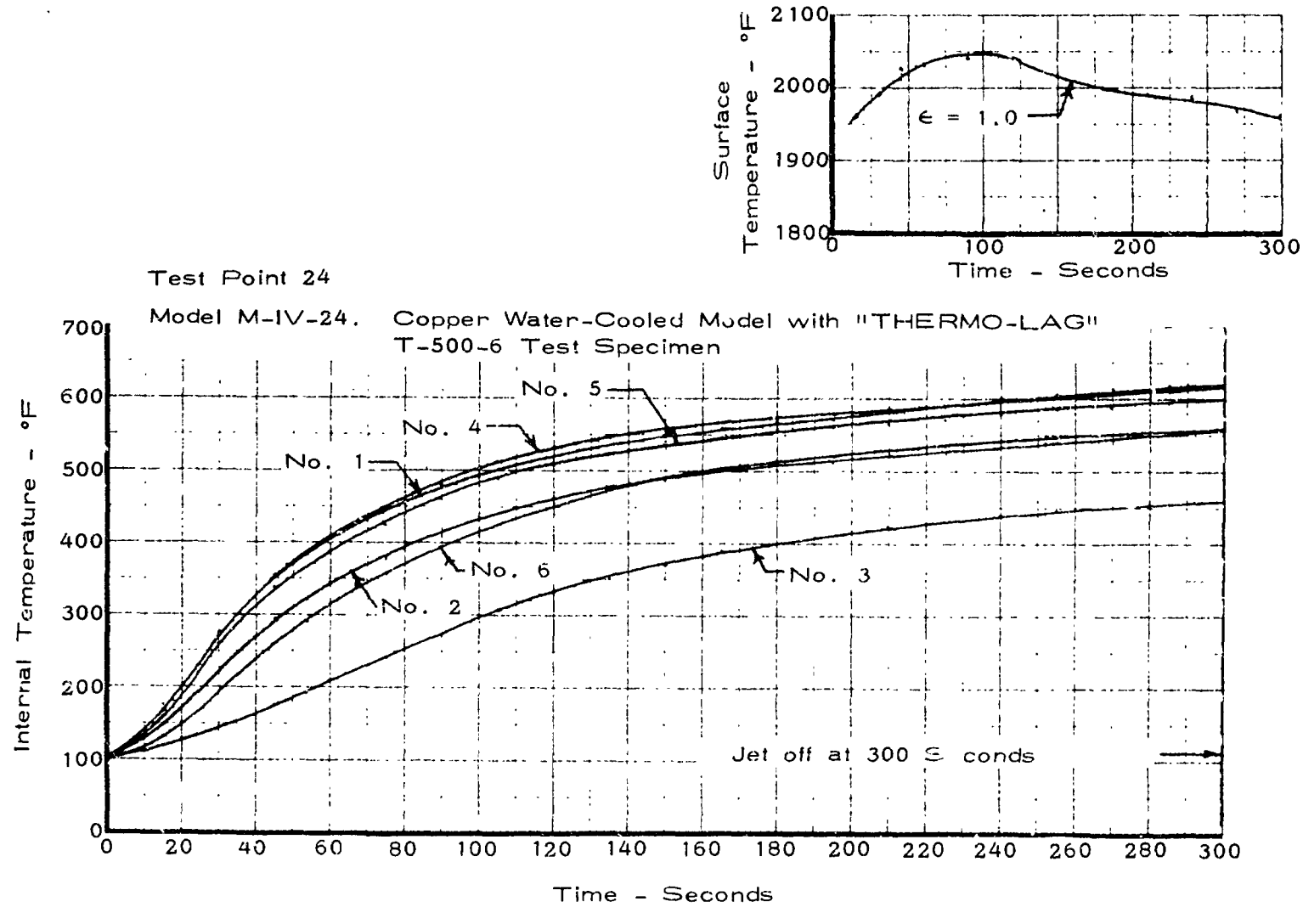


Figure A-103. Temperature-Time History of Model M-IV-24

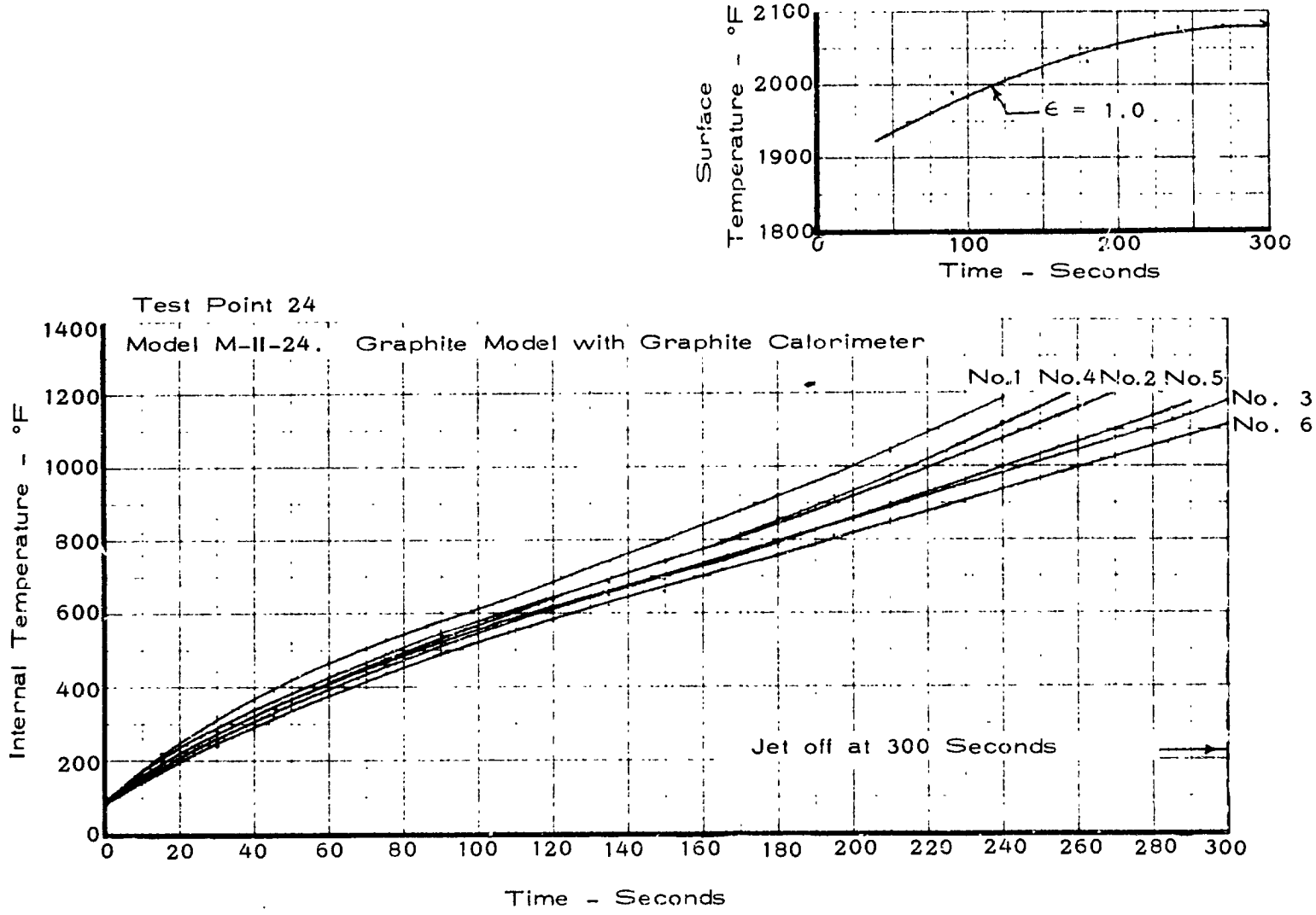


Figure A-104. Temperature-Time History of Model M-II-24

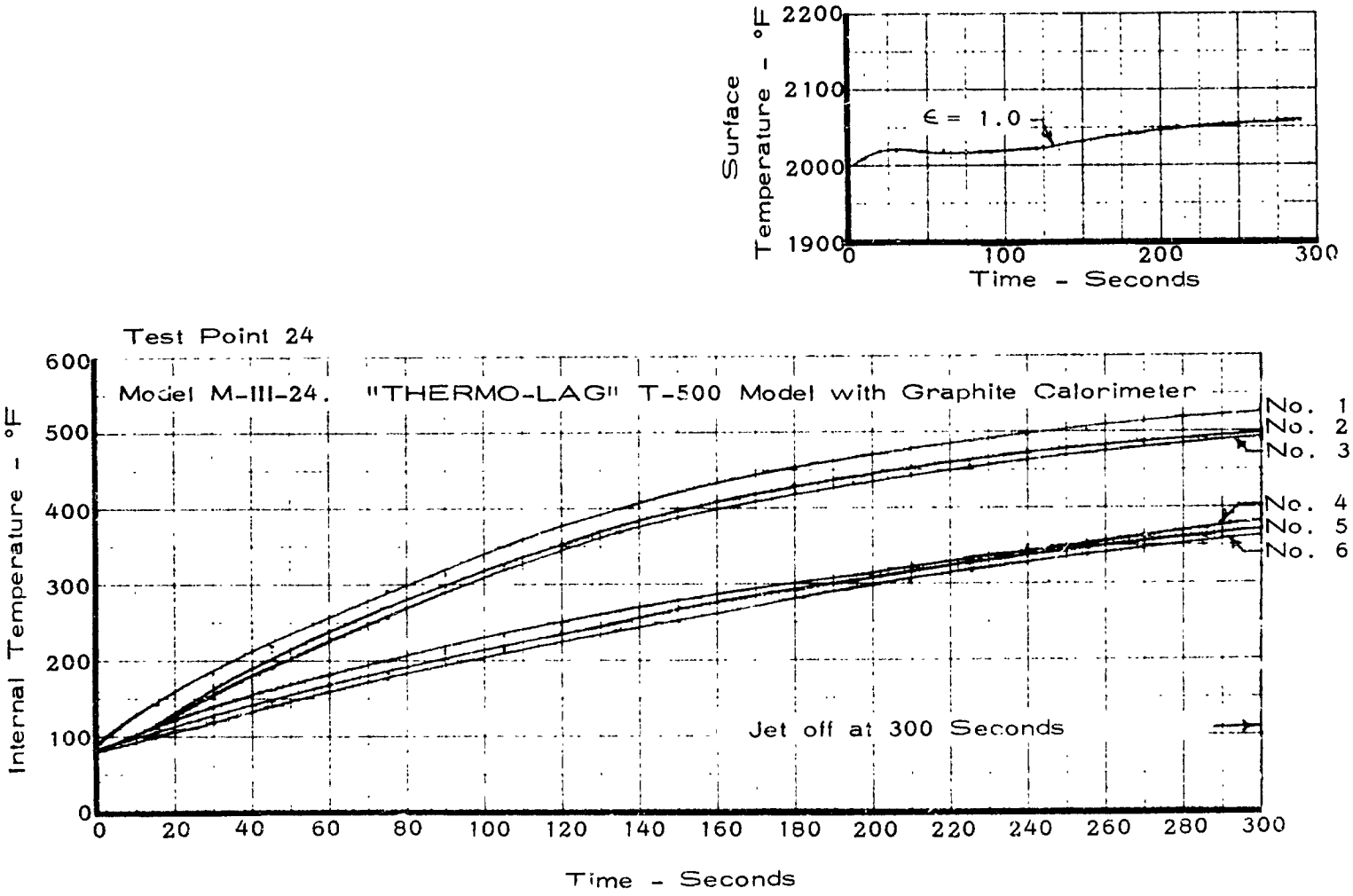


Figure A-105. Temperature-Time History of Model M-III-24

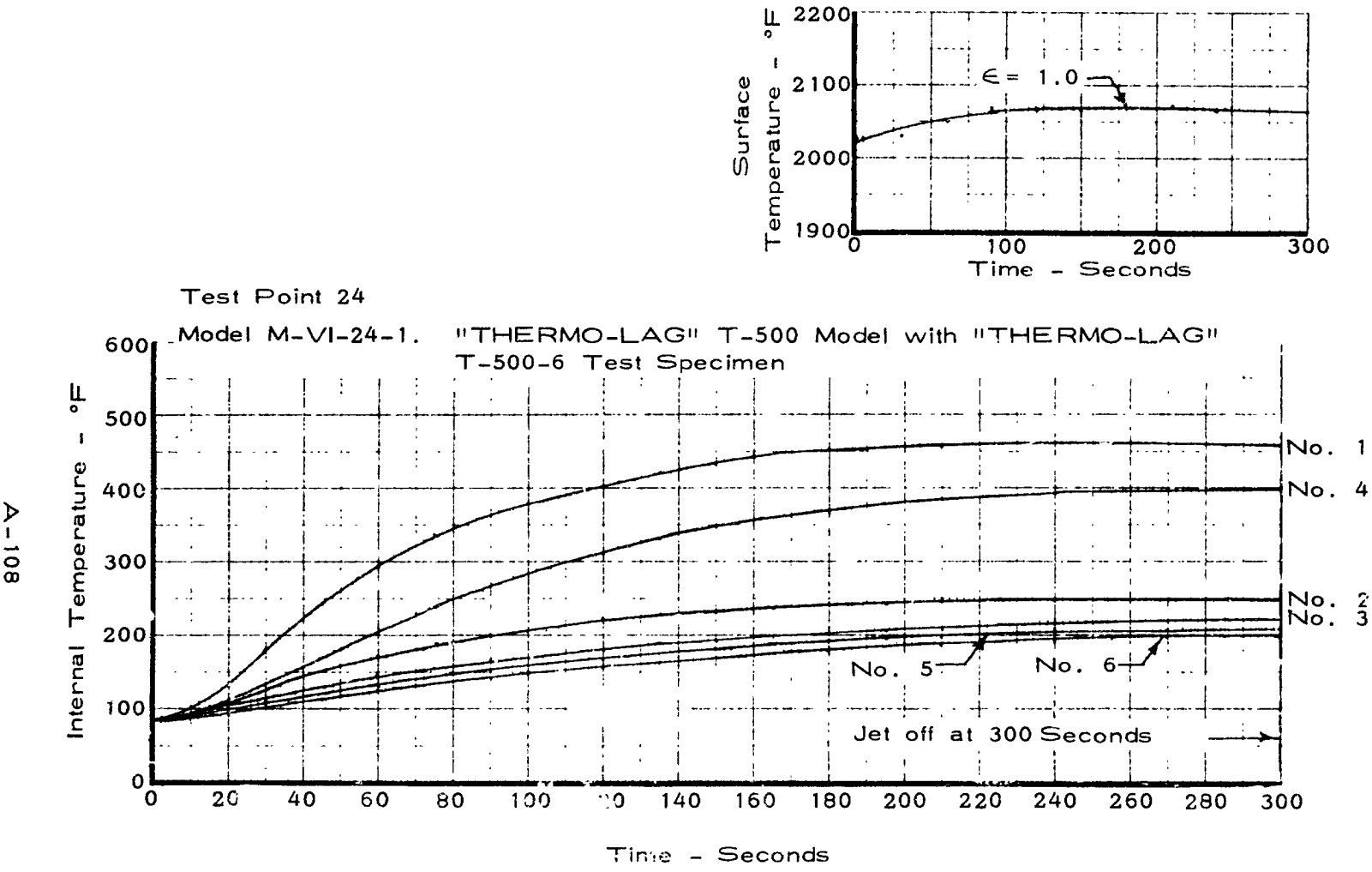


Figure A-106. Temperature-Time History of Model M-VI-24-1

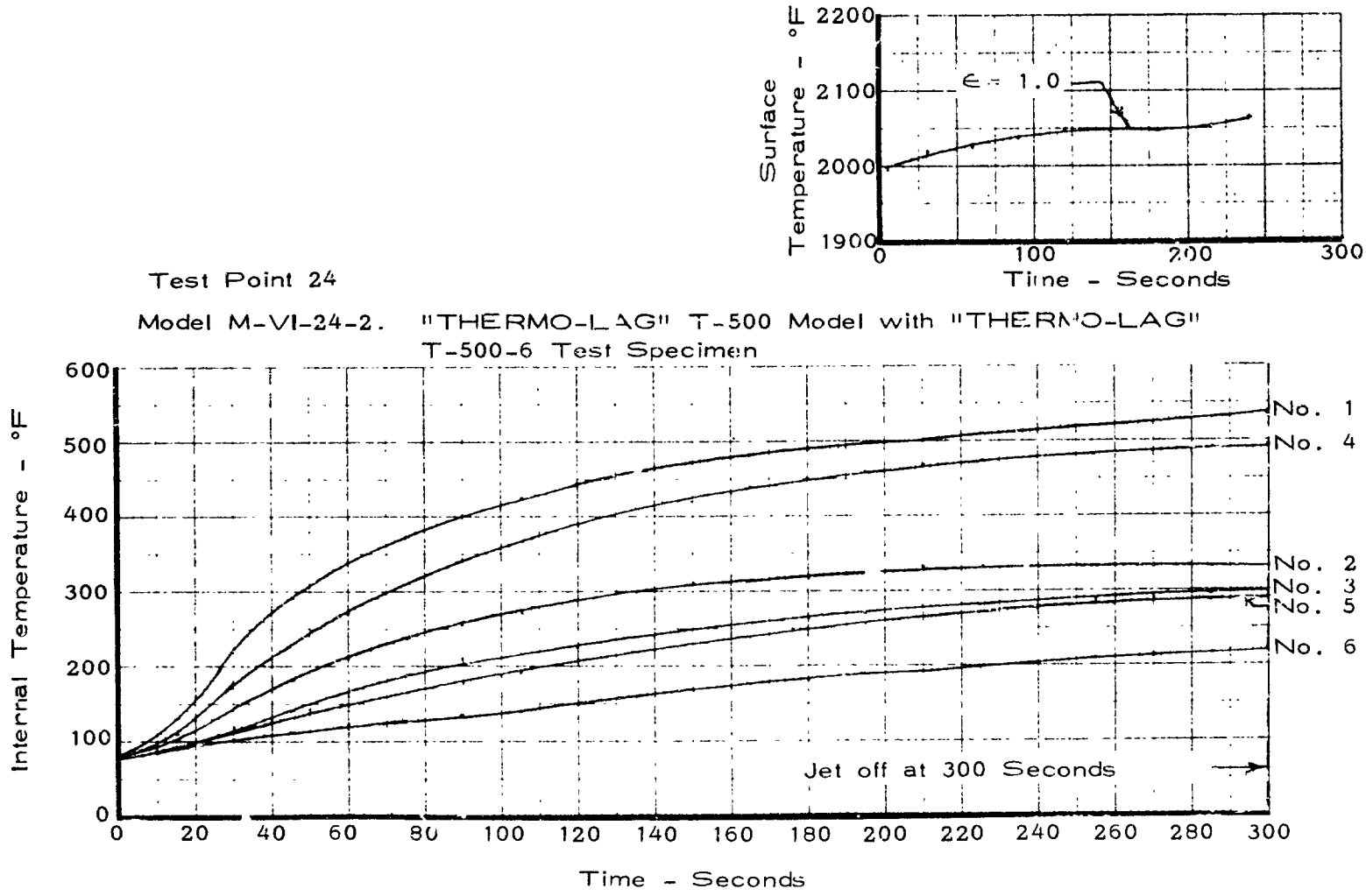


Figure A-107. Temperature-Time History of Model M-VI-24-2